UNIVERSITÀ DEGLI STUDI DI TRIESTE

XXVIII CICLO DEL DOTTORATO DI RICERCA IN

SCIENZE E TECNOLOGIE CHIMICHE E FARMACEUTICHE

Synthesis and Characterization of Novel Nanomaterials Based on Nanocrystalline Cellulose

Settore scientifico-disciplinare CHIM/06

DOTTORANDO / A
Ana Herreros López

COORDINATORE
Chiar.mo Prof. Mauro Stener

SUPERVISORE DI TESI
Chiar.mo Prof. Maurizio Prato

COSUPERVISORE DI TESI
Dr. Caroline A. Ahad Hadad

ANNO ACCADEMICO 2014 / 2015

A mi familia

Abstract

For the last few decades, our society has developed at an increasing rate, reaching an unprecedented degree of sophistication in many different fields. In recent years, concerns about environmental impact have grown into a strong trend in current research towards the development of sustainable materials. In this context, cellulose has become attractive for its ubiquity and abundance, as it originates from higher plants, tunicate, bacteria and algae.

Nanocrystalline cellulose (NCC), a rod-shaped nanoscale material with exceptional strength and physicochemical properties, can be prepared from this inexpensive renewable biomass. In addition to its potential use as a reinforcing agent for industrial biocomposites, pristine NCC exhibits low toxicity and poses no serious environmental concerns, providing impetus for its use in bioapplications.

The chemistry of NCC is dominated by the abundance of hydroxyl groups on its surface. These can be readily converted into other functional groups, or used directly to bind compounds in a non-covalent way. Both approaches are followed in this Thesis to obtain new NCC-based hybrid nanomaterials, with applications ranging from energy to catalysis to drug delivery. In all cases, the synthesis and full characterization are presented.

After a general introduction to cellulose in Chapter 1, covering its structure, derivatives, properties and applications, in Chapter 2 the preparation of nanocrystalline cellulose is described, as well as the oxidation of its surface. The full characterization of both materials is discussed. These two products are the starting materials for further modifications in the Chapters that follow.

In Chapter 3, the covalent functionalization of NCC to introduce azide function is presented. Alkynyl dendrons of PAMAM type are then introduced and linked *via* click chemistry to the previously introduced azide groups. The resulting functionalized cellulose nanocrystals have been used as templates for the preparation of stable and monodisperse gold nanoparticles in aqueous media. These NCC-supported particles are proposed as sustainable catalysts. The catalytic performance and recyclability/reusability of this new hybrid material were studied for the model reaction of 4-nitrophenol reduction with sodium borohydride, with outstanding results.

In Chapter 4, the biocompatibility of cellulose is harnessed for photodynamic therapy (PDT). Oxidized NCC is used as starting material to attach different C_{60} derivatives as active photosensitizers for the production of singlet oxygen. The functionalization is combined with the introduction of a fluorescent probe, in a one-pot reaction, for bioimaging purposes. In this case, a carbodiimide coupling is used to perform the functionalization. The ability of the new hybrid

materials to produce singlet oxygen is analyzed and a study of the cell uptake and phototoxicity is also carried out.

Finally, in Chapter 5 oxidized NCC is used as a dispersing and stabilizing agent for the exfoliation of 2D materials in water. The stability of the suspension and the quality of the resulting flakes and sheets are evaluated first. Then, the film-forming ability of NCC is exploited for the production of self-standing films containing 2D materials. The morphology and conductivity of the films are studied, as well as their performance as counter electrodes in dye-sensitized solar cells, as an alternative to Pt, currently the most widely used material for this application.

Riassunto

Negli ultimi decenni, la nostra società si è sviluppata ad un tasso crescente, raggiungendo un livello di sofisticazione inaudito in molti campi diversi. In anni recenti, le preocupazioni sull'impatto ambientale hanno nutrito una forte tendenza nella ricerca attuale verso lo sviluppo di materiali sostenibili. In questo senso, la cellulosa è diventata attraente per la sua ubiquità e abbondanza, perchè proviene da piante superiori, tunicati, batteri e alghe.

La cellulosa nanocristallina (NCC), un materiale su scala nanometrica a forma di bastoncino con eccezionali resistenza e caratteristiche fisicochimiche, può essere preparata da questa biomassa rinnovabile e poco costosa. Oltre al suo uso potenziale come agente di rinforzo per biocompositi industriali, la NCC presenta bassa tossicità e non rappresenta problemi ambientali seri, il che fomenta il suo utilizzo in applicazioni biotecnologiche.

La chimica della NCC è dominata dall'abbondanza di gruppi idrossilici sulla sua superficie, che possono essere facilmente convertiti in altri gruppi funzionali, oppure utilizzati direttamente per legare composti in modo non covalente. Entrambi gli approcci sono utilizzati in questa Tesi per ottenere nuovi nanomateriali ibridi per applicazioni che vanno dall'energia alla catalisi e al drug delivery. In tutti i casi si presentano la sintesi e la caratterizzazione completa.

Dopo una introduzione generale sulla cellulosa nel Capitolo 1, dove si descrivono la struttura, i derivati, le proprietà e le applicazioni, nel Capitolo 2 si presenta la preparazione della cellulosa nanocristallina, così come l'ossidazione della sua superficie. Si presenta e discute anche la caratterizzazzione completa di entrambi materiali. Questi due prodotti sarano i materiali di partenza per ulteriori modifiche nei Capitoli successivi.

Nel Capitolo 3 si propone una modificazione covalente della NCC per introdurre gruppi azide sulla superficie. Questi vengono poi usati per attacare dei dendroni di tipo PAMAM tramite una reazione di click chemistry. I materiali ibridi così ottenuti servono come template per la sintesi di nanoparticelle d'oro stabili e monodisperse in mezzo acquoso. Queste nanoparticelle supportate su NCC si propongono come catalizzatori sostenibili. La attività catalitica e la riciclabilità / riutilizzo de questi nuovi materiali ibridi sono state studiate mediante la reazione modelo della riduzione di 4-nitrofenolo con boroidruro di sodio, con ottimi risultati.

Nel capitolo 4 la biocompatibilità di cellulosa viene sfruttata per la terapia fotodinamica (PDT). In questo caso, la NCC ossidata è usata come materiale di partenza su cui attacare diversi derivati di C_{60} come fotosensibilizzanti per la produzione di ossigeno singletto. Questa funzionalizzazione si combina con l'introduzione di un fluoroforo, in una reazione *one-pot*, per scopi di bioimaging. Qua si ha utilizzato un accoppiamento carbodiimmide per eseguire la funzionalizzazione. La capacità di

produrre ossigeno singletto di questi nuovi materiali ibridi è stata valutata. Infine, l'assorbimento dalle cellule e la fototossicità sono state analizzate.

Nel Capitolo 5, la NCC ossidata viene utilizzata come disperdente e stabilizzante per esfoliare materiali 2D in acqua. Si è valutata la stabilità delle sospensioni e la qualità dei fiocchi risultanti. L'abilità filmogena della NCC viene poi sfruttata per produrre film contenenti materiali 2D (grafene e sulfuro di molibdene). La morfologia e la conducibilità dei film sono state studiate, così come il loro adempimento come elettrodi alternativi al platino in celle solari di nuova generazione. Questo è al momento il materiale più ampiamente utilizzato per questa applicazione.

Acknowledgements

This Thesis is the culmination of over three years of intense work, and it could not have happened without many people. First and foremost I would like to thank Prof. Maurizio Prato for the opportunity he gave me to be part of his group, for the funding and for the means to carry out the research reported here. I would also like to thank Dr. Caroline Hadad, who co-directed this work and watched closely over me. She has been an example both in the lab and outside.

I would like to thank the colleagues of the Organic Chemistry department at the University of Padova, who treated me kindly when I went there for short research visits. In particular Profs. Tommaso Carofiglio and Marcella Bonchio have been a constant support pillar for my work.

Prof. Tatiana da Ros has protected the PhD students in the lab, keeping a caring eye on all of us. Dr. Valeria La Parola at the University of Palermo and Dr. Luis Yate at biomaGUNE (San Sebastián, Spain) did the XPS measurements presented here. Dr. Valentina Rapozzi at the University of Udine carried out the biological tests and helped me interpret the data. Dr. Victoria Bracamonte was key for the electrochemistry measurements and their interpretation. Mr. Claudio Gamboz had endless patience teaching me how to use the TEM, and advised me on sample preparation and on how to get the most out of the instrument. Dr. Marco Carini, who finished his PhD when I was half-way with mine, kindly provided the C_{60} I used. To all of them, my sincerest thank you.

I would like to acknowledge the PhD students of the Prato group. We were all foreign strangers when we started, and have become a family in this time. In particular I want to thank “las chicas”: Valentina for enlivening the work under the fume hood we shared; Agniezska for her quick sense of humor (and the lemon vodka!); Tanja for her constant availability for everything and anything, and her sensible approach to life.

María, Cristina and I studied together in Spain before starting this adventure. We have shared spaces, friends and experiences in these years, and I hope we still do in the future.

I want to thank Arturo for being my confidant, sharing his pains and listening to mine. Also Jenni and Manu, whose joy was a breath of fresh air to the lab. We have shared a lot both inside and outside the lab, and I wish them the best for their own Theses.

I would like to acknowledge the post-docs of the group, in particular Jose for his optimism and unwavering faith in Chemistry; Alex, Andrea and Nuria, for the good times we spent together. During their stays, visiting students Jesús, Dania, Magda, and Iro shared labs, conversations and moments with me. Likewise the Master students who did their final Theses in the lab during my

time, Silvia, Lorenzo, Alexa and Federico contributed to my daily life. I would like to extend my thanks to the rest of the group.

Laura was the first person I met in Trieste outside University. I want to thank her and Cristina Moya all the good times we had together.

Verónica and Maribel were my predecesors and my first link to Trieste.

Prof. Julián Rodríguez directed my Master Thesis, and encouraged me to pursue a PhD when I finished. I want to thank him for his bet on me, and for caring about me and my work.

My friends Miguel, Luismi and Raquel have been by my side since school times, and I am grateful they are an important part of my life.

I am most grateful to my family. My parents Ana and Francisco have encouraged and supported me every step of the way, accepting that I leave to pursue my dreams. My brother Paco and my sister Celia with Javier are always there for me. And Menta, whose company made writing a lighter burden.

Last, but not least, I want to thank Fernando for his patience, his support and his counsel. He made the difficult moments more bearable. We met during my PhD, and he has become a central part of my life.

I am glad I came to Trieste for this adventure. Although the city gave me an unfriendly first impression, it has conquered a place in my heart.

Trieste, March 2016

Agradecimientos

Esta Tesis es la culminación de más de tres años de intenso trabajo, y no habría sido possible sin la influencia y participación de muchas personas. En primer lugar quiero agradecer al Prof. Maurizio Prato la oportunidad que me dio de ser parte de su grupo, así como la financiación y los medios para llevar a cabo la investigación que presento aquí. Me gustaría también agradecer el esfuerzo de la Dra. Caroline Hadad, que co-dirigió este trabajo y me siguió de cerca. Ella ha sido un ejemplo tanto dentro como fuera del laboratorio.

Quiero agradecer también a los compañeros y colegas del departamento de Química Orgánica de la Universidad de Padua el buen trato que me dieron durante mis breves estancias. En particular los Profesores Tommaso Carofiglio y Marcella Bonchio han sido un pilar constante en mi trabajo.

La Profesora Tatiana da Ros fue la protectora de los estudiantes de Doctorado en el laboratorio, y estuvo siempre pendiente de nosotros. La Dra. Valeria La Parola de la Universidad de Palermo y el Dr. Luis Yate del biomaGUNE (San Sebastián) realizaron las medidas de XPS presentadas aquí. La Dra. Valentina Rapozzi de la Universidad de Udine llevó a cabo los tests biológicos y me ayudó a interpretar los datos. La Dra. Victoria Bracamonte fue clave para las medidas de electroquímica y su interpretación. El Sr. Claudio Gamboz tuvo la paciencia infinita de enseñarme a usar el TEM, y me dio consejos sobre la preparación de la muestra y cómo sacarle el máximo partido al instrumento. El Dr. Marco Carini, que terminó su tesis cuando yo estaba a mitad de la mía, me cedió amablemente el C_{60} que usé. A todos ellos, mi más sincero agradecimiento.

Querría reconocer también a los demás estudiantes de Doctorado del grupo Prato. Cuando llegamos éramos todos extranjeros y desconocidos, y en este tiempo nos hemos convertido en una familia. En particular quiero agradecer a “las chicas”: Valentina por hacer más ameno el trabajo en la campana que compartíamos; Agniezska por su fino sentido del humor (y por el vodka de limón!); Tanja por su constante disponibilidad para cualquier cosa, y por su madurez.

María, Cristina y yo estudiamos juntas en España antes de comenzar esta aventura. Hemos compartido espacios, amigos y experiencias en estos años, y espero que sigamos haciéndolo en el futuro.

Quiero agradecer a Arturo el ser mi confidente, compartiendo sus problemas y escuchando los míos. Cuando llegaron, Jenni y Manu trajeron un soplo de aire fresco al laboratorio. Juntos hemos compartido mucho tanto dentro como fuera del laboratorio, y les deseo lo mejor en sus respectivas Tesis.

Les doy las gracias también a los post-docs del grupo, en especial a Jose por su optimismo y su fe inquebrantable en la Química; y a Alex, Andrea y Nuria por los buenos ratos que pasamos juntos. Durante sus estancias, compartí laboratorio, conversaciones y momentos con los doctorandos visitantes Jesús, Dania, Magda e Iro. Igualmente los estudiantes de Master del laboratorio durante mi periodo allí, Silvia, Lorenzo, Alexa y Federico participaron en mi vida diaria. Quiero extender también mis agradecimientos al resto del grupo.

Laura fue la primera persona de fuera de la Universidad que conocí en Trieste. Quiero agradecerle a ella y a Cristina Moya todos los buenos ratos que pasamos juntas.

Verónica y Maribel fueron mis predecesoras y mi primer contacto con Trieste.

El Prof. Julián Rodríguez dirigió mi Tesis de Master, y me animó a realizar el Doctorado cuando la terminé. Quiero agradecerle su apuesta por mí, y también el que se preocupara por mí y mi trabajo.

Mis amigos Miguel, Luismi y Raquel han estado a mi lado desde el instituto, y estoy agradecida de que sean una parte importante de mi vida.

Mi mayor reconocimiento es para mi familia. Mis padres Ana y Francisco me han animado y apoyado cada paso de este camino, y aceptaron mi decisión aunque implicase irme lejos. Mi hermano Paco y mi hermana Celia con Javier han estado y están siempre ahí para mí. Y Menta, cuya compañía hizo la escritura más llevadera.

Por último pero no menos importante, quiero agradecer a Fernando su paciencia, su apoyo y su consejo. Él hizo los momentos difíciles más soportables. Nos conocimos durante mi Doctorado, y se ha convertido en una parte central de mi vida.

Estoy contenta de haber venido a Trieste para esta aventura. Aunque me resultó antipática en un primer momento, ha conquistado un lugar en mi corazón.

Trieste, Marzo de 2016

Table of Contents

List of abbreviations

4-AP	4-aminophenol
4-NP	4-nitrophenol
AFM	Atomic Force Microscopy
AGU	Anhydroglucose Unit
AuNP	Gold Nanoparticle
CD_3OD	Methanol-d4 (tetradeuteromethanol)
$CDCL_3$	Chloroform-d (deuterochloroform)
CE	Counterelectrode
CV	Cyclic voltammetry
DMF	Dimethylformamide
EDA	Ethylene diamine
EDC	*N*-(3-dimethylaminopropyl)-*N*'-ethylcarbodiimide
EG	Expanded grapheme
E_{on}	Onset potential
FITC	Fluorescein isothiocyanate
FT-IR	Fourier-transform Infrared
FTO	Fluorine Tin Oxide
i_p	Peak current
MES	2-(*N*-morpholino)ethanesulfonic acid
NCC	Nanocrystalline cellulose
NHS	*N*-hydroxysuccinimide
NMP	*N*-methylpyrrolidine
NMR	Nuclear Magnetic Resonance

O_D-CB	Ortho-dichlorobenzene
ox-NCC	surface-oxidized Nanocrystalline cellulose
PAMAM	Poly(amidoamine)
PDT	Photodynamic Therapy
PS	Photosensitizer
SPR	Surface Plasmon Resonance
TEM	Transmission Electron Microscopy
TEMPO	2,2,6,6-tetramethylpiperidine-1-oxyl
TGA	Thermogravimmetric Analysis
UV-Vis	Ultraviolet-visible spectrometry
XPS	X-ray Photoelectron Spectroscopy

Chapter 1: Introduction

Cellulose is the most abundant renewable organic material produced on Earth, being widely distributed in higher plants, also present in several marine animals (tunicates), and to a lesser degree in algae, fungi, bacteria, invertebrates, and even amoeba.[1] Cellulose is a fibrous, tough, water-insoluble substance that plays a major role as structural component of plant cell walls. Its ubiquity has supposed that this polymer became a material of choice from ancient times, in the form of wood and plant fibers as an energy source, for building materials and for clothing. Empirical knowledge of dying cellulose fibers or preparing charcoal has also accompanied us for many centuries. Its use in the form of paper and board goes back to the Egyptian papyri, and since then it has also played a central role in the recording and transmission of human culture.

As a chemical raw material, cellulose has been used for about 150 years, even before its polymeric nature was completely recognized and understood. It was not until 1838 that Anselme Payen first isolated this fiber and coined the name cellulose.[2] Since then, cellulose has been subject of a lot of research. Advancing insights into the structural features and reactivity of cellulose have allowed stepwise the creation of novel types of materials.[3] Breakthroughs on the industrial evolution of cellulose were the discovery of cellulose nitrate, namely nitrocellulose, followed by the technical synthesis of partially functionalized cellulose nitrate plasticized with camphor, better known under the trade name of Celluloid. The development of the particularly important large-scale viscose process for producing rayon fiber and filament is still practiced today with an output of about 3 million tons annually worldwide. It makes use of the formation of cellulose xanthogenate, (i.e. a water-soluble, less-stable anionic ester), prepared by reaction of cellulose with aqueous sodium hydroxide and CS_2 and its decomposition by spinning in an acid bath.[4] Other materials for coatings, films, membranes, building materials, drilling techniques, pharmaceuticals, and foodstuffs were obtained by the large-scale production of cellulose derivatives.[5]

Industrial development efforts today are mainly focused on nanotechnology, defined as the study of matter with at least one dimension in the nanometer range. This interest comes up from the discovery of new fascinating properties when materials dimensions are restricted to the nanoscale. In this context, it could appear that the possibilities, as far as cellulose is concerned, are fully exploited. However, this is far

from true. New nature based nanomaterials, isolated from cellulose arise with a myriad of opportunities still to offer in the framework of sustainable development.

1.1. Cellulose structure

Cellulose is a linear high molecular weight homopolymer composed of D-glucopyranose units covalently linked by β-1,4-glycosidic bonds. Every glucose unit is rotated 180° with respect to its neighbors, and the repeating unit comprises a dimer of glucose, known as cellobiose (Figure 1). In a cellulose chain, all D-glucopyranose rings, so called anhydroglucose units (AGU), adopt a $^1C_4$ chair conformation, the lowest free energy conformation of the molecule. As a consequence, all the hydroxyl groups are positioned in the equatorial plane, while the hydrogen atoms are in axial position. Each monomer bears free hydroxyl groups at the C-2, C-3 and C-6 atoms. The ability of these hydroxyl groups to form hydrogen bonds with those of adjacent ring molecules further stabilizes the linkage and results in the linear configuration of the cellulose chain. Besides, each cellulose chain possesses a directional chemical asymmetry with respect to the termini of its molecular axis: one end is a chemically reducing functionality (i.e., a hemiacetal unit) and the other has a non-reducing end (i.e., a pendant hydroxyl group). The degree of polymerization (DP) of the cellulose chain is estimated between 10000 – 15000 AGU depending on the source material.

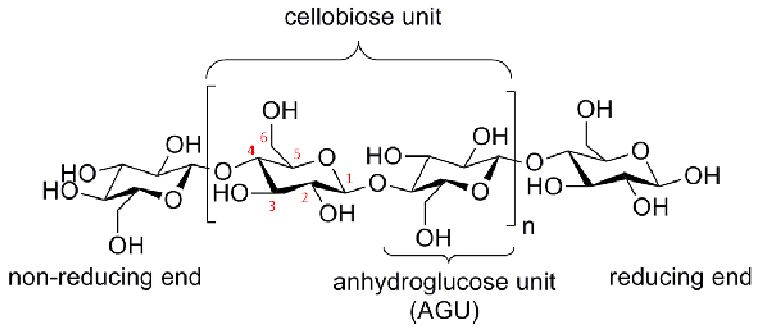

Figure 1. Molecular structure of cellulose.[6]

In nature, cellulose does not occur as an isolated molecule, but is found as assemblies of individual cellulose chains forming fibers. This is because individual molecules undergo spinning in a hierarchical order at the site of biosynthesis. During this process, van der Waals and intermolecular hydrogen bonds between hydroxyl groups of neighbor molecules assist the parallel stacking of multiple chains. Approximately 36 chains are assembled together to form elementary fibrils (protofibrils). These protofibrils further aggregate into larger units known as microfibrils, of typically 5-50 nm width. As a consequence of biopolymerization process, the order is not uniform along the whole structure. Defects are generated where the microfibrils are distorted by internal strain in the fiber and proceed to tilt and twist (Figure 2).[7]

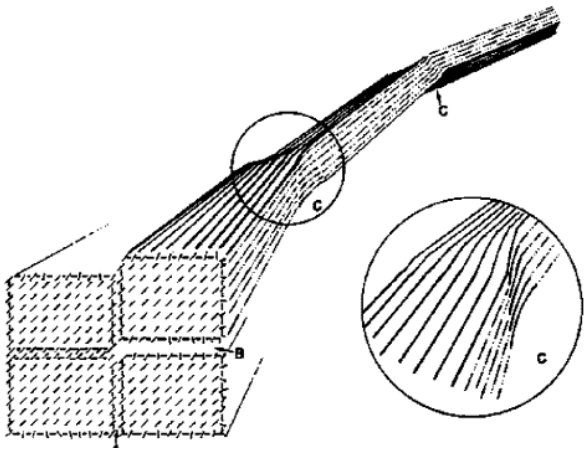

Figure 2. Schematic representation of the microfibril illustrating the microstructure and strain distorted regions (defects).[7]

These domains are less ordered or amorphous regions within the microfibril. Microfibrils further assemble in the common cellulose fibers that together with other polymers (i.e. hemicelluloses, lignin) give rise to the known plant tissue, structural component of plants and trees (Figure 3).

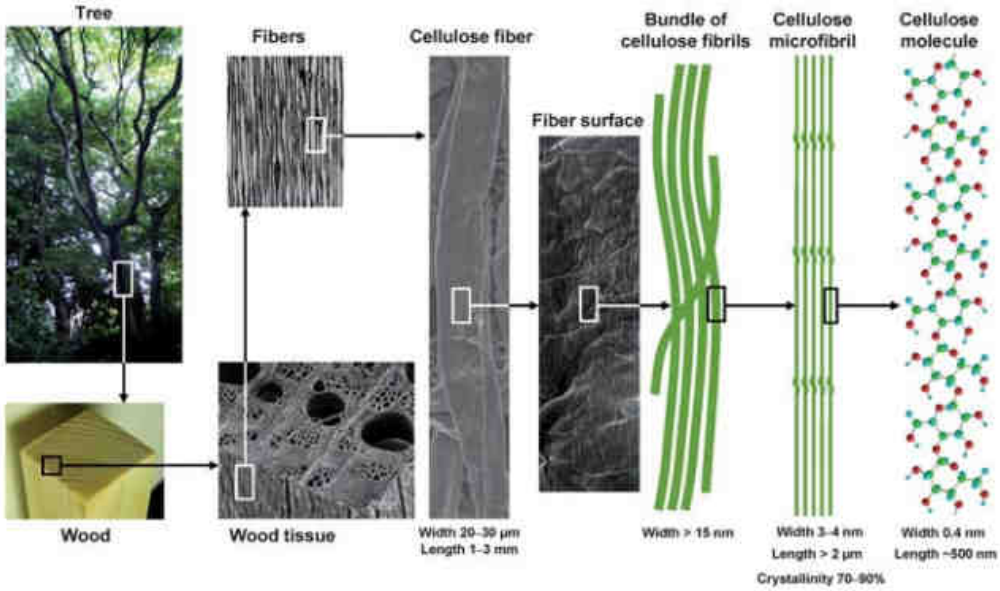

Figure 3. Schematic representation of the hierarchical structure in cellulose.[8]

This very complex network of van der Waals forces, intra- and inter-molecular hydrogen bonding arrangement can vary widely, giving rise to different ordered hydrogen bond systems, which in turn results in various types of supramolecular semi-crystalline structures.

Four interconvertible polymorphs of cellulose have been identified, namely I, II, III and IV, differing in unit cell dimensions and, possibly, in chain polarity.[9]

In nature, cellulose is only produced in the form of cellulose I, and thus, this polymorph is commonly referred to as “natural” cellulose. Its structure is metastable and can be converted either to cellulose II or III. Cellulose II is the second most

extensively studied allomorph for its technical relevance, as it is the form present in commercial products such as cellophane, Rayon and Tencel™ synthetic fibers.[5] It can be obtained by chemical regeneration (solubilization and recrystallization) or mercerization (swelling in concentrated sodium hydroxide solution). Cellulose III is obtained upon liquid ammonia treatment of either cellulose I or II, and subsequent thermal treatment produces cellulose IV.[10]

Concerning crystalline structure of cellulose I, evidences of the existence of two suballomorphs (Iα) and (Iβ) was found in 1984 by cross-polarization magic angle spinning (CP-MAS).[11] These two allomorphs coexist in various proportions depending on the cellulose source.[12,13] It has been shown that Iα structure is prevalent in algae and bacteria,[14] whereas Iβ is the mayor component in higher plants and tunicates.[15] In both structures, cellulose chains adopt a "parallel-up" fashion.[13] This means that all cellulose chains are arranged such that the 1-4 linkage points in the same direction. Iα corresponds to a triclinic P1 unit cell containing one chain that has two adjacent glucose residues related by pseudo two-fold screw-axis symmetry. Iβ has a monoclinic P21 unit cell containing two conformationally distinct chains, which are referred to as the corner and center chains (Figure 4).[16] Iα, a metastable phase, can be converted to the more thermodynamically stable Iβ phase by high-temperature annealing in various media.[17]

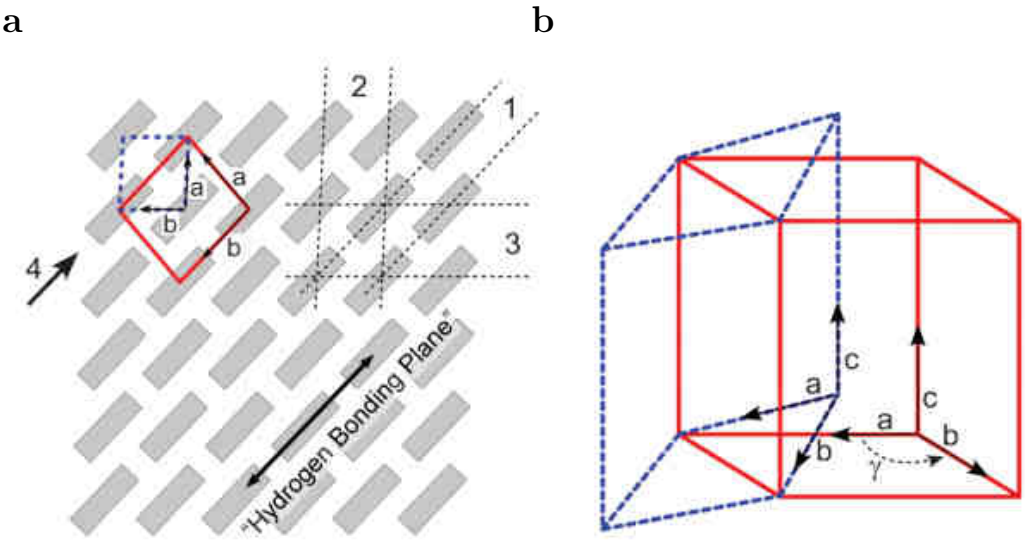

Figure 4. Schematic of the unit cells for cellulose Iα (triclinic, dashed line) and Iβ (monoclinic, solid line) projection along the chain direction with the Iα and Iβ unit cells superimposed on the cellulose I crystal lattice, showing the parallelogram shape of both unit cells when looking down the c-axis (a)[18] and relative configuration of Iα with respect to Iβ unit cell (b).[19]

Understanding the hydrogen bonding patterns within cellulose Iα and Iβ structures has been the subject of much debate. Since all hydroxyl groups are equatorial to the ring plane, it is common practice to acknowledge that the intra- and interchain hydrogen bonding is most prevalent within the so called "hydrogen-bonding" plane. Two coexisting hydrogen bonding networks (A and B) have been proposed (Figure 5).[20] The intra-chain hydrogen bonding is dominated by the strong O3-H-O5 bond. This intra-chain hydrogen bonding is responsible for the rigid and linear shape of

each cellulose chain.[21,22] The existence of hydrogen bonds extending from the O(3)-H hydroxyl to the O(5) ring oxygen of the next unit across the glycosidic linkage in native crystalline cellulose can be concluded from X-ray diffraction, NMR and IR spectroscopy.[23,24] To date, intermolecular hydrogen between only the OH group at the C-6 and C-3' (' means of the neighboring chain) positions of cellulose molecules adjacently located in the same lattice plane is assumed. The number of weak interchain hydrogen bonds in cellulose Iβ is believed to be greater than in the Iα, what is supposed to contribute to the higher stability of this polymorph.[21] The intermolecular hydrogen bonding in cellulose is responsible for the sheet-like nature of the native polymer.[25]

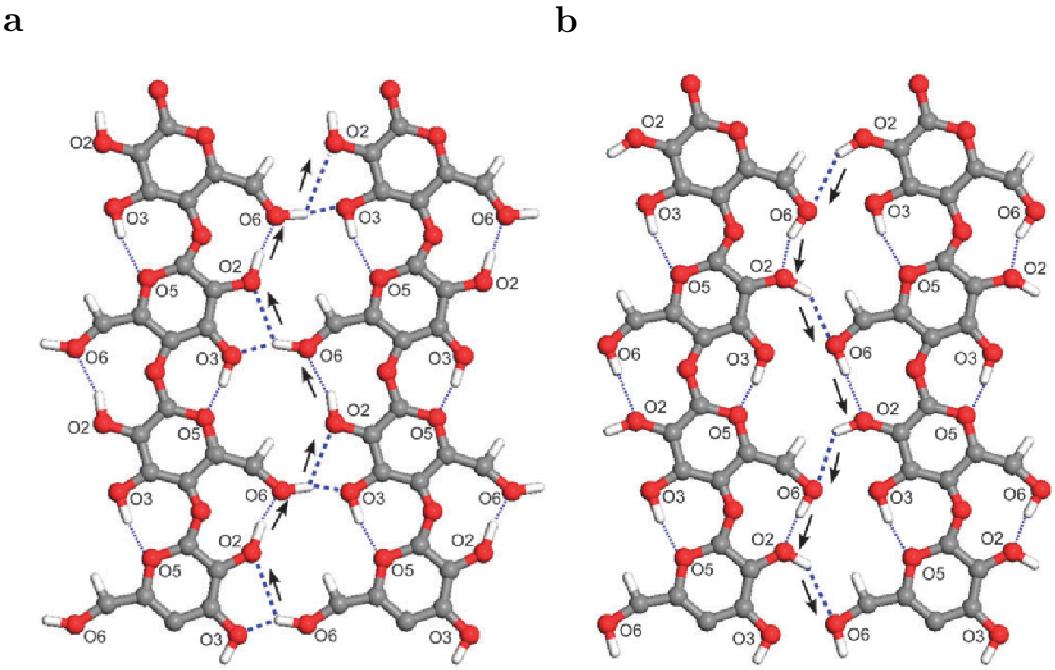

Figure 5. Schematics of two suggested hydrogen bonding cooperative networks: A (a), and B (b), within the hydrogen-bonded plane. Thin dotted lines highlight the intrachain hydrogen bonding, while the thick dotted line shows the interchain hydrogen bonding. Arrows show the donor–acceptor–donor directions.[26]

1.2. Nanocellulose families

The structure of cellulose permits to obtain different materials in the nanometer range, both by bottom up or top down approaches. Such isolated cellulosic materials with one dimension in the nanometer range are referred to generically as nanocelluloses. On the basis of their dimensions, which in turn depend mainly on the processing conditions, nanocelluloses may be classified in three main subcategories. The first one consists on the biosynthesis by microorganisms from low molecular weight sugar in a culture medium, and is known as bacterial nanocellulose (BNC). The top down methods involve the disruption of the hierarchical structure of cellulose fibers. According to their morphology, cellulose fibers can be laterally disintegrated into their substructural nano-scale fibrils resulting in nanofibrillated cellulose (NFC), or can be dissociated transversely at the amorphous regions present along the fiber

leading to nanometric and highly crystalline defect-free rod-like fragments, so called nanocrystalline cellulose (NCC). In a unique manner, these nanocelluloses combine important cellulose properties, such as hydrophilicity and broad chemical-modification capacity, with the specific features of nanoscale materials, mainly caused by the very large surface area of these materials.

1.2.1. Bacterial Nanocellulose (BNC)

Besides being a dominant component of cell walls in plants, cellulose is also secreted extracellularly as cellulose fibers by several bacterial species. The most known *Acetobacter G. xylinus* species (Figure 6a) produce such bacterial cellulose by cultivation in aqueous culture media containing carbon and nitrogen sources during a time period of days. The resulting cellulosic network structure is in the form of a pellicle of randomly assembled ribbon shaped fibrils less than 100 nm wide (Figure 6b), which are in turn composed of a bundle of much finer nanofibrils (2 to 4 nm in diameter).[27] These bundles are relatively straight, continuous and dimensionally uniform, with morphology depending on the specific bacteria and culturing conditions.[28,29]

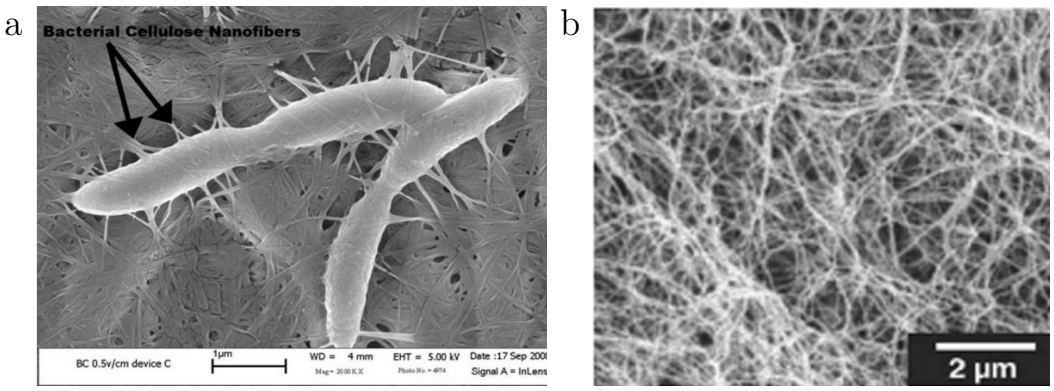

Figure 6. Scanning electron micrographs of *Acetobacter Xylinum* cells embedded and producing cellulose (a)[30] and of a bacterial cellulose pellicle (b).[31]

1.2.2. Nanofibrillated Cellulose (NFC)

This type of nanocellulose was first introduced by Turbak *et al.* in the 1980s.[32] The process basically consists on the disintegration of cellulose fibers along their axis to isolate nanofibrils. Typically, suspensions of wood-based cellulose fibers are forced through mechanical devices and the treatment is repeated several times (i.e. number of passes). This mechanical treatment promotes the delamination of fibers and liberates sub-structural fibrils that after every pass become smaller, more uniform in diameter, but also less crystalline due to mechanical damage.[33] The mechanical treatments comprise high pressure homogeneization, microfluidization or grinding (Figure 7a and b)[34] Other reported methods are high-speed blending, cryocrushing, high-intensity ultrasonication, and steam explosion, [35] but these are still in a very early stage and far from being scaled up. The major drawback from a commercial point of view is the very high energy consumption amounting to over 25000 kWh per

ton in the production of NFC as a result of the required multiple passes through the homogenizers. Another concern is the extensive clogging of the homogenizer.[36]

Generally, chemical or enzymatic methods are applied in order to weaken the interfibrillar hydrogen bonds prior to treatment and aid the separation of cellulose microfibrils.[26]

Using the above-mentioned technologies, NFCs have been prepared from numerous cellulosic sources including soft and hard woods, sugar beet pulp, banana, potato, wheat straw, bamboo and also from some seaweed.[27,35] The microfibrils thus generated have a high aspect ratio, with lengths up to several micrometers and widths ranging from 10 to a few hundred nanometers depending on the nature of the cellulose used (Figure 7c). NFCs normally exhibit gel-like characteristics in water, with pseudoplastic and thixotropic properties.[36]

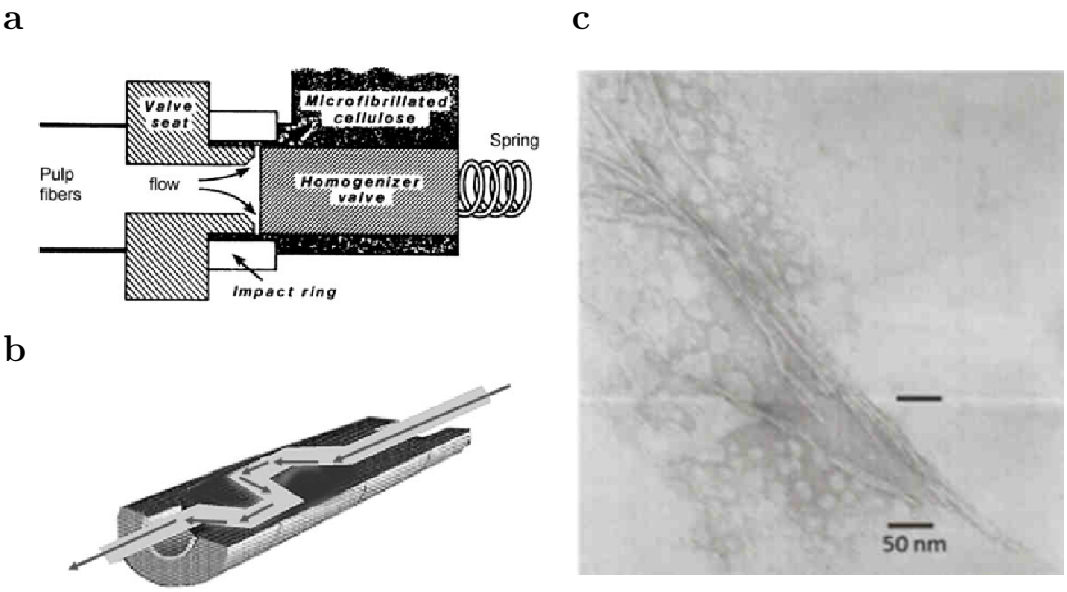

Figure 7. Some devices used for the delamination of fiber cell walls to make NFC. High-pressure homogenizer, in which fibers are pressed through a slit between the valve seat and the pressurized homogenizer valve (a), interior view of a high-pressure microfluidizer, in which the fiber suspension is pumped through narrow slits under high pressure (b)[32] and TEM image of NFC (c).[37]

1.2.3. Nanocrystalline Cellulose (NCC)

Nanocrystalline cellulose is typically extracted from cellulosic biomass using strong acid hydrolysis. They are generated by the liberation of crystalline regions of cellulosic fibers by hydrolysis with mineral acids.

As already mentioned, amorphous and crystal parts of cellulose are sequentially distributed along the fiber. The crystalline parts are strongly packed and thus more resistant to acid attack. Therefore, the chemical process involves the cleavage and disruption of the more readily accessible amorphous regions to liberate rodlike crystalline cellulose sections (Figure 8a). When the desired level of depolymerization has been reached, the acidic mixture is diluted, and the residual acids and impurities are fully removed by centrifugation and extensive dialysis.[1,36,38]

Compared to NFC, NCCs have smaller size and very limited flexibility (Figure 8b), as they do not contain amorphous regions but instead exhibit elongated crystalline rod-like shapes, with widths and lengths of 5–70 nm and 100 nm and 1000 nm, respectively.[36]

The dimensions of the nanocrystals released are strongly influenced by the starting cellulose sources and their degree of crystallinity (Table 1). Cotton, wood, and Avicel yield a narrow distribution of highly crystalline nanorods with widths and lengths of of 5–10 and 100–300 nm,[39] whereas other sources, such as tunicates, bacteria, and algae, generate crystals with larger polydispersities.[40,41] The nanocrystals may also show different geometries, depending on their biological source; for example, algal cellulose membrane displays a rectangular structural arrangement, whereas both bacterial and tunicate cellulose chains have twisted-ribbon geometry.[41,42] The size of resulting crystals is also dependent on hydrolysis parameters, such as temperature or type of mineral acid (Table 1).[43]

Table 1. Overview of the dimensions of cellulose nanocrystals depending on the source and acid employed during the hydrolysis.[44]

Source	Acid	Length (nm)	Width (nm)
Wood[45]	H_2SO_4	100-300	3-5
Cotton[46]	HCl	100-150	5-10
Microcrystalline cellulose (MCC)[47]	H_2SO_4	200-400	<10
Tunicates[48]	H_2SO_4	>1000	10-20
Bacteria[49]	H_2SO_4	100-1000	10-50
Bacteria[50]	HCl	160-420	15-25

The acid employed in the hydrolysis also determines the surface functionality. NCC prepared from HCl is weakly negatively charged, whereas during hydrolysis with H_2SO_4, sulfate groups are introduced on the surface of nanocrystals. Owing to their highly repulsive character, NCC suspensions prepared with sulfuric acid exhibit higher colloidal stabilities. The effect of such parameters has been extensively reviewed,[44] and will be further discussed in Chapter 2.

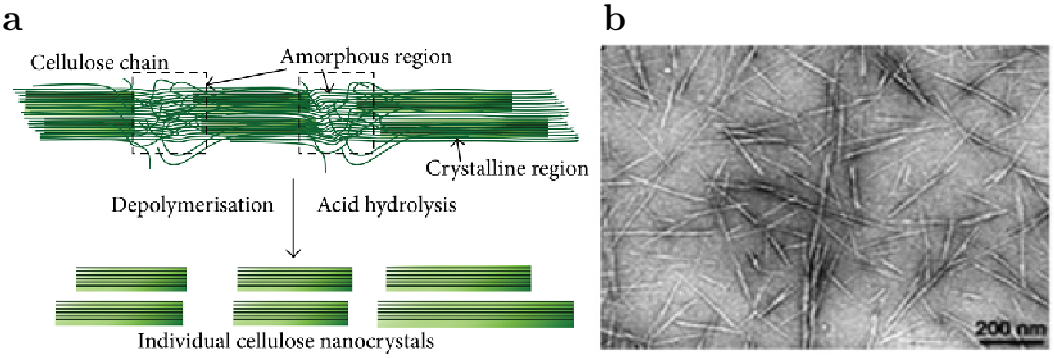

Figure 8. Schematic representation of cellulose acid hydrolysis process NCC (a)[51] **and TEM image of NCC (b).**[37]

As the material employed in this work was uniquely nanocrystalline cellulose (NCC), from this point on, the discussion will be focused on this particular material. Hereafter, its main properties, methods of functionalization and applications are overviewed.

NCC properties

1.2.4. Mechanical properties

Most studies on NCC mechanical properties have focused on the measurement of elastic modulus. The elastic modulus is a mechanical property of linear elastic solid materials. It defines the relationship between stress (force per unit area) and strain (proportional deformation) in a material.

Due to the higher crystallinity of NCC, a higher elastic modulus with respect to cellulose should be expected, since the contribution of amorphous fraction becomes smaller. Indeed, theoretical calculations and indirect experimental measurements using atomic force microscopy (AFM), X-ray diffraction analysis, inelastic X-ray scattering, Raman scattering, etc. were used to calculate the elastic properties of NCC.

Tunicate NCC has been used as idealized particle because of its longer length, larger cross-section, low size distribution and higher crystallinity. The experimental elastic modulus of the NCC obtained from tunicates was determined using a three-point bending test with AFM, where the AFM tip measured the applied force and the bending displacement of individual NCC. The elastic modulus in this case was found to be ~150 GPa.[52] Sturcova *et al.* used *in situ* combination of tensile experiments with Raman spectroscopy, and they found a value of ~143 GPa,[53] which is much more than that of steel wire and Kevlar®-49 (~112 GPa).

In another study, transverse elastic modulus of NCC was also determined by comparing the experimental force–distance curves with three-dimensional finite elemental calculations.[54] This measurement proved that the transverse modulus of an individual NCC lies in the range of 18–50 GPa.[54]

1.2.5. Liquid crystallinity

Due to its rod-like structure, it is intrinsic to NCC the particularity of forming lyotropic liquid crystalline phases at a given concentration. A lyotropic liquid crystal is by definition a dispersion of anisotropic macromolecular entities in a solvent. In these systems, phase transitions are strongly influenced by aspect ratio of the nanorods and very susceptible to changes on the nanoparticle concentration. Depending on particle properties and external conditions, the liquid crystalline ordered phase can be described as: nematic (rod-like molecules oriented along one axis, called the director, with a long range orientational order but a short range positional order), chiral nematic or cholesteric (the nematic microstructure is twisted along an axis).[55]

For concentrated NCC, Gray *et al.* discovered that when the cellulose crystallites were sufficiently short and uniform (always less than 100 nm) and had a high degree of sulfates esterified onto the surface, chiral nematic ordered structures formed and arranged themselves in a staircase-like helical superstructure along the director (Figure 9).[56,57] The thickness of the layer structure up to a complete turn of the director is the pitch (p) of the helix.

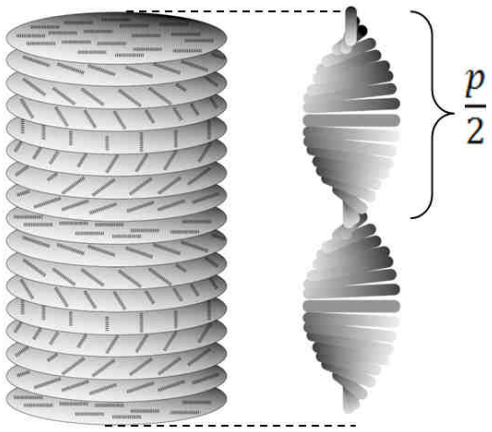

Figure 9. Schematic representation of chiral nematic phase in NCC.[58]

In dilute systems, the rotation of nanoparticles is merely governed by Brownian motion. However, in a semi-dilute system, rotation of nanoparticles start to be hindered until the concentration reaches the limit where the particles motion is confined to small volumes, known as isotropic concentration. Once a certain equilibrium concentration is reached, the system is in the biphasic region, where there is an equilibrium between some particles in the anisotropic phase with those in the isotropic phase. As concentration increases even more, the system becomes fully liquid crystalline, this is, domains of NCC coalesce to form unidirectional and self oriented or anisotropic phase (Figure 10).[1]

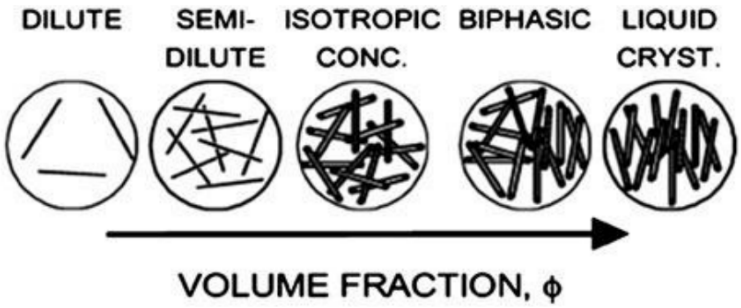

Figure 10. Phase behavior of fluid dispersed rods.[59]

The alignment of NCC creates a microscopic shear birefringence that can be observed through cross-polarizers (Figure 11). Nevertheless, after a certain period of time at rest, the suspension can spontaneously separate into an isotropic and anisotropic phase (Figure 11).[60]

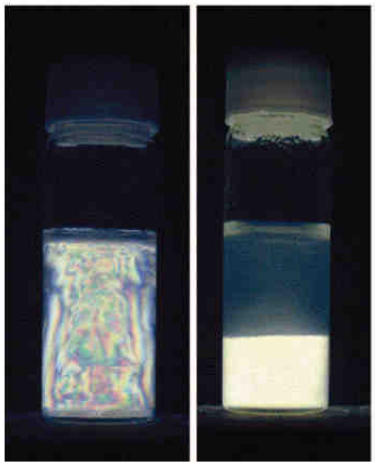

Figure 11. Aqueous 0.63% (w/w) NCC suspension observed between cross-polarizers. Immediately after shearing the suspension shows many iridescent birefringence patterns (lef); after 1 week, the suspension separates into the upper isotropic and the lower anisotropic phases (right).[61]

Equilibrium concentration, where isotropic and anisotropic phases coexist may be strongly affected by hydrolysis conditions, mineral acid used in the hydrolysis, size of the particles,[45] concentration, as well as by external stimuli, such as temperature, ionic strength and other external forces.[38] For instance, the addition of electrolytes was showed to have a huge effect in the critical concentration for phase separation. It was found that increasing electrolyte decreased anisotropic phase formation, and decreased also the chiral nematic pitch.[39] The phase separation and chiral nematic pitch was also influenced by the nature of NCC counterions.[62] In general, the critical concentration increases with increasing counterion size. Chiral nematic phase of an aqueous NCC dispersion can also be modified by magnetic field. The chiral nematic axis was aligned in the field direction by applying a static magnetic field, forming highly regular patterns. On the other hand, when a rotating magnetic field was applied to the dispersion a nematic-like alignment was also observed.[48]

1.2.6. Rheological properties

Rheology studies the flow of matter, primarily in a liquid state, but also as 'soft solids' or solids under conditions in which they respond with plastic flow rather than deforming elastically in response to an applied force.[63] The study of rheological properties of NCC is focused either in the gelation properties through viscosimetric measurements, or the investigation of its liquid crystalline behavior through rheological characterizations.

Nanocelluloses easily tend to form hydrogel structures, (i.e. materials composed mainly by water that is contained in a hydrophilic polymeric matrix). The viscosity of NCC dispersions increases steeply with concentration and two critical values can be determined, namely, the overlap and the gelation concentration, which depend strongly on the aspect ratio of the crystals.[64] Marchessault *et al.* first demonstrated that the hydrodynamic properties of the whiskers are directly related to particle size and the length distributions.[65] A typical shear rate viscosimetry profile for NCC presents three different regions. At low shear rates, a first region (region I) is

observed, with higher viscosity values corresponding to shear thinning and indicating the initial alignment of the domains formed by the whiskers. At intermediate shear rates, the second region appears (region II), a plateau indicating that these domains are aligned in the flow direction. At higher shear rates, a second shear thinning region (region III) is observed because of the breaking down of these domains giving rise to individual alignment of the whiskers. This behavior is characteristic of liquid crystals.[66] The explanation for such behavior is that at a critical shear rate, the nanocrystals align due to their rod-like nature, greatly easing their flow. Under enough shear the chirality of the suspensions breaks down in favor of a simple nematic structure. Diffraction/scattering and SEM have also confirmed this hypothesis.[67–69] Additionally, the time constant of relaxation is highly dependent upon aspect ratio with higher aspect ratios staying aligned for longer times after shear.[44]

1.2.7. Film-forming properties

An inherent property of cellulose nanocrystals is the spontaneous formation of self-standing films upon drying.[66] As the concentration increases, a point is reached where the mobility of the rod-like nanocrystals becomes severely constrained, resulting in gelation or glass formation. As it is often found with cellulose at larger length scales, drying from the wet state results in cooperative and essentially irreversible hydrogen bonding, and subsequently film formation. For NCC, this irreversibility depends on the residual water content: below about 4% w/w water, the nanocrystals will not redisperse.[70,71]

1.2.8. Optical properties

NCC films typically show high transparency. The optical properties of nanocellulose films can be investigated by determining the regular light transmittance with a UV-visible spectrometer.[72] Interestingly, under controlled conditions, NCC maintains the chiral nematic order upon drying, giving rise to optically active iridescent films. This property relies on the ability to reflect polarized light over a specific wavelength range.[73] The reflected wavelength depends on the chiral nematic pitch, and it is this, together with the incident angle, that determines the color of the film. The pitch of the suspension itself is controlled by the axial ratio and charge of the nanocrystals, their polydispersity and the ionic strength of the medium. [70]

Therefore, optical properties of the films can be tuned by changing preparation conditions.[74] For instance, some studies have established that by adding an electrolyte or providing ultrasonic energy to the NCC suspension,[73] one could control the reflection wavelength of iridescent solid NCC films (Figure 12). By increasing the ionic strength of the system, a decrease in the chiral nematic pitch of the suspension can be achieved *via* tightening the helix of the system. In this way, it is possible to obtain films that reflect in different regions of the wavelength spectrum. While salt-free NCC suspensions reflect in the IR region, the addition of a specific amount of NaCl to the suspension yields films that reflect in the visible and ultraviolet regions of the spectra.[74]

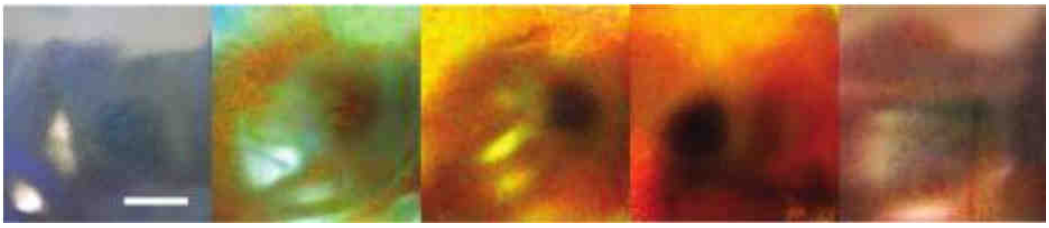

Figure 12. NCC films produced from suspensions treated with increasing applied ultrasonic energy (0, 250, 700, 1800, and 7200 J/g NCC) from left to right. Viewing is normal to the film surface under diffuse lighting. Scale marker = 1 cm.[73]

As previously mentioned, the chiral-nematic phase formed by colloidal NCC aqueous suspension above a critical concentration can also be affected by a strong magnetic field. When a magnetic field is applied during drying of the NCC suspension, it is possible to obtain films with highly ordered texture, independently of the ionic strength of the original suspension.[75] Aligned ultra-thin films of NCC were obtained by using a convective-shear assembly setup. By using this setup, order achieved by the NCC was similar to that obtained by high electric field. Such alignment was explained in terms of a force balance including hydrodynamic, surface tension and electrostatic interactions. Surface strength was improved as a result of the crystals alignment, which was expected to broaden application ranges of these materials.[38]

1.3. NCC functionalization

The high surface area of NCC, as well as the abundance of hydroxyl groups on its surface, makes this material suitable for many types of surface modifications. NCC surface functionalization may be divided in two main categories: covalent attachment or non-covalent interactions of molecules on its surface. Any of the many reactions known from the chemistry of alcohols can be applied, offering the possibility to virtually introduce any chemical species on its surface. Surface functionalization allows in this way the tailoring of particle properties and the type of interactions that the material exhibits with its surroundings, expanding the application field of NCC.[27]

1.3.1. Covalent functionalization

The first type of modification reactions is the covalent attachment of different entities to hydroxyl groups present on NCC surface. As mentioned previously, each AGU bears three hydroxyl groups. The reactivity of these groups is heterogeneous, since the hydroxyl group at the 6 position is a primary alcohol whereas those in the 2 and 3 positions are secondary alcohols. It has been reported that on the structure of cellulose, the hydroxyl group at the 6 position can react ten times faster than the other OH groups, while the reactivity of the hydroxyl group on the 2 position was found to be twice that of at the 3 position.[76] Indeed, due to steric effects derived from the supramolecular structure of cellulose, OH groups in 6 position are more available to eventual reacting agents. Therefore, it is normally acknowledged that functionalization of NCC takes place at the OH in 6 position. The main covalent reactions reported on the surface of NCC are schematically represented in Figure 13, and are described hereafter.[26]

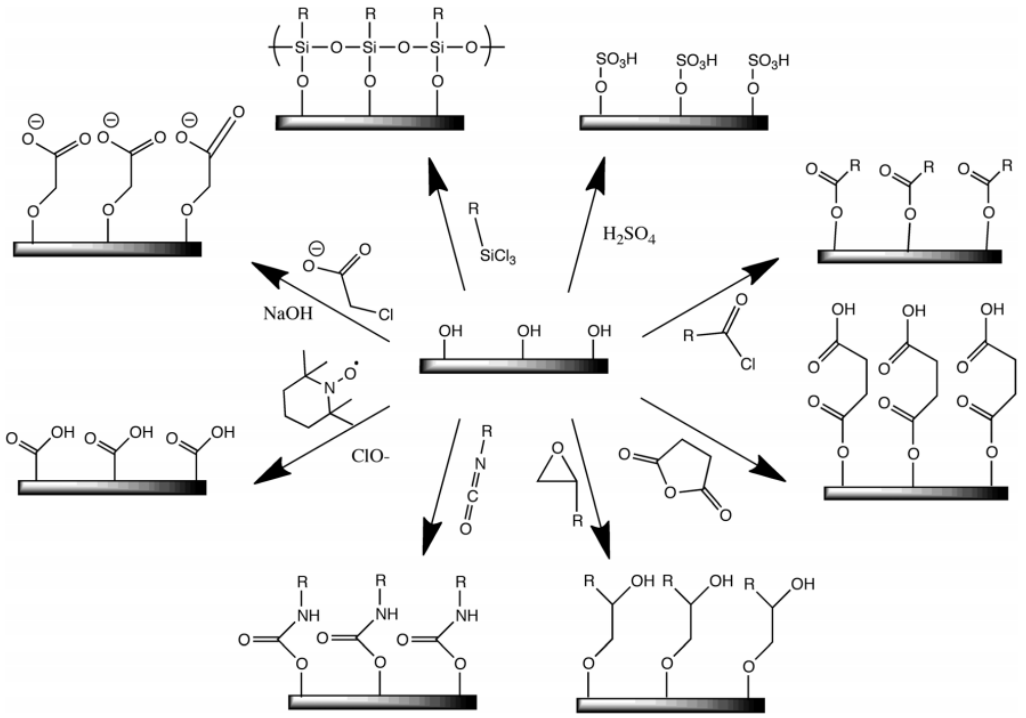

Figure 13. Common covalent modification chemistries of NCC surface: (clockwise from top-right) sulfuric acid treatment provides sulfate esters, carboxylic acid halides create ester linkages, acid anhydrides create ester linkages, epoxides create ether linkages, isocyanates create urethane linkages, TEMPO mediated hypochlorite oxidation creates carboxylic acids, halogenated acetic acids create carboxymethyl surfaces, and chlorosilanes create an oligomeric silylated layer.[26]

Sulfonation

Sulfonation of NCC is normally an indirect consequence of using sulfuric acid for hydrolysis, and it occurs through the esterification of the hydroxyl groups. As mentioned above, they are crucial to obtain stable colloidal suspension with liquid crystal behavior, and therefore optically active films, yet at the expense of thermal stability.[28]

It is however challenging to precisely control the esterification degree, as it depends on many variables, such as hydrolysis time, temperature, acid to NCC ratio, etc. An alternative approach consists on submitting NCC generated by hydrochloric acid hydrolysis to a post-treatment with sulfuric acid. This technique has been successfully used to introduce sulfate moieties on NCC surface in a controlled manner.[60,77] Another possibility lies on the facile desulfonation of NCC prepared by sulfuric acid hydrolysis in order to tune the sulfate content on the surface of NCC, either by mild alkaline treatment or thermal treatment.[78,79]

Esterification

One of the most extensively performed modifications of NCC is esterification reaction, for its simplicity and straightforwardness. It has been mainly used as a way to confer NCC solubility in organic media, being the most common acetylation. Analogous to cellulose fibers, the acetylation of nanocellulose proceeds gradually upon the addition of a dry mixture of acetic anhydride and acetic acid in the presence of a small amount of catalyst such as sulfuric or perchloric acid.[27]

When the reaction is performed in acetic acid at 60 ºC using sulfuric acid as catalyst, and at a moderate degree of acetylation the NCC keep their integrity and the modification occur only at their surface. A straightforward method for the surface acetylation of NCC by transesterification of vinyl acetate was proposed by Çetin *et al.* The reaction of vinyl acetate with the hydroxyl groups of cellulose nanowhiskers obtained from cotton linters was examined with potassium carbonate as catalyst. During the first stage of the reaction, in DMF at 95 ºC, only the surface of the nanowhiskers was modified, while their dimensions and crystallinity remained unchanged and the solubility of NCC in organic solvents such as THF was notably improved.[80]

Apart from acetylation, esterification reactions other other moieties were also attempted following different strategies. Yuan *et al.* developed a method that used alkenyl succinic anhydride aqueous emulsions simply mixed with NCC aqueous suspensions, freeze dried, and the resulting solid heated to 105 ºC.[81] The obtained derivative possessed a highly hydrophobic character and it was easily dispersible in solvents with widely different polarities from DMSO to 1,4-dioxane. Esterification of NCC with organic fatty acid chlorides, having aliphatic chains of different lengths, namely hexanoyl chloride, lauroyl chloride and stearoyl chloride, has also been reported. The reaction was conducted under reflux for 4 h using triethylamine (TEA) as catalyst and neutralizing agent for the *in situ* formed hydrochloric acid. The reduction of the polar character allowed enhancing the nonpolar nature of original NCC, thereby allowing the use of nonpolar polymers as matrices for the processing of nanocomposite materials.[82]

Interestingly, Spinella *et al.* proposed a one-pot concurrent acid hydrolysis, and esterification reactions were investigated using biobased di- and trifunctional organic acids (citric, malonic or malic), rather than strong mineral acids. The reaction was carried out in the presence of catalytic amounts of HCl and resulted in the introduction of free carboxylic acid functionality onto the NCC surface.[83]

Etherification

Another well known reaction for hydroxyl groups is the etherification. Etherification involves the reaction of an alcohol with an alkylating agent in the presence of a base. Typical alkylating agents include alkyl halides (chlorides, bromides, iodides) or, less commonly, alkyl sulfonates.

Etherification was used to very easily introduce cationic charges on NCC surface. Such surface cationizations proceed *via* a nucleophilic addition of the alkali-activated cellulose hydroxyl groups to the epoxy moiety of epoxypropyltrimethyl-ammonium

chloride (EPTMAC). These modifications led to stable aqueous suspensions of NCC with unexpected gelling and rheological properties. Shear birefringence was observed, but no liquid crystalline chiral nematic phase separation was detected for these cationic NCC most likely due to the high viscosity of the suspension.[84]

In a relevant example, Dong *et al.* used this type of reaction to prepare fluorescently labeled NCC, following a three step procedure. First, the surface of the nanocrystals was decorated with epoxy functional groups through nucleophilic addition of alkali-activated cellulose hydroxyl groups with epichlorohydrin. Then, the epoxy groups were opened with ammonium hydroxide to introduce primary amino groups, that were finally reacted with the isothiocyanate group of fluorescein isothiocyanate (FITC) molecule to form a thiourea.[85]

Silylation

Silylation refers to the introduction of silyl group (R_3Si) into a molecule. Generally the substrate (hydroxyl groups on NCC in this case) is deprotonated with a suitable strong base followed by treatment with a silyl chloride.

NCC from tunicate was partially sililated with a series of alkyldimethylchlorosilanes, where the alkyl chain ranged from isopropyl to n-dodecyl. The reaction was carried out in toluene at room temperature, and in the presence of imidazole to neutralize the released hydrochloric acid. Partially silylated NCC was reported to be dispersible in various solvent of low polarity while keeping the nanosized structure and optical properties on the dispersed state.[86]

Sililated NCC was also reported as an intermediate step for further functionalization. Aminosilanes were first grafted onto NCC to covalently attach fluorescent moieties afterwards.[87]

However, this approach is not a very convenient choice, since it requires the use of toxic solvents such as toluene. In addition, long reaction times were reported to destroy both, morphology and crystalline structure of the particles, due to the high affinity of silanes toward hydroxyl groups, evidencing the need of controlled reaction conditions for a successful modification.[86]

TEMPO oxidations

(2,2,6,6-Tetramethylpiperidine-1-oxyl)-mediated (or TEMPO mediated) oxidation of NCC has been used to convert the hydroxymethyl groups on its surface to their carboxylic form. This oxidation reaction, which is highly selective for primary hydroxyl groups, is also "green" and simple to implement.[88] It permits to tune the NCC surface properties by the introduction of carboxylic groups and it is often used as an intermediate step to introduce alternative functionalizations on NCC. This reaction will be described in detail in Chapter 2.

Amidation

Amidation of NCC implies previous oxidation of hydroxyl groups on NCC to carboxylic groups, typically using TEMPO oxidation, followed by covalent attachment of amine derivatives. This coupling approach is particularly interesting

since it takes place in very mild conditions and can be applied to attach biomolecules (proteins) and other useful molecules containing amine groups. Nanoparticles conjugated with biomolecules (such as proteins, DNA, enzymes or antibodies etc.) offer unique opportunities in numerous applications including biosensing, catalytic reactions, targeted drug delivery and directed self-assembly leading to high ordered nanoscale materials.[89] Moreover, grafting of molecules to NCC through an amide linkage has the advantage of greater stability than that of an ester linkage or adsorptive binding against severe chemical conditions, such as acid, base, or heating.

In most of the reported examples, this coupling was accomplished through the activation of carboxylic acids with a carbodiimide derivative as the first step. From the variety of available coupling agents, the most extensively found in literature for NCC couplings is *N*-(3-Dimethylaminopropyl)-*N′*-ethylcarbodiimide hydrochloride (EDC · HCl), accompanied by *N*-Hydroxysuccinimide (NHS) to avoid rearrangement of the unstable intermediate *O*-acylisourea to the stable *N*-acylurea (Figure 14). Since the reaction is pH dependent it is common practice to carry out the reaction in aqueous or buffer media (pH = 6 – 10) at room temperature.[27]

Araki *et al.* used this coupling to attach polyethylene glycol (PEG) chains to NCC surface. The freeze-dried PEG grafted microcrystal could be redispersed in water or non aqueous solvents and the chiral nematic behavior of NCC in suspension was preserved.[46] Barazzouk *et al.* grafted different fluorescent aminoacids, and tryptophan based peptides of 2, 4, 6 and 8 aminoacid residues using this method (Figure 14).[91,92] In this case, carbodiimide activation and coupling was performed in two steps, rather than the preferred one-pot, to prevent undesired reactions between peptides molecules containing both amino and carboxylic groups. In another example, Mangalam *et al.* used a similar procedure to successfully graft single-stranded oligonucleotides with an amino modifier on NCC. The molecular recognition ability of the oligomeric base pairs was then utilized by duplexing complementary

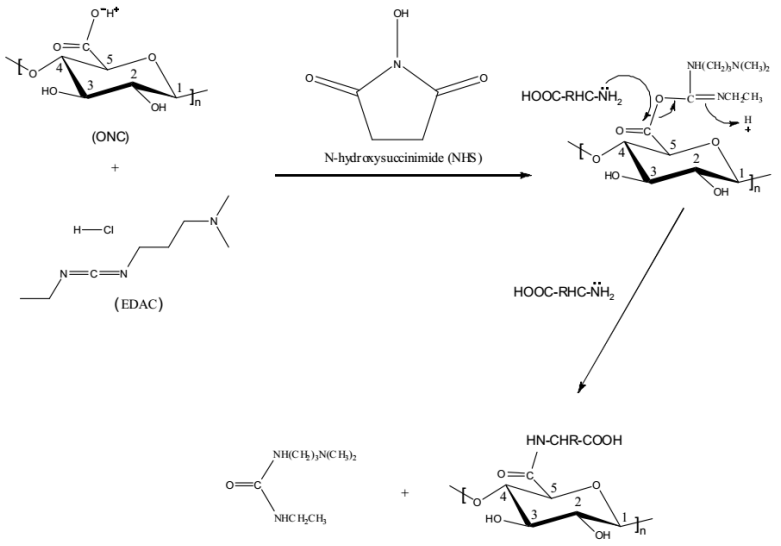

Figure 14. Illustration of the coupling mechanism between oxidized nanocellulose (here reffered to as ONC) and an amino acid (H_2N–CHR–COOH, where R is an organic substituent.[90]

oligonucleotides grafted onto separate NCC populations. The resulting nanomaterials hybridized under suitable conditions to form bonded structures and this hybridization was reversible by raising the temperature above the melting temperature of the duplexed DNA.[93]

Click chemistry

"Click chemistry" is a term introduced by K. B. Sharpless in 2001 to describe reactions that are high yielding, wide in scope, require simple purification methods, are stereospecific, simple to perform, and can be conducted in easily removable or benign solvents. The premier example of click chemistry reaction is the azide-alkyne Huisgen cycloaddition: a 1,3-dipolar copper catalyzed cycloaddition between an azide and a terminal or internal alkyne to give a 1,2,3-triazole. Obviously, when it comes to NCC it is a requisite the introduction of either triple bond or azide functions in a previous step.

The ''clicking'' approach on NCC was first introduced by Filpponen *et al.*, who attempted to link together two sets of NCC, one bearing an azide derivative and the other an alkyne moiety.[94] Both sets were prepared through amidation of TEMPO-mediated oxidized NCC. Subsequently, the Cu(I)-catalyzed Huisgen 1,3-dipolar cycloaddition between the azide and the alkyne surface-activated NCC was employed to bring together the nanorods in a gel-like nanomaterial (Figure 15).

A click chemistry approach was also used for the site-specific immobilization of a model protein at one tip of nanocrystalline cellulose (NCC). Click reaction between reducing end functionalized NCC bearing azide groups and β-casein micelles bearing acetylene groups resulted in mushroom-like conjugated nanoparticles in different arrangements. The strategy developed could be useful for building novel functional self assembled nanobiomaterials and have potential in nanomedicine, immunoassay and drug delivery applications.[89] Feese *et al.* appended a porphyrin derivative onto NCC surface *via* the Cu(I)-catalyzed Huisgen Meldal Sharpless 1,3-dipolar cycloaddition between azide groups on the cellulosic surface and porphyrinic alkynes.[96] The NCC-grafted porphyrin showed excellent efficiency toward the photodynamic inactivation of several bacteria. In another important study, an imidazolium bromide salt was grafted to NCC using Huisgen 1,3-dipolar cycloaddition and the bromide anion was successfully exchanged for bistriflimide and an anionic dye, providing the opportunity to synthesize a wide variety of ion exchange systems or catalysts using NCC as a support.[97]

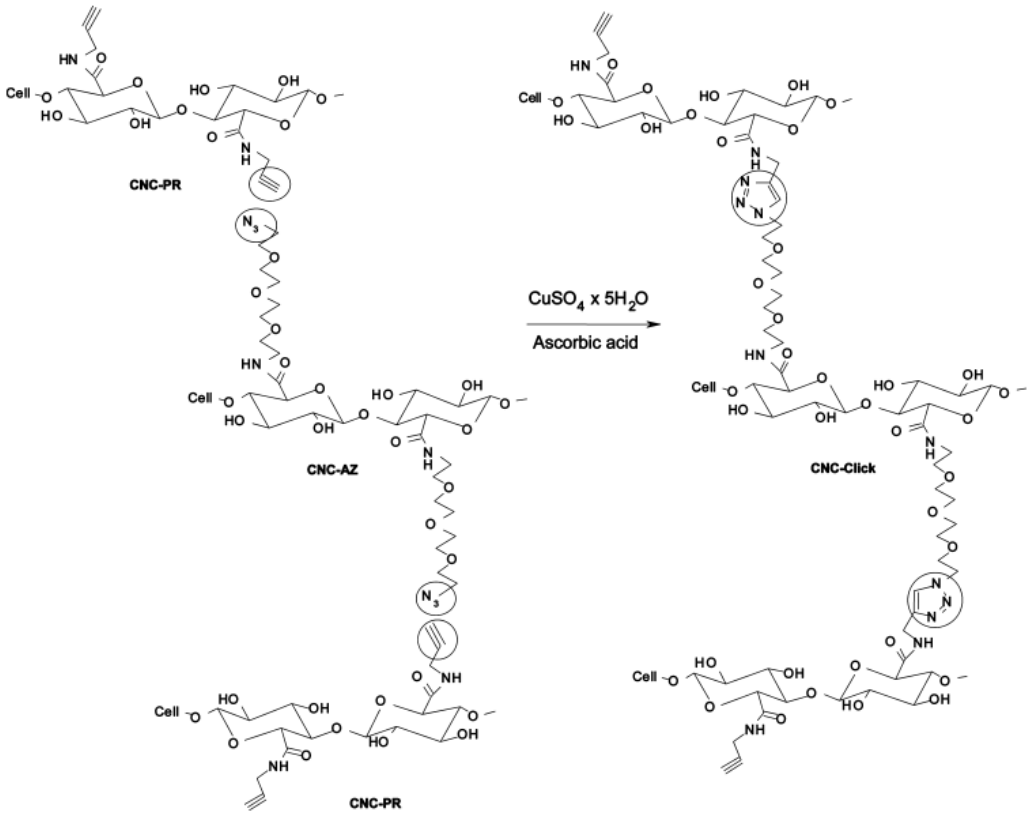

Figure 15. Schematic Representation of the Formation of CNC[1]-Based Nanoplatelet Gels.[95]

Polymer grafting

Another strategy frequently used to improve the dispersability and compatibility of NCC into more hydrophobic matrices is polymer grafting. Two different approaches can be attempted to graft polymer brushes on the surface of NCC, namely "grafting onto" or "grafting from".[27] The "grafting onto" method consists on building the polymer chains out of NCC and then attaching them to its surface. In this way a full characterization of the polymer is possible and a better control on the synthesis and properties is achieved. Yet, steric hindrance can drive to a low surface grafting density during the grafting reaction since the chains already grafted on NCC could prevent others to reach available reactive sites. Alternatively, in the ''grafting from'' approach polymer brushes can be grown *in situ* from nanocellulose directly using the surface hydroxyl groups as initiating sites for ring opening polymerization (ROP).[98] The grafting from methodology increases the grafting density of the polymer brushes on the surface at cost of the synthesis control. Eventually, NCC surface can be modified to introduce different initiator sites needed for controlled polymerization techniques such as atom transfer radical polymerization (ATRP) and other radical

[1] CNC (cellulose nanocrystals) is a common acronym in the literature, equivalent to NCC.

polymerization techniques.[99] ATPR allows for precise control over the grafting that produces well defined monodisperse particles.

Polymers introduced on NCC following the "grafting onto" approach include polycaprolactone *via* an isocyanate-mediated coupling reaction or pre-synthesized waterborne polyurethane. Azzam *et al.* grafted thermosensitive amine-terminated polymers onto the surface of previously modified NCC by a peptidic coupling reaction, leading to unusual properties like colloidal stability at high ionic strength, surface activity, and thermoreversible aggregation.[100]

Following the "grafting from" approach, Morandi *et al.* employed 2-bromoisobutyryl bromide to introduce initiating sites for ATRP. By changing reaction conditions, they achieved different grafting degree and/or different polymeric chain lengths. These particles were tested for their capacity to absorb 1,2,4-trichlorobenzene pollutant from water. The results obtained showed that they absorbed the equivalent of 50% of their weight in pollutant.[99] ROP polymerization was also used to grow polycaprolactone chains on the surface of NCC, where $Sn(Oct)_2$ was used both as a grafting and polymerizing agent. Moreover, similar grafting processes have also been applied under microwave irradiation in order to enhance the grafting efficiency.[101]

1.3.2. Non-covalent functionalization

The second type of modifications consists on non-covalent interactions typically made *via* adsorption of surfactants onto NCC. These interactions occur through hydrophilic affinity, electrostatic attractions, hydrogen bonds or van der Waals forces. This approach has been mostly used to overcome the lack of dispersability of NCC in organic media and integrate them in composite matrix.

For instance, sulfuric acid derived NCC provides a charged surface to adsorb surfactants, as for example stearic acid and cetyl tetramethylammonium bromide (CTAB).[102] Also, different quaternary ammonium salts were adsorbed on TEMPO oxidized NCC, thanks to the presence of negatively charged carboxylic groups on its surface.[103] Other examples opted for the use of non-ionic surfactants to disperse NCC in polystyrene-based composite fibers.[104]

1.4. NCC applications

As it has been shown, the wide possibilities of NCC functionalization allow the introduction of an extensive variety of molecules. This incredibly expands the range of fields were NCC materials can find a potential application, ranging from composites,[105] to catalysis,[106] and more recently to biomedicine.[107] In this section, a general overview with some representative examples of NCC-based materials for different applications is presented. Other examples, for more specific applications will be detailed in the next Chapters.

1.4.1. Composites

The main application of NCC has been as reinforcement of polymeric matrix in nanocomposite materials until not long ago. NCC has properties that render it competitive in comparison to the most used inorganic fillers (carbon nanotubes,

hydroxyapatite, gold, silver, clay or silica) currently used: it is strong, light and highly resistant to temperature, wear, erosion and corrosion, and inexpensive.[38]

Favier *et al.* were the first authors to report the use of NCC as reinforcing fillers in a poly(styrene-co-butyl acrylate) (poly(S-co-BuA))-matrix. Following this trend, the incorporation of nanocrystalline cellulose from different sources into composite materials with enhanced properties has been investigated thoroughly. NCC can be functionalized either to improve the dispersability within the matrix or confer new properties in order to obtain stimuli responsive or smart composites.

One example of the latter is the study reported by Biyani *et al.* NCC from tunicates was functionalized with a coumarin derivative (7-coumaryl-(6-isocyanatohexyl) carbamate) to afford coumarin-derivatized NCC (Cou-NCC).[108] Coumarin undergoes dimerization reactions upon exposure to ultraviolet (UV) light with a wavelength of >300 nm. Such effect was exploited to prepare a light responsive nanocomposite by reinforcing a rubbery ethylene oxide–epichlorohydrin copolymer (EO–EPI) matrix with Cou-NCC. The as-prepared nanocomposites showed a significantly increased tensile storage modulus (E′) in comparison to the neat EO–EPI. For example, E′ at 25 °C increased from 4 MPa to 199 MPa upon introduction of 10% w/w Cou-NCC. E′ increased further to 291 MPa upon irradiation with 365 nm UV light, whereas control nanocomposites with neat NCC did not display any significant increase in E′ under the same conditions (Figure 16).[108]

Capadona *et al.* presented another stimuli responsive nanocomposite inspired by the sea cucumber dermis. In this case, NCC was used as filler in a rubbery host polymer. The dry composite exhibited a high elastic modulus of 800 MPa. When put in an aqueous ambient, the swelling acted as a chemical regulator. The presence of water produced competitive hydrogen bonding with NCC and consequently weakening of interaction among nanocrystals. In these conditions elastic modulus was drastically reduced to 20 MPa.[109]

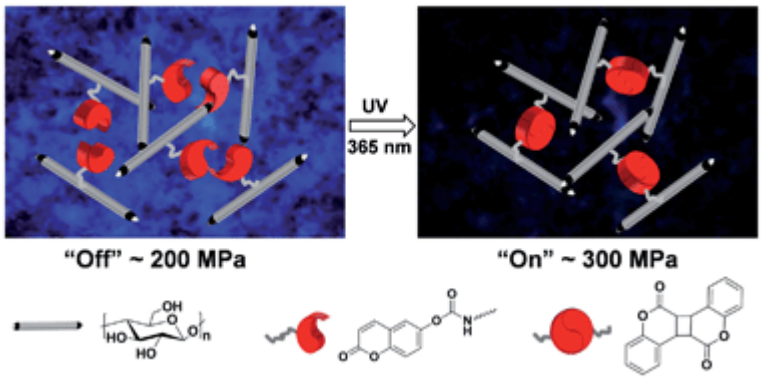

Figure 16. Schematic representation of the photoswitchable Cou-NCC composite.[108]

1.4.2. Bioapplications

Hydrophilicity, biocompatibility and the possibility of chemical modifications, such as the incorporation of fluorescent dyes or drugs onto their surface, are the main characteristics that make nanocellulosic materials attractive for biomedical applications. To date, many researchers have investigated the design, fabrication, and processing of this nanomaterial for potential use in medicine. Depending on the type of nanocellulosic material, their application within the field of biomedicine is more oriented towards specific applications. In the case of NCC, due to its small size and high surface area, research efforts are focused on their use as drug delivery carrier for internalization into cells.

Roman *et al.* investigated whether NCC would exhibit any toxicity towards human brain microvascular endothelial cells (HBMECs). Cellular uptake studies based on the use of NCC labeled with FITC were also carried out.[110] The results from these studies demonstrated no toxicity of NCC towards HBMECs over the 0-500 μg/ml concentration range, what could be due to the low uptake of NCC found after 24 hours exposure. Later on, the toxicity of NCC against nine cell lines was assessed, and no signs of cytotoxicity were found at the concentration range and exposure time studied (0-50 μg/ml and 48 hours respectively).[111]

Surface charge and conjugation of non-cytotoxic elements to NCC are also important considerations for the use of NCC as a natural carrier into cells for bioimaging and drug delivery applications. Mahmoud *et al.* investigated the effects of NCC derivatives surface charge on cell internalization using negatively charged fluorescein isothiocyanate (FITC) and positively charged rhodamine B isothiocyanate (RBITC). Positively charged NCC–RBITC was internalized by human embryonic kidney 293 (HEK 293) and *Spodoptera frugiperda* (Sf9) insect cells with no observed cytotoxicity. Negatively charged NCC–FITC was not internalized by the cells due to repulsive forces between the anionic NCC–FITC and the anionic cellular membrane at physiological pH (Figure 17).[112]

NCC was also used for the targeted delivery of chemotherapeutic agents to cancer cells. Folic acid (FA) grafted NCC conjugates (FITC–NCC–FA) were synthesized and *in vitro* folate-receptor-mediated uptake by human and rat brain tumor cells studied. It was found that the cellular binding/uptake of the FITC–NCC–FA by the folate receptor, which is overexpressed by several types of cancer cells, was significantly higher than that of the free FA. This study suggested that the FA-conjugated NCC showed potential for cancer targeting.[113] In a different approach, Jackson *et al.* took advantage of the negative charges present on NCC from acid hydrolysis to bind ionizable drugs such as tetracycline and doxorubicin, which were rapidly released over a 1 day period. The release profile seemed to indicate that a weakly bound fraction of the drug was released quickly and a strongly bound fraction was released more slowly. Fluorescence studies with bound fluorescein also showed that cellular uptake of these nanocomplexes by KU-7 human bladder cancer cells was possible with little cytotoxic effect observed.[102]

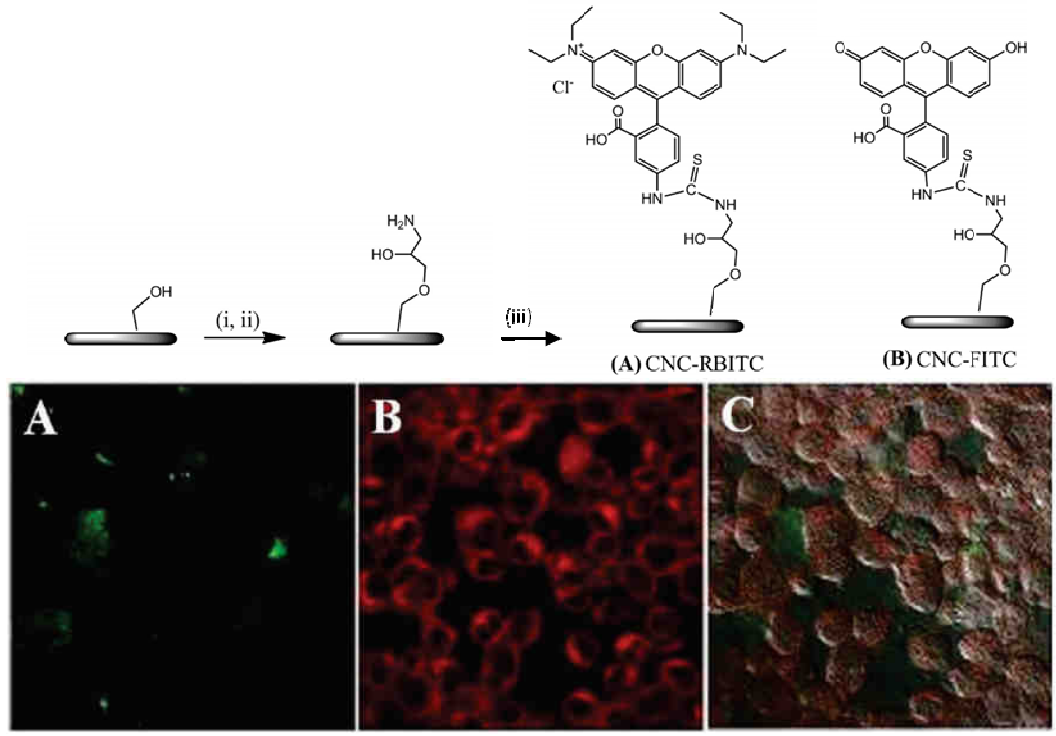

Figure 17. Schematic Illustration for the Synthesis of the CNC-RBITC conjugate: (i) Epichlorohydrin, NaOH, 60 °C; (ii) NH_4OH, NaOH pH 12; (iii) RBITC or FITC, Sodium Borate, Sodium Chloride, Ethylene Glycol, Tartaric Acid and Sucrose (top), confocal images of Sf9 cells incubated with a mixture of 0.1 mg/mL CNC-RBITC and 0.1 mg/mL CNC-FITC. (A) FITC fluorescence field, (B) RBITC fluorescence field, and (C) both FITC and RBITC fluorescence fields (down).[112]

The interaction of NCC with cells *in vivo* has been unfortunately less explored, although is crucial for further development of NCC systems as drug vectors. In a interesting study, Colombo *et al.* functionalized NCC with a fluorescent dye, and thoroughly assessed its interaction with living organisms, in particular with mice. They demonstrated that the NCC derivative was well tolerated by healthy mice after systemic injection; it was rapidly excreted, thus avoiding bioaccumulation in filter organs such as the kidneys and liver; transiently migrated in bones; and was able to penetrate in the cytoplasm of cancer cells without inducing material-related detrimental effects in terms of cell survival (Figure 18). They suggested that the peculiar tropism to the bones is due to the chemical interaction between the Ca^{2+} of the bone matrix and the active surface of negatively-charged NCC. This feature, together with the ability to penetrate cancer cells, makes NCC a potential nanodevice for theranostics in bone tumors.[114]

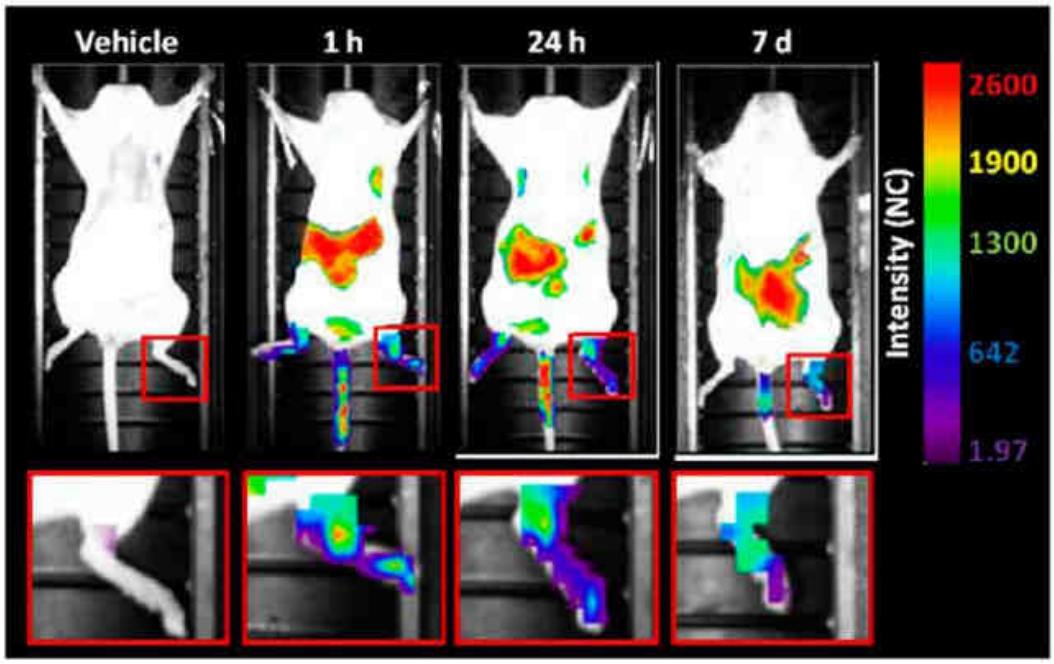

Figure 18. Optical imaging scans acquired before and at 1 h, 24 h, and 7 d, respectively, after NCC intravenous injection (a single dose of 120 µL at a concentration of 35 µg/mL). Three different regions of interest (ROIs) were processed. They were the abdominal area, the tail, and the distal left hind limb. In the red squares (bottom panels), a higher magnification of the distal hind limb is shown. The fluorescence intensity signal was measured as normalized photon counts (NC) and is shown as a pseudocolor scale bar.[114]

1.4.3. Energy and electronic applications

NCC is an intrinsic insulator, which induces to think that it has no potential in electronics or energy storage films, where conducting or semiconducting materials are needed. However, these devices typically need a flexible support. Normally these supports consist of petroleum-based plastic polymers, which are expensive and not environmentally friendly. On the contrary, NCC is low-cost, low-weight, flexible, and recyclable, and so a useful substrate for more environmentally friendly electronic devices. This, combined with the ability of nanocelluloses to incorporate other functional materials, provides many opportunities for applications in electronic, electrochemical and optical devices. NFC is usually preferred for these kind of applications, for its higher porosity and flexibility. However, there are still some examples including NCC.

Flexible electronics

Gaspar *et al.* reported for the first time the preparation of a thin transparent nanopaper-based field effect transistor (FET) where NCC was simultaneously used as the substrate and as the gate dielectric layer in an 'interstrate' structure, since the device was built on both sides of the NCC films: on one side a GIZO (Ga_2O_3–In_2O_3–ZnO; 1:2:2 mol%) layer (the active oxide semiconductor) and on the opposite side of the nanocrystalline cellulose membrane an IZO (In_2O_3–ZnO; 5:2 mol%) film serving as the gate electrode (Figure 19). The NCC film FET presented good stability in air

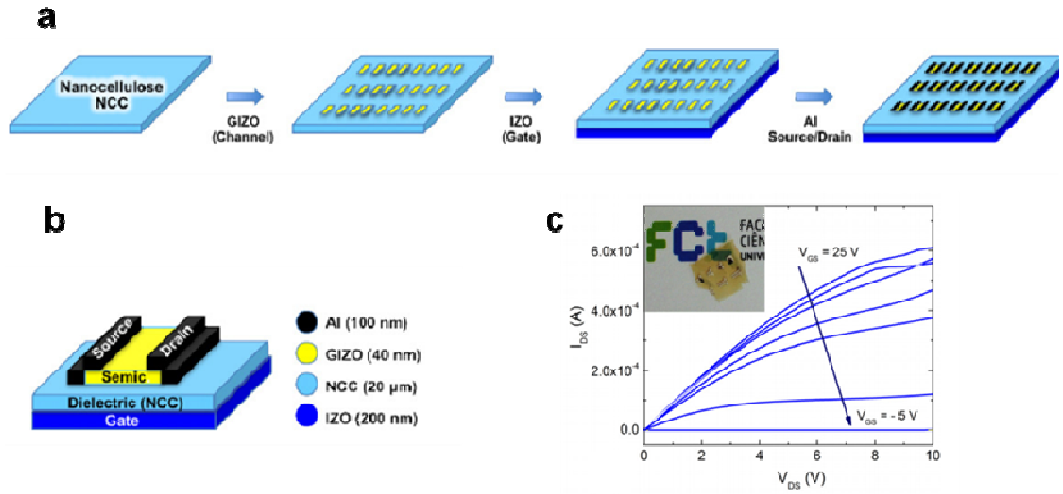

Figure 19. Schematics of the process of fabrication of FETs using NCC as the gate dielectric (a), the corresponding staggered-bottom gate structure (b) and output characteristics for the GIZO field effect transistor with an NCC membrane prepared by evaporation as the gate dielectric (the step for the gate voltage was 5 V, starting from −5 and going to 30 V) (c). The inset in c shows an optical photograph of a fully processed FET.[115]

ambient conditions, after two weeks of being processed, without any type of encapsulation or passivation layer. The results obtained were competitive with the state of the art for conventional cellulose paper.[115]

Najafabadi *et al.* reported on efficient organic light-emitting diodes (OLEDs) with an inverted top-emitting green electrophosphorescent OLEDs on recyclable NCC substrates (Figure 20a). The average current efficacy of devices on NCC was 32.5 ± 14.1 cd/A at 10 cd/m^2 and 42.7 ± 9.8 cd/A at 100 cd/m^2, similar to that achieved on glass substrates (Figure 20b).[116] OLEDs fabricated on recyclable and biodegradable substrates are a step towards the realization of a sustainable OLED technology.

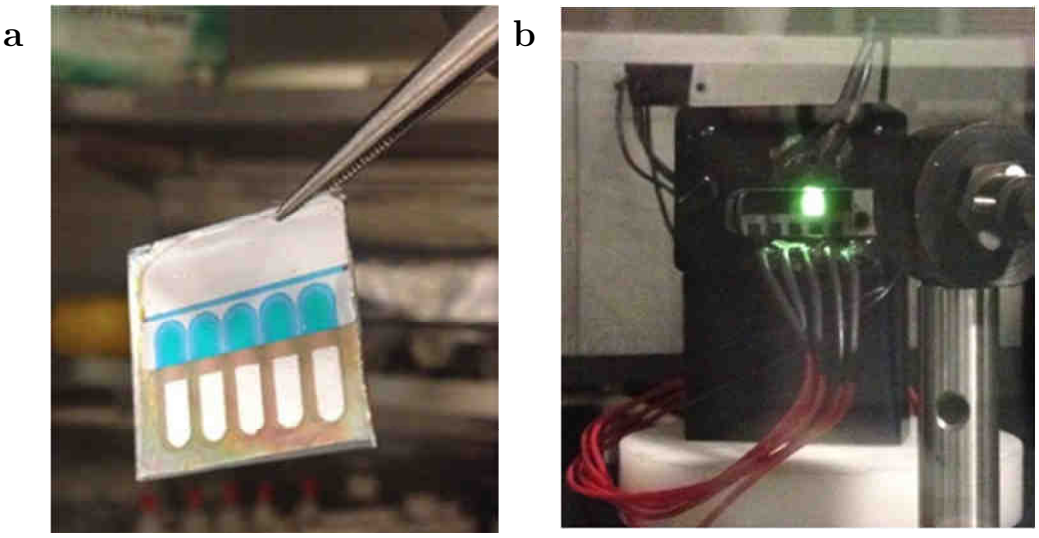

Figure 20. Photograph of five inverted top-emitting OLEDs on a NCC substrate mounted on glass (left), and an illuminated OLED on NCC substrate (right).[116]

Energy Storage Devices

As a promising candidate for energy application using NCC, Tuukkanen *et al.* reported printable and disposable supercapacitors fabricated from solution-processed carbon nanotube (CNT) composite material as active electrodes and nanocellulose (NCC) as separator. NCC is a robust separator material used instead of conventional polymer separator films. The fabrication of supercapacitors on flexible substrates from solution-processable materials enables their low-cost and high throughput mass production. Flexible, low-cost supercapacitors are interesting interim power sources for autonomous energy harvesting systems such as ubiquitous sensory networks and disposable low end products (Figure 21).[117]

Zhou *et al.* proposed for the first time efficient polymer solar cells fabricated on optically transparent NCC substrates. The solar cells fabricated on the NCC substrates displayed good rectification in the dark and reached a power conversion efficiency of 2.7%, still modest with respect to the state of the art for this type of solar cells (~10%).[118] Efficient and easily recyclable organic solar cells on NCC substrates are expected to be an attractive technology for sustainable, scalable, and environmentally-friendly energy production.[119]

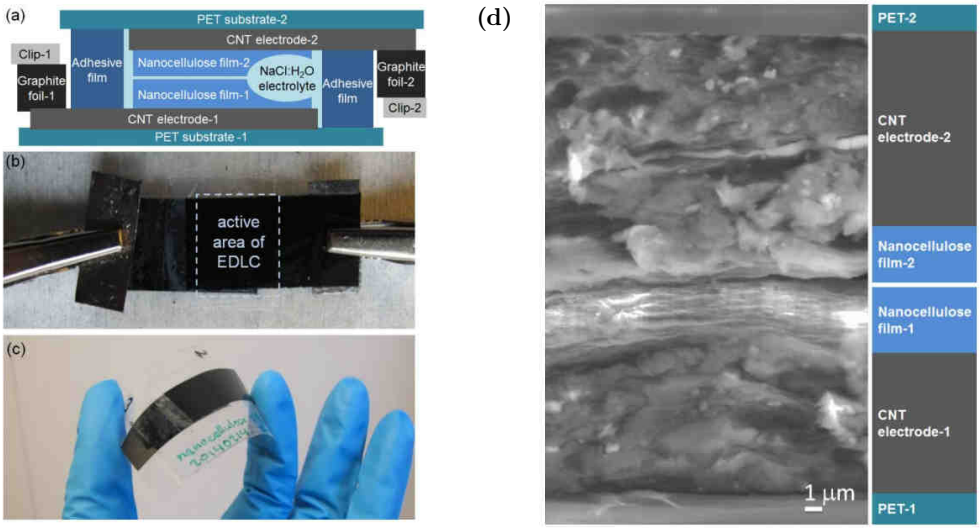

Figure 21. Schematic side-view of used supercapacitor architecture (a), top-view of the assembled supercapacitor during the electrical characterization (b), photo of the bent device (c) and SEM micrograph of the cross-section of the supercapacitor (d)[117].

Sensors

Another significant area for NCC applications is sensors. Nanopaper-based sensors are likely to be simple, portable, disposable, low power-consuming and inexpensive devices that will find wide use in medicine, detecting explosives, toxic substances, or pollutants.

Hassan *et al.* prepared highly fluorescent nanocellulosic material via surface modification of NCC with terpyridines followed by supramolecular assembly of terpyridine-modified perylene dye onto the terpyridine-modified cellulose nanocrystals

(CTP) via Ru^{III}/Ru^{II} reduction. In addition, further self-assembly of terpyridine units with azide functional groups onto CTP-Ru^{II}-PeryTP was possible *via* repeating the Ru^{III}/Ru^{II} reduction protocol to prepare supramolecular fluorescent nanocrystals with azide functionality (CTPRu^{II}-PeryTP-Ru^{II}-AZTP), as represented in Figure 22. They proposed this derivative as potential bio-sensing device since the terminal azide groups can easily react with antigens via "click chemistry" reaction.[120]

Chauhan *et al.* proposed a straightforward synthetic method for the covalent attachment of a pH-sensitive dye to NCC in a one-step procedure, which exploited a vinylsulfone reactive moiety. The resulting material provided an innovative clue to nanostructured optodes, i.e. pH responsive nano-materials that are amenable to a multi-format application environment, with adaptive textures, forms, and patterns. Their results addressed the fabrication of flat-membranes, pH-sensitive sticks, and printable inks, carved within the common motif of a biocompatible nanocellulose matrix (Figure 23). [121]

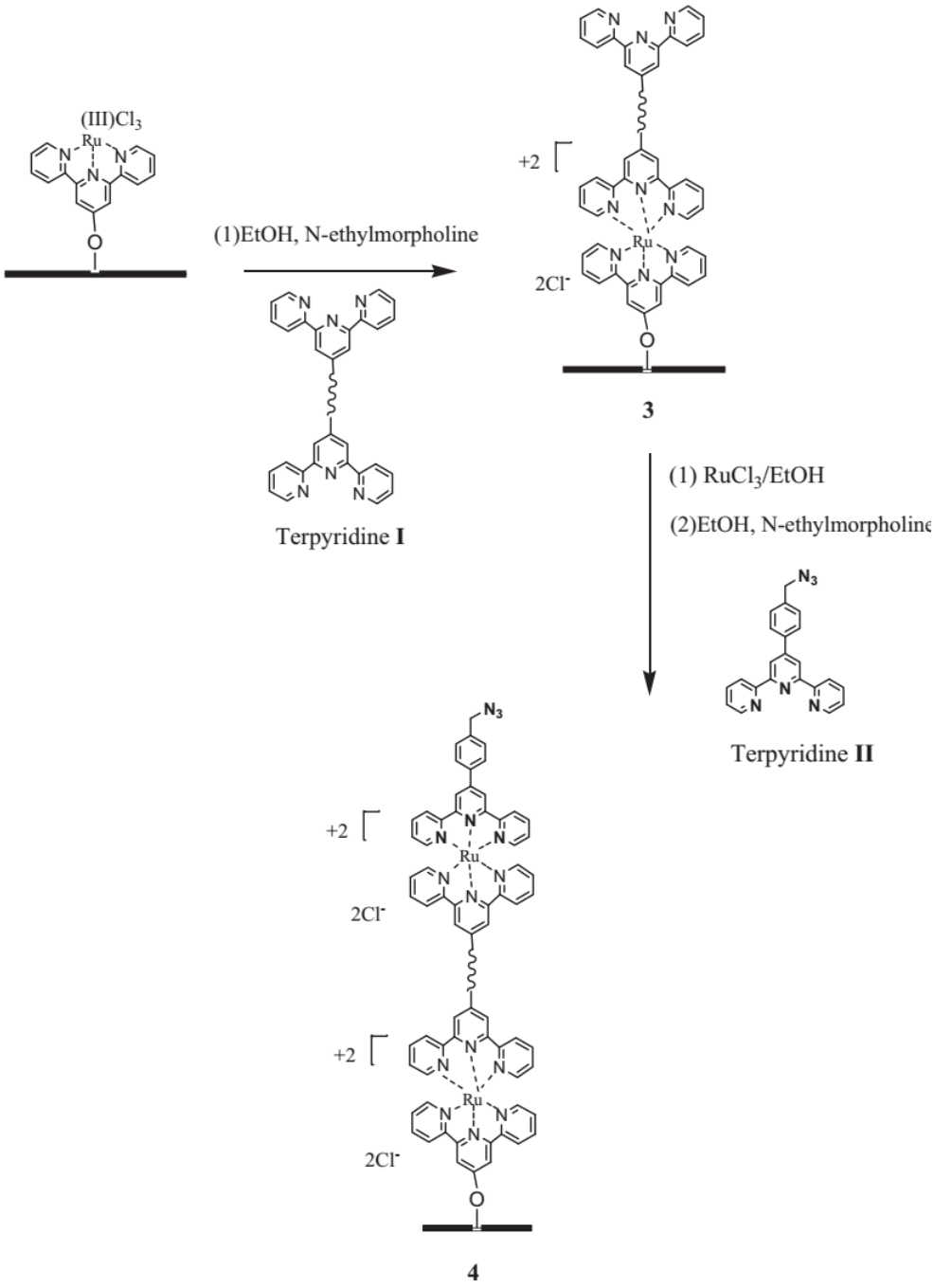

Figure 22. Preparation of supramolecular CTP-Ru^{II}-PeryTP (3) and CTP-Ru^{II}-PeryTP-Ru^{II}-AZTP (4) nanocellulosic derivatives. Curved line represents perylene motifs.[120]

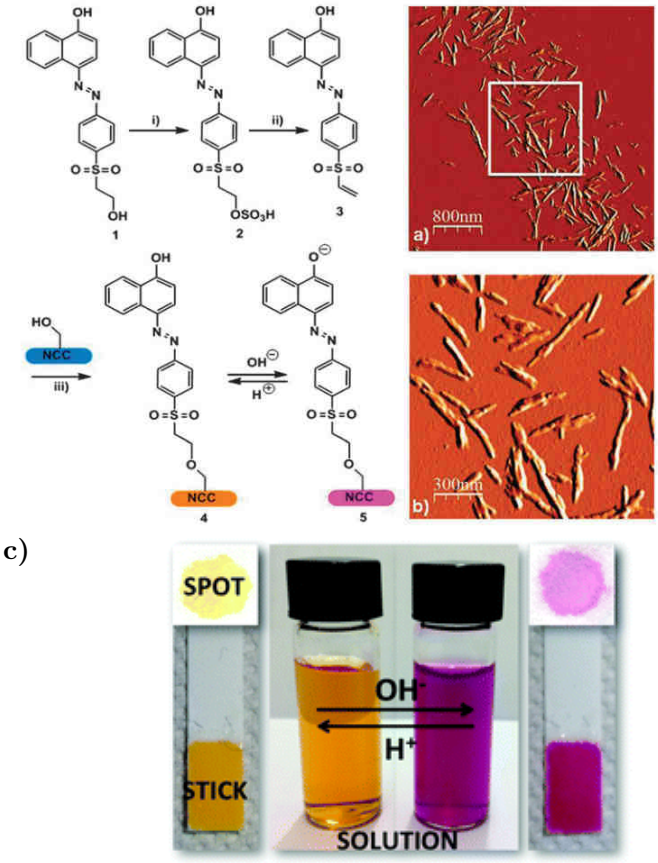

Figure 23. Synthesis of 4: (i) 96% H_2SO_4, 45 min, 45 ºC, yield: 74%; (ii) NaOH 1 M until pH = 10; (iii) NCC suspension in water, yield: 37%. Inset: (a) AFM image of 4 (a), AFM image of the marked region (b) and NCC pH sensor in suspension and deposited on paper (c).[121]

In a last example, nanocrystalline cellulose was also converted into fluorescent nanoparticles by functionalization with pyrene moieties (Py-NCC) following a three-step procedure. An enhancement of the fluorescence emission of pyrene after functionalization to NCC was observed. Py-NCC was evaluated for its sensing ability towards metal ions and exhibited high selectivity towards Fe^{3+} among other screened metal ions with good discrimination between Fe^{2+} and Fe^{3+}. The excellent selectivity for Fe^{3+} over a wide linear concentration range was observed through changes in the emission spectra. Spectroscopic analyses proved that the coordination interaction between Fe^{3+} and pyrene-modified cellulose nanocrystals leads to the recognition process. This sensing nanomaterial could be employed as a chemosensor for Fe^{3+} and promoted for many applications in chemical, environmental, and biological systems.[122]

1.5. Conclusions

NCC is an emerging nanomaterial, with unique advantages among other nanostructured materials, such as renewability, availability, sustainability, lack of toxicity and biocompatibility. In addition, the high abundance of reactive hydroxyl groups on its surface renders this nanomaterial one of the most chemically versatile materials for nanodevice development.

So far, most of the research has focused on characterizing the morphological, mechanical, optical, and liquid crystalline properties of NCC and it has been principally applied in nanocomposite fabrication. Nevertheless, various surface modification processes have recently arisen to manipulate the functionality of NCC in order to obtain high added value materials without affecting its inherent properties.

This trend shows promise in exploring and revealing innovative possibilities for this long known material in a wide range of new industrial applications, such as high-performance biodegradable material science, electronics, biomedical engineering, drug delivery, catalysis, etc. Innovations in nanotechnology related to renewable nanomaterials such as NCC are anticipated to provide technologically advanced products in a more environmentally friendly fashion, as it is required from the point of view of sustainable development.

1.6. References

(1) Habibi, Y.; Lucia, L. A.; Rojas, O. J. Cellulose Nanocrystals: Chemistry, Self-Assembly , and Applications. *Chem. Rev.* **2010**, *110*, 3479–3500.

(2) Payen, A. Mémoire Sur La Composition Du Tissu Propre Des Plantes et Du Ligneux. *Comptes Rendus 7*, 1052–1056.

(3) Krässig, H.; Schurz, J.; Steadman, R. G.; Schliefer, K.; Albrecht, W.; Mohring, M.; Schlosser, H. Cellulose Esters. *Ullmann's Encycl. Ind. Chem.* **2012**, *6*, 565–582.

(4) C. F. Cross, B. T. Bevan, C. B. Thiokohleneilureester Der Celluloee. *Ber. Dtsch. Chem. Ges* **1893**, *26*, 1090–1097.

(5) Klemm, D.; Heublein, B.; Fink, H. P.; Bohn, A. Cellulose: Fascinating Biopolymer and Sustainable Raw Material. *Angew. Chemie - Int. Ed.* **2005**, *44*, 3358–3393.

(6) Olsson, C.; Westman, G. Direct Dissolution of Cellulose: Background, Means and Applications. In *Cellulose - Fundamental Aspects*; Ven, T. van de, Godbout, L., Eds.; 2013.

(7) Rowland, S. P.; Roberts, E. J. The Nature of Accessible Surfaces in the Microstructure of Cotton Cellulose. *J. Polym. Sci. Part A-1 Polym. Chem.* **1972**, *10*, 2447–2461.

(8) Fujisawa, S.; Saito, T.; Isogai, A. Nano-Dispersion of TEMPO-Oxidized Cellulose/aliphatic Amine Salts in Isopropyl Alcohol. *Cellulose* **2012**, *19*, 459–466.

(9) Klemm, P. D. D.; Schmauder, Prof. Dr. H. P. Heinze, P. D. T. Cellulose. *Biopolym. Polysaccharides II Polysaccharides from Eukaryotes* **2002**, *6*, 275–287.

(10) Marrinan, H. J.; Mann, J. Infrared Spectra of the Crystalline Modifications of Cellulose. *J. Polym. Sci.* **1956**, *21*, 301–311.

(11) VanderHart, D. L.; Atalla, R. H. Studies of Microstructure in Native Celluloses Using Solid-State ^{13}C NMR. *Macromolecules* **1984**, *17* (c), 1465–1472.

(12) O'sullivan, A. Cellulose: The Structure Slowly Unravels. *Cellulose* **1997**, *4*, 173–207.

(13) Nishiyama, Y. Structure and Properties of the Cellulose Microfibril. *J. Wood Sci.* **2009**, *55*, 241–249.

(14) Yamamoto, H.; Horn, F. In Situ Crystallization of Bacterial Cellulose I. Influences of Polymeric Additives, Stirring and Temperature on the Formation Celluloses I_α and I_β as Revealed by Cross Polarization/magic Angle Spinning (CP/MAS)13C NMR Spectroscopy. *Cellulose* **1994**, *1*, 57–66.

(15) Belton, P.; Tanner, S.; Cartier, N. High-Resolution Solid-State ^{13}C Nuclear Magnetic Resonance Spectroscopy of Tunicin, an Animal Cellulose. *Macromolecules* **1989**, *22* (4), 1615–1617.

(16) Nishiyama, Y.; Johnson, G. P.; French, A. D.; Forsyth, V. T.; Langan, P. Neutron Crystallography, Molecular Dynamics, and Quantum Mechanics

Studies of the Nature of Hydrogen Bonding in Cellulose Iβ. *Biomacromolecules* **2008**, *9*, 3133–3140.

(17) Kaplan, H.; Seireg, A. Lateral Thermal Expansion of Cellulose Iβ and IIII Polymorphs. *J. Polym. Sci. Part B Polym. Phys.* **2002**, *40*, 1095–1102.

(18) Imai, T.; Putaux, J. L.; Sugiyama, J. Geometric Phase Analysis of Lattice Images from Algal Cellulose Microfibrils. *Polymer* **2003**, *44*, 1871–1879.

(19) Wada, M.; Heux, L.; Sugiyama, J. Polymorphism of Cellulose I Family: Reinvestigation of Cellulose IVl. *Biomacromolecules* **2004**, *5*, 1385–1391.

(20) Nishiyama.Y; Sugiyama.J; Chanzy.H; Langan.P. Crystal Structure and Hydrogen Bonding System in Cellulose Iα from Synchrotron X-Ray and Neutron Fiber Diffraction. *J Am Chem Soc* **2003**, *125*, 14300–14306.

(21) Nishiyama.Y; Sugiyama.J; Chanzy.H; Langan.P. Crystal Structure and Hydrogen Bonding System in Cellulose Iα from Synchrotron X-Ray and Neutron Fiber Diffraction. *J Am Chem Soc* **2003**, *125*, 14300–14306.

(22) Langan, P.; Nishiyama, Y.; Chanzy, H. X-Ray Structure of Mercerized Cellulose II at 1 Å Resolution. *Biomacromolecules* **2001**, *2* (JUNE 2001), 410–416.

(23) Gardner, K.; Blackwell, J. The Structure of Native Cellulose. *Biopolymers* **1974**, *13* (1974), 1975–2001.

(24) Liang, C. Y.; Marchessault, R. H. Infrared Spectra of Crystalline Polysaccharides. III. Mercerized Cellulose. *J. Polym. Sci.* **1960**, *43*, 85–100.

(25) Gautam, S. P.; Bundela, P. S.; Pandey, A. K.; Awasthi, M. K.; Sarsaiya, S. A Review on Systematic Study of Cellulose. *J. Appl. Nat. Sci.* **2010**, *2*, 330–343.

(26) Moon, R. J.; Martini, A.; Nairn, J.; Simonsen, J.; Youngblood, J. Cellulose Nanomaterials Review: Structure, Properties and Nanocomposites. *Chem Soc Rev* **2011**, *40* (4), 3941–3994.

(27) Habibi, Y. Key Advances in the Chemical Modification of Nanocelluloses. *Chem. Soc. Rev.* **2014**, *43*, 1519–1542.

(28) Lin, N.; Dufresne, A. Surface Chemistry, Morphological Analysis and Properties of Cellulose Nanocrystals with Gradiented Sulfation Degrees. *Nanoscale* **2014**, *6*, 5384–5393.

(29) Gatenholm, P.; Klemm, D. Bacterial Nanocellulose as a Renewable Material for Biomedical Applications. *MRS Bull.* **2010**, *35* (March), 208–213.

(30) http://www.vtnews.vt.edu/articles/2008/11/2008-693.html.

(31) Nakagaito, A. N.; Iwamoto, S.; Yano, H. Bacterial Cellulose: The Ultimate Nano-Scalar Cellulose Morphology for the Production of High-Strength Composites. *Appl. Phys. A Mater. Sci. Process.* **2005**, *80*, 93–97.

(32) Turbak, A. F.; Snyder, F. W.; Sandberg, K. R. Microfibrillated Cellulose, a New Cellulose Product: Properties, Uses, and Commercial Potential. *J Poly Sc* **1983**, *37*, 815–827.

(33) Iwamoto, S.; Nakagaito, A. N.; Yano, H. Nano-Fibrillation of Pulp Fibers for the Processing of Transparent Nanocomposites. *Appl. Phys. A Mater. Sci. Process.* **2007**, *89*, 461–466.

(34) Wågberg, L.; Decher, G.; Norgren, M.; Lindström, T.; Ankerfors, M.; Axnäs, K. The Build-up of Polyelectrolyte Multilayers of Microfibrillated Cellulose and Cationic Polyelectrolytes. *Langmuir* **2008**, *24* (10), 784–795.

(35) Missoum, K.; Belgacem, M. N.; Bras, J. Nanofibrillated Cellulose Surface Modification: A Review. *Materials* **2013**, *6*, 1745–1766.

(36) Klemm, D.; Kramer, F.; Moritz, S.; Lindström, T.; Ankerfors, M.; Gray, D.; Dorris, A. Nanocelluloses: A New Family of Nature-Based Materials. *Angew. Chemie - Int. Ed.* **2011**, *50*, 5438–5466.

(37) Kim, J. H.; Shim, B. S.; Kim, H. S.; Lee, Y. J.; Min, S. K.; Jang, D.; Abas, Z.; Kim, J. Review of Nanocellulose for Sustainable Future Materials. *Int. J. Precis. Eng. Manuf. - Green Technol.* **2015**, *2* (2), 197–213.

(38) Peresin, M. S. A Mini-Review on Properties of Nanocrystalline Cellulose and Its Potential Applications. *Rev. Investig. Apl.* **2013**, *7* (2), 58–73.

(39) Dong, X. M.; Kimura, T.; Gray, D. G. Effects of Ionic Strength on the Isotropic - Chiral Nematic Phase Transition of Suspensions of Cellulose Crystallites. *Langmuir* **1996**, *12* (8), 2076–2082.

(40) Favier, V.; Chanzy, H.; Cavaille, J. Y. Polymer Nanocomposites Reinforced by Cellulose Whiskers. *Macromolecules* **1995**, *28*, 6365–6367.

(41) Elazzouzi-Hafraoui, S.; Nishiyama, Y.; Putaux, J. L.; Heux, L.; Dubreuil, F.; Rochas, C. The Shape and Size Distribution of Crystalline Nanoparticles Prepared by Acid Hydrolysis of Native Cellulose. *Biomacromolecules* **2008**, *9*, 57–65.

(42) Itoh, T. Brown Jr., R. M. Development of Cellulose Synthesizing Complexes in Boergesenia and Valonia. *Protoplasma* **1988**, *9*, 50–57.

(43) Dong, X. M. Effect of Microcrystallite Preparation Conditions on the Formation of Colloid Crystals of Cellulose. *Cellulose* **1998**, *5*, 19–32.

(44) George, J.; Sabapathi, N. S. Cellulose Nanocrystals: Synthesis, Functional Properties and Applications. *Nanotechnol. Sci. Appl.* **2015**, *8*, 45.

(45) Beck-Candanedo, S.; Roman, M.; Gray, D. G. Effect of Reaction Conditions on the Properties and Behavior of Wood Cellulose Nanocrystal Suspensions. *Biomacromolecules* **2005**, *6*, 1048–1054.

(46) Araki, J.; Wada, M.; Kuga, S. Steric Stabilization of a Cellulose Microcrystal Suspension by Poly (ethylene Glycol) Grafting Steric Stabilization of a Cellulose Microcrystal Suspension by Poly (ethylene Glycol) Grafting. *Cellulose* **2001**, No. 17, 21–27.

(47) Bondeson, D.; Mathew, A.; Oksman, K. Optimization of the Isolation of Nanocrystals from Microcrystalline Cellulose by Acid Hydrolysis. *Cellulose* **2006**, *13*, 171–180.

(48) Kimura, F.; Kimura, T.; Tamura, M.; Hirai, A.; Ikuno, M.; Horii, F. Magnetic Alignment of the Chiral Nematic Phase of a Cellulose Microfibril Suspension. *Langmuir* **2005**, *21* (11), 2034–2037.

(49) George, J.; Bawa, A. S.; Siddaramaiah. Synthesis and Characterization of Bacterial Cellulose Nanocrystals and Their PVA Nanocomposites. *Adv. Mater. Res.* **2010**, *123-125*, 383–386.

(50) George, J.; Siddaramaiah. High Performance Edible Nanocomposite Films Containing Bacterial Cellulose Nanocrystals. *Carbohydr. Polym.* **2012**, *87* (3), 2031–2037.

(51) Lee, H. V; Hamid, S. B.; Zain, S. K. Conversion of Lignocellulosic Biomass to Nanocellulose: Structure and Chemical Process. *Sci. World J.* **2014**, *2014*, 1–22.

(52) Iwamoto, S.; Wh, K.; Isogai A, I. T. Elastic Modulus of Single Cellulose Microfibrils from Tunicate Measured by Atomic Force Microscopy. *Biomacromolecules* **2009**, *10*, 2571–2576.

(53) Šturcová, A.; Davies, G. R.; Eichhorn, S. J.; Sturcová, A.; Davies, G. R.; Eic; Eichhorn, S. J. Elastic Modulus and Stress-Transfer Properties of Tunicate Cellulose Whiskers. *Biomacromolecules* **2005**, *6*, 1055–1061.

(54) Lahiji, R. R.; Xu, X.; Reifenberger, R.; Raman, A.; Rudie, A.; Moon, R. J.; Service, U. S. F.; Drive, G. P. Atomic Force Microscopy Characterization of Cellulose Nanocrystals. **2010**, *26* (4), 4480–4488.

(55) Davis, V. Liquid Crystalline Assembly of Nanocylinders. *J. Mater. Res.* **2011**, *26*, 140–153.

(56) Dong, X. M. Effect of Microcrystallite Preparation Conditions on the Formation of Colloid Crystals of Cellulose. *Cellulose* **1998**, *5*, 19–32.

(57) Revol, J. F.; Bradford, H.; Giasson, J.; Marchessault, R. H.; Gray, D. G. Helicoidal Self-Ordering of Cellulose Microfibrils in Aqueous Suspension. *Int. J. Biol. Macromol.* **1992**, *14*, 170–172.

(58) Westmann, M. B. and G. *Cellulose: Fundamental Aspects and Current Trends*; Poletto, M., Ornaghi, H. L., Eds.; InTech, 2015.

(59) Davis, V. A.; Ericson, L. M.; Parra-Vasquez, A. N. G.; Fan, H.; Wang, Y.; Prieto, V.; Longoria, J. a.; Ramesh, S.; Saini, R. K.; Kittrell, C.; Billups, W. E.; Adams, W. W.; Hauge, R. H.; Smalley, R. E.; Pasquali, M. Phase Behavior and Rheology of SWNTs in Superacids. *Macromolecules* **2004**, *37*, 154–160.

(60) Araki, J.; Wada, M.; Kuga, S.; Okano, T. Birefringent Glassy Phase of a Cellulose Microcrystal Suspension. *Langmuir* **2000**, *16* (16), 2413–2415.

(61) Araki, J.; Kuga, S. Effect of Trace Electrolyte on Liquid Crystal Type of Cellulose Microcrystals. *Langmuir* **2001**, *17* (14), 4493–4496.

(62) Dong, X. M.; Gray, D. G. Effect of Counterions on Ordered Phase Formation in Suspensions of Charged Rodlike Cellulose Crystallites. *Langmuir* **1997**, *13* (7), 2404–2409.

(63) Schowalter, W. R. *Mechanics of Non-Newtonian Fluids*; Press, P., Ed.; Ekevier: Amsterdam, 1978.

(64) Salajkova, M.; Noh, J.; Park, J. H.; Lagerwall, J. P. F.; Schu, C. Cellulose Nanocrystal-Based Materials: From Liquid Crystal Self-Assembly and Glass Formation to Multifunctional Thin Films. **2014**, *6* (August 2013), 1–12.

(65) Marchessault, R. H.; Morehead, F. F.; Koch, M. J. Some Hydrodynamic Properties of Neutral Suspensions of Cellulose Crystallites as Related to Size and Shape. *J. Colloid Sci.* **1961**, *16*, 327–344.

(66) Shafiei-Sabet, S.; Hamad, W. Y.; Hatzikiriakos, S. G. Rheology of Nanocrystalline Cellulose Aqueous Suspensions. *Langmuir* **2012**, *28*, 17124–17133.

(67) Orts, W. J.; Godbout, L.; Marchessault, R. H.; Revol, J. F. Enhanced Ordering of Liquid Crystalline Suspensions of Cellulose Microfibrils: A Small Angle Neutron Scattering Study. *Macromolecules* **1998**, *31* (97), 5717–5725.

(68) Ebeling, T.; Paillet, M.; Borsali, R.; Diat, O.; Dufresne, A.; Cavaill, J. Y.; Chanzy, H. Shear-Induced Orientation Phenomena in Suspensions of Cellulose Microcrystals, Revealed by Small Angle X-Ray Scattering. *Langmuir* **1999**, *15* (19), 6123–6126.

(69) Yoshiharu, N.; Shigenori, K.; Masahisa, W.; Takeshi, O. Cellulose Microcrystal Film of High Uniaxial Orientation. *Macromolecules* **1997**, *30* (110), 6395–6397.

(70) Mu, X.; Gray, D. G. Formation of Chiral Nematic Films from Cellulose Nanocrystal Suspensions Is a Two-Stage Process. *Langmuir* **2014**, *30*, 9256–9260.

(71) Beck, S.; Bouchard, J.; Berry, R. Dispersibility in Water of Dried Nanocrystalline Cellulose. *Biomacromolecules* **2012**, *13*, 1486–1494.

(72) Dufresne, A. Nanocellulose: A New Ageless Bionanomaterial. *Mater. Today* **2013**, *16* (6), 220–227.

(73) Beck, S.; Bouchard, J.; Berry, R. Controlling the Reflection Wavelength of Iridescent Solid Films of Nanocrystalline Cellulose. *Biomacromolecules* **2011**, *12*, 167–172.

(74) Revol, J. F.; Godbout, L.; Gray, D. G. Solid Self-Assembled Films of Cellulose with Chiral Nematic Order and Optically Variable Properties. *J. pulp Pap. Sci. 24* (5), 146–149.

(75) Revol, J. F.; Godbout, L.; Dong, X.-M.; Gray, D. G.; Chanzy, H.; Maret, G. Chiral Nematic Suspensions of Cellulose Crystallites; Phase Separation and Magnetic Field Orientation. *Liq. Cryst.* **1994**, *16*, 127–134.

(76) Dufresne, A. *Nanocellulose. From Nature to High Performance Tailored Materials*; De Gruyter: Berlin, 2012.

(77) Araki, J.; Wada, M.; Kuga, S.; Okano, T. Influence of Surface Charge on Viscosity Behavior of Cellulose Microcrystal Suspension. *J. Wood Sci.* **1999**, *45*, 258–261.

(78) Kalashnikova, I.; Bizot, H.; Cathala, B.; Capron, I. Modulation of Cellulose Nanocrystals Amphiphilic Properties to Stabilize Oil/water Interface. *Biomacromolecules* **2012**, *13*, 267–275.

(79) Jiang, F.; Esker, A. R.; Roman, M. Acid-Catalyzed and Solvolytic Desulfation of H_2SO_4 Hydrolyzed Cellulose Nanocrystals. *Langmuir* **2010**, *26* (5), 17919–17925.

(80) Çetin, N. S.; Tingaut, P.; Özmen, N.; Henry, N.; Harper, D.; Dadmun, M.; Sèbe, G. Acetylation of Cellulose Nanowhiskers with Vinyl Acetate under Moderate Conditions. *Macromol. Biosci.* **2009**, *9*, 997–1003.

(81) Yuan, H.; Nishiyama, Y.; Wada, M.; Kuga, S. Surface Acylation of Cellulose Whiskers by Drying Aqueous Emulsion. *Biomacromolecules* **2006**, *7*, 696–700.

(82) Junior de Menezes, A.; Siqueira, G.; Curvelo, A. A. S.; Dufresne, A. Extrusion and Characterization of Functionalized Cellulose Whiskers Reinforced Polyethylene Nanocomposites. *Polymer* **2009**, *50*, 4552–4563.

(83) Spinella, S.; Maiorana, A.; Qian, Q.; Dawson, N. J.; Hepworth, V.; McCallum, S. a.; Ganesh, M.; Singer, K. D.; Gross, R. a. Concurrent Cellulose Hydrolysis and Esterification to Prepare a Surface-Modified Cellulose Nanocrystal Decorated with Carboxylic Acid Moieties. *ACS Sustain. Chem. Eng.* **2016**, *4*, 1538–1550.

(84) Hasani, M.; Cranston, E. D.; Westman, G.; Gray, D. G. Cationic Surface Functionalization of Cellulose Nanocrystals. *Soft Matter* **2008**, *4*, 2238–2244.

(85) Dong, S.; Roman, M. Fluorescently Labeled Cellulose Nanocrystals for Bioimaging Applications. *J. Am. Chem. Soc.* **2007**, *129*, 13810–13811.

(86) Goussé, C.; Chanzy, H.; Excoffier, G.; Soubeyrand, L.; Fleury, E. Stable Suspensions of Partially Silylated Cellulose Whiskers Dispersed in Organic Solvents. *Polymer* **2002**, *43*, 2645–2651.

(87) Qiang Yang, X. P. A Facile Approach for Fabricating Fluorescent Cellulose. *J. Appl. Polym. Sci.* **2010**, *117*, 3639–3644.

(88) Isogai, A.; Saito, T.; Fukuzumi, H. TEMPO-Oxidized Cellulose Nanofibers. *Nanoscale* **2011**, *3*, 71–85.

(89) Karaaslan, M. a.; Gao, G.; Kadla, J. F. Nanocrystalline Cellulose/β-Casein Conjugated Nanoparticles Prepared by Click Chemistry. *Cellulose* **2013**, *20*, 2655–2665.

(90) Barazzouk, S.; Daneault, C. Amino Acid and Peptide Immobilization on Oxidized Nanocellulose: Spectroscopic Characterization. *Nanomaterials* **2012**, *2*, 187–205.

(91) Barazzouk, S.; Daneault, C. Amino Acid and Peptide Immobilization on Oxidized Nanocellulose: Spectroscopic Characterization. *Nanomaterials* **2012**, *2*, 187–205.

(92) Barazzouk, S.; Daneault, C. Tryptophan-Based Peptides Grafted onto Oxidized Nanocellulose. *Cellulose* **2012**, *19*, 481–493.

(93) Mangalam, A. P.; Simonsen, J.; Benight, A. S. Cellulose/DNA Hybrid Nanomaterials. **2009**, *10*, 497–504.

(94) Sadeghifar, H.; Filpponen, I.; Clarke, S. P.; Brougham, D. F.; Argyropoulos, D. S. Production of Cellulose Nanocrystals Using Hydrobromic Acid and Click Reactions on Their Surface. *J. Mater. Sci.* **2011**, *46*, 7344–7355.

(95) Filpponen, I.; Argyropoulos, D. S. Regular Linking of Cellulose Nanocrystals via Click Chemistry: Synthesis and Formation of Cellulose Nanoplatelet Gels. *Biomacromolecules* **2010**, *11*, 1060–1066.

(96) Feese, E.; Sadeghifar, H.; Gracz, H. S.; Argyropoulos, D. S.; Ghiladi, R. A. Photobactericidal Porphyrin-Cellulose Nanocrystals: Synthesis, Characterization, and Antimicrobial Properties. *Biomacromolecules* **2011**, *12*, 3528–3539.

(97) Eyley, S.; Thielemans, W. Imidazolium Grafted Cellulose Nanocrystals for Ion Exchange Applications. *Chem. Commun.* **2011**, *47*, 4177–4179.

(98) Habibi, Y.; Goffin, A.-L.; Schiltz, N.; Duquesne, E.; Dubois, P.; Dufresne, A. Bionanocomposites Based on Poly(ε-Caprolactone)-Grafted Cellulose Nanocrystals by Ring-Opening Polymerization. *J. Mater. Chem.* **2008**, *18*, 5002.

(99) Morandi, G.; Heath, L.; Thielemans, W. Cellulose Nanocrystals Grafted with Polystyrene Chains through Surface-Initiated Atom Transfer Radical Polymerization (SI-ATRP). *Langmuir* **2009**, *25* (12), 8280–8286.

(100) Azzam, F.; Heux, L.; Jean, B.; Putaux, J. L. Preparation by Grafting Onto, Characterization and Properties of Thermally Responsive Polymer - Decorated Cellulose Nanocrystals. **2010**, *11*, 3652–3659.

(101) Hua, C.; Peng, S. M.; Dong, C. M. Synthesis and Characterization of Linear-Dendron-like Poly(ε-Caprolactone)-B-Poly(ethylene Oxide) Copolymers via the Combination of Ring-Opening Polymerization and Click Chemistry. *Macromolecules* **2008**, *41*, 6686–6695.

(102) Jackson, J. K.; Letchford, K.; Wasserman, B. Z.; Ye, L.; Hamad, W. Y.; Burt, H. M. The Use of Nanocrystalline Cellulose for the Binding and Controlled Release of Drugs. *Int. J. Nanomedicine* **2011**, *6*, 321–330.

(103) Johnson, R. K.; Zink-Sharp, A.; Glasser, W. G. Preparation and Characterization of Hydrophobic Derivatives of TEMPO-Oxidized Nanocelluloses. *Cellulose* **2011**, *18*, 1599–1609.

(104) Sengupta, R.; Chakraborty, S.; Bandyopadhyay, S.; Dasgupta, S.; Mukhopadhyay, R.; Auddy, K.; Deuri, A. S. Dispersion of Cellulose Crystallites by Nonionic Surfactants in a Hydrophobic Polymer Matrix. *Polym. Eng. Sci.* **2009**, *47*, 21–25.

(105) Lee, K. Y.; Aitomki, Y.; Berglund, L. A.; Oksman, K.; Bismarck, A. On the Use of Nanocellulose as Reinforcement in Polymer Matrix Composites. *Compos. Sci. Technol.* **2014**, *105*, 15–27.

(106) Kaushik M. Moores, A. Review: Nanocelluloses as Versatile Supports for Metal Nanoparticles and Their Applications in Catalysis. *Green Chem.* **2016**, *18*, 622–637.

(107) Jorfi, M.; Foster, E. J. Recent Advances in Nanocellulose for Biomedical Applications. *J. Appl. Polym. Sci.* **2015**, *132*, 41719.

(108) Biyani, M. V.; Weder, C.; Foster, E. J. Photoswitchable Nanocomposites Made from Coumarin-Functionalized Cellulose Nanocrystals. *Polym. Chem.* **2014**, *5*, 5501–5508.

(109) Capadona, J. R.; Shanmuganathan, K.; Tyler, D. J.; Rowan, S. J.; Weder, C. Stimuli-Responsive Polymer Nanocomposites Inspired by the Sea Cucumber Dermis. *Science* **2008**, *319*, 1370–1374.

(110) Roman, M.; Dong, S.; Hirani, A.; Lee, Y. W. Cellulose Nanocrystals for Drug Delivery. **2010**, 81–91.

(111) Dong, S.; Hirani, A. A.; Colacino, K. R.; Lee, Y. W.; Roman, M. Cytotoxicity and Cellular Uptake of Cellulose Nanocrystals. *Nano Life* **2012**, *2* (3), 1241006.

(112) Mahmoud, K. A.; Mena, J. A.; Male, K. B.; Hrapovic, S.; Kamen, A.; Luong, J. H. T. Effect of Surface Charge on the Cellular Uptake and Cytotoxicity of Fluorescent Labeled Cellulose Nanocrystals. *ACS Appl. Mater. Interfaces* **2010**, *2* (10), 2924–2932.

(113) Dong, S.; Cho, H. J.; Lee, Y. W.; Roman, M. Synthesis and Cellular Uptake of Folic Acid-Conjugated Cellulose Nanocrystals for Cancer Targeting. *Biomacromolecules* **2014**, *15*, 1560–1567.

(114) Colombo, L.; Zoia, L.; Violatto, M. B.; Previdi, S.; Talamini, L.; Sitia, L.; Nicotra, F.; Orlandi, M.; Salmona, M.; Recordati, C.; Bigini, P.; La Ferla, B. Organ Distribution and Bone Tropism of Cellulose Nanocrystals in Living Mice. *Biomacromolecules* **2015**, *16*, 2862–2871.

(115) Gaspar, D.; Fernandes, S. N.; de Oliveira, A. G.; Fernandes, J. G.; Grey, P.; Pontes, R. V; Pereira, L.; Martins, R.; Godinho, M. H.; Fortunato, E. Nanocrystalline Cellulose Applied Simultaneously as the Gate Dielectric and the Substrate in Flexible Field Effect Transistors. *Nanotechnology* **2014**, *25*, 094008.

(116) Najafabadi, E.; Zhou, Y. H.; Knauer, K. A.; Fuentes-Hernandez, C.; Kippelen, B. Efficient Organic Light-Emitting Diodes Fabricated on Cellulose Nanocrystal Substrates. *Appl. Phys. Lett.* **2014**, *105*, 063305.

(117) Tuukkanen, S.; Lehtim??ki, S.; Jahangir, F.; Eskelinen, A. P.; Lupo, D.; Franssila, S. Printable and Disposable Supercapacitor from Nanocellulose and Carbon Nanotubes. *Proc. 5th Electron. Syst. Technol. Conf. ESTC 2014* **2014**.

(118) He, Z.; Zhong, C.; Su, S.; Xu, M.; Wu, H.; Cao, Y. Enhanced Power-Conversion Efficiency in Polymer Solar Cells Using an Inverted Device Structure. *Nat. Photonics* **2012**, *6* (9), 593–597.

(119) Zhou, Y.; Fuentes-Hernandez, C.; Khan, T. M.; Liu, J.-C.; Hsu, J.; Shim, J. W.; Dindar, A.; Youngblood, J. P.; Moon, R. J.; Kippelen, B. Recyclable Organic Solar Cells on Cellulose Nanocrystal Substrates. *Sci. Rep.* **2013**, *3*, 1536.

(120) Hassan, M. L.; Moorefield, C. M.; Elbatal, H. S.; Newkome, G. R.; Modarelli, D. a.; Romano, N. C. Fluorescent Cellulose Nanocrystals via Supramolecular Assembly of Terpyridine-Modified Cellulose Nanocrystals and Terpyridine-Modified Perylene. *Mater. Sci. Eng. B Solid-State Mater. Adv. Technol.* **2012**, *177* (4), 350–358.

(121) Chauhan, P.; Hadad, C.; López, A. H.; Silvestrini, S.; La Parola, V.; Frison, E.; Maggini, M.; Prato, M.; Carofiglio, T. A Nanocellulose-Dye Conjugate for Multi-Format Optical pH-Sensing. *Chem. Commun.* **2014**, *50*, 9493–9496.

(122) Zhang, L.; Li, Q.; Zhou, J.; Zhang, L. Synthesis and Photophysical Behavior of Pyrene-Bearing Cellulose Nanocrystals for Fe^{3+} Sensing. *Macromol. Chem. Phys.* **2012**, *213*, 1612–1617.

Chapter 2: Production of Nanocrystalline Cellulose (NCC) and controlled oxidation of its surface.

2.1. Introduction

2.1.1. Preparation of nanocrystalline cellulose (NCC)

As previously mentioned, there are different kinds of nanocellulosic materials depending on the cellulose processing method to obtain them. In this chapter, we will focus only on nanocrystalline cellulose (NCC), which is the term commonly used for the cellulose nanocrystals prepared from natural cellulose by acid hydrolysis.

The cellulose fiber is composed of alternating crystalline and amorphous domains. These amorphous regions may be considered as structural defects where the fiber is twisted and therefore are more accessible to acid attack.[1] During the acid hydrolysis process, the hydronium ions penetrate the cellulose chains in the amorphous regions promoting the hydrolytic cleavage of the glycosidic bonds, favoured by the release of internal strain.[2] In this way, selective disruption of amorphous domains is achieved yielding rod-like nanocrystals.

The chemical and physical properties of the nanocrystals obtained are strongly influenced by many factors. Morphology and crystallinity will depend on the source of raw material chosen for its production,[3] whereas surface charge and colloidal stability will be mainly affected by the acid used in its synthesis.[4] Also other hydrolysis parameters must be carefully controlled, such as temperature, time or acid concentration. Most results point out that longer hydrolysis times, along with higher temperatures give rise to shorter nanocrystals with higher surface charge and narrower size distribution.[5,6] Thus, NCC features can be tailored and should be precisely known, for being key properties that determine functionality and application of the material.

Diverse procedures have been developed for different raw materials. Among the most common sources employed there are plant-based materials such as cotton,[7] cotton

linters,[8] ramie,[9] flax,[10] hemp,[11] sisal,[12] wheat straw,[13] palm,[14] wood,[5] sugar beet,[15] and microcrystalline cellulose (MCC).[16] Additionally, NCC can be obtained from bacterial cellulose,[17] tunicates,[18] and valonia.[19]

Concerning the type of acid, hydrochloric and sulfuric acids are by far the most extensively used. Nanocrystals from hydrolysis with sulfuric acid display better colloidal stability than those obtained with HCl. The explanation for this behavior lies in the different surface charge for both nanocrystals (Figure 1). NCC obtained from hydrochloric acid are almost neutral, presenting reduced dispersibility in water and tending to flocculate.[20] On the other hand, nanocrystals from hydrolysis with H_2SO_4 undergo some sulfation on their surface due to the grafting of anionic sulfate groups through esterification.[21] The strong repulsion between the anionic sulfate ester groups avoids aggregation of nanocrystals in suspension. Besides, the pKa value of sulfate groups is around 1.9, which makes them stable over a wide range of pH values. Very few examples have been reported in literature for the production of crystalline cellulose nanoparticles with phosphoric[22] or hydrobromic[23] acids. Nonetheless, they appear to behave analogously to sulfuric and hydrochloric acids, respectively. Hydrolysis with phosphoric acid has been shown to introduce some charged phosphoric ester groups, yielding NCC with good colloidal stability.[22] Not only the surface properties, but also the dimensions of the dispersed particles influence the stability of NCC suspensions. Typically, smaller nanoparticles with a low aspect ratio are dispersed more homogeneously in solution.[24]

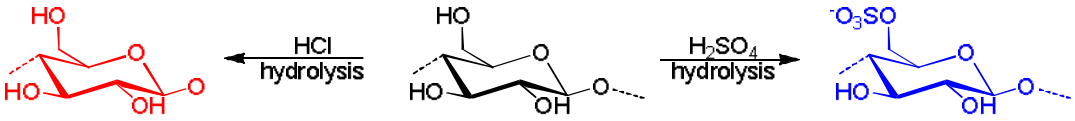

Figure 1. Schematic representation of different surface on nanocrystals obtained from H_2SO_4 or HCl hydrolysis.

As described in the first chapter, another remarkable feature of NCC is the abundance of hydroxyl groups on its surface. It does not only provide high hydrophilicity, but also permits the introduction of diverse functionalities on the surface of NCC.[25] The main challenge with chemical functionalization is to find a reagent and reaction medium that enable modification of the nanocrystal surface without affecting the inner part and the crystalline structure. One of the many possibilities is the oxidation using radical TEMPO catalyst that we proceed to discuss in detail hereafter.

2.1.2. TEMPO oxidations

The molecule 2,2,6,6-tetramethylpiperidine-1-oxyl (TEMPO) belongs to the nitroxide radical family. Firstly introduced by Semmelhack *et al.*,[26] for the oxidation of different organic alcohols to the corresponding aldehydes, this reaction has been widely used for the selective oxidation of primary hydroxyl groups in the presence of secondary ones. Experimental evidences support a mechanism in which a secondary oxidant transforms TEMPO in an oxoammonium salt that works as the primary oxidant, transforming the alcohol into its aldehyde derivative. This results in the

formation of a N-hydroxylamine molecule that is oxidized to TEMPO radical, thus completing the catalytic cycle, described in Figure 2. However, in the presence of water, the reaction could not be stopped at the aldehyde. In aqueous media, the aldehyde equilibrates with the corresponding hydrate that can be oxidized *via* a similar mechanism to the carboxylic acid.[27]

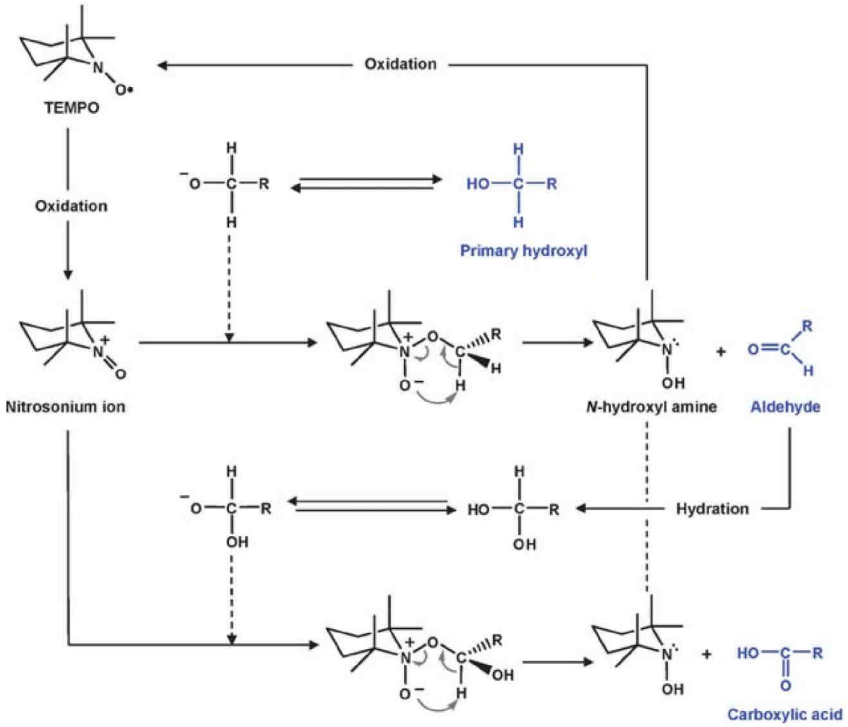

Figure 2. General mechanism for the TEMPO mediated oxidation of primary alcohols.[28]

TEMPO oxidation of cellulose

Many examples on the application of TEMPO mediated oxidation to carbohydrates can be found in literature since it was first reported by De Nooy et al. in 1995,[29] and this oxidation of carbohydrates generally gives uronic acids as main oxidation products. In particular, TEMPO mediated oxidation of cellulose is generally carried out in presence of NaOCl and NaBr as secondary oxidant and co-oxidant, respectively. The addition of NaBr generates the more reactive hypobromite (OBr^-), which has been shown to accelerate the reaction.[29]

The proposed reaction mechanism shows that two molar equivalents of hypochlorite are needed to transform a single anhydroglucose primary alcohol to the corresponding carboxylate, whereas only catalytic amounts of TEMPO and NaBr are required, since they are regenerated in the course of the reaction (Figure 3).

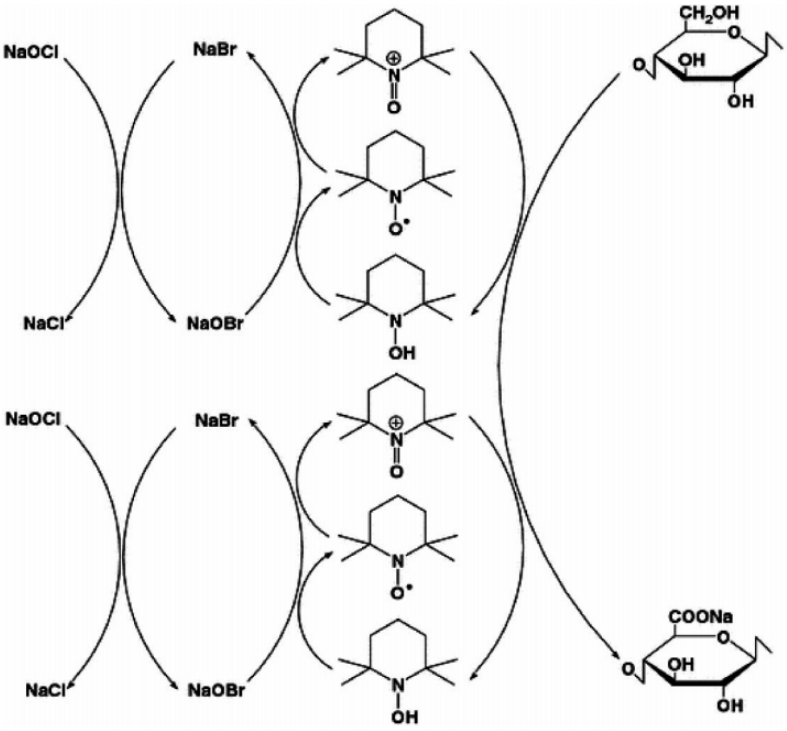

Figure 3. Scheme of the TEMPO mediated oxidation of hydroxymethyl groups in cellulose.[4]

Although the reaction proceeds either under basic or acidic media, it is preferable alkaline pH, allowing faster and more selective towards primary alcohols. This fact might be explained for the more compact five membered transition state generated when reaction takes place in basic media, respect to the linear one formed at acid pH (Figure 4).[30] Besides, TEMPO radicals can disproportionate into oxoammonium salts and hydroxylamines under acidic catalysis. Thus, pH must be maintained by adding dilute alkali solution, which is continuously consumed by the protons released during the reaction. Most TEMPO mediated oxidations of cellulose are carried out in aqueous media at basic pH (9-11).

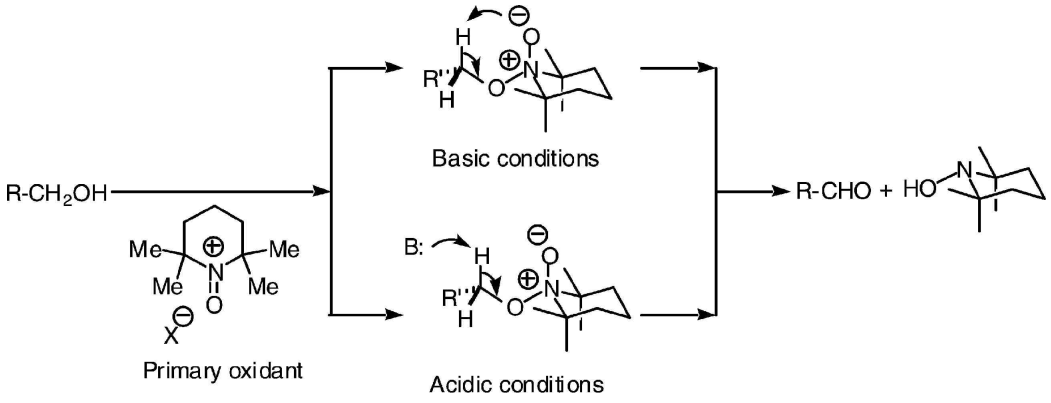

Figure 4. TEMPO oxidation transition state in acid or basic conditions.[31]

TEMPO oxidation of nanocellulose

For the first time in 2001, Araki *et al.* reported the TEMPO oxidation on NCC. The oxidation was performed on nanocrystals obtained from HCl hydrolysis of CF11 cellulose, as an intermediate step to promote grafting of polymeric chains.[32] It was demonstrated that after TEMPO mediated oxidation, the initial morphology of NCC was preserved and the dispersibility in water was improved thanks to electrostatic repulsions between the newly introduced carboxylic groups. Similar results were obtained by Habibi *et al.* after TEMPO mediated oxidation of NCC obtained through HCl hydrolysis of cellulose from tunicate. In this work, the authors also reported that various degrees of oxidation can be predicted and achieved by using specific amounts of the primary oxidizing agent, namely, NaOCl.[33]

More recently, Okita *et al.* demonstrated that a maximum degree of oxidation can be reached depending on the nature of the nanocrystals, and more specifically their size and shape. They calculated the total content of oxidized groups introduced according to the average crystal size (C_A), expressed as mean value between C_1 and C_2 (Figure 5a). They demonstrated how with a C_A of 4 nm, the maximum degree of oxidation (DO) achieved (expressed as mol carboxylic groups/mol of monomer unit was 0.3, whereas when C_A grew up to 10 nm, the maximum degree of oxidation was roughly 0.1 (Figure 5b).

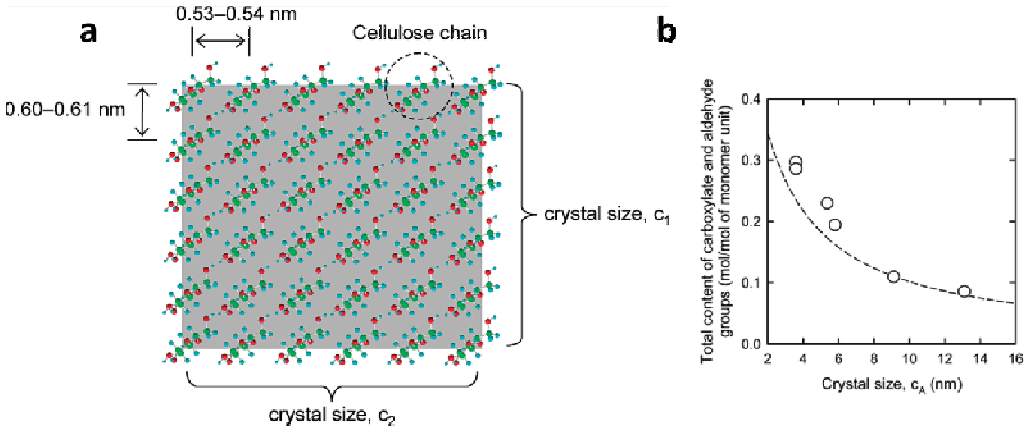

Figure 5. Schematic representation of a single cellulose nanocrystal geometry (a) and variation of the maximum degree of oxidation with the crystal geometry (b).[34]

The introduction of carboxylic groups, apart from modifying the surface physical properties of the nanocrystals, is particularly important from a chemical point of view. As it has been mentioned in the introduction, this reaction is often employed as an intermediate step for further functionalization of the nanocrystals, enabling new functionalization routes not possible with pristine NCC.[35,36]

2.2. Aim of the work

This Chapter is dedicated to describing the production of nanocrystalline cellulose starting from microcrystalline cellulose. We will also describe how reaction conditions affect the degree of oxidation achieved with TEMPO-mediated oxidation of the NCC surface, and investigate how oxidation of the nanocrystals affect the material properties. This reaction has been employed here as an effective way to introduce carboxylic groups on the crystal surface in a controlled manner,[33] enabling alternative functionalization strategies.

For all materials, the full characterization will be presented, in order to have a complete reference for the Chapters that follow.

2.3. Results and discussion

2.3.1. Production of Nanocrystalline cellulose (NCC)

In this work, we chose microcrystalline cellulose (MCC) as starting material to obtain nanocrystalline cellulose (NCC). The hydrolysis was performed with H_2SO_4 at 64 % wt, while stirring at 45 ºC for 2 hours, as described by Bondeson *et al.*[16] After that time, the reaction was stopped by adding cool water (10 fold) and left to settle. Then, most of the water was removed and the solid dialyzed against MilliQ water for 3 days, until neutral pH was reached. Finally, the suspension was submitted to centrifugation (9000 r.p.m for 10 min) and sonication steps where supernatants were collected, in order to separate non-hydrolyzed MCC from NCC (Figure 6a).

Very stable suspensions of NCC in water were obtained, with a yield of ~30% (of initial weight), similar to the optimized values reported in literature.[16] The low yield has been ascribed to the disintegration of amorphous regions and degradation of crystalline parts during hydrolysis.[23] As can be seen in Figure 6b and c, MCC is completely insoluble in water, whereas after hydrolysis, NCC suspensions present a remarkable stability due to the combined effects of reduction in size and introduction of charged sulfate groups on its surface.

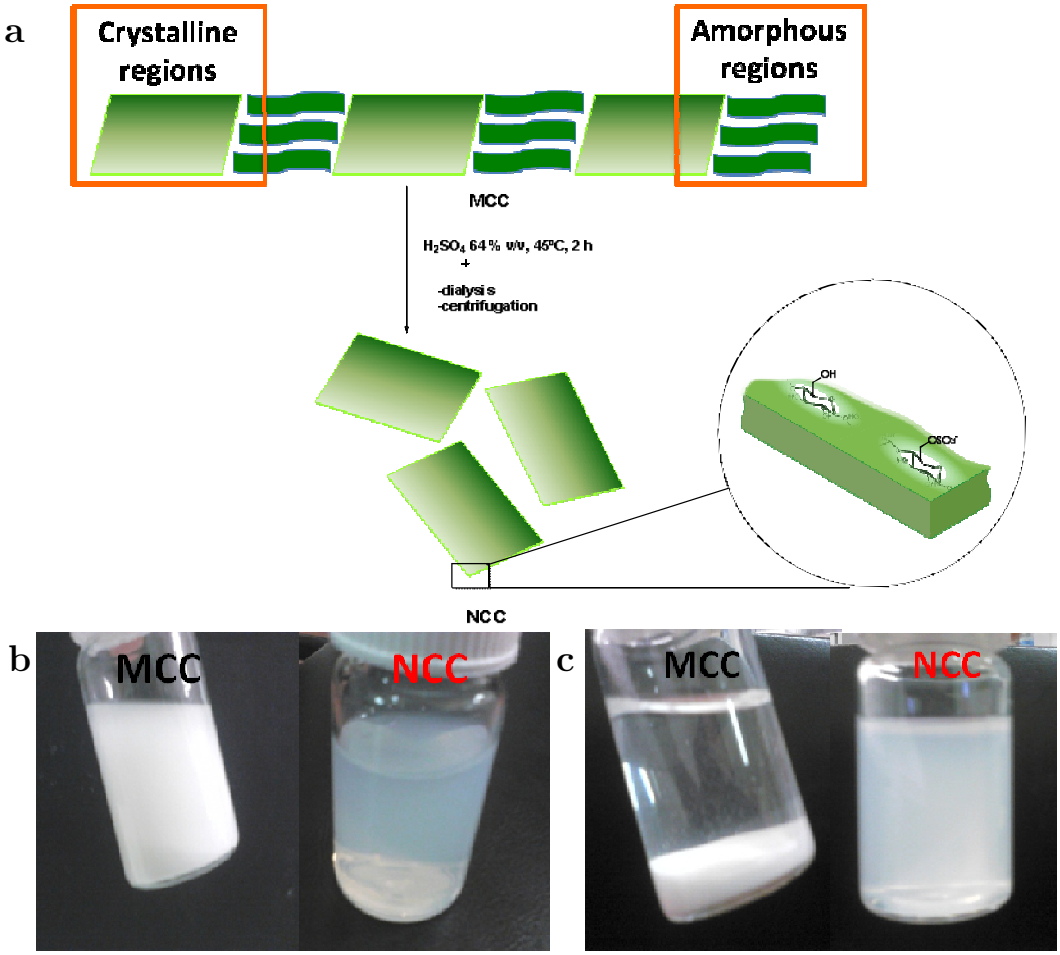

Figure 6. Schematic representation of NCC production reaction (a), suspensions of MCC and NCC in water at t =0 (b) and t = 5 days (c).

2.3.2. TEMPO oxidation of Nanocrystalline cellulose (NCC)

Synthesis of oxidized nanocellulose (ox-NCC)

The strategy followed consisted on oxidizing the primary hydroxyl groups present on the surface of the obtained NCC. TEMPO/NaOCl/NaBr mixture was used, in basic medium, following conditions previously reported in literature (Figure 7).[37]

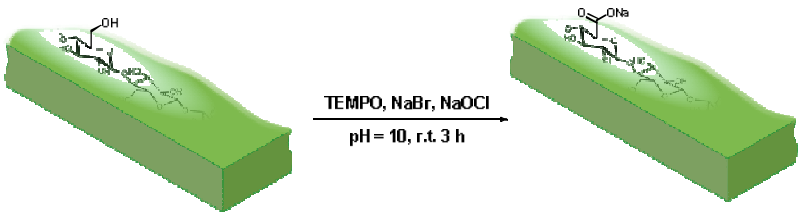

Figure 7. Schematic representation of NCC oxidation reaction.

We attempted to control the degree of oxidation achieved on the surface of **NCC** by changing some parameters, and more precisely the ratio of **NCC** to oxidant.[33] Different NaOCl amounts with respect to that of **NCC** were used, keeping the rest of parameters, such as temperature, time and pH, constant. These conditions are summarized in Table 2.

Table 2. Reaction conditions for the oxidation of NCC.

Sample	Ratio NCC/NaOCl	Yield (%)
ox-NCC_1	8	53
ox-NCC_2	2	52
ox-NCC_3	0.21	56

After that, reaction was quenched by adding ethanol and then pH neutralized adding HCl and/or NaOH 0.5 N. Suspensions were filtered and extensively washed with water. In all cases, yields were around 50 % (of initial weight). This low yield may be due to interparticle electrostatic repulsion, as the better dispersed crystallites would be partially lost during the filtration step. The resulting dispersions were stable at room temperature for months. A comparison between the dispersions obtained in H_2O using the different reaction condition is presented in Figure 8. It is possible to observe from the images higher transparency of the samples as the degree of oxidation is increased (best appreciated in the bottom surface of the vials). This suggests an improvement in the solubility due to the introduction of carboxylic groups in the reaction, since these groups are negatively charged and induce repulsion between nanocrystals, avoiding aggregation.

Figure 8. Suspensions of ox-NCC_1 (left), ox-NCC_2 (middle) and ox-NCC_3 (right) in water.

Conversion of -COONa groups to –COOH.

The carboxylic groups introduced on the surface of NCC through TEMPO oxidation are in the form of carboxylic sodium salt. As the pH is above the pKa of the carboxylic groups they are deprotonated, and the available counterion is sodium coming from the reaction medium (NaOCl and NaBr).

However, counterion can be easily exchanged for proton, by simple acidic treatment of the samples. This may be interesting in order to further prove the presence of carboxylic groups on the surface of ox-NCC, using adequate characterization tools described in the following section.

For this reason, ox-NCC_4 was prepared dispersing ox-NCC_3 in a 0.1 N solution of HCl by sonication for 15 min. After stirring for 30 min at room temperature, suspension was filtered and washed with water until pH 4 -5 was reached, yielding ox-NCC_4 in 86% yield.

2.3.3. Characterizations

Conductimetric titration

The carboxylic content of oxidized cellulose samples (ox-NCC) was determined by conductimetric titration. The cellulose samples were suspended in 0.01 M hydrochloric acid solutions. After 10 min under stirring, suspensions were titrated with 0.01 M NaOH. Typical titration curves are shown in Figure 9.

These curves present three different regions. The first one, with decreasing conductivity due to the titration of H^+ ions present from HCl through addition of NaOH. The second one is a plateau, where the OH^- groups are being consumed by weak acid groups, in particular, the carboxylic acid groups on the surface of **ox-NCC**. When carboxylic groups are consumed, conductivity of the suspension starts to increase again due to the added OH^- coming from NaOH in excess.[38]

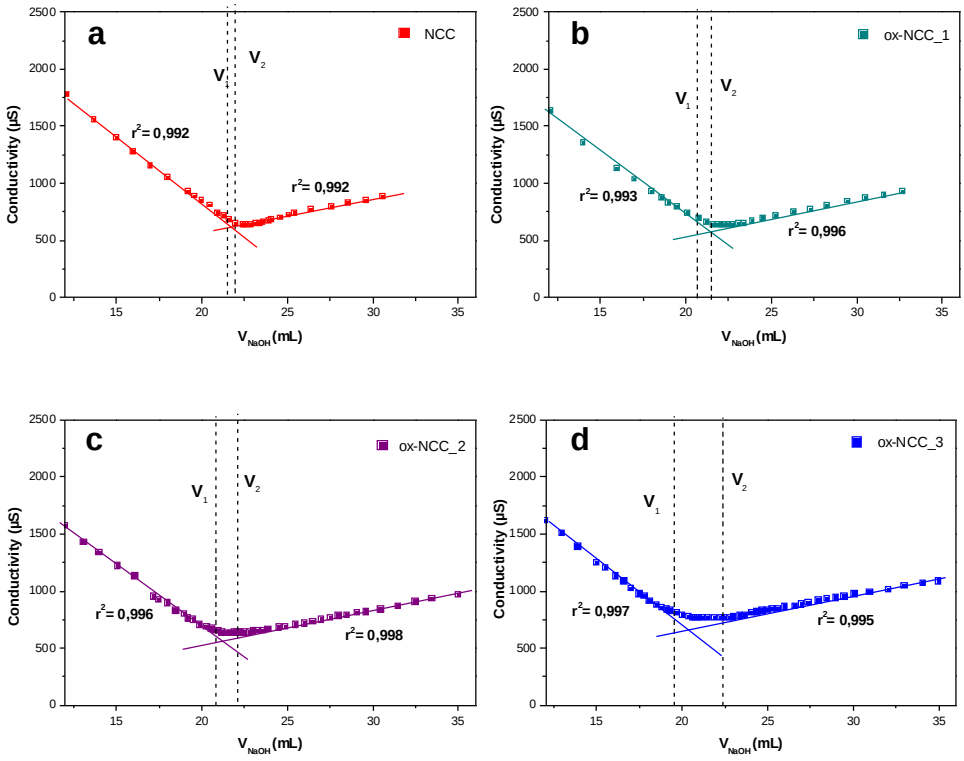

Figure 9. Conductimetric titration curves for NCC (a), ox-NCC_1 (b), ox-NCC_2 (c) and ox-NCC_3 (d).

By applying linear regressions to the first and third region of the graphics, we can determine the starting and ending points of the plateau region, and calculate the amount of carboxylic acid groups on ox-NCC and the resulting degree of oxidation (DO), which is given by the following equation[39]:

$$DO = \frac{162 \times C \times (V_2 - V_1)}{w - 36 \times C \times (V_2 - V_1)} \qquad (1)$$

Where 162 is the molecular weight of anhydroglucose unit (AGU) in g/mol, **C** is the concentration of NaOH (mol/L), $\mathbf{V_1}$ and $\mathbf{V_2}$ are the volume of NaOH (in L), **w** the weight (in g) of the dried ox-NCC sample and 36 is the difference between molecular weight of an AGU and the one of the sodium salt of an anhydroglucuronic acid moiety.[33]

For the obtained **NCC** before TEMPO oxidation, as expected, a low DO of 0.02 was obtained, since there are no carboxylic groups on the surface of non-oxidized NCC. This positive value can be attributed to the sulfate ester groups introduced during acid hydrolysis.[40] DO values for ox-NCC_1, ox-NCC_2 and ox-NCC_3 of 0.05, 0.09 and 0.15, respectively were obtained.

The DO can be also expressed as mmols of carboxylic groups per gram of NCC. This can be also calculated from the volume of NaOH needed for the titration of carboxylic groups, as equivalents of NaOH of known concentration added. These were

0.33, 0.53 and 0.87 $mmolg^{-1}$ of NCC for ox-NCC_1, ox-NCC_2 and ox-NCC_3 respectively.

These results confirmed that there was a good correlation between amount of NaOCl oxidant added for the reaction and DO of nanocrystals obtained (Table 3).

Table 3. Results of oxidation for different ox-NCC samples with respect to amount of oxidant added.

Sample	Ratio NCC/NaOCl	DO	mmol COONa/ g NCC
ox-NCC_1	8	0.05	0.33
ox-NCC_2	2	0.09	0.53
ox-NCC_3	0.21	0.15	0.87

The maximum DO achieved was in good agreement within the range of DO (0.09 – 0.3) found in literature.[34]

Thermogravimetric analysis (TGA)

It is well known that the thermal stability of a polymer depends on its composition but also on the intermolecular interactions. The chain cleavage or the bond dissociation occurs when the supplied thermal energy exceeds the bond dissociation energy of the respective chemical bonds.[41]

In order to study the thermal stability of all samples, thermogravimetric analysis (TGA) of all samples were carried out under N_2 atmosphere. Normalized thermogravimetric curves of weight loss (TG) and derivative of weight loss (DTG) for MCC, NCC and ox-NCC_3 are depicted in Figure 10. In the case of cellulose, thermal degradation is known to involve dehydration, depolymerization and decomposition of glycosyl units, with formation of a charred residue afterwards.[42] Charring is a chemical process of incomplete combustion that most solid organic compounds exhibit. The char residue burns without the presence of flames, being usually considered a flame retardant.

For MCC, typical curve was obtained, with onset temperature of decomposition at 305 ºC and low percentage of char residue close to 0 (3 %),[43] whereas NCC starts to decompose at 148 ºC leaving a char residue of 34 %. From DTG curves is more clearly observed that the decomposition temperature shifted from 350 to 173 ºC. Lower thermal stability may be attributed to the smaller size in the case of nanocrystals, but also to the introduction of sulfate groups on NCC surface during the acid hydrolysis process with H_2SO_4. It has been reported that elimination of sulfuric acid in sulfated anhydroglucose unit requires less energy than removal of water, therefore desulfation of NCC at low temperature takes place,[44] and the release of sulfuric acid molecules promotes in turn further removal of the ring hydroxyl groups.[45] Moreover, evidences show a correlation between number of sulfate groups introduced on NCC and amount of charred residue.[46]

Ox-NCC_3 shows also lower stability than MCC, in this case due to the introduction of carboxylic groups onto the surface of the nanocrystals. However, it is worth noting that basic conditions necessary for the TEMPO oxidation causes the removal of

sulfate groups,[4] having as a consequence a higher thermal stability of nanocrystals after oxidation respect to the starting NCC.

The DTG in ox-NCC_3 is resolved into two peaks, at 266 ºC and 332 ºC which are attributed to the loss of oxidized sodium anhydroglucuronic units in first place and the core fractions.[47] The second peak is also shifted to lower temperatures when compared to the original MCC, what has been reasonably explained for the much smaller particle size in ox-NCC_3, which greatly increased exposed surface area to heat flow.[48]

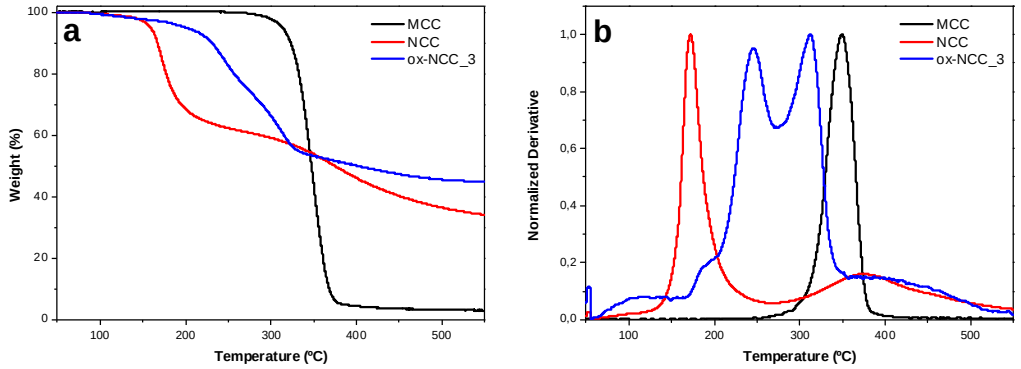

Figure 10. Normalized TG (a) and DTG (b) curves of MCC, NCC and ox-NCC_3 under N_2 atmosphere.

Weight loss and derivative of weight loss of all ox-NCC are presented in Figure 11. The onset temperature of decomposition slightly decreased with the increasing of oxidation degree (Figure 11a), being 233 ºC, 217 ºC and 175 ºC for ox-NCC_1, ox-NCC_2 and ox-NCC_3 respectively. In all cases, the decomposition of ox-NCC is resolved into two peaks (Figure 11b), ascribed as previously mentioned, to the decomposition of sodium anhydroglucoronic units and inner fractions. This is in accordance with the results observed, since the loss attributed to sodium anhydroglucuronic units is higher as oxidation degree increased. The trend observed would be consistent with a higher number of carboxylic groups on the most oxidized sample.

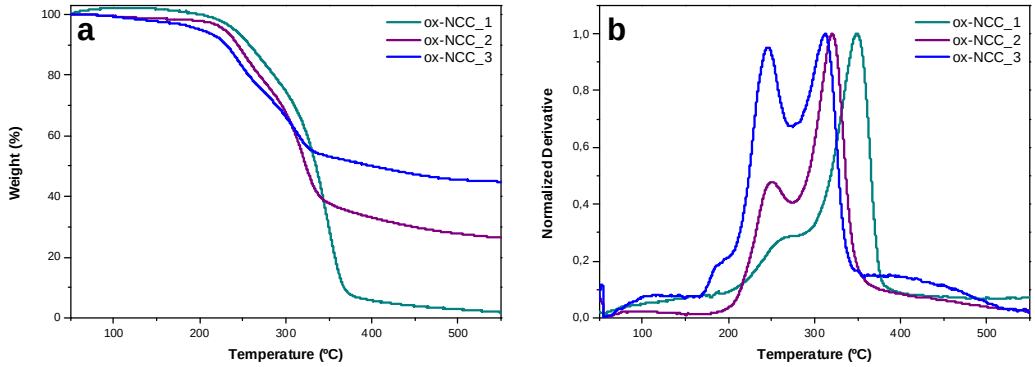

Figure 11. Normalized TG (a) and DTG (b) curves of ox-NCC_1, ox-NCC_2 and ox-NCC_3 under N_2 atmosphere.

In addition, percentages of char residue were 2, 26, and 45 % for ox-NCC_1, ox-NCC_2 and ox-NCC_3, respectively. This trend suggested a flame retardant effect from carboxylic groups on NCC.

When **ox-**NCC_3 sample is subjected to acid treatment with HCl 0.1 N, the conversion of –COONa groups on its surface into –COOH takes place, reflected by a decreasing in the thermal stability of the material (Tonset = 164 ºC) caused in turn by the decarbonation of the formed anhydroglucuronic acid groups (Figure 12a). Additional two weight loss peaks corresponding to the thermal decomposition of core fractions, although thermal decomposition mechanism in this particular case was unclear (Figure 12b). Removal of sodium had as a consequence a slight decrease in the char residue percentage from 45 % in ox-NCC_3 to 31 % for ox-NCC_4.

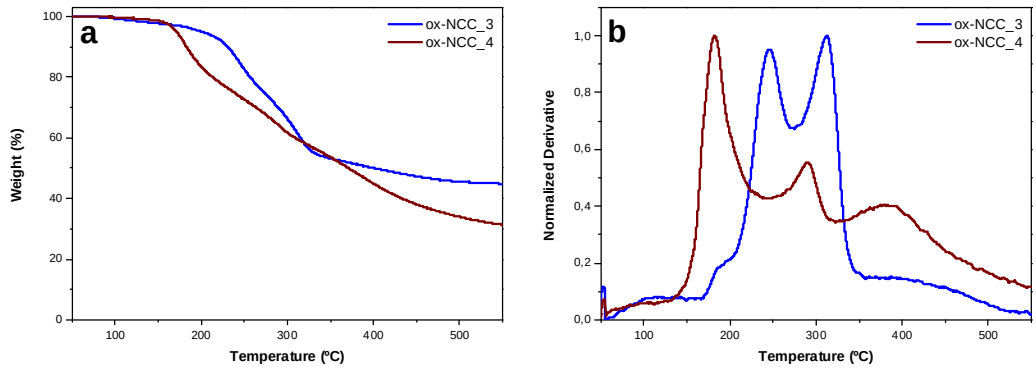

Figure 12. Normalized TG (a) and DTG (b) of ox-NCC_3 and ox-NCC_4 under N_2 atmosphere.

Infrared spectroscopy

The FT-IR spectrum of MCC shows characteristic bands, such as the hydrogen bonded OH stretching around 3400 cm^{-1}, the CH stretching at 2900 cm^{-1}, the OH bending of adsorbed water at 1635 cm^{-1}, the CH_2 bending at 1430 cm^{-1}, the CH bending at 1380 cm^{-1}, the C-O stretching at 1058 and 1035 cm^{-1}, and the OH out-of-plane bending at 687 cm^{-1}.[49] The FT-IR spectrum of NCC is not significantly different from the one of untreated cellulose (Figure 13).

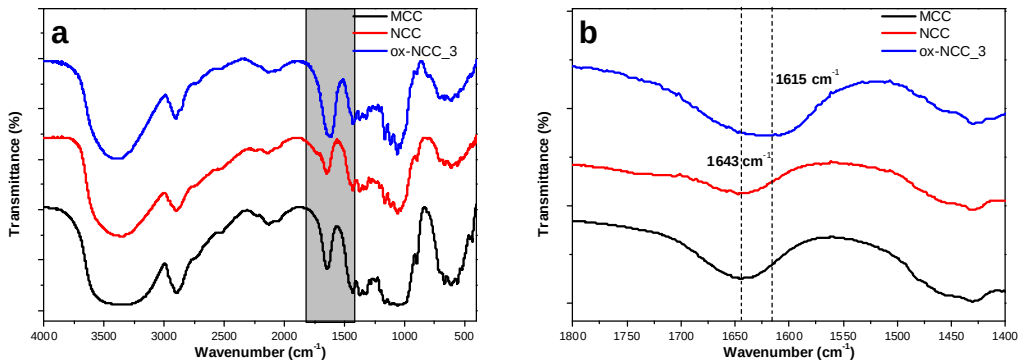

Figure 13. FT-IR spectra of MCC, NCC and ox-NCC_3 (a) and carbonyl groups stretching region of the spectra (b) (KBr pellets).

FT-IR of ox-NCC_3 is also presented in Figure 13 for comparison. The most important change is the appearance of the carboxyl groups (C=O) stretching band at 1620 cm^{-1} attributed to sodium carboxylate groups (−COONa).[50]

Concerning the different ox-NCC, FT-IR spectra were essentially the same, only the relative intensities of the band at 1615 cm^{-1} varying (Figure 14). Following Habibi et al., the measurement of the intensity of this band and its comparison with the band near 1050 cm^{-1} allowed us to confirm the variation of DO between the three ox-NCC samples.[33] We obtained 0.07, 0.1 and 0.11 for ox-NCC_1, ox-NCC_2 and ox-NCC_3, respectively. These values are within a small linear factor of those obtained with the conductimetry measurements. Considering the lack of smoothness of the IR spectrum in the 1050 cm-1 region, we conclude that both estimates are in good agreement.

Furthermore, the conversion of ox-NCC_3 (-COONa) to ox-NCC_4 (-COOH) can be verified by FT-IR.The absorption band due to C=O streching of sodium carboxyl groups at 1615 cm^{-1}, shifted to 1733 cm^{-1} for ox-NCC_4, as evidenced in Figure 15 eliminating the interference with the absorbed water band (around 1640 cm^{-1}. Moreover, the absorption band around 1400 cm^{-1} due to C-O symmetric streching of dissociated caboxylic groups disapeared in ox-NCC_4, which indicates that the sodium carboxylate groups in ox-NCC_3 were converted to free carboxyl groups by the acid treatment.[50] Based on this analysis, the success of the chemical oxidization of cellulose nanocrystals was clearly verified by FT-IR.

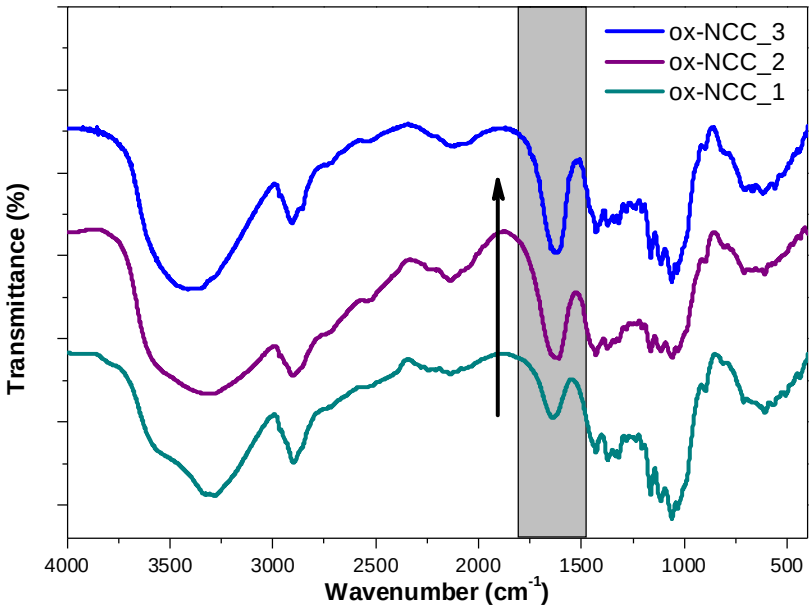

Figure 14. FT-IR spectra of ox-NCC_1, ox-NCC_2 and ox-NCC_3.

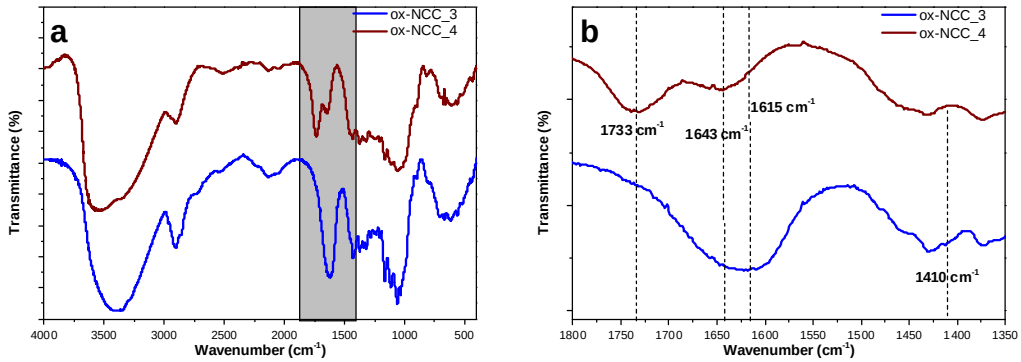

Figure 15. FT-IR spectra of ox-NCC_3 and ox-NCC_4 (a) and carbonyl group stretching region of the spectra (b).

Raman spectroscopy

Raman spectra of MCC, NCC and ox-NCC_3 were registered using a laser source at 785 nm (Figure 16). FT-Raman spectrometers using NIR or red excitation lasers avoid the fluorescence of the samples which normally blank the Raman signals.

The monomer unit for cellulose, the β-D-glucose residue, possesses no symmetry and thus all the vibrational modes are both infrared and Raman active. A particular mode will produce a band at approximately the same frequency in each case, but due to the different physical processes, in general the bands will be of different relative intensity.[51]

Raman spectrum of cellulose is quite complex and can be divided in three different regions. The bands between 1200 and 1450 cm^{-1} are attributable to modes involving considerable coupling between methine bending, methylene rocking and wagging, and COH in-plane bending motions; these are angle bending coordinates involving one bond to a hydrogen atom and the other to a heavy atom. Bands in this region were sharper and less intense in NCC and ox-NCC_3 respect to MCC. Below 1200 cm^{-1}, significant contributions from ring stretching begin and these modes, together with C–O stretching motions, dominate between 950 and 1150 cm^{-1}. This region is very similar in the three spectra, although relative ratio between samples may vary. The region between 400 and 700 cm^{-1} is dominated by the heavy atom bending, both C–O and ring modes, although some ring stretching coordinates still make minor contributions. In some instances O–H out of- plane bending motions may make minor contributions in this region as well. Below 400 cm^{-1} ring torsions start to dominate.[52]

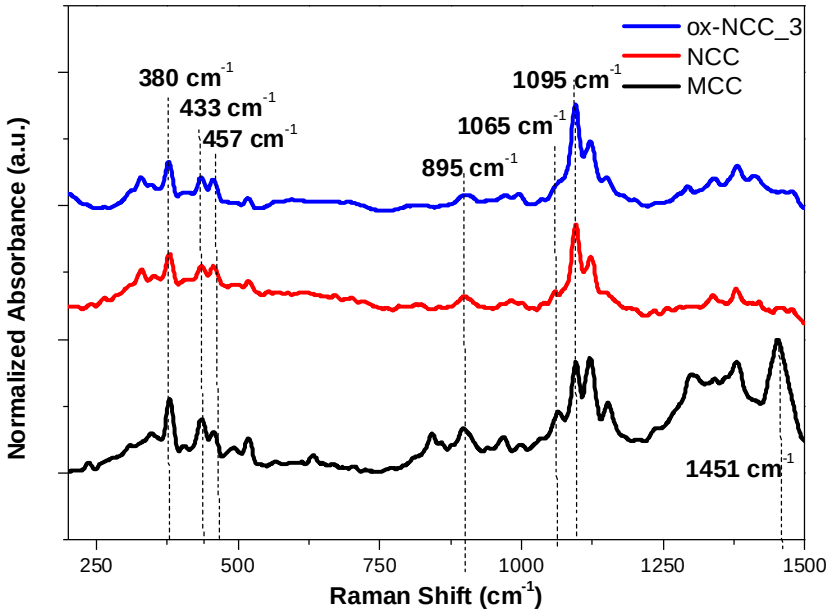

Figure 16. Raman spectra of MCC, NCC and ox-NCC_3 at 785 nm laser source.

Raman spectroscopy turns out to be a very useful tool to study the crystallinity of cellulosic materials. There are two different methods to estimate the crystallinity of cellulose reported in literature. The first one claims that the methylene bending mode is strongly influenced by the degree of crystallinity of cellulose, appearing at 1482 cm^{-1} for crystalline form and 1462 cm^{-1}, and therefore the intensity ratio of these characteristic lines is suitable for the quantification of crystallinity.[53] The other one is the method proposed by Agarwal *et al.* which uses the intensity ratio for bands at 380 and 1096 cm^{-1} with excellent regression and shows good sensitivity to crystallinity change.[54] The latter method was chosen in this study because of its better correlation with crystallinities determined by other techniques. The univariate method of Agarwal *et al.* compares the peak intensity ratio I_{380}/I_{1096} according to equation 2:

$$X_{Raman} = \frac{\left(I_{380}/I_{1096}\right) - 0.0286}{0.0065} \qquad (2)$$

We obtained X_{Raman} of 80 and 95 % for MCC and NCC, respectively, confirming that acid hydrolysis treatment of MCC gave as a result nanocrystals with higher degree of crystallinity. For ox-NCC_3, X_{Raman} was 91 %, proving that the oxidation treatment did not affect the crystallinity of the material. We assumed that ox-NCC_1 and **ox-**NCC_2 had similar degrees of crystallinity, being the treatment for ox-NCC_3 the most aggressive.

X-ray Photoelectron Spectroscopy

X-ray photoelectron spectroscopy (XPS) is a quantitative spectroscopic technique that measures the surface elemental composition of a material. This useful technique,

which has been widely applied to investigate cellulose and nanocellulose derivatives, focuses on the chemical changes resulting from surface modification.

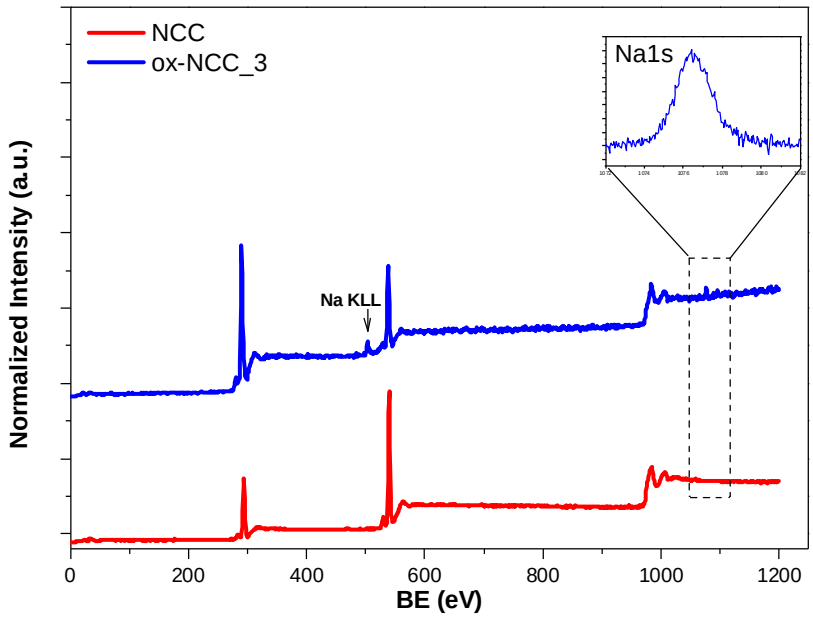

Figure 17. XPS survey of NCC and ox-NCC_3.

XPS analysis of MCC, NCC and ox-NCC_3 were performed (Figure 17). As expected, the main elements detected were carbon and oxygen, centered at 284 and 532 eV, respectively

Figure 18 shows the C 1s fitted spectra of the samples. In the spectra the expected positions of the C-C and C-H bonds assigned at around 285.0 eV, C-O bonds at around 286.5 eV and C=O bonds at around 288.5 eV are shown. The major component in all samples is the one attributed to C-O bonds.

In theory the O/C ratio of pure cellulose is 0.83 and it contains no C–C component. As shown in Table 4, the XPS of our reference MCC shows an O/C ratio of 0.70, with a minor contribution of the C–C component (Figure 18a), which is normally ascribed to non-cellulosic carbon. The O/C atomic ratio of NCC measured by XPS slightly decreased to 0.64 (Table 4), and the C–C component relative contribution was larger with respect to MCC (Figure 18b). On ox-NCC_3, the found O/C ratio was 0.31 (Table 4) and the C-C contribution was even slightly higher than in NCC (Figure 18c). These results are at first sight incongruous with what should be expected from the surface modification steps carried out on NCC surface. Nevertheless, they are in accordance with other reported studies in literature.[55,56]

This phenomenon has been explained in terms of aggregation and surface passivation.[57] In water, an excellent hydrogen bonding solvent, the surface OH groups not involved in intra- and inter- chain hydrogen bonds in cellulose stay clean and accessible. Upon drying however, these groups have to adapt to the hydrophobic media and are passivated to minimize surface energy by accumulation of air-borne contaminants, seen as the C–C carbon peak in XPS data. This phenomenon,

noticeable on NCC is substantially higher on NCC due to the higher total surface area.

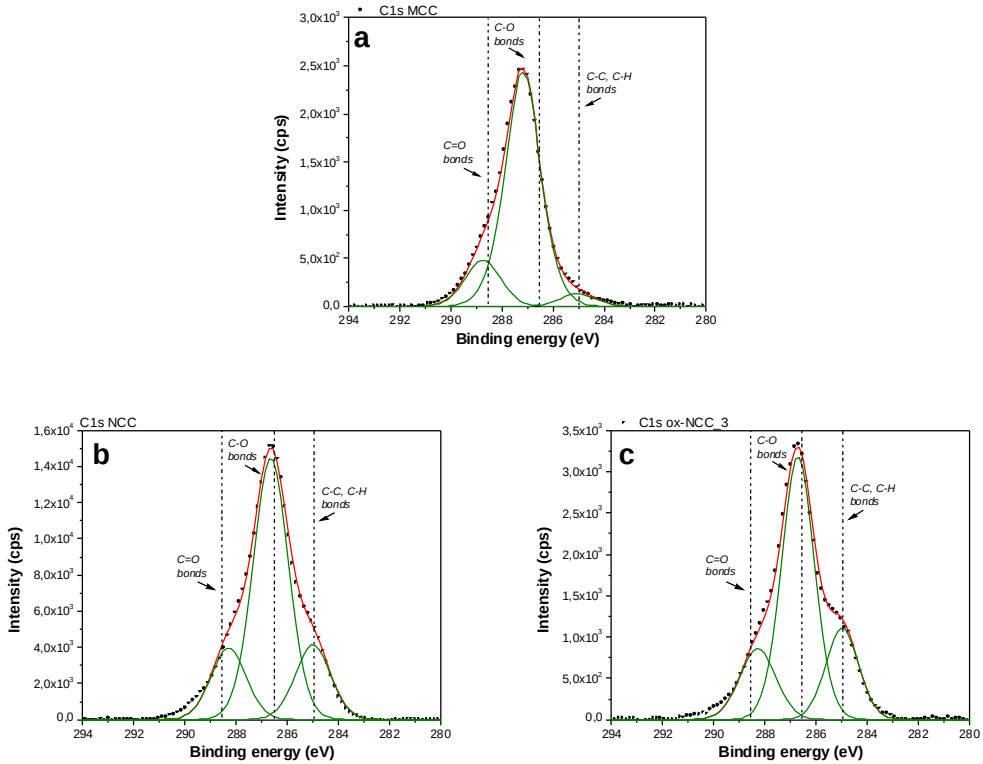

Figure 18. C1s regions of MCC (a), NCC (b,) and ox-NCC_3 (c).

Table 4. Surface chemical compositions of the samples

Sample	O/C	Na/C	S/C
MCC	0.7	-	-
NCC	0.43	-	0.015
Ox-NCC	0.31	0.01	-

As a consequence, the C1s region of XPS spectra gives no reliable information about surface modification, since the relative intensity of the different components is altered by the presence of air borne contaminants on dried NCC. This also affects to the O/C found, what avoids confirming the oxidation of NCC with this technique. However, the presence other elements can be analyzed in order to confirm such functionalization. For instance, sulfur was found in NCC, in the zone at 170 eV, in ratio sulfur to carbon (S/C) of 0.015 that was absent in MCC and would come from the sulfate ester groups formed on the surface of NCC during acid hydrolysis (Table 4). As expected, sulfur was not detected after oxidation process due to the removal of sulfate groups because of the basic conditions used for reaction. It is important to note, that after oxidation, sodium was also found in the sample, that was absent in NCC, and that would correspond to the sodium carboxylic groups (Table 4).

Atomic force microscopy (AFM)

Apart from discussion on NCC surface chemistry, the morphology of nanocrystals should be checked, and the geometrical dimensions should be defined. AFM was used to study the morphology and determine the nanoparticle thickness by topography measurements. Figure 19a and b show examples of tapping mode AFM images from NCC and ox-NCC_3, respectively, deposited onto silicon wafer surfaces. A preliminary statistical analysis of the whole pictures in terms of height distribution led to inconclusive results, most probably due to particle superimposition during drying. Height profiles are shown below the corresponding image. Aggregation of nanocrystals occurred, allowing the formation of films with very flat surface. Longitudinal line profiles on images showed that the height could typically vary from 4 to 18 nm.

It was shown that both samples exhibited the typical and expected rod-like or needle-like morphology, with a length of about 100–300 nm and a width of about 10–30 nm. For the statistical measurements of the mean length and width, transmission electron microscopy (TEM) images were used, in order to avoid the tip broadening effect in AFM.

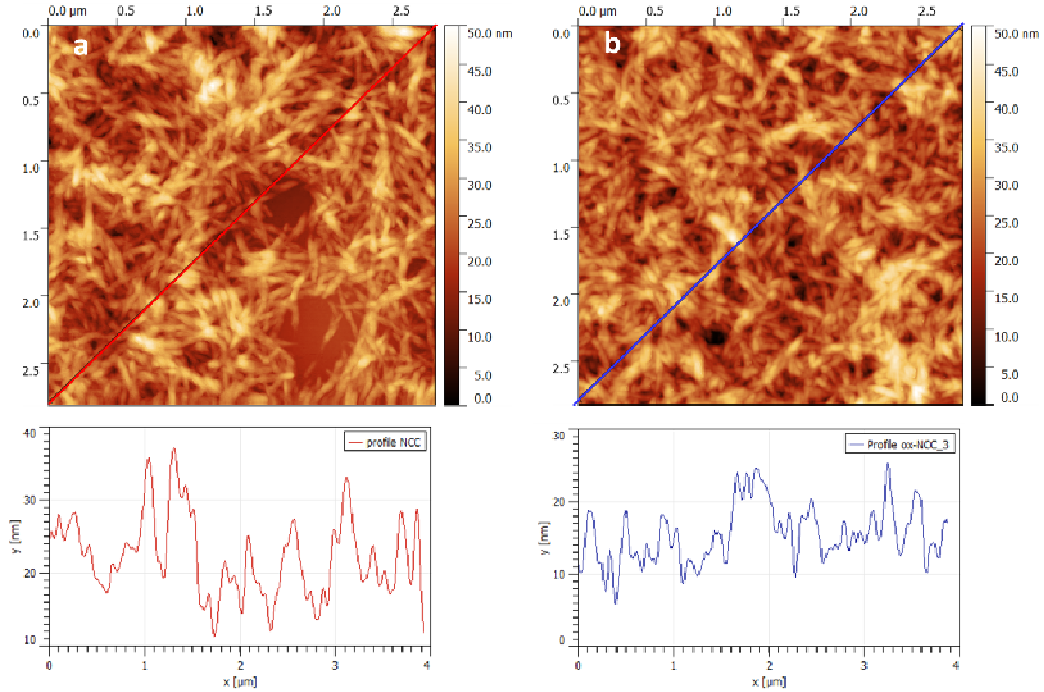

Figure 19. AFM images of NCC (a) and ox-NCC_3 (b). Height profiles are shown below the corresponding images.

Transmission electron microscopy (TEM)

In order to further study the morphology of the nanocrystals, TEM analysis of the samples were carried out. For that purpose, a drop of NCC or ox-NCC_3 suspension in water was deposited on carbon coated electron microscope grids To overcome the low contrast of the material, samples were stained with uranyl acetate solution.

In both cases, bundles of nanocrystals were observed in the TEM images in different extents and it was not common to find individual or isolated crystallites, even in the case of ox-NCC_3, despite its high dispersibility.

Mean length and width of nanocrystals for both samples was measured by counting 100 particles in each case, and corresponding distributions are shown in Figure 20. We observed that there is not significant difference in the size of the nanocrystals between these two samples. Length and width values were found to be 135 ± 40 and 9.21 ± 2.4 nm, respectively, for NCC and, 153 ± 39 and 8.84 ± 2.1 nm for **ox-**NCC_3. Since the oxidation conditions for ox-NCC_1 and ox-NCC_2 were similar and milder than for ox-NCC_3 in any case, we reasoned that their morphology would not have been either affected by the treatment.

Therefore, we could conclude that oxidation treatment did not have any detrimental effect in the morphology of nanocrystals.

As noted in this Chapter introduction, Okita *et al.* measured the degree of oxidation and correlated it to the average crystallite transverse size. The average crystal width we observed (Figure 20f) is in good agreement with their results. Our DO of 0.15 for ~9 nm width in ox-NCC_3 lies between 0.19 (5.8 nm) and 0.11 (9.1 nm).[34]

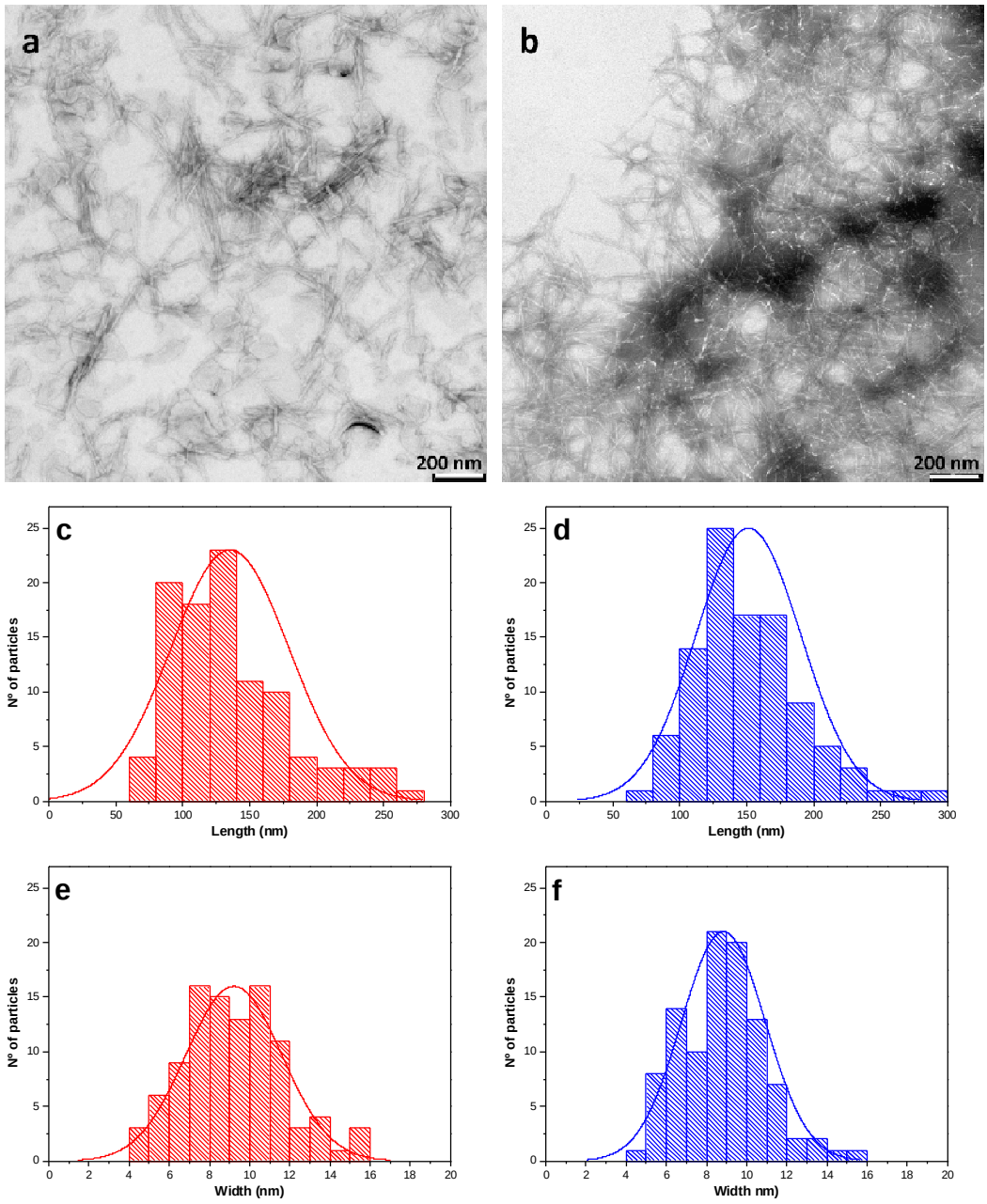

Figure 20. TEM images, length and width distributions for NCC (a, c, e) and ox-NCC_3 (b, d, f).

2.4. Conclusions

In brief, we described the preparation of our starting material, nanocrystalline cellulose (NCC). The properties of the NCC obtained, such as thermal properties, morphology measurements or degree of crystallinity, were evaluated and results found in accordance with literature.

Moreover, controlled oxidation of hydroxyl groups on the surface of NCC to carboxylic acids was successfully achieved. NCC was oxidized with sodium hypochlorite together with of sodium bromide and catalytic amounts of TEMPO radical, under various conditions. After this TEMPO mediated oxidation, the different ox-NCC obtained were characterized in terms of carboxylate contents, thermal stability, crystallinities, crystal sizes and morphology, and compared with the starting material NCC. It was demonstrated that the oxidation degree could be varied in a controlled manner by changing ratio of oxidant respect to NCC, as already reported in literature. In addition, oxidation of NCC improved its water solubility, as well as their thermal properties. It is also important to highlight that crystallinity of NCC was not compromised, neither the shape of the nanocrystals.

In conclusion, TEMPO oxidation was an effective way to tune the surface of NCC, without affecting their integrity and inherent properties. In our particular case, the oxidation can be considered as an intermediate step to open the way for further functionalization of the nanocrystals, as it will be described in the next Chapters.

2.5. Experimental

2.5.1. Generalities:

All reagents and solvents were used as received or purified using standard procedures. Milli-Q water was used in all experiments (System MilliQ plus). Microcrystalline Avicel® cellulose powder was purchased from Aldrich and used without further purification.

2.5.2. Techniques:

The carboxylate content of the water-insoluble fractions was determined by the electric conductivity titration method using a HANNA HI8733 conductimeter. To a dried sample (0.03 g), then 0.1 M HCl (15 mL) was added and the mixture was sonicated to prepare well-dispersed slurries. A 0.01 M NaOH solution was added up to pH 11. The carboxylate content of the sample was determined from the conductivity curves.

Thermogravimetric analyses were performed on TgaQ500 (TA instruments) under N_2, by equilibrating at 50 °C, and following a ramp at 10°C/min up to 600 °C (approximately 1 mg of each compound).

Infrared spectra were recorded with a Fourier-transform infrared (FT-IR) spectrometer (Perkin-Elmer 2000). Spectral width ranged from 4000 to 400 cm^{-1}, a 4 cm^{-1} resolution and an accumulation of 8 scans. Samples were prepared as KBr pellets (approximately 1 % sample in anhydrous KBr).

Raman spectra were collected with an Invia Renishaw micro-spectrometer (100x) and a laser source at 785 nm. Solid samples on glass slide were measured without further preparation.

Transmission electron microscopy (TEM) measurements were performed on a TEM Philips EM208, using an accelerating voltage of 100 kV. Samples were prepared by drop casting from dispersion (0.01% w/v) onto a TEM grid (200 mesh, nickel, carbon only), followed by staining with a 2 wt % uranyl acetate solution.

Atomic force microscopy (AFM) images were obtained with a Nanoscope IIIa, VEECO Instrument. As a general procedure to perform AFM analyses, tapping mode using a n-type silicon µmash® SPM probe (HQ:NSC15/ALBS) with tip height 12-18 µm, cone angle $< 40^o$ (Resonant frequency 325 kHz; force constant 40 N/m) (MikroMasch) from drop cast of samples in an aqueous solution (concentration of ~0.1 mg/mL) on a Si wafer substrate was performed. The obtained AFM-images were analyzed with S3 Gwyddion 2.35.

The X-ray photoelectron spectroscopy (XPS) analyses were performed with a VG-Microtech ESCA 3000Multilab, equipped with a dual Mg/Al anode. The spectra were excited by the un-monochromatized Al Kα source (1486.6 eV) run at 14 kV and 15 mA. The analyser was operated in the constant analyser energy (CAE) mode. For the individual peak energy regions, a pass energy of 20 eV set across the hemispheres was used. Survey spectra were measured at 50 eV pass energy. The pressure in the

analysis chamber was in the range of 10^{-8} Torr during data collection. The constant charging of the samples was removed by referencing all the energies to that of C-C bond (C1s) set at 285.1 eV. The invariance of the peak shapes and widths at the beginning and at the end of the analyses ensured the absence of differential charging. Analyses of the peaks were performed with the software provided by VG, based on non-linear least squares fitting program using a weighted sum of Lorentzian and Gaussian component curves after background subtraction according to Shirley and Sherwood. Atomic concentrations were calculated from peak intensities using the sensitivity factors provided with the software. The binding energy values are quoted with a precision of ± 0.15 eV and the atomic percentage with a precision of ± 10%.

2.5.3. Syntheses

Nanocellulose crystalline (NCC) preparation: Microcrystalline cellulose (10 g) was suspended in MilliQ water (45 mL) and cooled at 0 ºC. Concentrated H_2SO_4 (98%, 43 mL) was added dropwise at 0 ºC, under vigorous stirring, until the desired acid concentration was reached (64% w/w). The mixture was then heated to 45 ºC and stirred for 2 h. Hydrolysis was stopped by 10-fold dilution with water. The suspension was left to settle down overnight, and then the supernatant was decanted and replaced with fresh water. After repeating this step twice, the suspension was transferred into dialysis tubes (12 kD cut-off) and dialyzed against MilliQ water for 3 days, until neutral pH was recorded outside the dialysis membrane. Suspension was centrifuged at 9000 rpm, re-dispersed by sonication and supernatants collected. This cycle was repeated until supernatants were clear. Yield: 2.75 g (28%).

ox-NCC_1-3 preparation: NCC was suspended in MilliQ water by sonicating for 15 min. A solution of TEMPO and NaBr in MilliQ water was added dropwise. NaOCl was slowly added to start the oxidation. The mixture was stirred at room temperature while keeping pH at 10 by adding small aliquots of NaOH 0.5 M. After 3 hours the reaction was stopped by adding a portion of EtOH and pH adjusted to 7 adding HCl 0.5 M. Suspension was concentrated by evaporation, filtered and the collected solid was washed with MilliQ water 3 times to remove salts.

	Ox-NCC_1	**Ox-NCC_2**	**Ox-NCC_3**
NCC (g)	0.5	0.5	1.2
TEMPO (mg, mmol)	14.75, 0.094	14.75, 0.094	35, 0.22
NaBr (mg, mmol)	167, 1.57	167. 1.57	379, 3.68
NaOCl 4% v/v (mL)	0.6	2.5	17
H_2O (mL)	100	100	220
EtOH (mL)	0.5	1	2.3
Yield (mg, %)	280, 56	265, 53	520, 50

ox-NCC_4 preparation: ox-NCC_3 (125 mg) was stirred in presence of HCl 1 M (3 mL) for 1 hour. Then suspension was sequentially filtered and washed with MilliQ water (three times). Yield: 108 mg, (86 %).

2.6. References

(1) Matos Ruiz, M.; Cavaillé, J. Y.; Dufresne, A.; Gérard, J. F.; Graillat, C. Processing and Characterization of New Thermoset Nanocomposites Based on Cellulose Whiskers. *Compos. Interfaces* **2000**, *7*, 117–131.

(2) Rowland, S. P.; Roberts, E. J. The Nature of Accessible Surfaces in the Microstructure of Cotton Cellulose. *J. Polym. Sci. Part A-1 Polym. Chem.* **1972**, *10*, 2447–2461.

(3) George, J.; Sabapathi, N. S. Cellulose Nanocrystals: Synthesis, Functional Properties and Applications. *Nanotechnol. Sci. Appl.* **2015**, *8*, 45.

(4) Habibi, Y.; Lucia, L. A.; Rojas, O. J. Cellulose Nanocrystals: Chemistry, Self-Assembly , and Applications. *Chem. Rev.* **2010**, *110*, 3479–3500.

(5) Beck-Candanedo, S.; Roman, M.; Gray, D. G. Effect of Reaction Conditions on the Properties and Behavior of Wood Cellulose Nanocrystal Suspensions. *Biomacromolecules* **2005**, *6*, 1048–1054.

(6) Elazzouzi-Hafraoui, S.; Nishiyama, Y.; Putaux, J. L.; Heux, L.; Dubreuil, F.; Rochas, C. The Shape and Size Distribution of Crystalline Nanoparticles Prepared by Acid Hydrolysis of Native Cellulose. *Biomacromolecules* **2008**, *9*, 57–65.

(7) Dong, X. M. Effect of Microcrystallite Preparation Conditions on the Formation of Colloid Crystals of Cellulose. *Cellulose* **1998**, *5*, 19–32.

(8) Roohani, M.; Habibi, Y.; Belgacem, N. M.; Ebrahim, G.; Karimi, A. N.; Dufresne, A. Cellulose Whiskers Reinforced Polyvinyl Alcohol Copolymers Nanocomposites. *Eur. Polym. J.* **2008**, *44*, 2489–2498.

(9) Peresin, M.; Habibi, Y.; Zoppe, J.; Pawlak, J.; Rojas, O. Nanofiber Composites of Polyvinyl Alcohol and Cellulose Nanocrystals: Manufacture and Characterisation. *Biomacromolecules* **2010**, *11*, 674–681.

(10) Cao, X.; Chen, Y.; Chang, P. R.; Muir, A. D.; Falk, G. Starch-Based Nanocomposites Reinforced with Flax Cellulose Nanocrystals. *Express Polym. Lett.* **2008**, *2* (7), 502–510.

(11) Dai, D.; Fan, M.; Collins, P. Fabrication of Nanocelluloses from Hemp Fibers and Their Application for the Reinforcement of Hemp Fibers. *Ind. Crops Prod.* **2013**, *44*, 192–199.

(12) Siqueira, G.; Tapin-Lingua, S.; Bras, J.; da Silva Perez, D.; Dufresne, A. Morphological Investigation of Nanoparticles Obtained from Combined Mechanical Shearing, and Enzymatic and Acid Hydrolysis of Sisal Fibers. *Cellulose* **2010**, *17*, 1147–1158.

(13) Rahimi, M.; Behrooz, R. Effect of Cellulose Characteristic and Hydrolyze Conditions on Morphology and Size of Nanocrystal Cellulose Extracted from Wheat Straw. *Int. J. Polym. Mater.* **2011**, *60* (May 2013), 529–541.

(14) Lani, N. S.; Ngadi, N.; Johari, A.; Jusoh, M. Isolation , Characterization , and Application of Nanocellulose from Oil Palm Empty Fruit Bunch Fiber as Nanocomposites. *J. Nanomater.* **2014**, *2014*, 702538.

(15) Azizi Samir, M. A. S.; Alloin, F.; Sanchez, J. Y.; El Kissi, N.; Dufresne, A.

Preparation of Cellulose Whiskers Reinforced Nanocomposites from an Organic Medium Suspension. *Macromolecules* **2004**, *37*, 1386–1393.

(16) Bondeson, D.; Mathew, A.; Oksman, K. Optimization of the Isolation of Nanocrystals from Microcrystalline Cellulose by Acid Hydrolysis. *Cellulose* **2006**, *13*, 171–180.

(17) Kalashnikova, I.; Bizot, H.; Cathala, B.; Capron, I. Modulation of Cellulose Nanocrystals Amphiphilic Properties to Stabilize Oil/water Interface. *Biomacromolecules* **2012**, *13*, 267–275.

(18) Favier, V.; Chanzy, H.; Cavaille, J. Y. Polymer Nanocomposites Reinforced by Cellulose Whiskers. *Macromolecules* **1995**, *28*, 6365–6367.

(19) Sassi, J. F.; Chanzy, H. Ultrastructural Aspects of the Acetylation of Cellulose. *Cellulose* **1995**, *2*, 111–127.

(20) Araki, J.; Wada, M.; Kuga, S.; Okano, T. Flow Properties of Microcrystalline Cellulose Suspension Prepared by Acid Treatment of Native Cellulose. *Colloids Surfaces A Physicochem. Eng. Asp.* **1998**, *142*, 75–82.

(21) Revol, J. F.; Bradford, H.; Giasson, J.; Marchessault, R. H.; Gray, D. G. Helicoidal Self-Ordering of Cellulose Microfibrils in Aqueous Suspension. *Int. J. Biol. Macromol.* **1992**, *14*, 170–172.

(22) Espinosa, S. C.; Kuhnt, T.; Foster, E. J.; Weder, C. Isolation of Thermally Stable Cellulose Nanocrystals by Phosphoric Acid Hydrolysis. *Biomacromolecules* **2013**, *14*, 1–27.

(23) Sadeghifar, H.; Filpponen, I.; Clarke, S. P.; Brougham, D. F.; Argyropoulos, D. S. Production of Cellulose Nanocrystals Using Hydrobromic Acid and Click Reactions on Their Surface. *J. Mater. Sci.* **2011**, *46*, 7344–7355.

(24) Klemm, D.; Kramer, F.; Moritz, S.; Lindström, T.; Ankerfors, M.; Gray, D.; Dorris, A. Nanocelluloses: A New Family of Nature-Based Materials. *Angew. Chemie - Int. Ed.* **2011**, *50*, 5438–5466.

(25) Habibi, Y. Key Advances in the Chemical Modification of Nanocelluloses. *Chem. Soc. Rev.* **2014**, *43*, 1519–1542.

(26) Semmelhack, M. F.; Schmid, C. R.; Cortés, D. A.; Chou, C. S. Oxidation of Alcohols to Aldehydes with Oxygen and Cupric Ion, Mediated by Nitrosonium Ion. *J. Am. Chem. Soc.* **1984**, *106* (22), 3374–3376.

(27) Nooy, E. J. De; Besemer, A. C. Selective Oxidation of Primary Alcohols Mediated by Nitroxyl Radical in Aqueous Solution. Kinetics and Mechanism. **1995**, *51* (29), 8023–8032.

(28) Isogai, A.; Saito, T.; Fukuzumi, H. TEMPO-Oxidized Cellulose Nanofibers. *Nanoscale* **2011**, *3*, 71–85.

(29) De Nooy, A. E. J.; Besemer, A. C.; Van Bekkum, H. Highly Selective Nitroxyl Radical-Mediated Oxidation of Primary Alcohol Groups in Water-Soluble Glucans. *Carbohydr. Res.* **1995**, *269*, 89–98.

(30) Fernández, M.; Tojo, G.; Tojo, G.; Fernandez, M. *Oxidation of Primary Alcohols to Carboxylic Acids*; Springer: New York, 2007.

(31) Fernández, M.; Tojo, G. *Oxidation of Primary Alcohols to Carboxylic Acids*; 2006.

(32) Araki, J.; Wada, M.; Kuga, S. Steric Stabilization of a Cellulose Microcrystal Suspension by Poly (ethylene Glycol) Grafting Steric Stabilization of a Cellulose Microcrystal Suspension by Poly (ethylene Glycol) Grafting. *Cellulose* **2001**, No. 17, 21–27.

(33) Habibi, Y.; Chanzy, H.; Vignon, M. R. TEMPO-Mediated Surface Oxidation of Cellulose Whiskers. *Cellulose* **2006**, *13*, 679–687.

(34) Okita, Y.; Saito, T.; Isogai, A. Entire Surface Oxidation of Various Cellulose Microfibrils by TEMPO-Mediated Oxidation. *Biomacromolecules* **2010**, *11* (100 mL), 1696–1700.

(35) Filpponen, I.; Argyropoulos, D. S. Regular Linking of Cellulose Nanocrystals via Click Chemistry: Synthesis and Formation of Cellulose Nanoplatelet Gels. *Biomacromolecules* **2010**, *11*, 1060–1066.

(36) Barazzouk, S.; Daneault, C. Tryptophan-Based Peptides Grafted onto Oxidized Nanocellulose. *Cellulose* **2012**, *19*, 481–493.

(37) Lin, N.; Bruzzese, C.; Dufresne, A. TEMPO-Oxidized Nanocellulose Participating as Crosslinking Aid for Alginate-Based Sponges. *ACS Appl. Mater. Interfaces* **2012**, *4*, 4948–4959.

(38) Araki, J.; Kuga, S. Effect of Trace Electrolyte on Liquid Crystal Type of Cellulose Microcrystals. *Langmuir* **2001**, *17* (14), 4493–4496.

(39) da Silva Perez, D.; Montanari, S.; Vignon, M. R. TEMPO-Mediated Oxidation of Cellulose III. *Biomacromolecules* **2003**, *4*, 1417–1425.

(40) Beck, S.; Method, M.; Bouchard, J. General Procedure for Determining Cellulose Nanocrystal Sulfate Half-Ester Content by Conductometric Titration. *Cellulose* **2015**, *22*, 101–116.

(41) Beyler, C. L.; Hirschler, M. M. SFPE Handbook 3. 110–131.

(42) George, J.; Ramana, K. V.; Bawa, a. S.; Siddaramaiah. Bacterial Cellulose Nanocrystals Exhibiting High Thermal Stability and Their Polymer Nanocomposites. *Int. J. Biol. Macromol.* **2011**, *48* (1), 50–57.

(43) Karim, M.; Chowdhury, Z.; Hamid, S.; Ali, M. Statistical Optimization for Acid Hydrolysis of Microcrystalline Cellulose and Its Physiochemical Characterization by Using Metal Ion Catalyst. *Materials* **2014**, *7*, 6982–6999.

(44) Julien, S.; Chornet, E.; Overend, R. P. Influence of Acid Pretreatment (H_2SO_4, HCl, HNO_3) on Reaction Selectivity in the Vacuum Pyrolysis of Cellulose. *J. Anal. Appl. Pyrolysis* **1993**, *27*, 25–43.

(45) Zhang, J.; Tang, M.; Viikari, L. Xylans Inhibit Enzymatic Hydrolysis of Lignocellulosic Materials by Cellulases. *Bioresour. Technol.* **2012**, *121*, 8–12.

(46) Roman, M.; Winter, W. T. Effect of Sulfate Groups from Sulfuric Acid Hydrolysis on the Thermal Degradation Behavior of Bacterial Cellulose. *Biomacromolecules* **2004**, *5*, 1671–1677.

(47) Fukuzumi, H.; Saito, T.; Okita, Y.; Isogai, A. Thermal Stabilization of TEMPO-Oxidized Cellulose. *Polym. Degrad. Stab.* **2010**, *95* (9), 1502–1508.

(48) Lu, P.; Hsieh, Y. Lo. Preparation and Properties of Cellulose Nanocrystals: Rods, Spheres, and Network. *Carbohydr. Polym.* **2010**, *82* (March), 329–336.

(49) Higgins, H. G.; Stewart, C. M.; Harrington, K. J. Infrared Spectra of Cellulose and Related Polysaccharides. *J. Polym. Sci.* **1961**, *51*, 59–84.

(50) Fujisawa, S.; Okita, Y.; Fukuzumi, H.; Saito, T.; Isogai, A. Preparation and Characterization of TEMPO-Oxidized Cellulose Nanofibril Films with Free Carboxyl Groups. *Carbohydr. Polym.* **2011**, *84* (1), 579–583.

(51) Blackwell, J.; Vasko, P. D.; Koenig, J. L. Infrared and Raman Spectra of the Cellulose from the Cell Wall of Valonia Ventricosa. *J. Appl. Phys.* **1970**, *41* (1970), 4375–4379.

(52) Atalla, R. H. Recent Developments in Spectroscopic and Chemical Characterization of Cellulose. *Polysaccharides Struct. Divers. fucntional versatility Second Ed.* **2005**, 123–157.

(53) Schenzel, K.; Fischer, S. Applications of Ft Raman Spectroscopy for the Characterization of Cellulose. *Lenzinger Berichte* **2004**, *83*, 64–70.

(54) Agarwal, U. P.; Reiner, R. S.; Ralph, S. A. Cellulose I Crystallinity Determination Using FT–Raman Spectroscopy: Univariate and Multivariate Methods. *Cellulose* **2010**, *17*, 721–733.

(55) Littunen, K.; Hippi, U.; Johansson, L. S.; Österberg, M.; Tammelin, T.; Laine, J.; Seppälä, J. Free Radical Graft Copolymerization of Nanofibrillated Cellulose with Acrylic Monomers. *Carbohydr. Polym.* **2011**, *84* (3), 1039–1047.

(56) Johansson, L.-S. Monitoring Fibre Surfaces with XPS in Papermaking Processes. *Mikrochim Acta* **2002**, *138*, 217–223.

(57) Johansson, L.; Tammelin, T.; Campbell, J. M.; Setälä, H.; Österberg, M. Experimental Evidence on Medium Driven Cellulose Surface Adaptation Demonstrated Using Nanofibrillated Cellulose. *Soft Matter* **2011**, *7*, 10917–10924.

Chapter 3: Synthesis and catalytic activity of gold nanoparticles (AuNPs) supported onto dendrimeric nanocellulose hybrids

3.1. Introduction

Gold nanoparticles (AuNPs), clusters of gold atoms with diameters of less than one micrometer, have been known or at least used since ancient times. They were mostly used as a method for staining glass. The most famous example is the 4th-century *Lycurgus Cup*, which changes color depending on the location of light source. Later on, in the Middle Age, colloidal gold was utilized for medical purposes. It was used as a therapy for several diseases, such as leprosy and epilepsy. The modern scientific evaluation of colloidal gold started in the 1850s, when Michael Faraday observed that colloidal gold solutions had properties that differed from the bulk gold. In the 20th century, AuNPs became the subject of substantial research, due to the discovery of their unique features and a better understanding of their synthesis methods. In the last decade, AuNPs have created great expectation in many research fields, ranging from electronics, to catalysis to biomedicine.[1,2]

AuNPs, as other nanosized materials, are known to develop new functionalities on the nanoscale that differ from both those of the bulk metal and the molecular compounds. At this scale, the properties become highly dependent on size and shape.[3] As the material is miniaturized, the confining dimension naturally decreases. As a consequence, the electron energy levels become discrete rather than continuous.[4] In this context, the particles behave electronically as zero-dimensional quantum dots (or quantum boxes) relevant to quantum-mechanical rules.[5] This phenomenon is commonly referred to as quantum confinement or quantum size effect.

The best known consequence of the quantum size effect in AuNPs is that the de Broglie wavelength of the valence electrons becomes of the same order as the size of the particle itself. When the dimensions of the metal are so reduced, the optical properties of small metal nanoparticles are dominated by collective oscillation of conduction electrons. When exposed to light, the oscillating electromagnetic field of the light induces a collective coherent oscillation of the free electrons (conduction

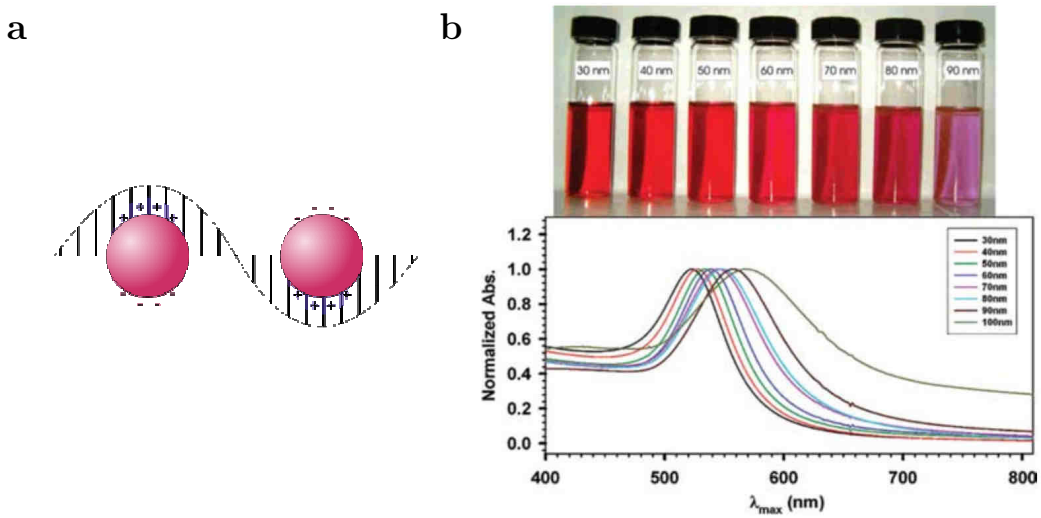

Figure 1. Schematic representation of surface plasmon resonance (SPR) (a) and UV SPR band for AuNPs with different sizes (b).[9]

band electrons) of the metal. This electron oscillation around the particle surface causes a charge separation, forming a dipole oscillation along the direction of the electric field of the light (Figure 1a). The amplitude of the oscillation reaches its maximum at a specific frequency, called surface plasmon resonance (SPR).[6] The SPR induces a strong absorption of the incident light and thus can be measured using a UV–Vis absorption spectrometer (Figure 1b). The SPR band intensity and wavelength depends on the factors affecting the electron charge density on the particle surface such as the particle size, shape, structure, composition and the dielectric constant of the surrounding medium, as theoretically described by Mie theory.[7,8] As a consequence, the color of AuNPs colloids varies depending on the size and aggregation state of the particles.[9] This property has stimulated interest in the use of nanoparticles for optical and photonic applications.[10]

Besides, in AuNPs, there is a gap between the valence band and the conduction band, unlike in bulk metals. The size induced metal-insulator transition, described in 1988 by Nimtz *et al.*,[11] is observed if the metal particle is small enough (about 20 nm) for size-dependent quantization effects to occur.[12,13] This phenomenon finds application in transistors, switches or biosensors.[14,15]

Finally, despite bulk gold is considered a noble metal, and therefore very unreactive, small clusters of gold are found to be catalytically active. One explanation comes from their shapes with more corners and edge atoms, which provide a higher reactivity. Thus shape and crystal structure differences can lead to different catalytic rates.

AuNPs are especially promising as catalysts in a variety of fundamental reactions such as reduction, oxidation, and C-C coupling. AuNPs catalysts can promote a number of reactions, under mild conditions, even at ambient temperature or less and with good selectivity compared to other metals, which makes them unique.[16] They have therefore the potential to reduce running costs of chemicals plants and could increase the selectivity of the reactions involved where applicable.

In general, when AuNPs have diameters of less than 10 nm, they exhibit their best catalytic properties due to the higher surface to volume ratio. Unfortunately, these large active surface areas render them unstable toward self-aggregation. To mitigate this phenomenon, different alternatives have been developed. Thus, they are usually encapsulated in solution or supported on solids giving rise to homogeneous and heterogeneous catalysts, respectively.

3.1.1. AuNPs manufacturing processes

Gold nanoparticles are commonly produced in solution by reducing chloroauric acid ($HAuCl_4$). After dissolving the acid, the solution is rapidly mixed with a reducing agent. Au^{3+} ions are reduced to Au^0 atoms, which act as center of nucleation around which further Au ions gets reduced. As more of these gold atoms are generated, the solution becomes supersaturated.[17] Gold then begins to precipitate in the form of sub-nanometer particles (Figure 2). If the solution is mixed in a vigorous manner, the particles tend to be uniform in size.

This reaction is normally carried out in the presence of stabilizers or "capping" agents that stick to the surface of the nanoparticles, avoiding further aggregation and subsequent precipitation. Stabilizers are typically molecules that contain sulfur, nitrogen, or oxygen, as they have high binding affinity to gold atoms. An alternative approach is to deposit AuNPs onto solid supports. An overview of the most commonly used methods is presented hereafter.

Sodium Citrate

Among the conventional methods for the synthesis of AuNPs by reduction of gold (III) derivatives in solution, the most popular one for a long time has been the citrate reduction of $HAuCl_4$ in water, which was introduced by Turkevitch in 1951,[19] and

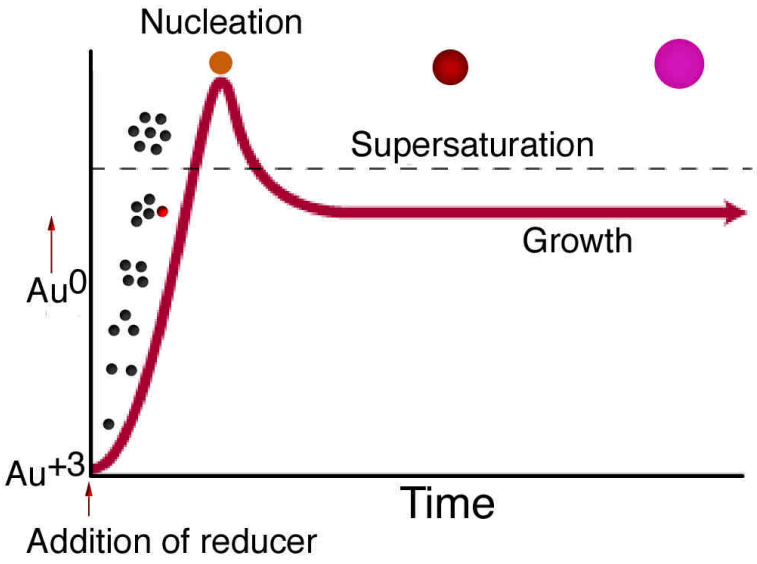

Figure 2. Schematic representation of AuNPs nucleation and growth processes.[18]

refined by G. Frens in 1970s,[20] is the simplest one available. On it, sodium citrate is employed both as reducing and capping agent. Generally, it is used to produce modestly monodisperse spherical gold nanoparticles suspended in water of around 10–20 nm in diameter. Larger particles can be produced, but this comes at the cost of monodispersity and shape. This method is very often used even now when a rather loose shell of ligands is required around the gold core in order to prepare a precursor to valuable AuNP-based materials.

Sulfur ligands

Later on, the Brust-Schiffrin method, published in 1994, provided a facile and effective method for AuNPs.[21] It involves the reaction of a $HAuCl_4$ solution with tetraoctylammonium bromide (TOAB) solution in toluene and sodium borohydride as an anti-coagulant and a reducing agent, respectively. First, $HAuCl_4$ is dissolved in water and $AuCl_4^-$ ions transferred from aqueous solution to toluene using TOAB as phase-transfer reagent. After adding dodecanethiol to the organic phase as a protecting ligand for the nanoparticles, $AuCl_4^-$ ions are reduced by adding an aqueous solution of the reducing agent, sodium borohydride (Figure 3).

This method supposed a breakthrough on the overall field since it allowed the facile synthesis of thermally stable and air-stable AuNPs of reduced dispersity and controlled size (2-6 nm) for the first time.[22] Other sulfur-containing ligands, such as xanthates,[23] disulfides,[24] di- and trithiols,[25] have been also used to stabilize AuNPs.

Other ligands

The Brust-Schiffrin or modified methods have been widely applied to the preparation of AuNPs due to their simplicity and versatility. In the syntheses, different types of organic compounds have been used as capping ligands to stabilize AuNPs, such as phosphine,[26] selenolate,[27] or amine groups.[28]

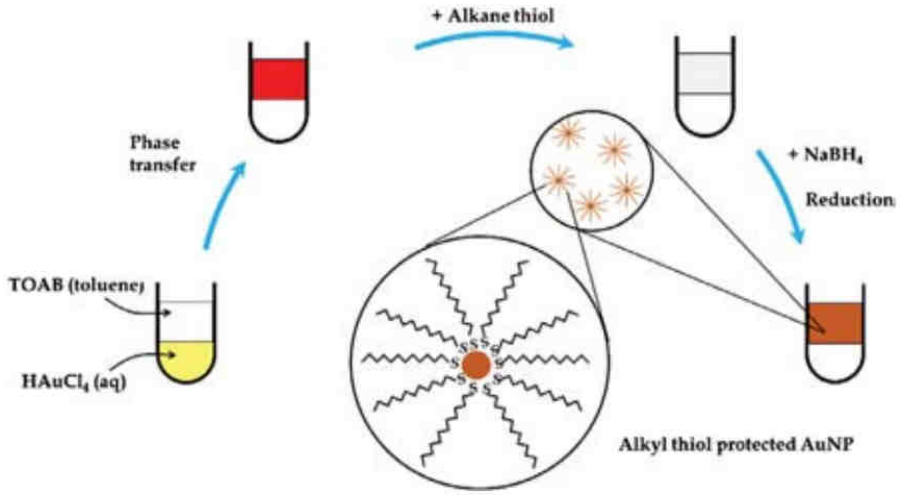

Figure 3. Schematic representation of AuNPs formation using Brust-Schiffrin method.

Polymers

Polymers provide stabilization for metal NPs through the steric bulk of their framework, but also by binding weakly to the NP surface through heteroatoms that can act as ligands. NPs are frequently prepared *in situ* within the polymer matrix, although polymerization of the matrix around the nanoparticles has also been attempted.[12] The type of polymer surrounding the metal nanoparticle plays an important role in AuNPs stabilization and control of their structure. The most commonly used polymers for the stabilization of AuNPs are polyvinylpyrrolidone (PVP) and polyethylene glycol (PEG).

Polymers present many advantages for AuNPs stabilization. They can act as both reducing and stabilizing agents for the AuNPs. Moreover, the AuNPs can be formed in hydrophobic environment, microemulsions, microspheres and be soluble in both water and organic media, promoting the compatibility and processability. In catalysis, polymers can interact with the substrates, playing an important role to improve the catalytic activity and selectivity of the nanoparticles. On the other hand, if the interaction between the macromolecules and metal nanoparticles is strong, the AuNPs are not accessible

Dendrimers

Dendrimers are macromolecules perfectly defined on the molecular level with very low polydispersity. These hyperbranched molecules were first discovered by Fritz Vogtle in 1978,[29] by Tomalia and co-workers,[30] and independently by Newkome,[31] in the early 1980s. The synthesis of dendrimers is always carried out stepwise, which permits an accurate control of its structure. Dendrimers are generally prepared using either divergent or convergent methods.[32] The most widely used is the divergent approach, in which dendrimers are constructed from the core to the exterior. By repetition of sequential reactions, new layers of branching units are incorporated to the core. Each time a new layer is added, a new generation is obtained. Generations can be grown up to more than ten, although the possibility to introduce defects in the structure increases with the generation. In the convergent approach, synthesis starts from the exterior, beginning with the synthesis of dendrimeric wedges, known as dendrons, which are in turn attached to the dendrimeric core.

Having shapes that resemble molecular trees or cauliflowers, they become globular after a few generations, and thus behave as molecular boxes that can entrap and stabilize metal NPs especially if they contain heteroatoms as in the case of PAMAM dendrimers (Figure 4).

PAMAM dendrimers were first synthesized by Tomalia and coworkers.[30] The synthetic process comprises two steps, starting from ammoniac or ethylene diamine (EDA). The first step is a Michael addition reaction to methylacrilate. The second step is the reaction with EDA, affording primary amine terminal groups. Both reactions occur with high yields and selectivity.

The formation of NPs stabilized by PAMAM dendrimers was first proposed more than a decade ago by the three research groups of Crooks, Tomalia and Esumi.[33–35] Crooks *et al.* prepared Pt and Pd nanoparticles encapsulated in PAMAM

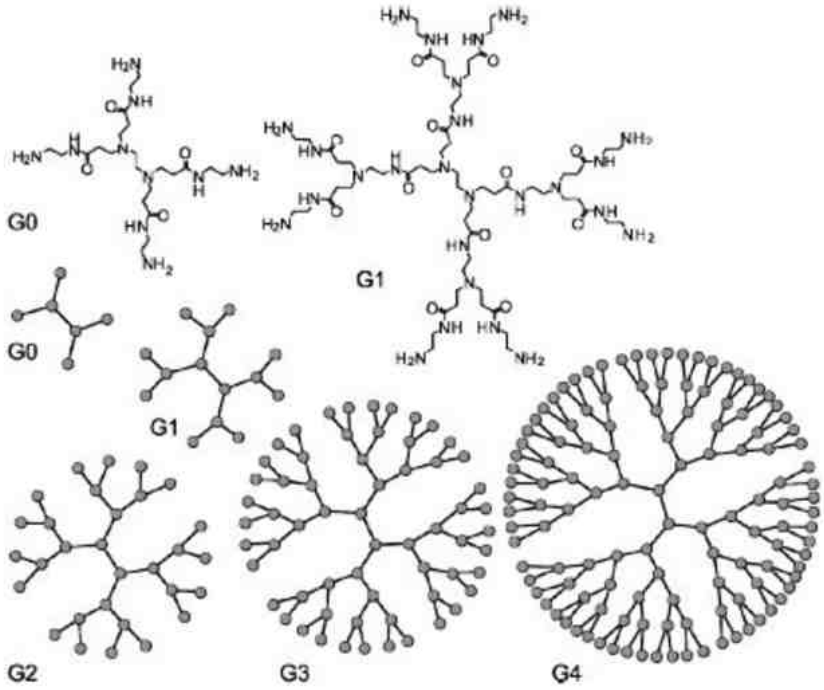

Figure 4. Schematic representation of PAMAM dendrimer structures.[37]

dendrimers.[36] The nanoparticles thus obtained exhibited high catalytic activity for the hydrogenation of alkenes in water. Esumi *et al.* prepared Au colloids by reduction of metal salt with UV irradiation in the presence of PAMAM dendrimers with generations from 0 to 5. The average particle sizes decreased with an increase of concentration of surface amino groups in the dendrimers.[35] It was reasoned that with low generation dendrimers, particles are too large to fit inside a single dendrimer, and are stabilized by the periphery of several dendrimer molecules surrounding the NP.

Since then, a variety of assemblies between PAMAM dendrimers and AuNPs have been reported.[38,39] Dendrimer templates are particularly suitable to host AuNPs, as they yield nanoparticles with a narrow size distribution. Moreover, a substantial fraction of the NPs remains available for catalytic reactions and the dendrimer terminal groups can be chosen to provide the desired solubility in organic or aqueous medium.

Solid supports for AuNPs

Alternatively, gold nanoparticles can be formed on solid supports by loading a gold precursor (usually a gold salt or complex) onto solid supports followed by reduction or calcination. During the reduction or calcination process, the gold cations are reduced into gold atoms that aggregate into gold nanoparticles. The extent of agglomeration during this stage depends on many factors such as the ambient, temperature, and duration of the process, as well as the nature of the solid supports. A large number of recent reports focus on the catalytic properties of AuNPs supported on metal oxides, including oxides of Si,[40] Al,[41] Ti,[42] Zr,[43] Ca,[44] Mg[45] and Zn.[46] Other reported supports are high surface silica,[47] silicates or aluminosilicates,[48] mesoporous silica,[49] various forms of carbon, as nanotubes[50] and diamond[51] or even zeolites.[52]

More recently, also some scattered reports about NCC@AuNPs nanocomposites have been reported. For example, photonic NCC@AuNPs hybrids have been reported under the form of free standing membranes,[53] mesoporous films,[54] and colloidal suspensions.[55] In addition, NCC@AuNPs composites have been used as matrices for enzyme immobilization.[56,57] Moreover, there are a few reports about AuNPs for catalytic applicaitons with NCC@AuNPs.[58,59] In the work of Lam *et al.* AuNPs of small size (~3 nm) were prepared separatedly and added to poly(diallyldimethylammonium chloride) (PDDA) coated NCC to avoid agglomeration. Wu et al.,[60] prepared and deposited AuNPs on cellulose nanocrystals under hydrothermal conditions using NCC as both reducing agent and stabilizing template (Figure 5a). Their results showed that the abundant electron-rich hydroxyl groups on the surface of NCC played a key role in the reduction and immobilization of AuNPs. The obtained nano- hybrid catalyst exhibited much better catalytic activity and stability than the unsupported AuNPs However, the loading of gold nanoparticles was relatively low, namely 3.79 wt%, and rather large AuNPs were obtained 10-30 nm.

In another recent example, PAMAM dendrimers were grafted on NCC. In this report, carboxylic groups on the cellulose nanocrystals have been used to graft amino-dendrimers by carbodiimine-mediated amidation.[61] In this work, high PAMAM generation (G6), requiring multi-step synthesis and extensive purification, was needed to achieve good catalytic activity (Figure 5b).

3.1.2. Reduction of 4-nitrophenol (4-NP) to 4-aminophenol (4-AP): a model reaction for the determination of AuNPs catalytic activity

Both types of systems (stabilized and supported) have been widely applied to different catalysis with outstanding results.[62,63] Nevertheless, a central problem in this field is the quantification of the catalytic activity of the nanoparticles affixed to

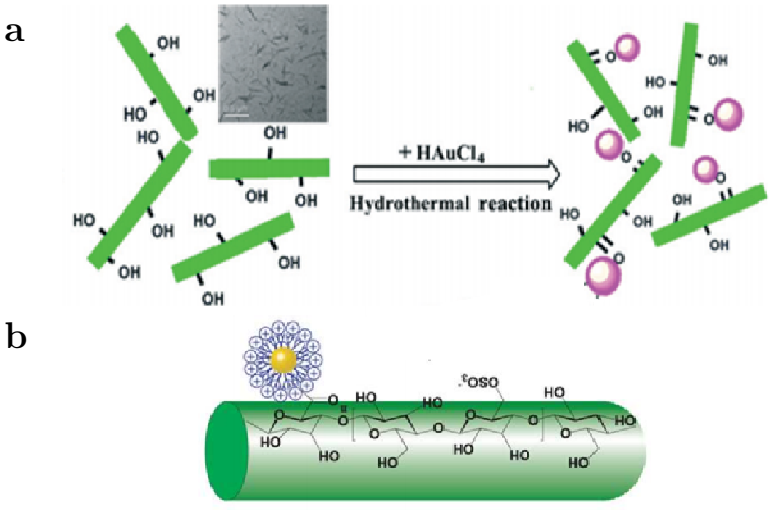

Figure 5. Schematic representation of AuNPs on NCC (a),[60] and on NCC-PAMAM(G6) (b).[61]

various carrier systems. To compare among AuNPs in a reliable way, a model reaction suitable for this purpose must be well-defined. Moreover, the degree of conversion should be easily monitored by a simple and fast technique.

The reduction of 4-nitrophenol (4-NP), a common byproduct from the production of pesticides, herbicides, and synthetic dyes,[64] to 4-aminophenol can (4-AP) be catalyzed by free or immobilized nanoparticles and proceeds in aqueous solution at ambient temperature. Moreover, it can be easily monitored via UV-Vis spectroscopy by the decrease of the strong adsorption of 4-nitrophenolate anion at 400 nm, leading directly to the rate constant.[65] Several isosbestic points in the spectra of the reacting mixtures demonstrate that no side reaction occurs.[66] Pal and coworkers were the first to identify the reduction of 4-NP to 4-AP by sodium borohydride (NaBH4) as such a model reaction.[67]

Although the reaction is thermodynamically viable, it is kinetically restricted in the absence of a catalyst because the kinetic barrier between the mutually repelling negative ions 4-NP and BH_4^- is very high.[68] The adsorption of reactant ions onto the particle surface contributes to overcoming this barrier. The reaction is surface-controlled and has been assessed to occur following a Langmuir-Hinshelwood mechanism.[69] In this type of mechanism, it is assumed that both reactants need to be adsorbed on the surface of the catalyst. The rate determining step is given by the reaction of the adsorbed species. Borohydride ions react with the surface of the nanoparticles and transfer a surface-hydrogen species to the surface of the particles.[70] Concurrently, 4-NP molecules are adsorbed on the surface of the nanoparticles.. The reduction of 4-NP, which is the rate-determining step, takes place by the reaction of adsorbed 4-NP with the surface hydrogen species. Detachment of the product 4-AP creates a free surface and the catalytic cycle can start again (Figure 6).

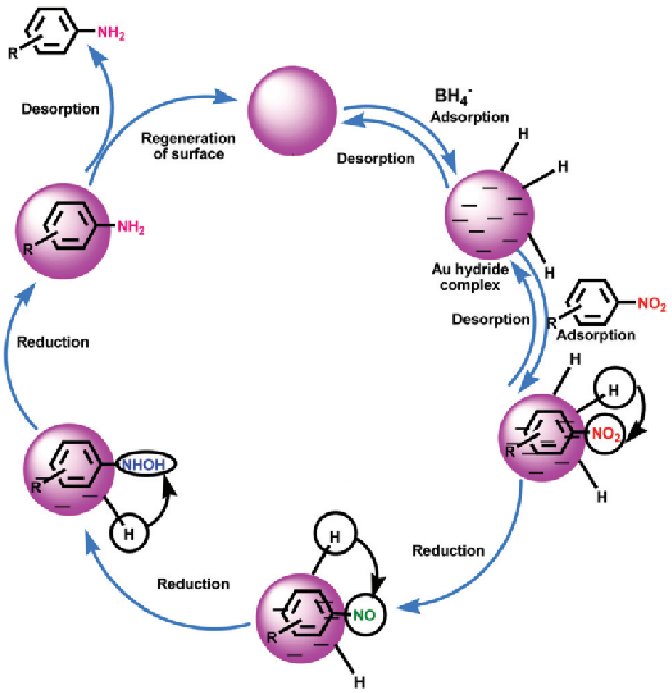

Figure 6. Schematic representation of the mechanism for 4-NP reduction to 4-AP catalyzed by AuNPs.[71]

The rate of the reaction, and therefore the goodness of the catalytic system used, is given by the rate constant (k). In the particular case of 4-nitrophenol reduction, the reaction is of second order, depending on the concentration of 4-nitrophenol and $NaBH_4$. However, $NaBH_4$ is tipically added in a huge excess so the reaction can be considered of pseudo-first order depending only on the concentration of 4-nitrophenol. In this way, the rate of consumption of 4-NP, r_t, obeys the following equation:

$$r_t = \frac{dC}{dt} = k_{app}C = kSC \qquad (1)$$

where k_{app} refers to the apparent rate constant, k is the normalized rate constant with respect to the surface area (S) available on the nanoparticles responsible for catalytic activity.[68] The correlation of $ln(C_t/C_0)$ *versus* the reduction time t has been found to be linear and the apparent rate constant (k_{app}) can be estimated from the slope.

Nevertheless, in catalyzed reactions, the kinetic constant is highly influenced by the amount of catalyst used, and thus k_{app} it is not an accurate method to compare among different catalysts. The activity of a catalyst is best expressed in terms of turn over frequency (TOF).[38,72–75] This value refers to the number of mols of substrate converted per mol of catalysts, in the unit of time (t).

$$TOF = \frac{mols\ of\ substrate\ converted}{(mols\ catalyst \times t)} \qquad (2)$$

TOF (h^{-1}) is an effective way to compare catalytic performance among different AuNPs catalysts. From the literature, there is a large degree of variability in the TOF values obtained for the AuNPs-catalyzed reduction of 4-NP. These factors may depend on the nanoparticle size, shape, polymeric support and stabilization agents used (Table 5).

Table 5. Comparison of AuNPs catalysts for the reduction of 4-NP.

Au support	TOF (h^{-1})	AuNPs diameter (nm)
Graphene hydrogel[76]	11.4	8-25
GO-Fe_3O_4[77, #]	484	3-7
PMMA[78, $]	89	6.9
HPEI[79, *]	90	15
Chitosan[80]	50	3.1
NCC[60, ¥]	109	10-30
NCC/PDDA[59, §]	212	3

#: graphene oxide-iron oxide nanocompostie,
$: poly(methyl methacrylate)
*: hyperbranched polyethylenimine,
§: poly(diallyldimethyl ammonium chloride) coated NCC.

3.1.3. Sustainability of AuNPs based catalysts

When it comes to develop a superior catalyst, apart from performance, one of the deciding criteria is cost; both in terms of production as well as environmental. Concerning sustainability, there are several issues that should be overcome. In the case of homogeneous catalysts the problems of catalyst recovery and pollution are unsolved. Normally, transition-metal catalysts are expensive, and are difficult to

reuse in a homogeneous catalysis system, which is reflected in high cost of the products. In addition, fine chemicals, especially pharmaceuticals, require rigorous purity; thereby general isolation applied in an organic workup procedure is difficult to eliminate all traces of -metal catalysts. Furthermore, such procedures also generate copious amounts of waste, making them environmentally unfavorable.

Due to these drawbacks, the development of heterogeneous catalysts is commonly considered as a more viable alternative. Heterogeneous catalysts are usually separated from the reaction medium by simple filtration and can be repeatedly reused, which considerably decreases the costs and production of waste. However, in heterogeneous catalysts it is often challenging to control the size and distribution of the nanoparticles. This type of catalysts commonly suffers from deposition scarcity, or undesired large size aggregates. Other concern is the sintering of nanoparticles during calcinations, operation and generation of the catalysts, that greatly reduces the catalytic activity.

Thus, the hybridization of AuNPs to obtain high performance catalysts in a sustainable manner remains challenging. On one hand, the design of a good catalyst should contemplate not only a high turnover frequency, but also a system easy to be recovered and reused. Moreover, the recent impulse towards a more sustainable technology increases the importance of using eco-compatible supports, preferably from renewable resources. Among the materials that have the potential to fulfill these stringent requirements is NCC

3.2. Aim of the work

In this chapter we opt for a different strategy to modify NCC, based on click-chemistry methodology to covalently decorate the surface of nanocrystalline cellulose (NCC) with amino-terminated, low generation PAMAM dendrons. The dendronized materials will then be used to produce some new nanohybrids (herein referred as NCC-G^{AT}_{n}@AuNPs) with AuNPs. By this way, it is possible to obtain heterogeneous catalysts with not only a high loading of gold onto the surface of NCC, combined with a low-cost and reduced step synthesis, but also a narrow size distribution of gold nanoparticles thanks to the presence of the dendron moiety. The reduction of 4-nitrophenol (4-NP) to 4-aminophenol (4-AP) in the presence of different generations of NCC-G^{AT}_{n}@AuNPs, as well as the stability and reusability of the catalysts wil also be evaluated.

3.3. Results and discussion

In first place, it will be presented the synthesis and characterization of the different dendrons and dendrimeric-NCC hybrid materials, which are our template to support AuNPs afterwards.

3.3.1. PAMAM dendrons synthesis

The synthesis of the different generations of dendrons started from the propargyl-amino focusing point and followed the classical PAMAM synthesis path reported in literature, as shown in Figure 7.[81] The synthesis was based on an iterated sequence of Michael addition between the amine functionality and acrylic acid ester, producing ester-terminated G^{ET}_n generations (n = 0, 1 and 2) followed by amidation with ethylene diamine, giving the corresponding amino-terminated G^{AT}_n generations (n = 0, 1, and 2). The identity of the various G^{ET}_n and G^{AT}_n dendrons was confirmed by ^{1}H-NMR, ESI-MS spectrometry and FT-IR and data were in accordance with the literature and are described in the experimental details of this Chapter.[82]

3.3.2. NCC-G_n hybrids syntheses and characterizations

Synthesis of NCC-N_3

The NCC employed in this study was produced in 28% yield by hydrolysis of microcrystalline cellulose with 64% sulfuric acid for 2 hours at 45°C, following the procedure described in Chapter 2. NCC was then subjected to methanesulfonylation with mesyl chloride in a 10:1 (v/v) mixture of pyridine:DMSO, and the corresponding

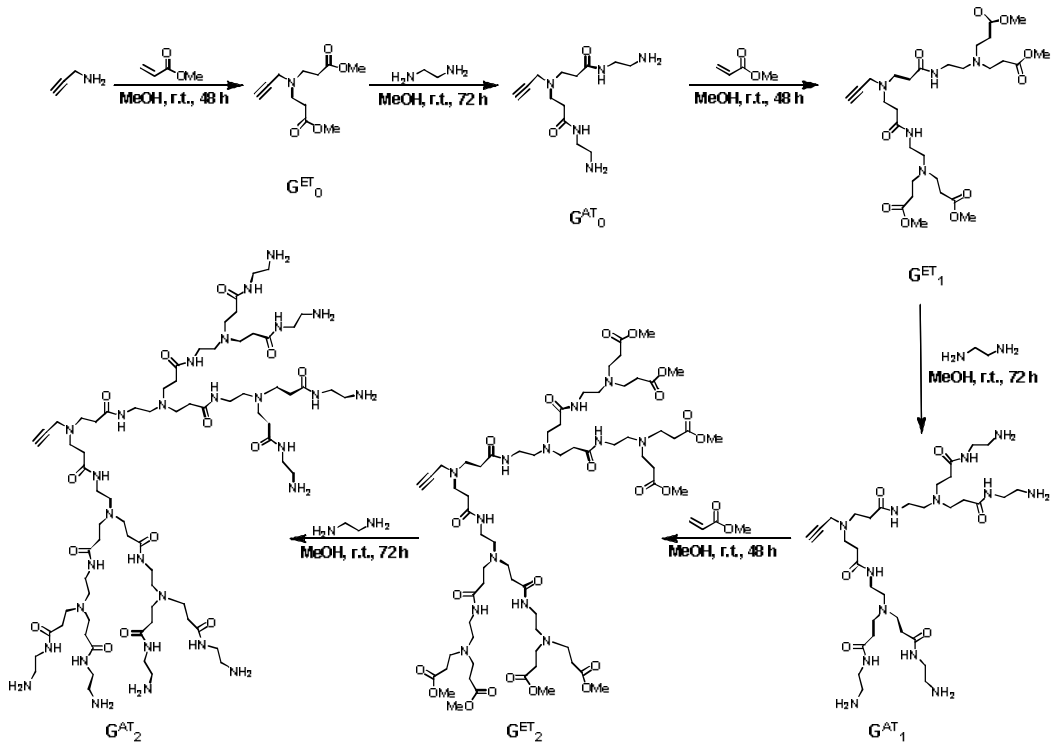

Figure 7. Synthesis of G^{ET}_n and G^{AT}_n PAMAM dendrons.

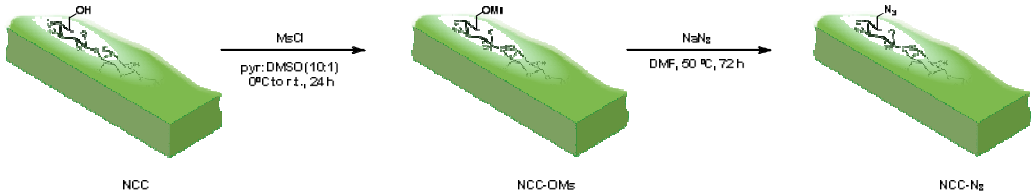

Figure 8. Synthesis of NCC-N_3.

mesylated derivative was obtained as a dark brown solid (71% yield). This step was followed by reaction with sodium azide in DMF at 50°C for 3 days, following a procedure reported in literature with some modifications.[83] After work-up, the corresponding NCC-N_3 derivative was produced as a pale-brown solid (75% yield) (Figure 8). Generally speaking, the stability of the NCC-OMs intermediate is limited, so the two reactions described above were always carried out in sequence.

Click reaction on NCC-N_3

Click-chemistry includes a collection of facile, convenient reactions that meets green chemistry requirements, such as atom economy and selectivity. The most notable example and the one used here, is the copper-catalyzed alkyne azide cycloaddition, so called Huisgen 1,3-dipolar cycloaddition.

The click-chemistry coupling with NCC-N_3 was carried out at the ester terminated dendron level since amino terminated dendrons could eventually inhibit the alkyne azido Huisgen cyclization by sequestering the copper catalyst. Thus, NCC-N_3 was dispersed in water and allowed to react for 3 days with a solution of the G^{ET}_n dendron in THF in the presence of Cu(II) sulfate/L-ascorbate mixture giving the ester terminated NCC-G^{ET}_n (n = -0.5, 0.5, and 1.5) adducts (74-98% yields). The subsequent amination step with ethylene diamine in methanol for 5 days at room temperature afforded the corresponding NCC-G^{AT}_n (n= 0, 1, and 2) derivatives (66-77% yields) as shown in Figure 9.

3.3.3. Characterizations

The success of the different moieties covalent attachment onto the surface of NCC was judged by diverse characterization techniques.

FT-IR

The success of the reactions could be easily followed with the aid of infrared spectroscopy. Figure 10 shows typical spectra of NCC, NCC-OMs and NCC-N_3 In all cases, spectra showed the bands coming from the NCC backbone that were discussed in detail in Chapter 2. After methanosulfonylation, no evident changes in the FT-IR spectrum were observed. The introduction of the azide functionality, however, was unequivocally confirmed by the appearance in the IR spectrum of the typical sharp stretching of -N_3 moiety at 2112 cm^{-1}.

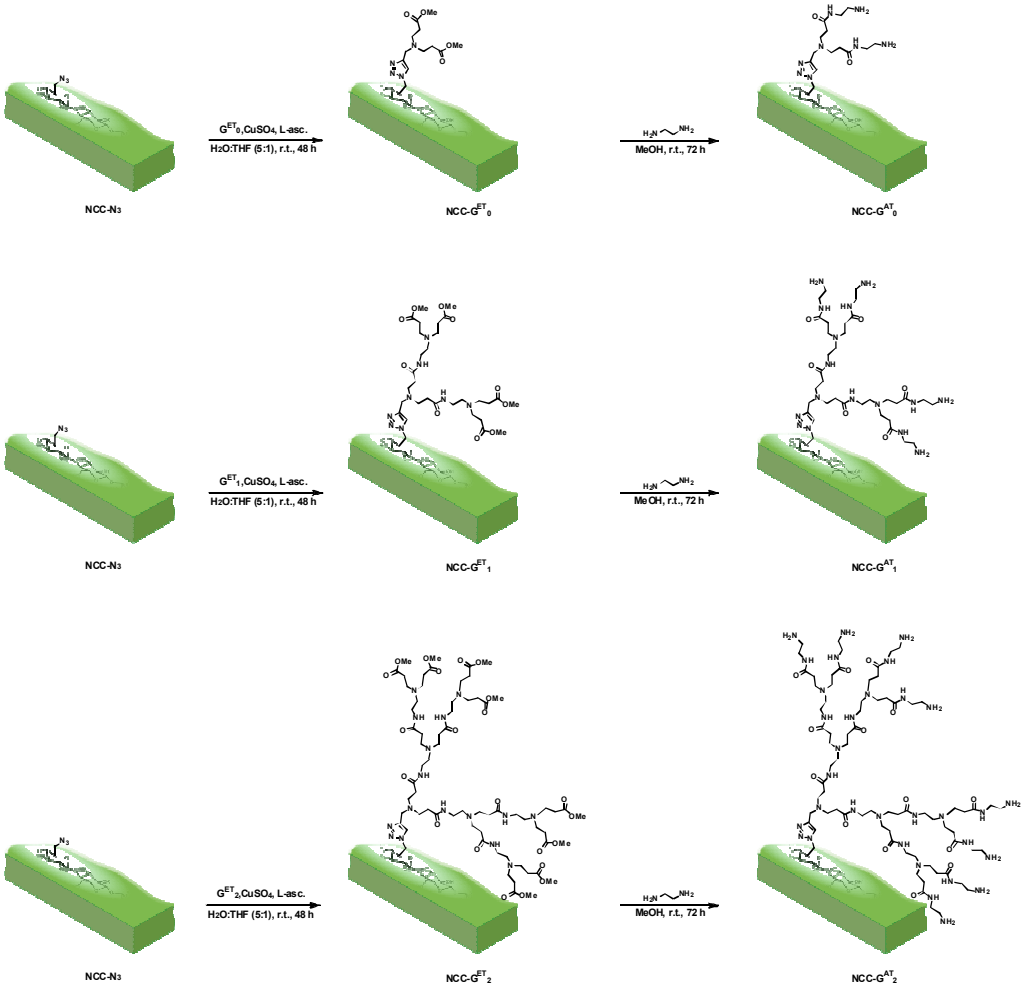

Figure 9. Synthetic route for NCC-G^{AT}_n preparation.

After click reaction, the azide band is seen to be eliminated due to the formation of the triazol ring between –N_3 groups in NCC-N_3 and triple bond from the added G^{ET}_n molecules during the click reaction. The resulting NCC-G^{ET}_n presented instead a characteristic ester carbonyl stretching band at about 1744 cm-1. Finally, after condensation with EDA the disappearance of the ester band took place, for the formation of the amide linkages between ester terminated dendrons on NCC and amine-groups from EDA (Figure 11). Unfortunately, interference with the bending signal of water adsorbed to NCC around 1640 cm^{-1}, did not allow to clearly observe the amide bands that should appear in the same region. (Figure 11). It is important to note that the ester band was more noticeable in NCC-G^{ET}_1 than in NCC-G^{ET}_0, and even more intense in NCC-G^{ET}_2, as expected from the higher density of ester groups in dendron molecules of higher generation. For NCC-G^{ET}_2 and NCC-G^{AT}_2, the amide II band started to be visible since the number of amide groups was also higher in these compounds.

In this way, the progress of the bands in FT-IR for the different derivatives with the different reactions demonstrated the covalent nature of the bonds formed on the surface of NCC in every step.

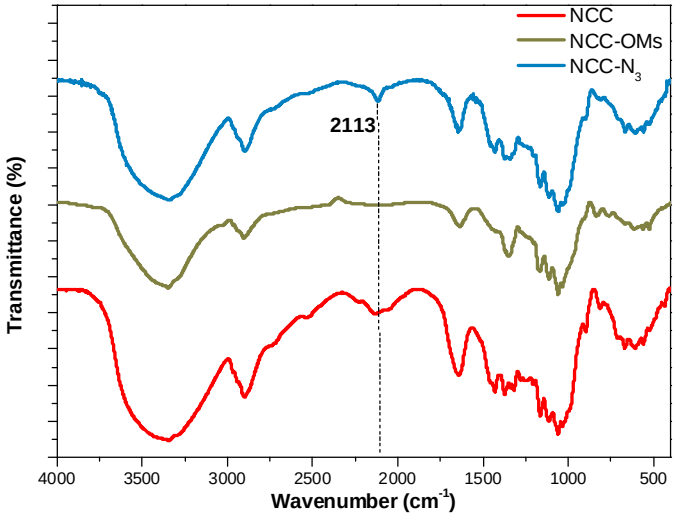

Figure 10.FT-IR spectra of NCC, NCC-OMs and NCC-N_3 (KBr pellets).

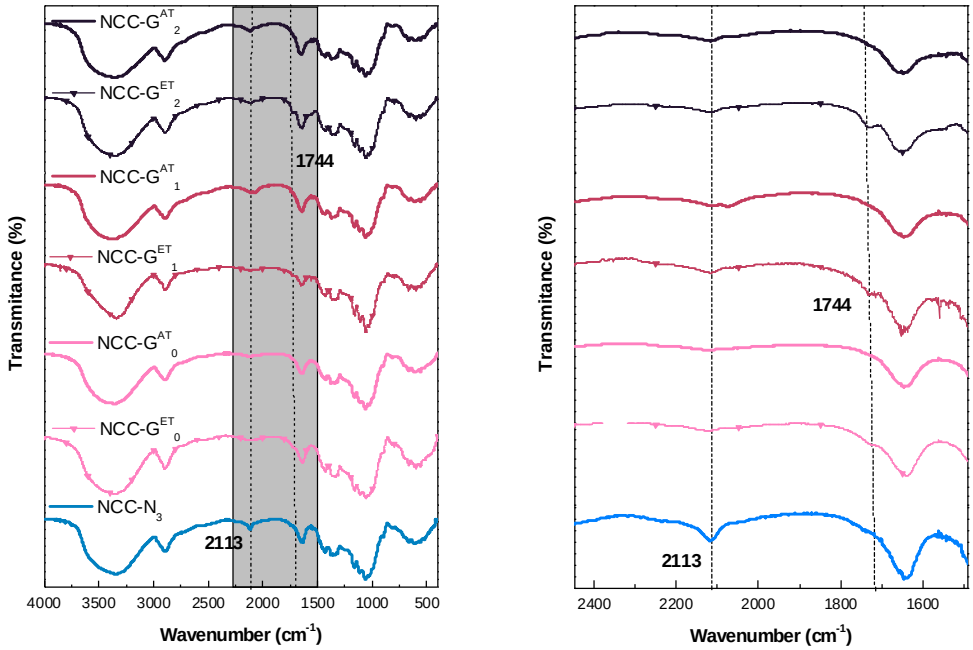

Figure 11. FT-IR spectra of NCC-N_3, NCC-G^{ET}_0, NCC-G^{AT}_0, NCC-G^{ET}_1, NCC-G^{AT}_1, NCC-G^{ET}_2 and NCC-G^{AT}_2 (left) and detail of the 2450-1500 cm^{-1} region (right) (KBr pellets).

Kaiser Test

The Kaiser test is a quantitative test for the presence or absence of aliphatic primary amino groups.[84] It is based on the reaction of ninhydrin with primary amines, which gives a product with a characteristic dark blue colour, known as Ruhemann's purple. For the quantitative estimation of amino groups, the next formula is applied:

$$NH_2\ loading\left(\frac{\mu mol}{g}\right) = \frac{A_{570} \times V \times 10^6}{\varepsilon \times l \times m} \qquad (3)$$

where, A_{570} nm is the absorbance of the Ruhemann's purple formed by the reaction measured using UV-Vis spectroscopy, V is the volume (mL), ε is the molar extinction coefficient (15000 $M^{-1} \cdot cm^{-1}$), l is the optical length (cm), m is the mass of compound (mg) and 10^6 is a unit conversion factor.

As expected, NCC-G^{AT}_n derivatives gave a positive Kaiser test thus allowing the spectrophotometric quantitative determination of terminal primary amino groups for the different generations. The results were 13, 41, and 61 μmol/g for NCC-G^{AT}_0, NCC-G^{AT}_1, and NCC-G^{AT}_2, respectively. It should be pointed out that the ratio between the amino contents for the different generations was 1:3.2:4.7 (normalized with respect to the NCC-G^{AT}_1 amino content), which is slightly different from the theoretical 1:2:4 ratio expected according the number of amino groups for each generation (i.e. 2 for NCC-G^{AT}_0, 4 for NCC-G^{AT}_1, and 8 for NCC-G^{AT}_2). This can be ascribed to some small defects (i.e. non-quantitative yields during each dendron synthesis step), which propagate through the different dendron generations.

X-ray photoelectron spectroscopy (XPS)

XPS was consistent with the above results. The survey spectra for NCC-G^{AT}_n are reported in Figure 12. As expected for NCC based materials, the most abundant elements were by far oxygen and carbon. After the introduction of -N_3 groups, nitrogen was also detectable in the sample and was present in all NCC-G_n. From the survey spectra, however, it was difficult to determine if some change in nitrogen bond region occurred after the introduction of the dendron moieties.

A more exhaustive investigation was carried out by analyzing Gaussian-Lorentian fitting of the peaks for NCC-N_3, NCC-G^{ET}_n and NCC-G^{AT}_n in the N1s region. For NCC-N_3, two components were found, at 400 and 402.6 eV, the first one attributed to N=N and the second one to C-N and N-H bonds (Figure 13a). Both types of nitrogen bonds come from the introduction of the azide function, which was the only source of nitrogen in NCC-N_3. The presence of the C-N component demonstrates that this functionality was attached to NCC in a covalent way through a C-N bond. After click reaction with dendron moieties, increasing intensity of the signals for the C-N and N-H bonds was observed due to the new C-N bonds coming from the formation of the triazol ring and the ester terminated dendron moieties (Figure 13b, c and f). The increment of this peak was also observable upon converting the ester-terminated derivatives (NCC-G^{ET}_n, n= -0.5, 0.5, and 1) to their corresponding amino-terminated (NCC-G^{AT}_n, n= 0, 1, and 2) counterparts (Figure 13d, e and g). Thus, the evolution of the N1s component in XPS measurements was in good accordance with the modifications in chemical composition after every step of reaction and with the observed results in infrared spectroscopy.

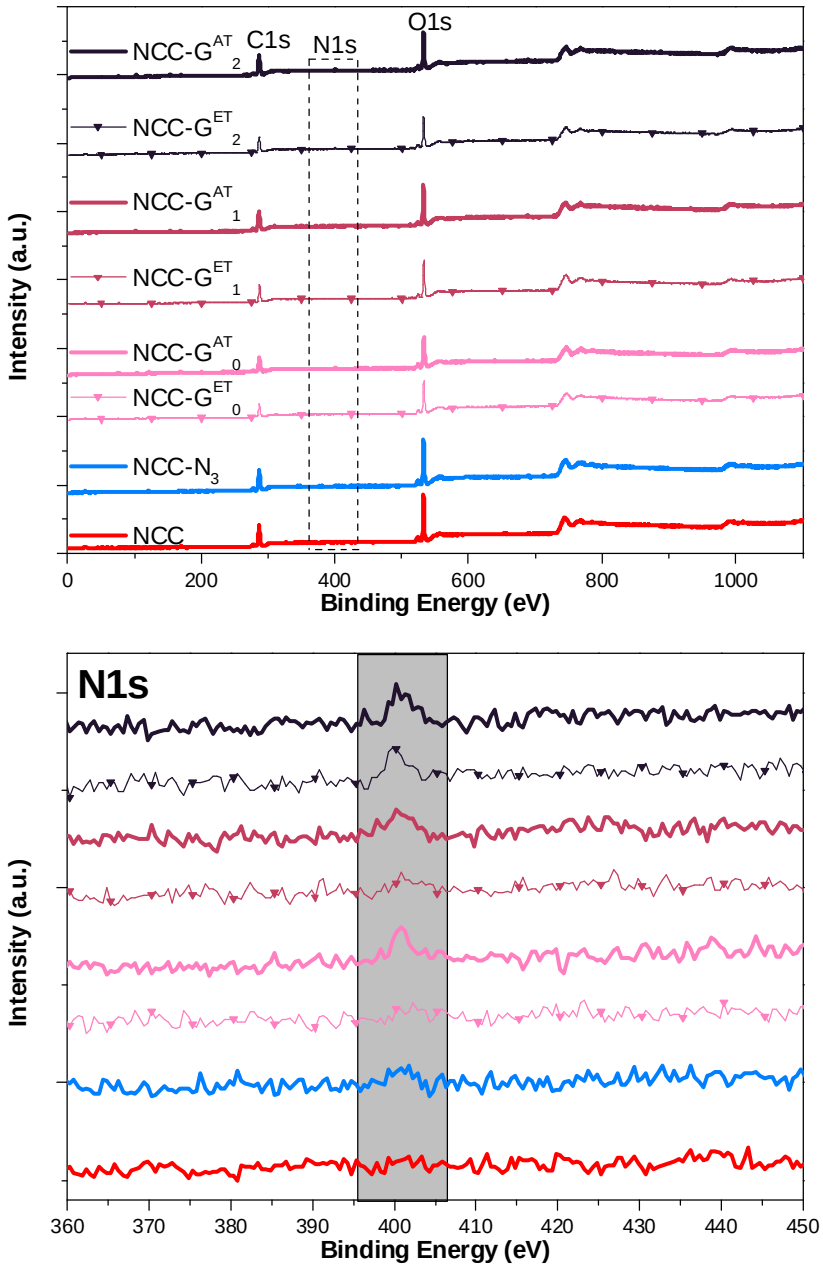

Figure 12. XPS survey spectra of NCC, NCC-N_3, NCC-G^{ET}_0, NCC-G^{AT}_0, NCC-G^{ET}_1, NCC-G^{AT}_1, NCC-G^{ET}_2 and NCC-G^{AT}_2 (top) and zoom of the N1s region (bottom).

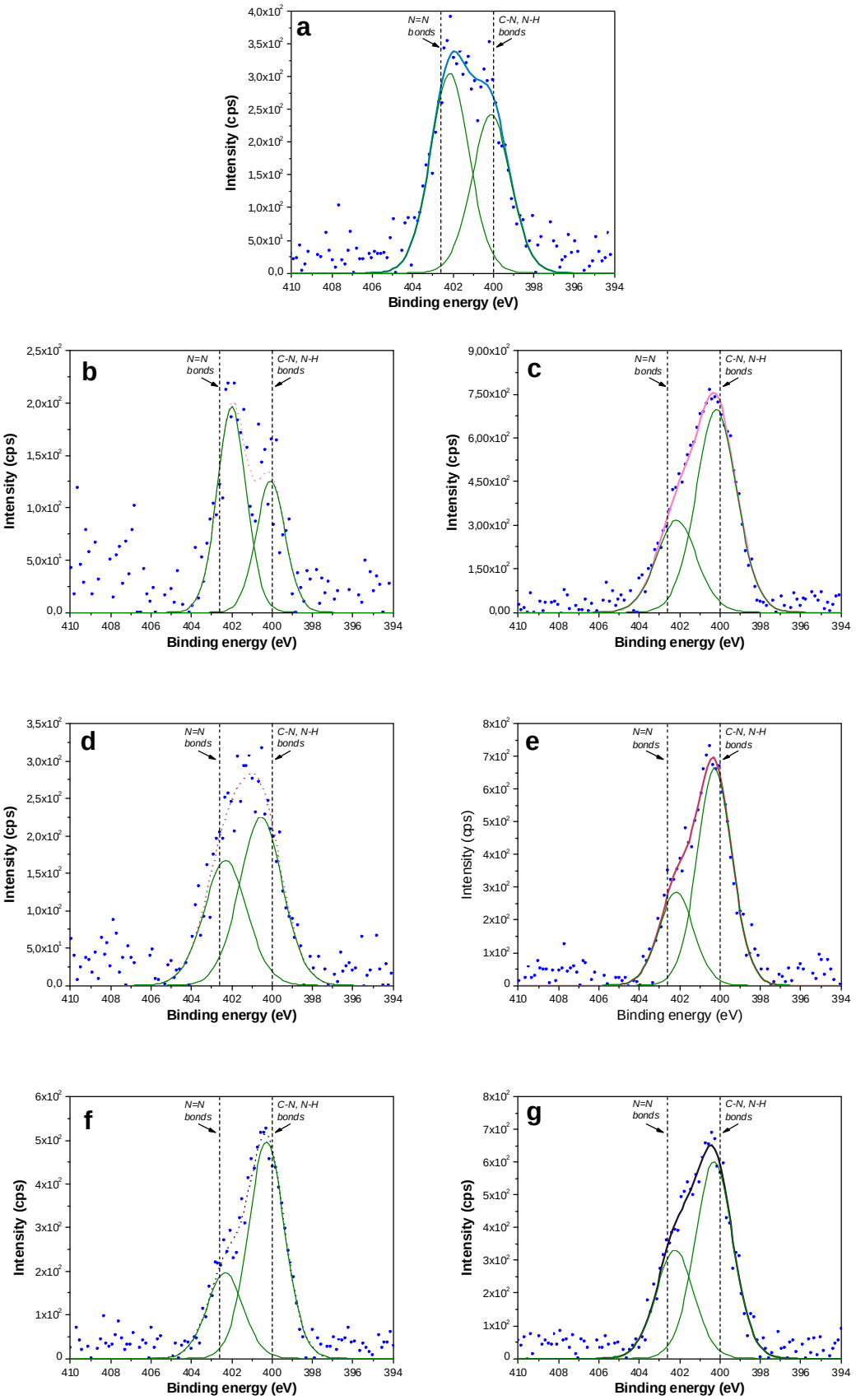

Figure 13. N1s fitted spectra of NCC-N_3 (a), NCC-G^{ET}_0 (b), NCC-G^{AT}_0 (c), NCC-G^{ET}_1 (d), NCC-G^{AT}_1 (e), NCC-G^{ET}_2 (f) and NCC-G^{AT}_2 (g).

Thermogravimetric analysis (TGA)

The thermal stability of all the materials was investigated by thermogravimetric analysis. Samples were first heated at 50 ºC for 10 min to remove eventual moisture residues and then temperature was ramped at 10 ºC per min up to 600 ºC in a N_2 atmosphere. Normalized TG and DTG of NCC, NCC-OMs and NCC-N_3 are showed in Figure 14. The profiles of all three compounds were very similar. A gradual shift to higher onset decomposition temperatures with every step of functionalization was the only appreciable change. The event of the weight loss in DTG shifted from 171.5 ºC in NCC to 191.0 ºC in NCC-OMs and 200.8 ºC in NCC-N_3. This was indicative of surface modification, in which –OMs groups are more stable on NCC with respect to the -SO_4 groups in pristine NCC. –N_3 groups were found to be more stable than –OMs, on NCC surface, providing higher thermal stability to the overall material, as showed in Figure 14b.

Neither the introduction of dendron moieties on the surface of NCC produced any drastic change in the thermal behavior of the materials. Profiles of NCC-N_3 and the different NCC-$G^{AT}{}_n$ were almost equal, as expected for their similar type of chemical bonding to NCC. A slightly better thermal stability with increasing dendron generation on NCC surface was noticed, being the loss weight centered at 205.7, 208.9 and 218.3 ºC for NCC-$G^{AT}{}_0$, NCC-$G^{AT}{}_1$ and NCC-$G^{AT}{}_2$, respectively. This phenomenon could be ascribed to the increased numbers of hydrogen bonds and better internal van der Waals' packing in PAMAM dendron moieties of higher generation, as these interactions contribute to thermal stability.[85,86]

Transmission electron microscopy (TEM)

TEM was carried out to check the morphology of the nanocrystals after every step of reaction. The samples were prepared as usual, by drop casting of the different NCC derivatives in aqueous suspensions onto a carbon coated TEM grid, followed by staining with uranyl acetate solution to improve the contrast. TEM images of NCC-N_3 and NCC-$G^{AT}{}_n$ derivatives (Figure 16) confirmed that the typical whisker-like morphology of the cellulose nanocrystals was maintained upon functionalization despite the mechanical stress deriving from extensive sonication and magnetic stirring required for the four-step synthesis.

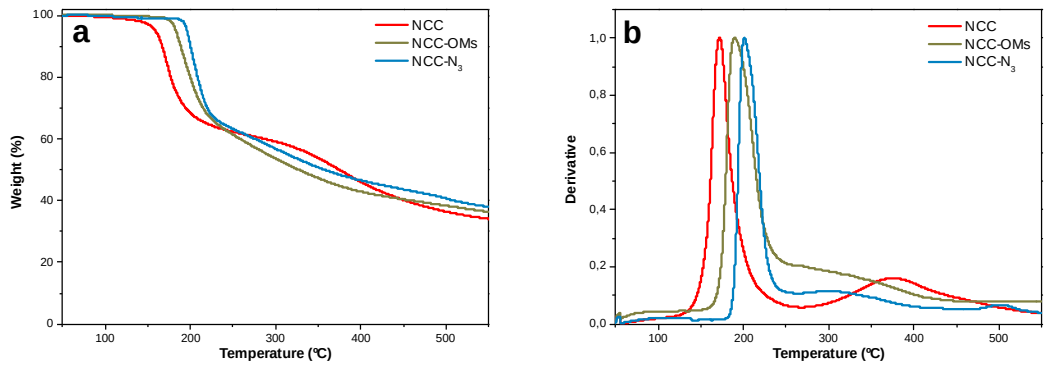

Figure 14. Normalized TG (a) and DTG (b) curves of NCC, NCC-OMs and NCC-N_3 under N_2 atmosphere.

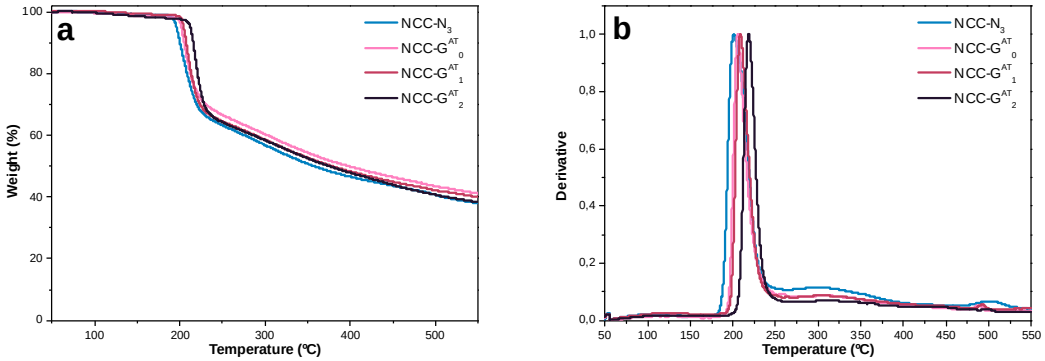

Figure 15. Normalized TG (a) and DTG (b) curves of NCC-N_3, NCC-$G^{AT}{}_0$, NCC-$G^{AT}{}_1$ and NCC-$G^{AT}{}_2$ under N_2 atmosphere.

All these characterization steps served to demonstrate the covalent attachment of PAMAM dendron moieties on the surface of NCC; preserving the morphology of the

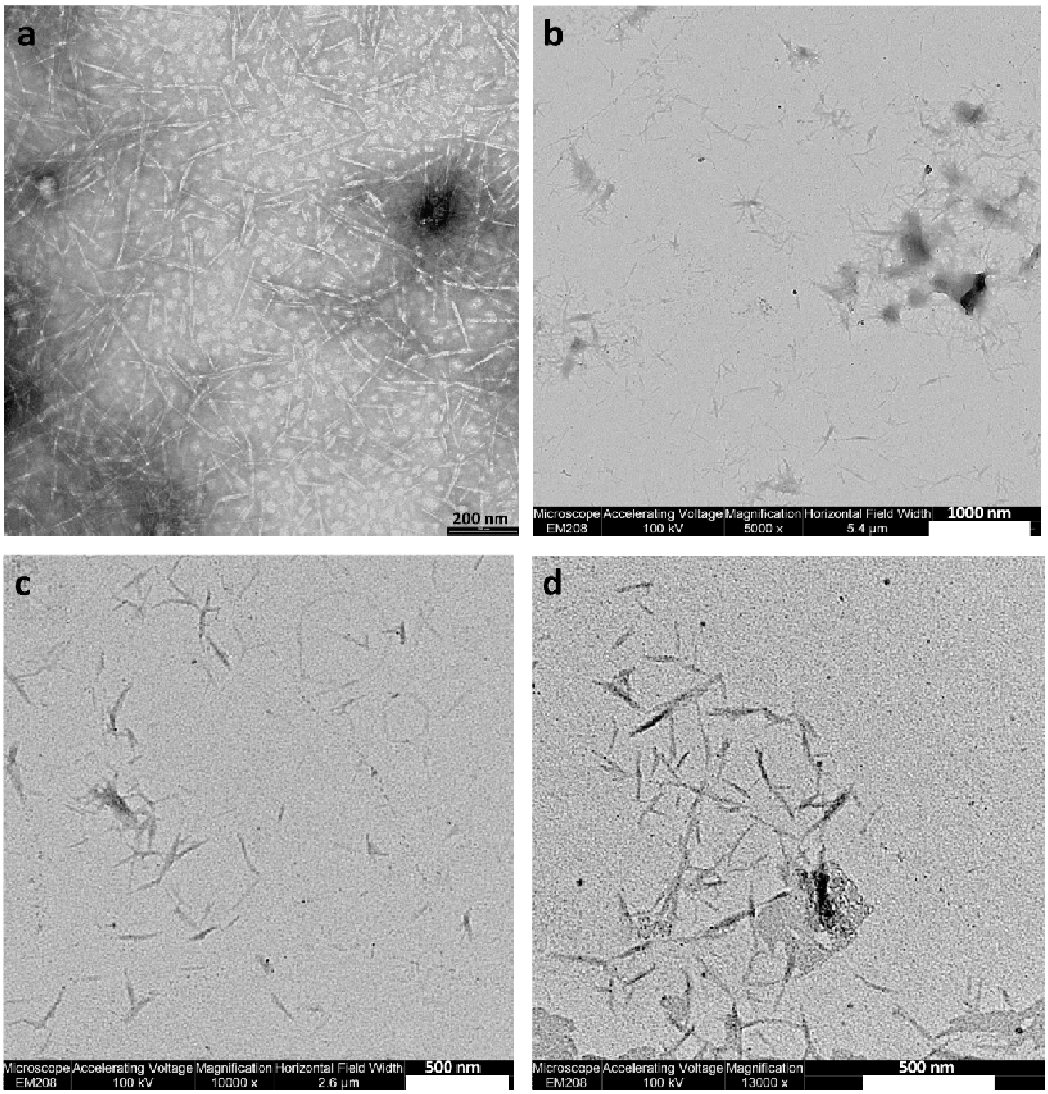

Figure 16. TEM images of NCC-N_3 (a), NCC-$G^{AT}{}_0$ (b), NCC-$G^{AT}{}_1$ (c) and NCC-$G^{AT}{}_2$ (d).

nanocrystals. These hybrids can thus be used as template for the stabilization of AuNPs.

3.3.4. Synthesis of AuNPs supported onto dendrimeric-NCC hybrids

The synthesis of AuNPs was carried out in aqueous environment by reduction of chloroauric acid with a freshly prepared solution of sodium borohydride in the presence of dendronized nanocellulose derivatives NCC-G^{AT}_{n}. After stirring for 1 hour at room temperature, reddish solutions of NCC-G^{AT}_{n}@AuNPs were obtained (Figure 17). These solutions were left undisturbed for 24 hours in order to settle down a small amount of aggregates. The surnatant was then transferred on top of a 0.1 μm filter and about 2/3 of the solution were filtered off with the purpose to remove some gold nanoparticles not bound to NCC-G^{AT}_{n} avoiding the aggregation the NCC-G^{AT}_{n}@AuNPs. The initial volume was restored with milliQ-water and the filtration reiterated until the filtered solution was colourless. The resulting suspensions were stable for weeks, with negligible amount of precipitate and presented pale pink color, typical of AuNPs (Figure 18).

The corresponding G^{AT}_{n}@AuNPs were also prepared following the same procedure and used without further purification in order to make a comparative study. Figure 19 shows images of blank AuNPs prepared with no stabilizer, and AuNPs stabilized with the different G^{AT}_{n}, 48 h after preparation. As expected, in absence of stabilizer, gold had aggregated completely. It is important to mention that in the conditions used, also G^{AT}_{0}@AuNPs and G^{AT}_{1}@AuNPs underwent complete aggregation within 24 to 48 h, what could be ascribed to an insufficient amount of amino groups in the dendron necessary for AuNPs stabilization. G^{AT}_{2}@AuNPs underwent aggregation to some extent, but the AuNPs remaining in suspension were stable for weeks.

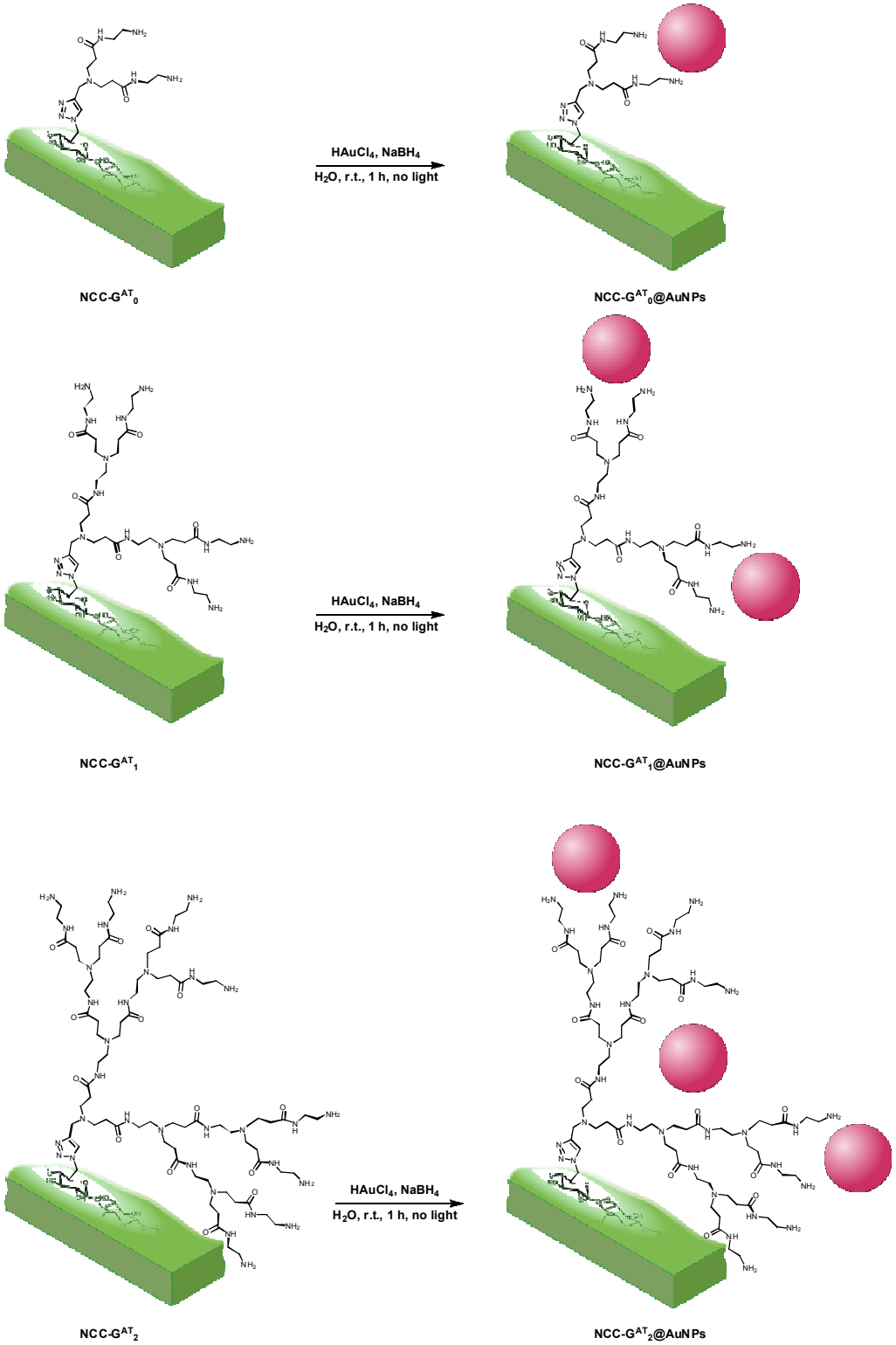

Figure 17. Synthesis of NCC-G$^{AT}_{n}$@AuNPs hybrids.

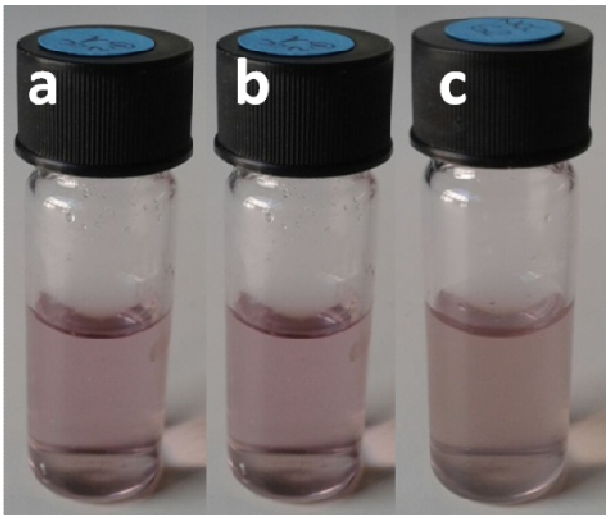

Figure 18. Suspensions of NCC-G^{AT}_0@AuNPs (a), NCC-G^{AT}_1@AuNPs (b) and NCC-G^{AT}_2@AuNPs (c) after 48 h.

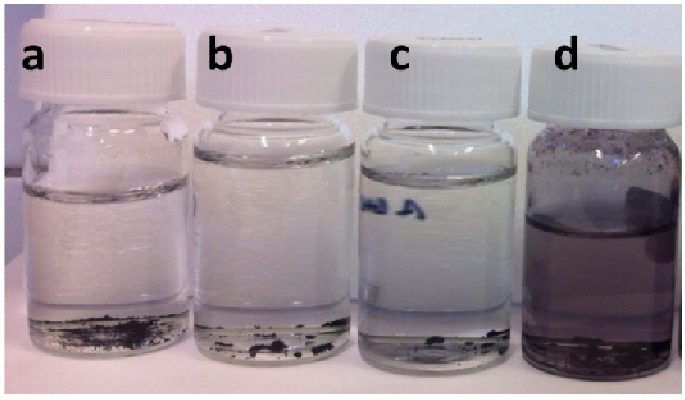

Figure 19. blank AuNPs (a), G^{AT}_0@AuNPs (b), G^{AT}_1@AuNPs (c) and G^{AT}_2@AuNPs (d) suspensions after 48 h.

3.3.5. Characterization of AuNPs supported onto dendrimeric-NCC hybrids.

Thermogravimetric analysis (TGA)

Although the information about chemical modification on NCC provided by TGA was limited, this technique was particularly useful to determine the gold loading on AuNPs containing samples. To this end, thermogravimetric experiments were carried out under air atmosphere. At 700 º C, the organic materials were fully removed (Figure 20, solid lines). Thus, it can be assumed that the difference in residue with the corresponding gold containing derivatives is solely the metallic part of the samples, actually in the form of gold oxide (Figure 20, lines with marker). In the case of NCC-G^{AT}_n@AuNPs, at T > 600 ºC, the slope of the curves was completely flat. Thus, it was safe to assume that no further decomposition would occur and that the residue is exclusively due to the AuNPs (Figure 20b, c and d). This was not the case of G^{AT}_2@AuNPs, which exhibited a non-zero slope at 600 ºC. In this case, residue was

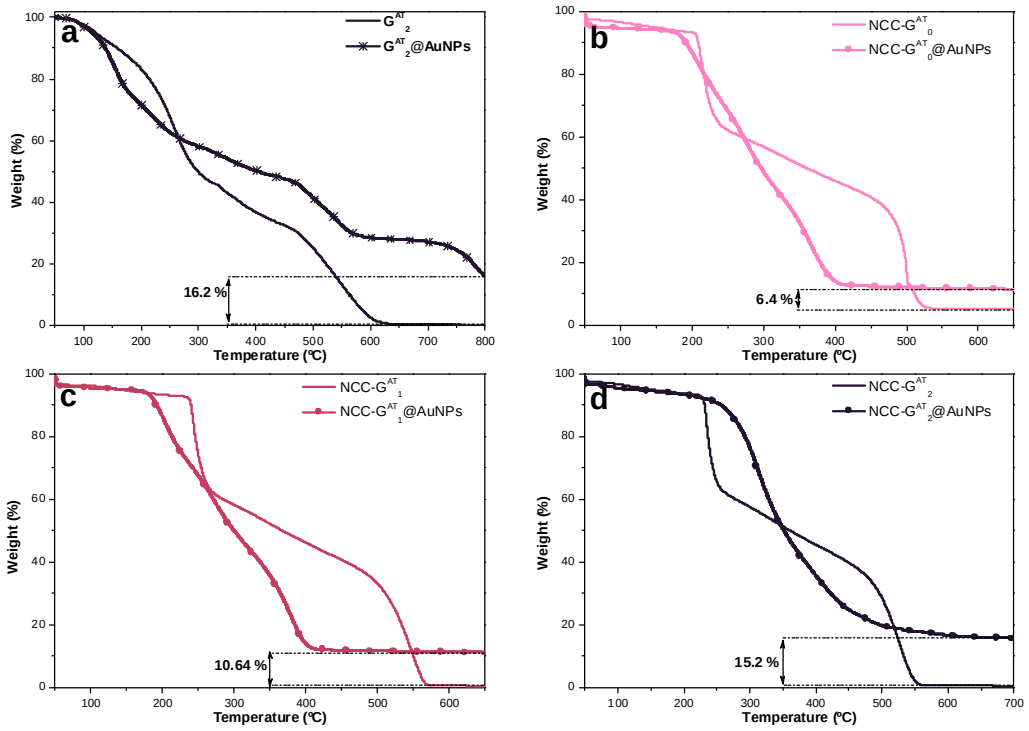

Figure 20. TG curves of GAT2 and GAT2@AuNPs (a), NCC-GAT0 and NCC-GAT0@AuNPs (b), NCC-GAT1 and NCC-GAT1@AuNPs (c), NCC-GAT2 and NCC-GAT2@AuNPs (d) under airatmosphere.

considered at 800 ºC. Mass residues of 16.2, 6.4, 10.64 and 15.2% were found for G^{AT}_2@AuNPs, NCC-G^{AT}_0@AuNPs, G^{AT}_1@AuNPs and G^{AT}_2@AuNPs, respectively.

Taking into account the initial mass of sample in the TGA experiments and the atomic weight of gold oxide, it is possible to estimate the AuNPs loading as amount of atomic gold per gram of material. For the free G^{AT}_2@AuNPs dendron, a gold content of 14.9 % (w/w) was found. In the case of NCC hybrid materials, the results were 5.68, 9.45, and 14.15% for NCC-G^{AT}_0@AuNPs, NCC-G^{AT}_1@AuNPs and NCC-G^{AT}_2@AuNPs respectively. The gold loading increased with increasing the generation of dendron attached to NCC. This provides an evidence of the stabilizing effect of the amino groups coming from the dendron moieties, since a higher amino content allowed the stabilization of a higher number of AuNPs.

UV-Vis spectroscopy

The position of the SPR is extremely sensitive to the size and aggregation state of the particles. Several authors discussed the problem of AuNPs sizing by their UV-Vis spectra, mainly focusing on the position of the SPR maximum. It has been found that the SPR band of AuNPs with size smaller than 10 nm appears at around 520 nm when registered in water. Nonetheless, for such small nanoparticles it is largely damped due to the phase changes resulting from the increased rate of electron-surface collisions compared to larger particles.[87,88] Increasing particle size red shifts the SPR wavelength and also increases the intensity.[89] Since the SPR may be affected by other factors, maximum of the SPR must be taken as an orientative measure of particle size.

The UV-Vis spectra of $G^{AT}{}_2$@AuNPs and all NCC-$G^{AT}{}_n$@AuNPs derivatives displayed the typical plasmonic band at approximately 520 nm, as seen in Figure 21. The similar positions of the bands for $G^{AT}{}_2$@AuNPs and all NCC-$G^{AT}{}_n$@AuNPs, and their low intentsities indicated a similar size of AuNPs in all cases, and with diameters around 10 nm.

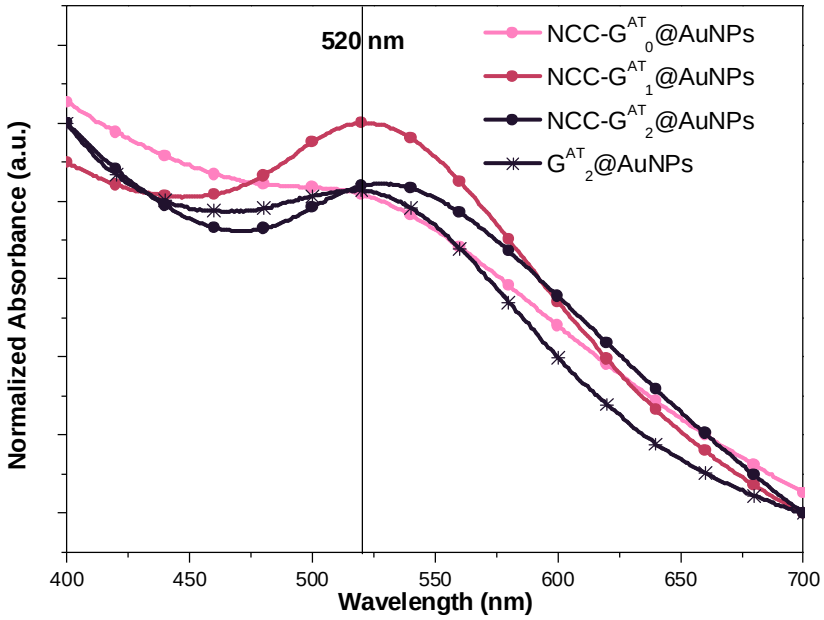

Figure 21. UV-Vis spectra of $G^{AT}{}_2$@AuNPs and NCC-$G^{AT}{}_0$@AuNPs, NCC-$G^{AT}{}_1$@AuNPs and NCC-$G^{AT}{}_2$@AuNPs.

Transmission electron microscopy (TEM)

TEM is the most common technique for obtaining accurate data about the average diameter and size distribution of gold nanoparticles. TEM images of the gold containing hybrid materials were registered and the diameter of the AuNPs was calculated from the digital images by measuring 100 AuNPs. In order to assess the role of NCC, sample $G^{AT}{}_2$@AuNPs was first analyzed. A typical image of $G^{AT}{}_2$@AuNPs is shown in Figure 22a. In general, well dispersed nanoparticles of uniform size and shape were observed. A mean diameter for AuNPs of about 7.5 nm was found (Figure 22b). This result is in agreement with literature, since when PAMAM dendrimers are used as templates, the dendrimer-stabilized nanoparticles are often larger than 5 nm.[90] $G^{AT}{}_2$ is a low-generation dendron and its reduced number of terminal amines and open structure cannot entrap a metal nanoparticle within the interior. Thus, the gold nanoparticles must be surrounded by multiple molecules of dendron rather than encapsulated in a single dendron cavity, resulting in a higher diameter of the nanoparticles.

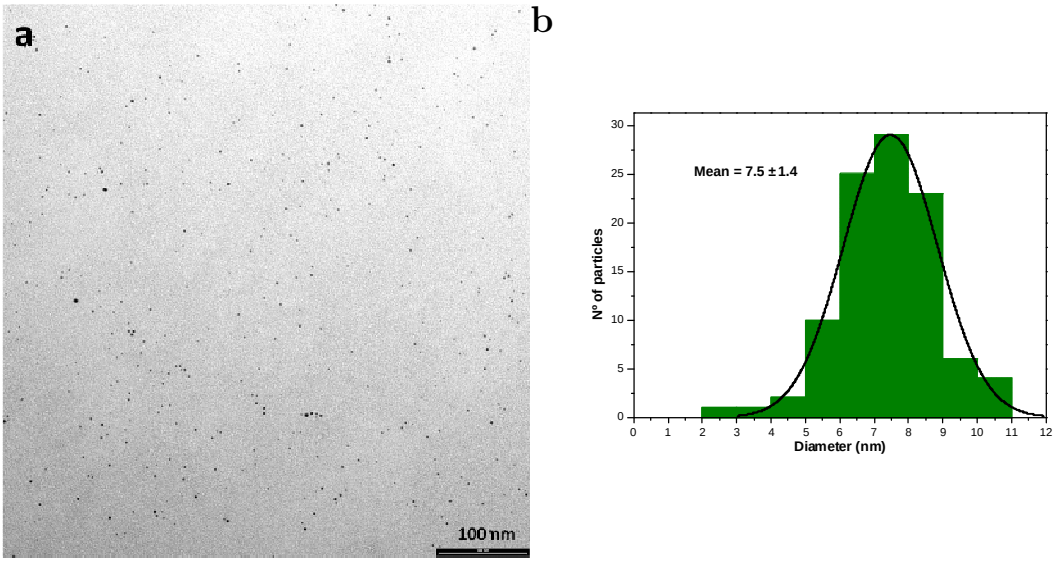

Figure 22. TEM image (a) and particle size histogram (b) of $G^{AT}{}_2$@AuNPs.

TEM images of NCC-$G^{AT}{}_0$@AuNPs, NCC-$G^{AT}{}_1$@AuNPs and NCC-$G^{AT}{}_2$@AuNPs are displayed in Figure 23a, c and e, respectively. For all NCC-$G^{AT}{}_n$@AuNPs systems, AuNPs were always together with NCC. AuNPs were well distributed on the surface of NCC with a minimal of aggregation, proving the stabilizing effect of the new hybrid materials and the success of the cleaning process to remove eventual free AuNPs. The diameter of AuNPs was around 3.5-4.3 nm in all cases (Figure 23b, d and f), smaller than those stabilized by free $G^{AT}{}_2$ dendron.The smaller sizes observed when NCC was introduced seem to indicate that the effect of anchoring the dendron on the NCC support should play an important role in the stabilization of the nanoparticle and consequently in the final size. The size distribution of the individual samples therefore does not obscure the predicted behavior for the surface plasmon band position.

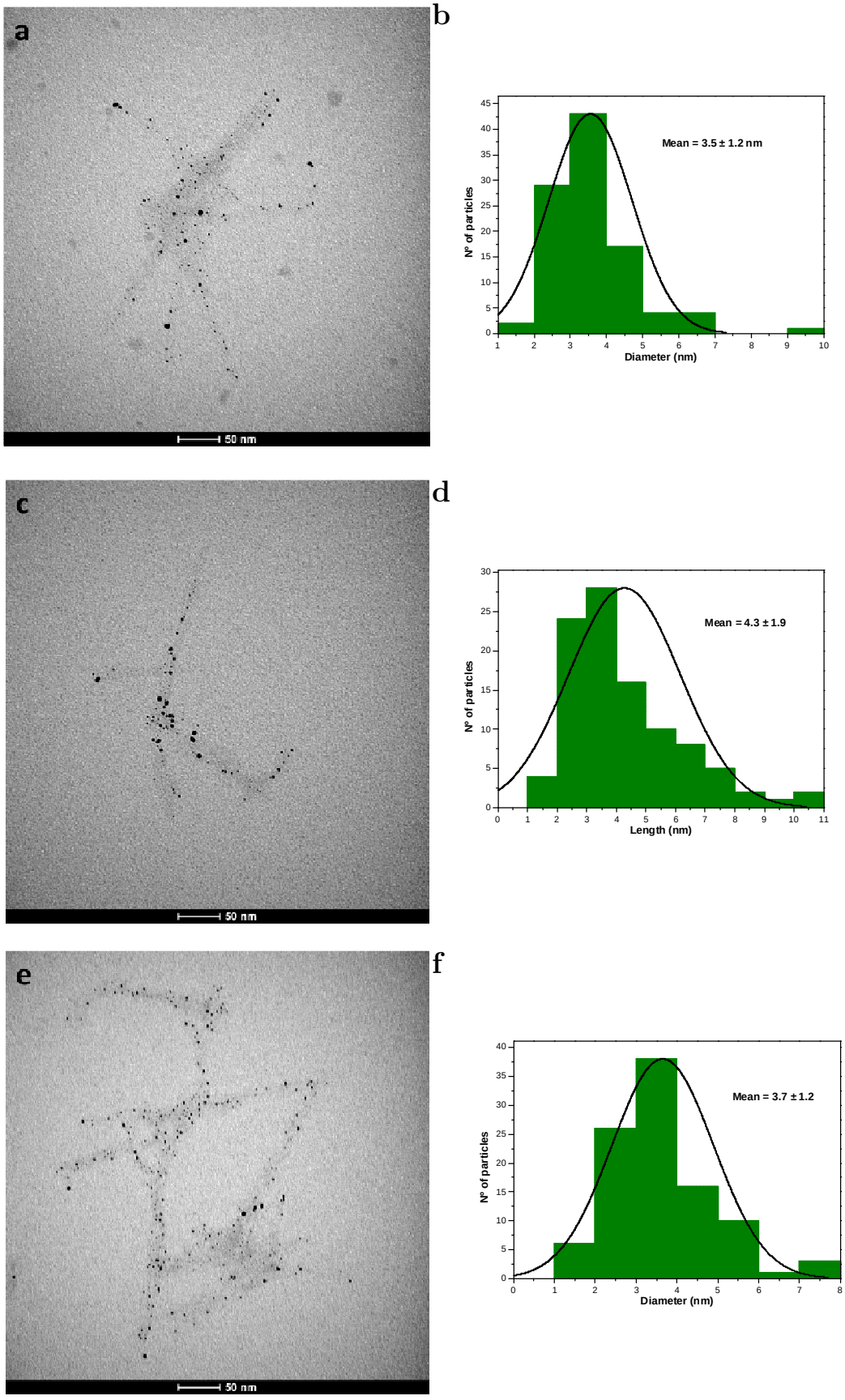

Figure 23. TEM images (a, c, e) and particle size histograms (b, d, f). of NCC-G$^{AT}{}_0$@AuNPs, NCC-G$^{AT}{}_1$@AuNPs and NCC-G$^{AT}{}_1$@AuNPs, respectively. (The scale bars represent 50 nm).

3.3.6. Catalytic activity of AuNPs

Reduction of 4-Nitrophenol (4-NP) to 4-Aminophenol (4-AP)

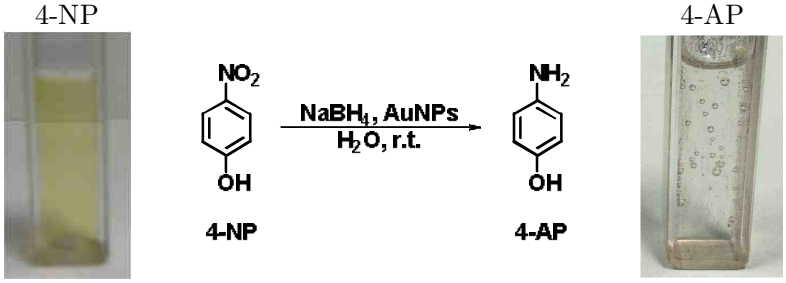

Figure 24. Reduction of 4-nitrophenol (left) to 4-aminophenol. (right)

As a preliminary study, we decided to test the catalytic performance of the NCC-G^{AT}_{n}@AuNPs derivative for the model sodium borohydride reduction of 4-nitrophenol (4-NP) to 4-aminophenol (4-AP) (Figure 24).

The reduction of 4-NP to 4-AP is a benchmark reaction for researchers in the field of catalytic reductions due to the fact that it allows a convenient monitoring of the reduction kinetic *via* UV-Vis spectroscopy by taking advantage of the disappearance of the 400 nm band belonging to the *p*-nitrophenol chromophore. For comparison purposes, we also determined the catalytic activity of the corresponding G^{AT}_{2}@AuNPs adduct which contained an amount of AuNPs comparable with that of NCC-G^{AT}_{2}@AuNPs (i.e. 14%). The experiment was carried out with a gold:4-NP = 1:17 ratio in the presence of a 80-fold excess of sodium borohydride to operate under pseudo-first order kinetics. In the presence of the various NCC-GATn@AuNPs hybrids, the yellow color of the nitro derivative faded completely in less than 5 minutes. In Figure 25, we report the UV-Vis spectra recorded during the reduction of 4-NP (normalized to absorbance at 400 nm at t = 0 min), using NCC-G^{AT}_{0}@AuNPs, NCC-G^{AT}_{1}@AuNPs and NCC-G^{AT}_{1}@AuNPs as catalysts (Figure 25a, b and c, respectively) and, for comparison, the non-supported G^{AT}_{2}@AuNPs (Figure 25d).

For all NCC-G^{AT}_{n}@AuNPs, the reaction was concluded within 4–5 min, whereas G^{AT}_{2}@AuNPs, under the same condtions of NCC-G^{AT}_{2}@AuNPs (in terms of gold added), the reaction took more than 15 minutes to finish. This suggested a beneficial effect of the NCC material as AuNPs support.

To better compare the performance of the different catalysts, the kinetic constants and the turn over frequency (TOF) were calculated. The kinetic constants were obtained by linearization of absorbance data by reporting the $\ln(A_t/A_0)$ vs. time, where A_0 was the initial absorbance and At the absorbance measured at the different times. Plot of the data for all the NCC-G^{AT}_{n}@AuNPs hybrids and for the reference G^{AT}_{2}@AuNPs are reported in Figure 26.

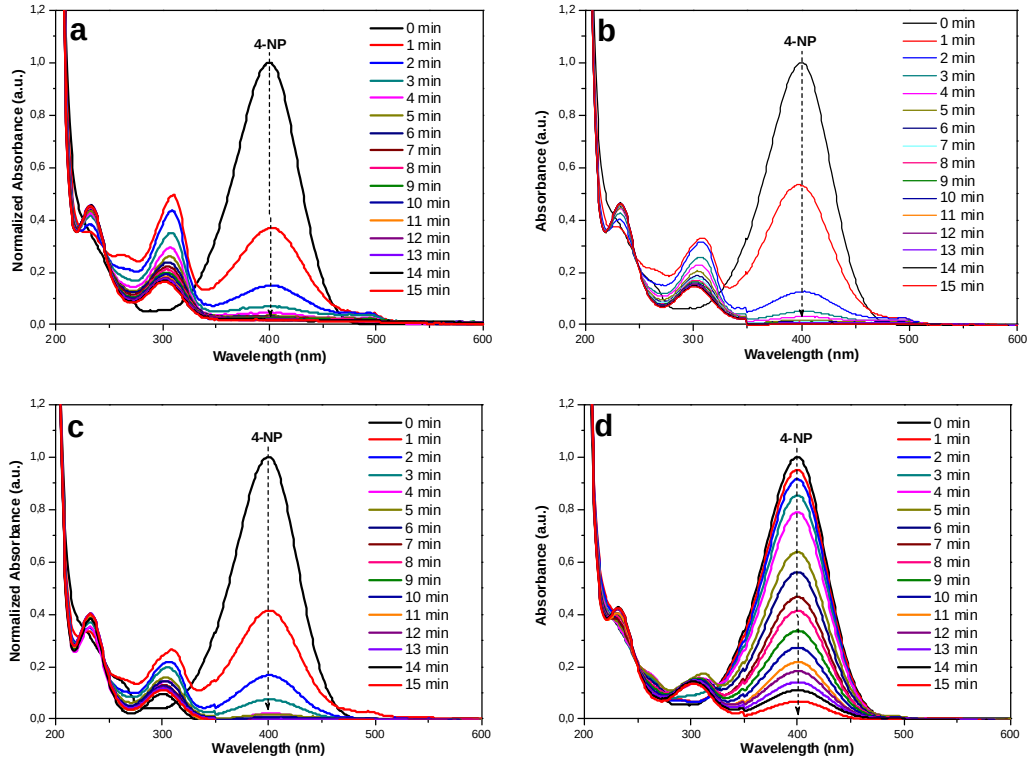

Figure 25. Successive UV-Vis spectra monitoring the reduction of 4-NP (0.12 mM) in the presence of (a) NCC-GAT0@AuNPs (V = 30 µL, c = 3.02 µM), (b) NCC-GAT1@AuNPs (V = 30 µL, c = 4.7 µM), (c) NCC-GAT2@AuNPs (V = 30 µL, c = 7.29 µM) and (d) GAT2@AuNPs (V = 30 µL, c = 6.33 µM).

Table 6 summarizes the kinetic constants (kapp, s^{-1}), the goodness of fitting (r^2 coefficient), and the turn over frequency (TOF, h^{-1}). The most active catalyst of the series is the NCC-G^{AT}_0@AuNPs giving pseudo-first order constant of $2.8 \cdot 10^{-3}$ s^{-1}, corresponding to a turn over frequency of 608 h-1. The non cellulosic G^{AT}_2@AuNPs derivative gave a kinetic constant of 7.8·10-4 s^{-1} (TOF=78 h^{-1}), then about three

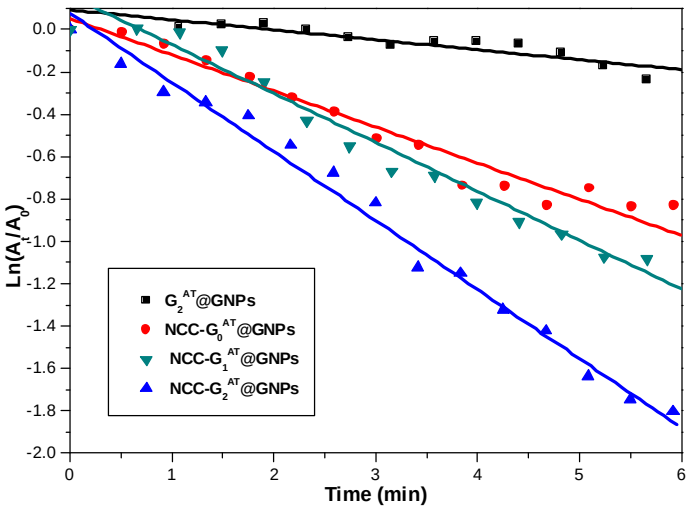

Figure 26. Plots of the Ln(A_t/A_0) vs. reaction time for 4-NP reduction using G^{AT}_2@AuNPs, NCC-GAT0@AuNPs, NCC-G^{AT}_1@AuNPs and NCC-G^{AT}_2@AuNPs as catalysts.

Table 6. Kinetic data for the different catalysts tested.

Catalyst	kapp (s^{-1})	r^2	TOF (h^{-1})
$G^{AT}{}_2$@AuNPs	$7.8x10^{-4}$	0.8152	78
NCC-$G^{AT}{}_0$@AuNPs	$2.8x10^{-3}$	0.9474	608
NCC-$G^{AT}{}_1$@AuNPs	$3.8x10^{-3}$	0.9787	367
NCC-$G^{AT}{}_2$@AuNPs	$5.4x10^{-3}$	0.9897	247

times slower than NCC-$G^{AT}{}_2$@AuNPs and about eight times slower than the more active catalyst NCC-$G^{AT}{}_0$@AuNPs. Since no significant difference in the gold loading between NCC-$G^{AT}{}_2$@AuNPs and $G^{AT}{}_2$@AuNPs was observed (14% in both cases), a higher activity of NCC-$G^{AT}{}_2$@AuNPs could be attributed to the smaller diameter of AuNPs supported on NCC-$G^{AT}{}_2$ (3.7 ± 1.2 nm) rather than $G^{AT}{}_2$ (7.5 ± 1.4 nm), which in turn corresponds to a higher active surface area. Comparing the catalytic performances of the various NCC-$G^{AT}{}_n$@AuNPs hybrids we found TOFs of 608, 367 and 247 h^{-1} for NCC-$G^{AT}{}_0$@AuNPs, NCC-$G^{AT}{}_1$@AuNPs and NCC-$G^{AT}{}_2$@AuNPs respectively. That clearly shows that AuNPs stabilized with lower generation dendrons are the best performant catalysts. This is possibly due to the fact that smaller dendrons resulted in less hindered AuNPs, and subsequently, more available for catalysis.

From these results, it is clear that our NCC-$G^{AT}{}_n$ catalysts improve the catalytic performance obtained with unsupported AuNPs only stabilized by PAMAM dendron ($G^{AT}{}_2$@AuNPs). Furthermore, the best performance was obtained using the lowest generation of dendron attached to NCC-$G^{AT}{}_0$@AuNPs, whereas with such low generation, the corresponding free dendron was not even able to stabilize AuNPs. This permits to minimize the steps of dendrimer growth reactions necessary to obtain stable AuNPs.

Our best performant catalysts also compares favorably with other AuNPs catalysts reported in literature for the reduction of 4-NP. As it has been shown in the introduction, TOF values of 90 h^{-1} can be found for AuNPs of around 15 nm stabilized by hyperbranched polymer. For supported AuNPs, a TOF of ~12 h^{-1} was obtained when AuNPs of 8-25 nm were embedded in a graphene-based hydrogel, or 484 h^{-1} when the support was graphene oxide (GO) for AuNPs diameter of 3- 7 nm. Our system also improves the value of 109 h^{-1} obtained with AuNPs of 10 – 30 nm supported on NCC. The better activity of our catalysts compared with these examples can be attributed, depending on the case, either to a smaller diameter of our AuNPs, or to a better exposure of the NPs surface to the reaction medium.

Recyclability

As it has been commented in the introduction, for the development of a sustainable catalysts, apart from a high TOF value, it is decidedly desirable the possibility to

reuse the catalyst without loss of activity for as long as possible. To verify the stability and recyclability of our catalysts, we reloaded the exhausted reaction medium with fresh aliquots of 4-NP. We tested the recyclability for 5 times and each time the reaction restarted with efficiency even higher than the first cycle (Figure 27). This observation, which holds also for the $G^{AT}{}_2$@AuNPs reference material, will require further investigation to assess if it is due to some morphological modifications of the hybrids or to a partial releasing of AuNPs in the reaction media. In this latter case, the NCC-$G^{AT}{}_n$@AuNPs hybrids (and to a lesser extent also $G^{AT}{}_n$@AuNPs) would play a role of a sponge releasing the active catalyst in the reaction medium.

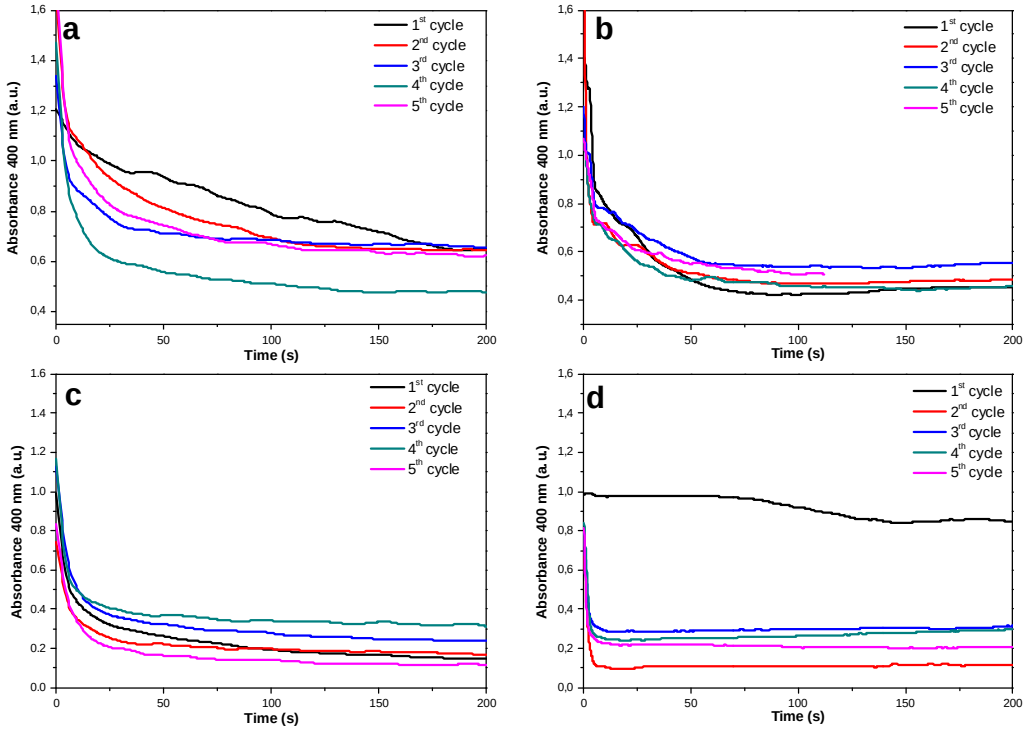

Figure 27. UV-Vis spectra monitoring absorbance at 400 nm vs. time (s) during 5 cycles of catalysis using NCC-$G^{AT}{}_0$@AuNPs (a), NCC-$G^{AT}{}_1$@AuNPs (b), NCC-$G^{AT}{}_2$@AuNPs (c) and $G^{AT}{}_2$@AuNPs (d).

3.4. Conclusions

In summary, a new series of hybrid materials composed of cellulose nanocrystals functionalized with PAMAM dendrons was synthesized and fully characterized. FT-IR, Kaiser test and XPS spectroscopy confirmed the covalent grafting of dendron moieties onto the nanocellulose surface. These novel materials were used as scaffold for the in situ preparation of gold nanoparticles (AuNPs).

By this way it was possible to obtain well-dispersed AuNPs, stable as aqueous suspension for months. The nanocellulose support permitted to obtain AuNPs with PAMAM dendrons of generations lower than that normally required for dendrons alone, avoiding the long synthesis and purification steps of dendrimer growth. The new materials obtained were evaluated as catalysts in the reduction of 4-NP, showing an enhancement in the activity compared to the non cellulose system $G^{AT}{}_2$@AuNPs or other supported AuNPs. Moreover, the recyclability and stability of the catalysts were tested by recharging fresh reactants: every time they were consumed, up to 5 cycles, with no loss of activity. From these pieces of evidence, we can conclude that the hybrid materials NCC-$G^{AT}{}_n$@AuNPs are promising catalysts, easy to scale-up and recycle by simple filtration or centrifugation.

On the basis of these results, our system could be extended to other Au catalyzed reactions towards the development of innovative catalysts for industrially relevant applications.

3.5. Experimental details

3.5.1. Chemicals.

All reagents and solvents were used as received or purified using standard procedures. Milli-Q water was used in all experiments (System MilliQ plus). Microcrystalline cellulose Avicel® powder was purchased from Aldrich and used without further purification.

3.5.2. Techniques

The optical properties were carried out by UV-Vis-NIR spectroscopy with a Cary 5000 spectrophotometer using 10 mm path length quartz cuvettes.

Infrared analyses were performed using a Fourier-transform infrared (FT-IR) spectrometer (Perkin-Elmer 2000) by the method of KBr pellets.

Thermal analyses were performed on TGA Q5000IR (TA Instruments) under N_2 or air, by equilibrating at 50 °C, and following a ramp at 10°C/min up to 600 ºC in (N_2) and 700-800 °C (in air), (approximately 1 mg of each compound).

TEM analyses were performed either on a TEM Philips EM208 or on a Tecnai G2 FEI – 100kV microscope. Samples were prepared by drop casting from dispersion onto a TEM grid (200 mesh, nickel, carbon only), followed in some cases by staining with a 2 wt% uranyl acetate solution and the images where analysed with the help of Fiji package for size measurements.

XPS experiments were performed in a SPECS Sage HR 100 spectrometer with a non monochromatic X ray source (Magnesium Kα line of 1253.6 eV energy and a power applied of 250 W and calibrated using the 3d5/2 line of Ag with a full width at half maximum (FWHM) of 1.1 eV. An electron flood gun was used to compensate for charging during XPS data acquisition. The selected resolution was 30 and 15 eV of Pass Energy and 0.5 and 0.15 eV/step for the survey and high resolution spectra, respectively. All Measurements were made in an ultra-high vacuum (UHV) chamber at a pressure around $8 \bullet 10$ 8 mbar. In the fittings Gaussian Lorentzian functions were used (after a Shirley background correction) where the FWHM of all the peaks were constrained while the peak positions and areas were set free.

NMR spectra were obtained on a Varian Inova spectrometer (500 MHz ^{1}H and 125 MHz ^{13}C) or on a JEOL Eclipse 400FT (400 MHz 1H). Chemical shifts are reported in ppm using the solvent residual signal as an internal reference ($CDCl_3$: $\delta H = 7.26$ ppm, $\delta C = 77.23$ ppm; CD_3OD: $\delta H = 3.31$ ppm, $\delta C = 49$ ppm). The resonance multiplicity is described as s (singlet), d (doublet), t (triplet), q (quartet), m (multiplet), br (broad signal). ESI-MS (5600 eV; MeOH) were performed on a Perkin-Elmer API1.

3.5.3. Synthesis of PAMAM dendrons

Synthesis of G^{ET}_0. 1 g of propargylamine (18 mmol, 1 eq.) was dissolved in methanol (20 mL) and cooled to 0 ºC. 6.57 mL of methyl acrylate (72 mmol, 4 eq.)

were added dropwise to the solution and then the mixture was allowed to reach room temperature and stirred for 48h. Solvent and excess of methyl acrylate were evaporated under reduced pressure. The resulting oil was diluted with 20 mL of methanol and the methanol was evaporated under reduced pressure to remove all traces of methyl acrylate. After repeating this operation 3 times, $\mathbf{G^{ET}_{-0.5}}$ was obtained as a brown oil (4 g, 97%). **^{1}H NMR** (500 MHz, $CDCl_3$) δ: 3.66 (s, 6H, 2xOCH_3), 3.41 (d, 2H, J = 2.4 Hz, CH_2), 2.83 (t, 4H, J = 7.1 Hz, 2xCH_2), 2.46 (t, 4H, J = 7.1 Hz, 2xCH_2), 2.19 (t, 1H, J = 2.4 Hz, CH). **^{13}C NMR** (125 MHz, $CDCl_3$) δ: 172.6, 77.9, 73.9, 51.6, 48.9, 41.8, 32.9. **IR** υ: 3280, 2960, 2840, 1736 (C=O), 1439, 843 cm^{-1}. **ESI-MS** m/z: 227.9 [M+H^+], 249.9 [M+Na^+].

Synthesis of $\mathbf{G^{AT}_0}$. $\mathbf{G^{ET}_0}$ (2 g, 8.8 mmol, 1 eq.) was dissolved in 20 mL of methanol. Then 3 mL of ethylenediamine (44 mmol, 5 eq.) were added and the mixture stirred at room temperature for 3 days. Solvent and excess of ethylendiamine were removed by evaporation under reduce pressure and traces of ethylendiamine were removed by azeotropic distillation in a mixture toluene/methanol (9:1) to give $\mathbf{G^{AT}_0}$ as a yellow oil (2.4 g, 96 %). **^{1}H NMR** (400 MHz, CD_3OD) δ: 3.45 (d, 2H, J = 2.3 Hz, CH_2), 3.24 (t, 4H, J = 6.3 Hz, 2xCH_2), 2.81 (t, 4H, J = 6.8 Hz, 2xCH_2), 2.71 (t, 4H, J = 6.3 Hz, 2xCH_2), 2.62 (t, 1H, J = 2.3 Hz, CH), 2.37 (t, 4H, J = 6.7 Hz, 2xCH_2). **^{13}C NMR** (125 MHz, CD_3OD) δ: 173.8, 77.3, 73.7, 49.1, 40.4, 38.4, 34.9, 33.3. **IR** υ: 3269 (NH_2), 1641, 1556 cm^{-1}. **ESI-MS** m/z: = 284.1 [M+H^+], 306.1 [M+Na^+].

Synthesis of $\mathbf{G^{ET}_1}$. This compound was prepared from $\mathbf{G^{AT}_0}$ (1.7 g, 6 mmol, 1 eq.) and methyl acrylate (3.26 mL, 36 mmol, 6 eq.) using the same procedure described for $\mathbf{G^{ET}_{-0.5}}$. $\mathbf{G^{ET}_{0.5}}$ was obtained as a yellow oil (3.6 g, 97 %). **^{1}H-NMR** (400 MHz, $CDCl_3$) δ: 3.65 (s, 12H, 4xOCH_3), 3.45 (d, 2H, J = 2.5 Hz, CH_2), 3.24 (t, 4H, J = 6.0 Hz, 2xCH_2), 2.84 (t, 4H, J = 6.0 Hz, 2xCH_2), 2.75 (t, 8H, J = 6.0 Hz, 4xCH_2), 2.42 (t, 8H, J = 6.0 Hz, 4xCH_2), 2.37 (t, 4H, J = 6.0 Hz, 2xCH_2), 2.17 (t, 1H, J = 6.0 Hz, CH). **^{13}C NMR** (125 MHz, $CDCl_3$) δ: 173.0, 171.9, 77.9, 73.4, 53.0, 51.6, 49.7, 49.3, 41.2, 37.1, 33.9, 32.7. **IR** υ: 3500-3400 (broad), 1736 (C=O), 1650, 1550 cm^{-1}. **ESI-MS**, m/z: = 628.3 [M+H^+], 650.3 [M+Na^+], 666.3 [M+K^+].

Synthesis of $\mathbf{G^{AT}_1}$. This compound was prepared from $\mathbf{G^{ET}_1}$ (2.2 g, 3.53 mmol, 1 eq.) and ethylenediamine (2.5 mL, 35.3 mmol, 10 eq.) using the same procedure described for $\mathbf{G^{AT}_0}$. $\mathbf{G^{AT}_1}$ was obtained as a yellow oil (2.6 g, > 99 %).**^{1}H NMR** (400 MHz, CD_3OD) δ: 3.45 (d, J = 2.5 Hz, 2H, CH_2), 3.25 (t, 12H, J = 6.5 Hz, 6xCH_2), 2.83-2.71 (m, 20H, 10xCH_2), 2.63 (bs, 1H, CH), 2.57 (t, 4H, J = 6.6 Hz, 2xCH_2), 2.38-2.31 (m, 12H, 6xCH_2). **^{13}C NMR** (125 MHz, CD_3OD) δ: 173.9, 173.1, 77.4, 73.8, 52.2, 52.0, 49.7, 49.2, 40.5, 40.3, 37.2, 33.5, 33.3. **IR** υ: 3400 (NH_2), 1645, 1555, 1018 cm^{-1}. **ESI-MS**, m/z: = 740.5 [M+H^+], 762.5 [M+Na^+].

Synthesis of $\mathbf{G^{ET}_2}$. This compound was prepared from $\mathbf{G^{AT}_1}$ (1.5 g, 2.03 mmol, 1 eq.) and methyl acrylate (1.83 mL, 20.3 mmol, 10 eq.) using the same procedure described for $\mathbf{G^{ET}_{-0.5}}$. $\mathbf{G^{ET}_{1.5}}$ was obtained as a yellow oil (2.8 g, 96 %). **^{1}H NMR**: (500 MHz, $CDCl_3$) δ: 3.65 (s, 24H, 8xOCH_3), 3.45 (bs, 2H, CH_2), 3.35-3.24 (m, 12H, 6xCH_2), 2.84-2.77 (m, 12H, 6xCH_2) 2.74 (t, 16H, J = 5.5 Hz, 8xCH_2), 2.56-2.50 (m, 12H, 6xCH_2), 2.42 (t, 16H, J = 6.0 Hz, 8xCH_2), 2.39-2.33 (m, 12H, 6xCH_2), 2.19 (bs, 1H, CH). **^{13}C NMR** (125 MHz, CD_3OD) δ: 173.0, 172.3, 172.1, 77.8, 73.5, 52.9, 52.1,

51.6, 49.9, 49.2, 48.7, 41.0, 39.4, 38.9, 37.2, 33.8, 32.6. **IR** υ: 3400 (broad), 1736, 1645, 1555, 1018 cm^{-1}. **ESI-MS**, m/z: 1429.6 [$M+H^+$], 1451.1 [$M+Na^+$].

Synthesis of G^{AT}_2. This compound was prepared from **G^{ET}_2** (1 g, 0.7 mmol, 1 eq.) and ethylenediamine (1 mL, 14 mmol, 20 eq.) using the same procedure described for **G^{AT}_0**. **G^{AT}_2** was obtained as a yellow oil (1.1 g, 95 %).**^{1}H NMR**: (400 MHz, CD_3OD) δ: 3.47 (bs, 2H, CH_2), 3.35-3.11 (m, 24H, 12xCH_2), 2.90-2.63 (m, 52H, 26xCH_2), 2.64-2.48 (m, 13H, CH, 6xCH_2), 2.47-2.25 (m, 24H, 12xCH_2). **^{13}C NMR** (125 MHz, CD_3OD) δ: 173.9, 173.4, 172.9, 76.9, 73.9, 53.2, 52.0, 51.6, 50.9, 49.7, 49.3, 45.1, 41.0, 40.5, 38.6, 37.2, 33.4, 31.8. **IR** υ: 3400 (NH_2), 1645, 1555, 1018 cm^{-1}. **ESI-MS**, m/z: = 1653.1 [M^+].

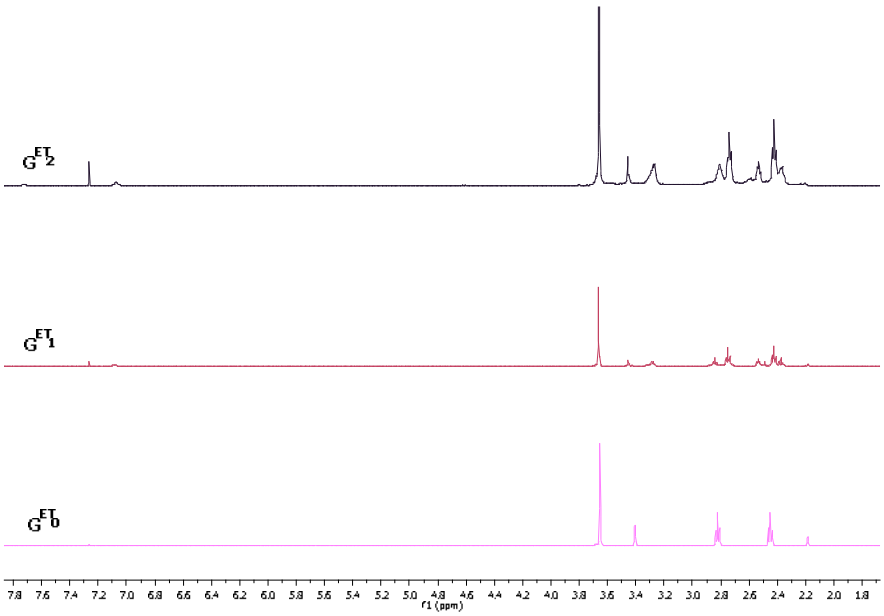

Figure 28. ^{1}H-NMR spectra of G^{ET}_0, G^{ET}_1 and G^{ET}_2 in $CDCl_3$.

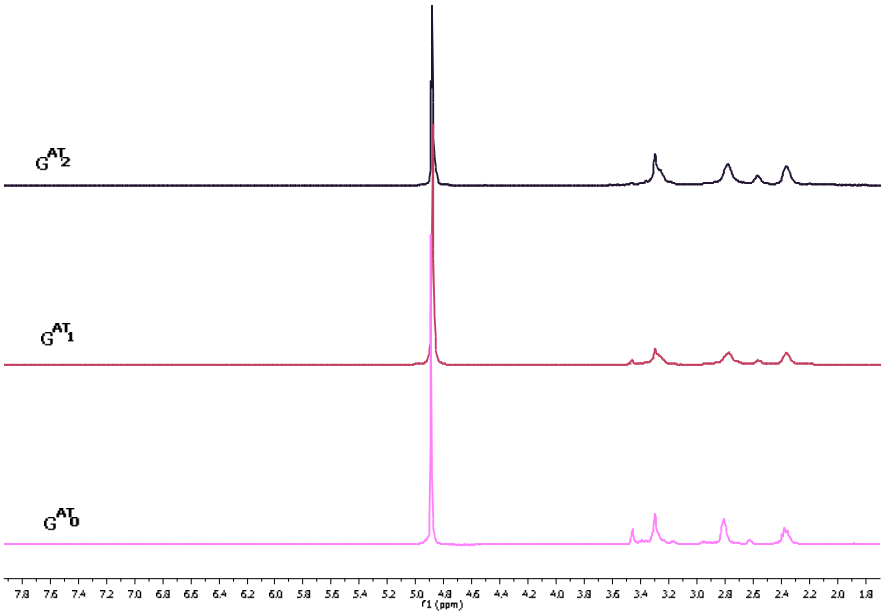

Figure 29. ^{1}H-NMR spectra of G^{AT}_0, G^{AT}_1 and G^{AT}_2 in CD_3OD.

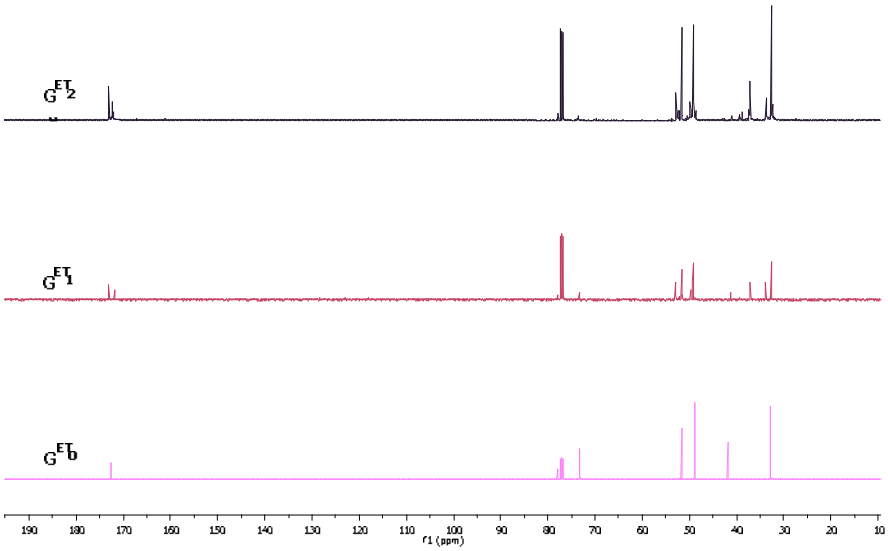

Figure 30. ^{13}C-NMR spectra of G^{ET}_0, G^{ET}_1 and G^{ET}_2 in $CDCl_3$.

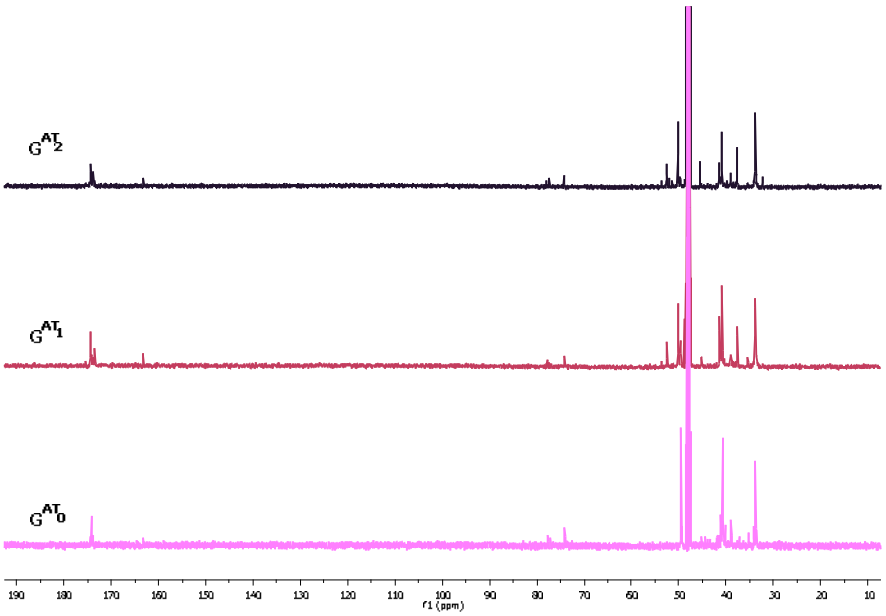

Figure 31. ^{13}C-NMR spectra of G^{AT}_0, G^{AT}_1 and G^{AT}_2 in CD_3OD.

3.5.4. Synthesis of NCC-based materials

Synthesis of nanocrystalline cellulose (NCC): NCC was prepared following the procedure described in Chapter 2.

Synthesis of NCC-OMs: Dried NCC (1.6 g) was grinded and dispersed in a mixture of anhydrous pyridine (80 mL) and DMSO (8 mL) by sonicating in an ice bath for 4 hours. The suspension was cooled to 0 ºC in a Pyrex tube and mesyl chloride (15.2 mL, 0.2 mol) was slowly added. Color changed immediately from white to yellow, and shortly after dark brown. The mixture was allowed to reach room

temperature and stirred for 24 hours. Then, the mixture was filtered on a Millipore membrane (JVWP 0.1 μm) and extensively washed with ethanol and then with water to give NCC-OMs as a dark brown solid (1.14 g, 71%).

Synthesis of NCC-N_3: NCC-OMs (1.1 g) was dispersed in DMF by sonicating for 45 minutes. Sodium azide (1.1 g, 0.017 mol) was added in small portions and the mixture was heated to 50 ºC and kept under stirring for 3 days. After cooling down, the mixture was filtered on a Millipore membrane (JVWP 0.1 μm) and extensively washed with ethanol and then with water to give NCC-N3 as a pale brown solid (820 mg, 75%).

Synthesis of NCC-G^{ET}_0: NCC-N_3 (160 mg) was dispersed in 160 mL of water by sonicating for 45 minutes. Dendron G^{ET}_0 (113 mg, 0.5 mmol) was dissolved in 8 mL of THF and added to NCC-N_3 under stirring. Copper sulfate (14.46 mg, 0.06 mmol) and L-ascorbate (43 mg, 0.21 mmol) were dissolved in 5 mL of water and added to the mixture. The mixture was stirred at r.t. for 3 days and then filtered on a Millipore membrane (JVWP 0.1 μm) and extensively washed with water, THF and methanol to give NCC-G^{ET}_0 as a pale brown solid (133 mg, 86%).

Synthesis of NCC-G^{AT}_0: NCC-G^{ET}_0 (90 mg) was dispersed in methanol (100 mL) by sonicating for 30 minutes. Ethylene diamine (1 mL, 55 mmol) was dissolved in methanol (100 mL) and was added dropwise to the suspension. The mixture was stirred at r.t. for 5 days. Then, the suspension was filtered on a Millipore membrane (JVWP 0.1 μm) and extensively washed with water until neutral pH to give NCC-G^{AT}_0 as a brownish solid (66 mg, 73%).

Synthesis of NCC-G^{ET}_1: This compound was prepared from NCC-N_3 (160 mg), dendron G^{ET}_1 (313 mg, 0.5 mmol), copper sulfate (14.46 mg, 0.06 mmol) and L-ascorbate (43 mg, 0.21 mmol) using the same procedure described for NCC-GET0. NCC-G^{ET}_1 was obtained as a pale brown solid (157 mg, 98%).

Synthesis of NCC-G^{AT}_1: This compound was prepared from NCC-GET1 (100 mg) and ethylene diamine (1 mL, 55 mmol) using the same procedure described for NCC-G^{AT}_0. NCC-G^{AT}_1 was obtained as a brownish solid (66 mg, 66%).

Synthesis of NCC-G^{ET}_2: This compound was prepared from NCC-N_3 (160 mg), dendron G^{ET}_2 (714 mg, 0.5 mmol), copper sulfate (14.46 mg, 0.06 mmol) and L-ascorbate (43 mg, 0.21 mmol) using the same procedure described for NCC-G^{ET}_0. NCC-G^{ET}_2 was obtained as a pale brown solid (118 mg, 74%).

Synthesis of NCC-GAT2: This compound was prepared from NCC-G^{ET}_2 (90 mg) and ethylene diamine (1 mL, 54 mmol) using the same procedure described for NCC-GAT0. NCC-G^{AT}_2 was obtained as a brownish solid (69 mg, 77%).

Gold Nanoparticles (AuNPs) supported on NCC-G^{AT}_n. In a typical experiment, 5 mL of NCC-G^{AT}_n (1 mg • mL-1) dispersion in MilliQ water was added to 14.79 mL of MilliQ water in a vial of 20 mL. $HAuCl_4$ (10 mM, 0.2 mL) and then $NaBH_4$ freshly prepared solution in NaOH 0.3 M (1M, 10 μL) were added to the solution in sequence and the vial was then sealed. The mixture was stirred for 1 hour at room temperature and without light. Solutions changed color first to yellowish due to the $HAuCl_4$ salt, and shortly after to different intensities of red. Suspension was

kept on the bench for one day to observe the presence of precipitate. Then, the supernatant was filtered and cleaned with water and kept under argon.

3.5.5. Synthesis of AuNPs

Gold Nanoparticles (AuNPs) stabilized with PAMAM dendrons G^{AT}_0-G^{AT}_2: In a typical experiment, 1 mL of dendron G^{AT}_2 (10 mM) solution in MilliQ water was added to 17.425 mL of MilliQ water in a vial of 20 mL. $HAuCl_4$ (10 mM, 1.5 mL) and then freshly prepared $NaBH_4$ solution in NaOH 0.3 M (1 M, 10 µL) were added to the solution. The vial was then sealed and the mixture stirred for 1 hour at room temperature and without light. Solutions changed color first to yellowish due to the $HAuCl_4$ salt, and shortly after to different intensities of red. For G^{AT}_0 and G^{AT}_1, molar ratios were adjusted in order to keep the same NH_2:Au^{3+} ratio. After 48 hours, all gold had completely precipitated in the case of dendrons G^{AT}_0 and G^{AT}_1, while G^{AT}_2 presented a pale pink color due to the presence of gold nanoparticles. Supernatant was kept under argon.

3.5.6. Catalysis

Catalysis. In a typical experiment, an aqueous suspension of NCC-GATn@AuNPs nanohybrids, or GAT2@AuNPs (30 µL, total Au content: 0.01-0.02 µmol) was added to a solution mixture (3 mL) consisting of 4-nitrophenol (4-NP) (0.12 mM) and NaBH4 (38.1 mM) and the reaction was monitored by UV-Vis spectroscopy.

Recyclability tests. In a typical experiment, an aqueous suspension of NCC-G^{AT}_n@AuNPs nanohybrids, or G^{AT}_2@AuNPs (30 µL, total Au content: 0.01-0.02 µmol) was added to a solution mixture (3 mL) consisting of 4-nitrophenol (4-NP) (0.12 mM) and $NaBH_4$ (38.1 mM). Absorbance at 400 nm was constantly monitored and fresh aliquots (50 µL of 4-NP 7 mM and $NaBH_4$ 2.3 M) were added to the consumed medium in order to replenish the initial concentration of 4-NP and keep the excess of $NaBH_4$. This process was repeated 5 times.

3.6. References

(1) Khan, M. S.; Vishakante, G. D.; Siddaramaiah H. Gold Nanoparticles: A Paradigm Shift in Biomedical Applications. *Adv. Colloid Interface Sci.* **2013**, *199-200*, 44–58.

(2) Alex, S.; Tiwari, A. Functionalized Gold Nanoparticles: Synthesis, Properties and applications—A Review. *J. Nanosci. Nanotechnol.* **2015**, *15* (3), 1869–1894.

(3) Alivisatos, A. P. Semiconductor Clusters, Nanocrystals and Quantum Dots. *Science* **1996**, *271*, 933–937.

(4) Kuemmeth, F.; Bolotin, K. I.; Shi, S. F.; Ralph, D. C. Measurement of Discrete Energy-Level Spectra in Individual Chemically Synthesized Gold Nanoparticles. *Nano Lett.* **2008**, *8*, 4506–4512.

(5) El-Sayed, M. A. Small Is Different: Shape-, Size-, and Composition-Dependent Properties of Some Colloidal Semiconductor Nanocrystals. *Acc. Chem. Res.* **2004**, *37* (5), 326–333.

(6) Ghosh, S. K.; Pal, T. Interparticle Coupling Effect on the Surface Plasmon Resonance of Gold Nanoparticles: From Theory to Applications. *Chem. Rev.* **2007**, *107*, 4797–4862.

(7) Wriedt, T. *The Mie Theory: Basics and Applications*; Hergert, W., Wriedt, T. (Eds. ., Eds.; Springer-Verlag: Berlin, Heidelberg, 2012.

(8) Mie, G. Beiträge Zur Optik Trüber Medien, Speziell Kolloidaler Metallösungen. *Ann. Phys.* **1908**, *330*, 377–445.

(9) Njoki, P. N.; Lim, I. I. S.; Mott, D.; Park, H. Y.; Khan, B.; Mishra, S.; Sujakumar, R.; Luo, J.; Zhong, C. J. Size Correlation of Optical and Spectroscopic Properties for Gold Nanoparticles. *J. Phys. Chem. C* **2007**, *111*, 14664–14669.

(10) Eustis, S.; El-Sayed, M. A. Why Gold Nanoparticles Are More Precious than Pretty Gold: Noble Metal Surface Plasmon Resonance and Its Enhancement of the Radiative and Nonradiative Properties of Nanocrystals of Different Shapes. *Chem. Soc. Rev.* **2006**, *35*, 209–217.

(11) Nimtz, G.; Marquardt, P. Size-Induced Metal-Insulator Transition in Metals and Semiconductors. *Small* **1988**, *86*, 66–71.

(12) Daniel, M. C.; Astruc, D. Gold Nanoparticles: Assembly, Supramolecular Chemistry, Quantum-Size-Related Properties, and Applications toward Biology, Catalysis, and Nanotechnology. *Chem. Rev.* **2004**, *104*, 293–346.

(13) Peter Marquardt and Gunter Nimtz. Size-Dependent Dielectric Response of Small Metal Particles. *Phys. Rev. B* **1991**, *43* (17), 245–247.

(14) Henglein, A. Physicochemical Properties of Small Metal Particles in Solution: "Microelectrode" Reactions, Chemisorption, Composite Metal Particles, and the Atom-to-Metal Transition. *J. Phys. Chem.* **1993**, *97*, 5457–5471.

(15) Schon, G.; Simon, U. A Fascinating New Field in Colloid Science - Small Ligand-Stabilized Metal-Clusters and Possible Application in Microelectronics. 1 State of the Art. *Colloid Polym. Sci.* **1995**, *273*, 101–117.

(16) Thompson, D. T. Using Gold Nanoparticles for Catalysis. *Nano Today* **2007**, *2* (4), 40–43.

(17) Tatarchuk, V. V.; Sergievskaya, A. P.; Druzhinina, I. a.; Zaikovsky, V. I. Kinetics

and Mechanism of the Growth of Gold Nanoparticles by Reduction of Tetrachloroauric Acid by Hydrazine in Triton N-42 Reverse Micelles. *J. Nanoparticle Res.* **2011**, *13*, 4997–5007.

(18) http://education.mrsec.wisc.edu/nanolab/gold/.

(19) Turkevich, J.; Garton, G.; Stevenson, P. C. The Color of Colloidal Gold. *J. Colloid Sci.* **1954**, *9*, 26–35.

(20) Frens, G. Particle Size and Sol Stability in Metal Colloids. *Kolloid-Zeitschrift Zeitschrift Polym.* **1972**, *250*, 736–741.

(21) Brust, M.; Walker, M.; Bethell, D.; Schiffrin, D. J.; Whyman, R. Synthesis of Thiol-Derivatised Gold Nanoparticles in. *Chem. Commun.* **1994**, 801–802.

(22) Liz-Marzán, L. M. Gold Nanoparticle Research before and after the Brust–Schiffrin Method. *Chem. Commun.* **2013**, *49*, 1994–1996.

(23) Tzhayik, O.; Sawant, P.; Efrima, S.; Kovalev, E.; Klug, J. T. Xanthate Capping of Silver, Copper, and Gold Colloids. *Langmuir* **2002**, *18* (c), 3364–3369.

(24) Porter, L. A.; Ji, D.; Westcott, S. L.; Graupe, M.; Czernuszewicz, R. S.; Halas, N. J.; Lee, T. R. Gold and Silver Nanoparticles Functionalized by the Adsorption of Dialkyl Disulfides. *Langmuir* **1998**, *14* (32), 7378–7386.

(25) Resch, R.; Baur, C.; Bugacov, A.; Koel, B. E.; Echternach, P. M.; Madhukar, A.; Montoya, N.; Requicha, A. A. G.; Will, P. Linking and Manipulation of Gold Multinanoparticle Structures Using Dithiols and Scanning Force Microscopy. *J. Phys. Chem. B* **1999**, *103*, 3647–3650.

(26) Weare, W. W.; Reed, S. M.; Warner, M. G.; Hutchison, J. E. Improved Synthesis of Small (dCORE ≈ 1 . 5 Nm) Phosphine-Stabilized Gold Nanoparticles. *J. Am. Chem. Soc.* **2000**, *122* (17), 12890–12891.

(27) Meng, X.; Xu, Q.; Wang, S.; Zhu, M. Ligand-Exchange Synthesis of Selenophenolate-Capped Au25 Nanoclusters. *Nanoscale* **2012**, *4*, 4161–4165.

(28) Leff, D. V.; Brandt, L.; Heath, J. R. Synthesis and Characterization of Hydrophobic, Organically- Soluble Gold Nanocrystals Functionalized with Primary Amines. *Langmuir* **1996**, *12* (c), 4723–4730.

(29) Buhleier E, Wehner W, V. F. “Cascade”- and “nonskid-Chain-Like” Synthesis of Molecular Cavity Topologies. *Synthesis.* **1978**, *9*, 155–158.

(30) Tomalia, D. A.; Baker, H.; Dewald, J.; Hall, M.; Kallos, G.; Martin, S.; Roeck, J.; Ryder, J.; Smith, P. A New Class of Polymers: Starburst-Dendritic Macromolecules. *Polymer Journal.* 1985, pp 117–132.

(31) Newkome, G. R.; YaolC, Z.; Baker, G. R.; Gupta, V. K. Cascade Molecules: A New Approach to Micelles. A [27]-Arborol. *J. Org. Chem* **1985**, No. 3, 2003–2004.

(32) F. Votgle, G. Richardt, N. W. *Dendrimer Chemistry: Concepts, Syntheses, Properties, Applications*; Wiley-VCH, Ed.; Weinheim, Germany, 2009.

(33) Crooks, R. M.; Zhao, M.; Sun, L.; Chechik, V.; Yeung, L. K. Dendrimer-Encapsulated Metal Nanoparticles: Synthesis, Characterization, and Applications to Catalysis. *Acc. Chem. Res.* **2001**, *34* (3), 181–190.

(34) Balogh, L.; Tomalia, D. A. Poly(amidoamine) Dendrimer-Templated Nanocomposites. 1. Synthesis of Zerovalent Copper Nanoclusters [5]. *J. Am. Chem. Soc.* **1998**, *120* (2), 7355–7356.

(35) Esumi, K.; Suzuki, A.; Aihara, N.; Usui, K. Preparation of Gold Colloids with UV

Irradiation Using Dendrimers as Stabilizer. *Langmuir* **1998**, *18* (16), 3157–3159.

(36) Zhao, M.; Crooks, R. M. Homogeneous Hydrogenation Catalysis with Monodisperse, Sendrimer-Wncapsulated Pd and Pt Nanoparticles. *Angew. Chem. Int. Ed.* **1999**, *38* (3), 364–366.

(37) http://www.nanotechnologies.qc.ca/projects/nanopatterning/nanopatterning.

(38) Esumi, K.; Isono, R.; Yoshimura, T. Preparation of Silver-, Platinum-, and Palladium-PAMAM Dendrimer Nanocomposites and Their Catalytic Activities for Reduction of 4-Nitrophenol. *Shikizai Kyokaishi* **2003**, *76* (12), 421–427.

(39) Guerra, J.; Rodrigo, A. C.; Merino, S.; Tejeda, J.; García-Martínez, J. C.; Sánchez-Verdú, P.; Ceña, V.; Rodríguez-López, J. PPV-PAMAM Hybrid Dendrimers: Self-Assembly and Stabilization of Gold Nanoparticles. *Macromolecules* **2013**, *46*, 7316–7324.

(40) Zheng, J.; Zhu, Z.; Chen, H.; Liu, Z. Nanopatterned Assembling of Colloidal Gold Nanoparticles on Silicon. *Langmuir* **2000**, *16*, 4409–4412.

(41) Ivanova, S.; Petit, C.; Pitchon, V. A New Preparation Method for the Formation of Gold Nanoparticles on an Oxide Support. *Appl. Catal. A Gen.* **2004**, *267*, 191–201.

(42) Yuzawa, H.; Yoshida, T.; Yoshida, H. Gold Nanoparticles on Titanium Oxide Effective for Photocatalytic Hydrogen Formation under Visible Light. *Appl. Catal. B Environ.* **2012**, *115-116*, 294–302.

(43) Dharuman, V.; Anjalidevi, C.; Manikandan, P. N.; Imra, H. Gold Nanoparticles Supported on Zirconium, Tin and Ruthenium Oxides for Reagentless Electrochemical Sensing of Hydrogen Peroxide. *Anal. Methods* **2015**, *7*, 3454–3460.

(44) Dumbre, D. K.; Choudhary, V. R.; Patil, N. S.; Uphade, B. S.; Bhargava, S. K. Calcium Oxide Supported Gold Nanoparticles as Catalysts for the Selective Epoxidation of Styrene by T-Butyl Hydroperoxide. *J. Colloid Interface Sci.* **2013**, *415*, 111–116.

(45) Costa, V. V.; Estrada, M.; Demidova, Y.; Prosvirin, I.; Kriventsov, V.; Cotta, R. F.; Fuentes, S.; Simakov, A.; Gusevskaya, E. V. Gold Nanoparticles Supported on Magnesium Oxide as Catalysts for the Aerobic Oxidation of Alcohols under Alkali-Free Conditions. *J. Catal.* **2012**, *292*, 148–156.

(46) Yazid, H.; Adnan, R.; Hamid, S. A.; Farrukh, M. A. Synthesis and Characterization of Gold Nanoparticles Supported on Zinc Oxide via the Deposition-Precipitation Method. *Turkish J. Chem.* **2010**, *34*, 639–650.

(47) Chen, Y.; Qiu, J.; Wang, X.; Xiu, J. Preparation and Application of Highly Dispersed Gold Nanoparticles Supported on Silica for Catalytic Hydrogenation of Aromatic Nitro Compounds. *J. Catal.* **2006**, *242*, 227–230.

(48) Chiang, C. W.; Wang, A.; Mou, C. Y. CO Oxidation Catalyzed by Gold Nanoparticles Confined in Mesoporous Aluminosilicate Al-SBA-15: Pretreatment Methods. *Catal. Today* **2006**, *117*, 220–227.

(49) Lee, B.; Ma, Z.; Zhang, Z.; Park, C.; Dai, S. Influences of Synthesis Conditions and Mesoporous Structures on the Gold Nanoparticles Supported on Mesoporous Silica Hosts. *Microporous Mesoporous Mater.* **2009**, *122* (February), 160–167.

(50) Jiang, K.; Eitan, A.; Schadler, L. S.; Ajayan, P. M.; Siegel, R. W.; Grobert, N.;

Mayne, M.; Reyes-Reyes, M.; Terrones, H.; Terrones, M. Selective Attachment of Gold Nanoparticles to Nitrogen-Doped Carbon Nanotubes. *Nano Lett.* **2003**, *3*, 275–277.

(51) Boyen, H. G.; Herzog, T.; Kästle, G.; Weigl, F.; Ziemann, P.; Spatz, J. P.; Möller, M.; Wahrenberg, R.; Garnier, M. G.; Oelhafen, P. X-Ray Photoelectron Spectroscopy Study on Gold Nanoparticles Supported on Diamond. *Phys. Rev. B* **2002**, *65*, 75412.

(52) Laursen, A. B.; Højholt, K. T.; Lundegaard, L. F.; Simonsen, S. B.; Helveg, S.; Schüth, F.; Paul, M.; Grunwaldt, J. D.; Kegnœs, S.; Christensen, C. H.; Egeblad, K. Substrate Size-Selective Catalysis with Zeolite-Encapsulated Gold Nanoparticles. *Angew. Chemie - Int. Ed.* **2010**, *49*, 3504–3507.

(53) Lukach, A.; Therien-Aubin, H.; Querejeta-Fernandez, A.; Pitch, N.; Chauve, G.; Methot, M.; Bouchard, J.; Kumacheva, E. Coassembly of Gold Nanoparticles and Cellulose Nanocrystals in Composite Films. *Langmuir* **2015**, *31*, 5033–5041.

(54) Schlesinger, M.; Giese, M.; Blusch, L. K.; Hamad, W. Y.; MacLachlan, M. J. Chiral Nematic Cellulose-Gold Nanoparticle Composites from Mesoporous Photonic Cellulose. *Chem. Commun. (Camb).* **2015**, *51*, 530–533.

(55) Liu, Q.; Campbell, M. G.; Evans, J. S.; Smalyukh, I. I. Orientationally Ordered Colloidal Co-Dispersions of Gold Nanorods and Cellulose Nanocrystals. *Adv. Mater.* **2014**, *26*, 7178–7184.

(56) Mahmoud, K. A.; Male, K. B.; Hrapovic, S.; Luong, J. H. T. Cellulose Nanocrystal/gold Nanoparticle Composite as a Matrix for Enzyme Immobilization. *ACS Appl. Mater. Interfaces* **2009**, *1* (7), 1383–1386.

(57) Mahmoud, K. A.; Lam, E.; Hrapovic, S.; Luong, J. H. T. Preparation of Well-Dispersed Gold/magnetite Nanoparticles Embedded on Cellulose Nanocrystals for Efficient Immobilization of Papain Enzyme. *ACS Appl. Mater. Interfaces* **2013**, *5*, 4978–4985.

(58) Wu, X.; Lu, C.; Zhou, Z.; Yuan, G.; Xiong, R.; Zhang, X. Green Synthesis and Formation Mechanism of Cellulose Nanocrystal-Supported Gold Nanoparticles with Enhanced Catalytic Performance. *Environ. Sci. Nano* **2014**, *1*, 71–79.

(59) Lam, E.; Hrapovic, S.; Majid, E.; Chong, J. H.; Luong, J. H. T. Catalysis Using Gold Nanoparticles Decorated on Nanocrystalline Cellulose. *Nanoscale* **2012**, *4* (February 2016), 997–1002.

(60) Wu, X.; Lu, C.; Zhou, Z.; Yuan, G.; Xiong, R.; Zhang, X. Green Synthesis and Formation Mechanism of Cellulose Nanocrystal-Supported Gold Nanoparticles with Enhanced Catalytic Performance. *Environ. Sci. Nano* **2014**, *1*, 71.

(61) Chen, L.; Cao, W.; Quinlan, P. J.; Berry, R. M.; Tam, K. C. Sustainable Catalysts from Gold-Loaded Polyamidoamine Dendrimer-Cellulose Nanocrystals. *ACS Sustain. Chem. Eng.* **2015**, *3*, 978–985.

(62) Corma, A.; Garcia, H. Supported Gold Nanoparticles as Catalysts for Organic Reactions. *Chem. Soc. Rev.* **2008**, *37*, 2096–2126.

(63) Mikami, Y.; Dhakshinamoorthy, A.; Alvaro, M.; García, H. Catalytic Activity of Unsupported Gold Nanoparticles. *Catal. Sci. Technol.* **2013**, *3*, 58–69.

(64) Vincent, T.; Guibal, E. Chitosan-Supported Palladium Catalyst. 3. Influence of Experimental Parameters on Nitrophenol Degradation. *Langmuir* **2003**, *19* (19), 8475–8483.

(65) Ghosh, S. K.; Mandal, M.; Kundu, S.; Nath, S.; Pal, T. Bimetallic Pt-Ni Nanoparticles Can Catalyze Reduction of Aromatic Nitro Compounds by Sodium Borohydride in Aqueous Solution. *Appl. Catal. A Gen.* **2004**, *268*, 61–66.

(66) Mei, Y.; Lu, Y.; Polzer, F.; Ballauff, M.; Drechsler, M. Catalytic Activity of Palladium Nanoparticles Encapsulated in Spherical Poly Electrolyte Brushes and Core-Shell Microgels. *Chem. Mater.* **2007**, *19* (14), 1062–1069.

(67) Pradhan, N.; Pal, A.; Pal, T. Silver Nanoparticle Catalyzed Reduction of Aromatic Nitro Compounds. *Colloids Surfaces A Physicochem. Eng. Asp.* **2002**, *196*, 247–257.

(68) Maolin Li, A.; Chen, G. Revisiting Catalytic Model Reaction P-nitrophenol/NaBH4 Using Metallic Nanoparticles Coated on Polymeric Spheres. *Nanoscale* **2013**, *5*, 11919–11927.

(69) Wunder, S.; Lu, Y.; Albrecht, M.; Ballauff, M. Catalytic Activity of Faceted Gold Nanoparticles Studied by a Model Reaction: Evidence for Substrate-Induced Surface Restructuring. *ACS Catal.* **2011**, *1*, 908–916.

(70) Gu, S.; Wunder, S.; Lu, Y.; Ballauff, M.; Fenger, R.; Rademann, K.; Jaquet, B.; Zaccone, A. Kinetic Analysis of the Catalytic Reduction of 4-Nitrophenol by Metallic Nanoparticles. *J. Phys. Chem. C* **2014**, *118*, 18618–18625.

(71) Layek, K.; Kantam, M. L.; Shirai, M.; Nishio-Hamane, D.; Sasaki, T.; Maheswaran, H. Gold Nanoparticles Stabilized on Nanocrystalline Magnesium Oxide as an Active Catalyst for Reduction of Nitroarenes in Aqueous Medium at Room Temperature. *Green Chem.* **2012**, *14*, 3164.

(72) Kumar, S. S.; Kumar, C. S.; Mathiyarasu, J.; Phani, K. L. Stabilized Gold Nanoparticles by Reduction Using 3,4- Ethylenedioxythiophene-Polystyrenesulfonate in Aqueous Solutions: Nanocomposite Formation, Stability, and Application in Catalysis. *Langmuir* **2007**, *23* (4), 3401–3408.

(73) Gao, Y.; Ding, X.; Zheng, Z.; Cheng, X.; Peng, Y. Template-Free Method to Prepare Polymer Nanocapsules Embedded with Noble Metal Nanoparticles. *Chem. Commun.* **2007**, 3720–3722.

(74) Lee, J.; Park, J. C.; Song, H. A Nanoreactor Framework of a Au@SiO_2 Yolk/shell Structure for Catalytic Reduction of P-Nitrophenol. *Adv. Mater.* **2008**, *20*, 1523–1528.

(75) Zeng, J.; Zhang, Q.; Chen, J.; Xia, Y. A Comparison Study of the Catalytic Properties of Au-Based Nanocages, Nanoboxes, and Nanoparticles. *Nano Lett.* **2010**, *10*, 30–35.

(76) Li, J.; Liu, C.; Liu, Y. Au/graphene Hydrogel: Synthesis, Characterization and Its Use for Catalytic Reduction of 4-Nitrophenol. *J. Mater. Chem.* **2012**, *22*, 8426–8430.

(77) Hu, J.; Dong, Y. L.; Chen, X. J.; Zhang, H. J.; Zheng, J. M.; Wang, Q.; Chen, X. G. A Highly Efficient Catalyst: In Situ Growth of Au Nanoparticles on Graphene Oxide-Fe_3O_4 Nanocomposite Support. *Chem. Eng. J.* **2014**, *236*, 1–8.

(78) Kuroda, K.; Ishida, T.; Haruta, M. Reduction of 4-Nitrophenol to 4-Aminophenol over Au Nanoparticles Deposited on PMMA. *J. Mol. Catal. A Chem.* **2009**, *298*, 7–11.

(79) Liu, Y.; Xu, L.; Liu, X.; Cao, M. Hybrids of Gold Nanoparticles with Core-Shell Hyperbranched Polymers: Synthesis, Characterization, and Their High Catalytic

Activity for Reduction of 4-Nitrophenol. *Catalysts* **2015**, *6* (1), 3.

(80) Chang, Y. C.; Chen, D. H. Catalytic Reduction of 4-Nitrophenol by Magnetically Recoverable Au Nanocatalyst. *J. Hazard. Mater.* **2009**, *165*, 664–669.

(81) Tomalia, D. A.; Naylor, A. M.; Goddard III, W. A. Starburst Dendrimers: Control of Size, Shape, Surface Chemistry, Topology and Flexibility in the Conversion of Atoms to Macroscopic Materials. *Angew. Chemie* **1990**, *102*, 119–157.

(82) Hua, C.; Peng, S. M.; Dong, C. M. Synthesis and Characterization of Linear-Dendron-like Poly(ε-Caprolactone)-B-Poly(ethylene Oxide) Copolymers via the Combination of Ring-Opening Polymerization and Click Chemistry. *Macromolecules* **2008**, *41*, 6686–6695.

(83) Sadeghifar, H.; Filpponen, I.; Clarke, S. P.; Brougham, D. F.; Argyropoulos, D. S. Production of Cellulose Nanocrystals Using Hydrobromic Acid and Click Reactions on Their Surface. *J. Mater. Sci.* **2011**, *46*, 7344–7355.

(84) Emil T. Kaiser, Robert L. Colescott, Charles D. Bossinger, P. I. C. Color Test for Detection of Free Terminal Amino Groups in the Solid-Phase Synthesis of Peptides. *Anal. Biochem.* **1970**, *34*, 595–598.

(85) Vogt, G.; Argos, P. Protein Thermal Stability: Hydrogen Bonds or Internal Packing? *Fold. Des.* **1997**, *2*, S40–S46.

(86) Querol, E.; Perez-Pons, J. A.; Mozo-Villarias, A. Analysis of Protein Conformational Characteristics Related to Thermostability. *Protein Eng.* **1996**, *9* (3), 265–271.

(87) Huang, X.; El-Sayed, M. A. Gold Nanoparticles: Optical Properties and Implementations in Cancer Diagnosis and Photothermal Therapy. *J. Adv. Res.* **2010**, *1* (February), 13–28.

(88) Kreibig, U.; Fragstein, C. V. The Limitation of Electron Mean Free Path in Small Silver Particles. *Z Phys.* **1969**, *224*, 307–323.

(89) Kreibig, U. Kramers Kronig Analysis of the Optical Properties of Small Silver Particles. *Z. Phys.* **1970**, *234*, 307–318.

(90) Shen, M.; Shi, X. Dendrimer-Based Organic/inorganic Hybrid Nanoparticles in Biomedical Applications. *Nanoscale* **2010**, *2*, 1596–1610.

Chapter 4: Nanocrystalline cellulose-fullerene (C_{60}) conjugates for photodynamic therapy (PDT)

4.1. Introduction

The therapeutic properties of light have been known for thousands of years. Ancient Egyptian, Indian and Chinese civilizations used light to treat various diseases, including psoriasis, rickets, or vitiligo.[1] At the end of the nineteenth century, Niels Finsen found that red-light exposure avoided the formation and discharge of smallpox pustules and could be used to treat this disease and he also used ultraviolet light from the sun to treat cutaneous tuberculosis. These findings granted Finsen the Nobel Prize in 1903. More than 100 years ago, researchers also observed that a combination of light and certain chemicals could induce cell death.[2] Experiments to test combinations of reagents and light led to modern photodynamic therapy (PDT).[3]

4.1.1. Photodynamic therapy (PDT)

PDT combines two individually non-toxic components that are combined to induce cellular and tissue effects in an oxygen-dependent manner.[4] The first component of PDT is a photosensitizer (PS): a light-absorptive molecule that localizes to a target cell and/or tissue. The second component involves the administration of light of a specific wavelength that activates the photosensitizer.[5] Most PS have two electrons with opposite spins located in an energetically lower energy orbital, the so-called highest occupied molecular orbital (HOMO), in their ground state. Absorption of a light photon induces an excited singlet state of the PS by promoting one electron with unchanged spin to a higher energy obital, called the lowest unoccupied molecular obital (LUMO). This excited singlet has a short lifetime and emits excess energy as fluorescence, heat, or undergoing an intersystem crossing (ISC). This ISC takes place by inverting spin of one electron to form a relatively long-lived triplet state (Figure 1).

The PS excited triplet can follow different processes.[6] One possibility is simply decay to the ground state. Alternatively, it can survive long enough to gain or donate and

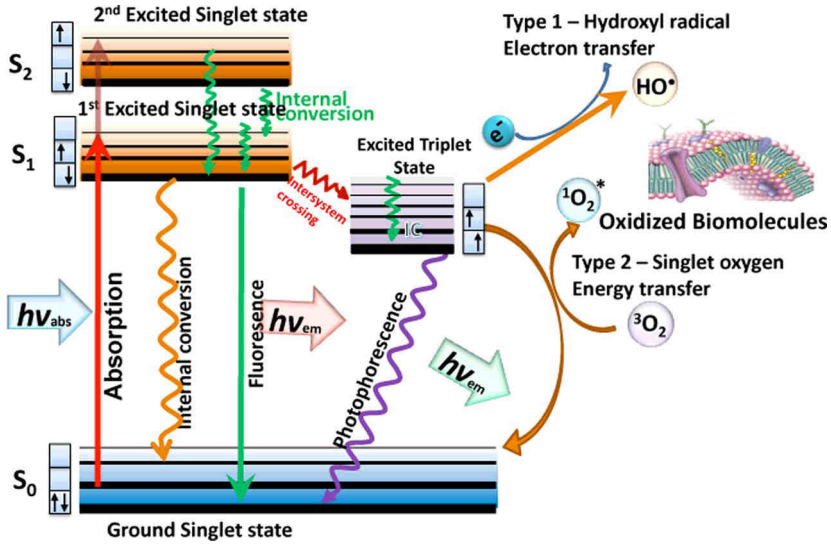

Figure 1. Jablonski's energy level diagram for photodynamic therapy.[7]

electron from neighboring molecules forming a radical. Subsequent electron donation from the PS radical anion to oxygen can produce a variety of oxygen radical species, namely superoxide, hydroxyl radicals and hydroperoxides. This reaction is known as a Type I process. A Type II process occurs when the triplet state transfers its energy to molecular oxygen O_2 (ground triplet state) and produce excited state singlet oxygen ($^1O_2$). Singlet oxygen, superoxide, hydroxyl radicals and hydroxyperoxides are commonly referred to as reactive oxygen species (ROS), which are responsible for cytotoxicity in PDT (Figure 1). Therefore, the efficient ISC process giving a high quantum yield of triplet state is essential for the generation of ROS. However, no clear relationship has been established between the efficiency of ISC and the chemical structure.

PDT is known to provoke tumor destruction through three different mechanisms.[8] In the first case, the ROS that are generated by PDT can kill tumour cells by damaging multiple cellular organelles and processes, which can ultimately disrupt normal physiology.[9] For example, ROS are involved in lipid peroxidation, a process that has been linked to cell death through effects on cellular phospholipids (major cell membrane components) through activation of sphingomyelinase and release of ceramide, which activates apoptosis.[10] ROS can also cause direct injury to proteins, and nucleic acids, leading to cell death. Protein oxidation and nitrosylation (carbonyl, nitration, and nitrotyrosine formation) can impair a wide variety of enzymatic processes and growth factors that can result in marked cellular dysfunction, whereas nucleic acid oxidation has been linked with physiologic and premature aging as well as DNA strand breaks, leading to necrosis and/or apoptosis.[11] PDT also damages the tumour-associated vasculature, leading to tumour infarction.[12] Finally, PDT can activate an immune response against tumour cells.[13] These three mechanisms can also influence each other. The relative importance of every individual process in the overall tumour response has not been clarified yet, but a combination of all these components is necessary for long-term tumour control.

These reactions occur in the immediate surroundings of the light-absorbing photosensitizer. Thus the biological response to the photosensitizer is activated only in the particular areas of tissue that have been exposed to light. Therefore, selectivity can be achieved controlling therapeutic gradient of photosensitizer concentration between tumor and normal tissues and precise delivery of light exposure within the tumor.[14] In general, PDT has several advantages over other more aggressive cancer therapies: PDT shows no long-term side effects when an effective PS is employed; it is a minimally-invasive procedure; treatments can be repeated at the same site if needed; PDT can be less costly than other cancer treatments and irradiation sessions are sufficiently short to allow treatment as an outpatient.[15] However, PDT presents limitations such as non-specific cellular uptake of PS by normal cells and short light penetration depth. Because its action occurs only at areas reachable by the light, the only sites of tumors treated by PDT are the lining of organs or just under the skin. However, recent developments in fiber-optic systems have spread the applicability of this technique to any endoscopically accessible tumors, including lung cancer, superficial gastric cancer, and even head and neck cancer.[15,16]

4.1.2. Photosensitizers in PDT

Some required features for a good photosensitizer are the presence of low levels of dark toxicity and large absorption bands in red or near-infrared regions of the spectrum, more precisely, in the so-called optical window (600 – 900 nm) for a better penetration of light (Figure 2). The reason for strong absorption bands is to help minimizing the dose needed to achieve the desired effect. PS should as well have high triplet and singlet oxygen quantum yields.

The most extensively studied photosensitizers so far are porphyrins,[18] which were identified in the mid-nineteenth century. The name "porphyrin" comes from the Greek word *porphyra*, meaning purple, and many pigments or dyes belong to this group of molecules, of which well-known examples are chlorophyll and hemoproteins. These derivatives are based in a tetrapyrrole aromatic nucleus, with a 22 π electron

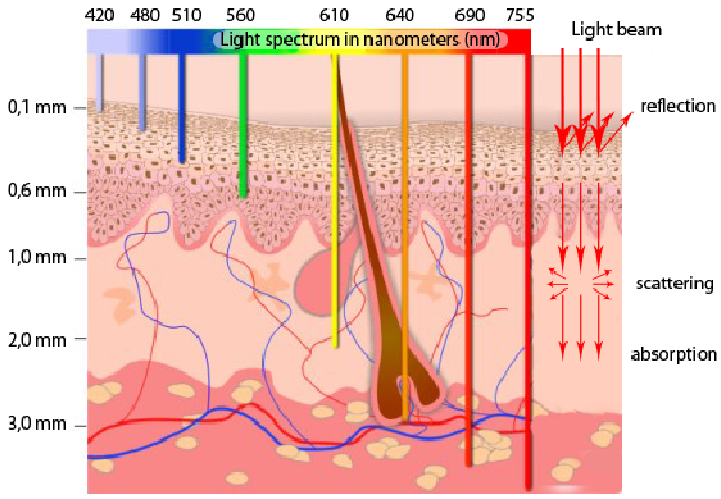

Figure 2. The propagation of light of different wavelengths in the tissues.[17]

system, responsible for their main absorption band at around 400 nm, known as Soret band, and a set of progressively less intense absorption bands as the spectrum goes to red wavelengths, known as the Q-bands. Other synthetic PS based on conjugated pyrrolic rings have been developed, as for example texaphyrins, porphycenes[19] and phthalocyanines.[20] The most accepted porphyrin based PS is probably Photofrin® (a mixture of oligomers formed by ether and ester linkages of up to eight porphyrin units), which currently approved for clinical use in more than 40 countries.[18] Nonetheless, to date there is no perfect PS that meets all the characteristics of an ideal PS.

4.1.3. Fullerene (C_{60}) as photosensitizer

Carbon fullerenes such as C_{60} have been at the center of the recent prosperity in nanoscale science and engineering. C_{60} consists of 60 carbon atoms arranged in 20 hexagons and 12 pentagons that form a perfectly symmetrical cage structure, approximately 1 nm in size. The symmetry and conjugated π-bond system of C_{60} results in a number of unique properties, including high reactivity to nucleophiles and electron affinity.[21]

The reason why fullerenes are seen as potential PDT agents is that they possess some of the characteristics that make them well suited as photosensitizing drug. Production of singlet oxygen by fullerenes is known to occur with quantum yields up to 0.95.[22] In addition, fullerenes are highly stable toward oxidation, a valuable characteristic that makes fullerenes almost immune to photobleaching compared with tetrapyrroles and synthetic dyes.[21]

Unfortunately, the extended π conjugated system, also renders pristine C_{60} highly hydrophobic and therefore insoluble in water and biological media, where it forms nano-aggregates that prevent its efficient photoactivity.[23] This supposes a major limitation for their application as drugs in biomedicine. However, when fullerenes are derivatized by introducing some functional groups to render them more soluble in water and biological media, their biological usefulness is markedly improved.[24] Different hydrophilic groups (Figure 3a), such as amphiphilic or hydrophilic side chains (Figure 3b)[25], or fused ring structures have been covalently attached to the spherical C_{60} core. Grafting of fullerenes onto dendrimers has been also proven to be a successful strategy (Figure 3c and d).[26,27]

Although water-solubility issue has been addressed by the functionalization of fullerene with hydrophilic groups, new problems might arise from this approach such as aggregation and clustering, together with singlet oxygen quantum yield decreasing due to perturbation of the fullerene π-system as a result of functionalization.[28] This latter problem could be mitigated through the formation of complexes between fullerenes and water-soluble hosts. [29,30] β-Cyclodextrin–[60]fullerene complexes can be achieved in a mixed organic solvent system containing DMF and toluene (typically 50–90% DMF, v:v), and subsequently removing the organic solvents and adding distilled water (Figure 3f). Furthermore, C_{60} embbeded in liposomes may be obtained using an exchange reaction between γ-cyclodextrin–[60]fullerene complex and different liposomes by heating at 80 ºC for 1 h (Figure 3f).[31] On the other hand, it has been recently shown that aqueous suspensions of fullerene nanoparticles with

concentrations up to 100 mg/L can be produced by various techniques, such as solvent exchange and prolonged stirring.[32] Finally, fullerenes have been physically embedded into solid matrices such as molecular sieves, zeolites, as well as covalently attached to mesoporous silica materials.[33]

Another important disadvantage is the main optical absorption band of fullerenes in the blue and green regions, whereas the absorption spectra of tetrapyrrole PS other than porphyrins have been designed to have substantial absorption peaks in the red or far-red regions of the spectrum. For PS to be useful in *vivo* it is considered that

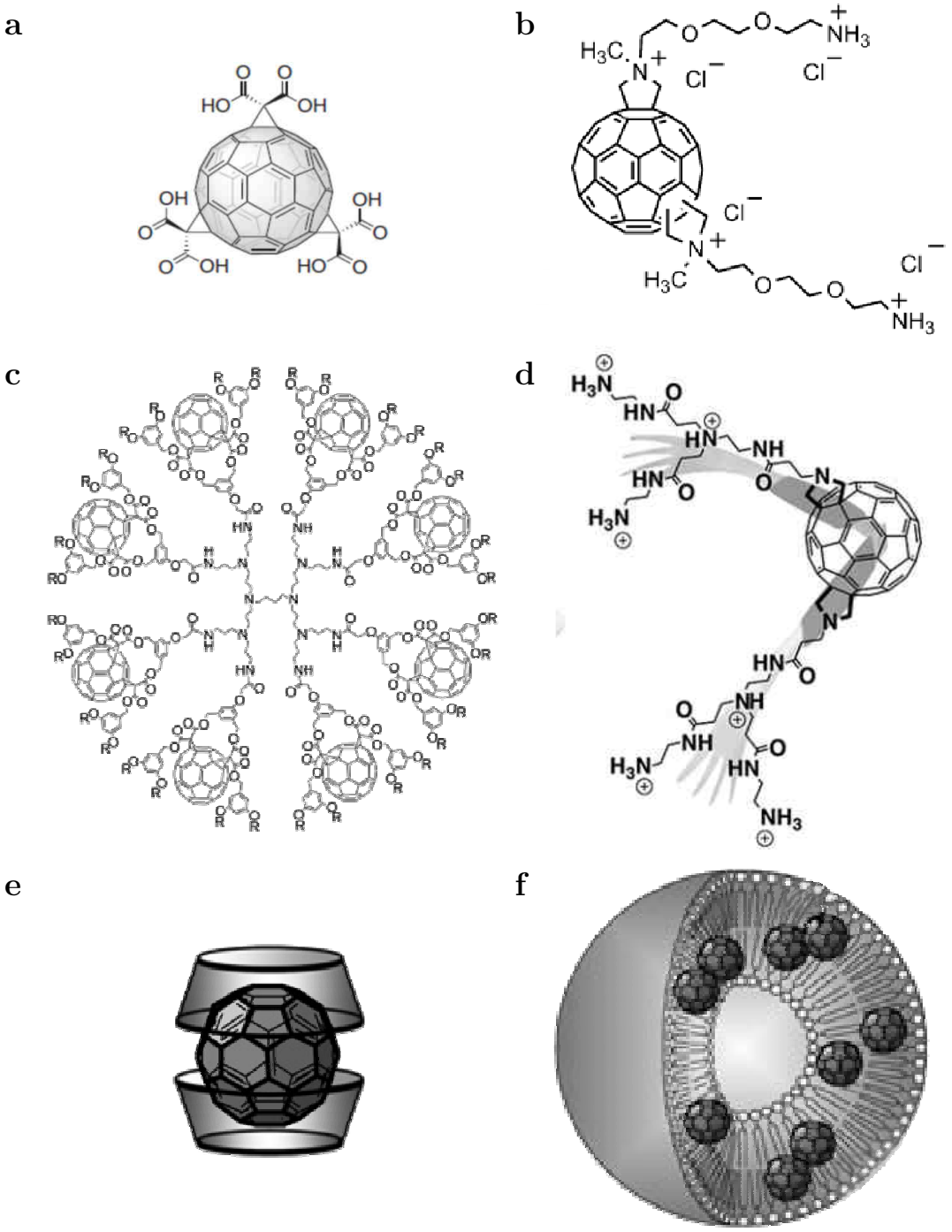

Figure 3. Schematic representation of strategies for solubilizing fullerenes: covalent functionalization with carboxylic groups (a),[34] polar chains (b) dendrimers (c, d),[26,27] complexation with cyclodextrins (e),[35] liposomes (f).[36]

the light used to excite them should be in the red/near-infrared spectral regions where scattering and absorption of light by tissue is minimized. This unfavorable feature of fullerenes may be addressed following different approaches, such as covalent attachment of light-harvesting antennae to fullerenes,[37] optical clearing agents[38] or by applying two-photon excitation where two near-infrared photons are simultaneously delivered to be equivalent to one photon of twice the energy.[39]

4.1.4. *In vitro* PDT with fullerenes (C_{60})

Phototoxicity using fullerenes have been widely studied *in vitro*. The first example of phototoxicity with fullerenes tested *in vitro* dates back to 1993, when Tokuyama *et al.* prepared a series of carboxylic acid fullerene derivatives and investigated their phototoxic response against (human cervical carcinoma) HeLa cells.[40] No toxicity was found in the dark when cells were incubated with the carboxylic acid functionalized C_{60} derivative, whereas cell growth inhibition was observed when cells were irradiated with fluorescent light (6 W) for 1 h every 24 h. When Burlaka *et al.* tested pristine C_{60} in water at a concentration of 10^{-5} M against Ehrlich carcinoma cells or rat thymocytes, finding a decreasing in the number of viable cells of 67 and 58 %, respectively.[41] In another study, the phototoxic effects of two water soluble C_{60} derivatives, a dendritic C_{60} monoadduct and a malonic acid tris-adduct was investigated on Jurkat cells. Cells were irradiated under UVA (400-320nm) or UVB (320-290nm) light, and tris-malonic C_{60} derivative exhibited better phototoxicity despite generating singlet oxygen in lower yield.[42] Mroz *et al.* compared the photodynamic activity of six functionalized fullerenes with one, two or three hydrophilic or cationic groups on three mouse cancer cell lines. They found that effectiveness was inversely proportional to the degree of substitution and a mono-pyrrolidinium C_{60} derivative induced apoptosis within 4/6 h after illumination.[43] More recently, Li *et al.* demonstrated C_{60} amino acid nanoparticles to be the most active photosensitizer against human liver cancer cells and induced cancer cells apoptosis after illumination, while these derivatives exhibited no significant cytotoxicity in the dark. Furthermore, when a ROS probe was added diffuse intracellular fluorescence was generated, suggesting phototoxicity was related with the generation of intracellular ROS.[44] In a different work, a water-soluble fullerene–glycine derivative was prepared, which self-assembled into nanospheres. This derivative showed cytotoxicity against HeLa cells upon irradiation of light in a dose dependent manner, whereas no cell inhibition was observed in total darkness for a fullerene–glycine derivative concentration >100 μg/mL.[45]

In some other cases, drug delivery vehicles have been employed with C_{60}. Ikeda *et al.* work, incorporated C_{60} into a lipid-membrane as drug carrier. Intracellular uptake in HeLa cells was found to induce cell death under visible light irradiation at high efficiency. Illumination with 136 J/cm^2 350–500 nm light killed 85% of cells in the case of cationic liposomes and apoptosis was demonstrated.[31] In a similar approach, Akiyama *et al.* solubilized unmodified C_{60} using various types of polyethylene glycol (PEG)-based block copolymer micelles. These complexes were studied in HeLa cancer cells, where the cationic block copolymer micelles delivered C_{60} into the cell and phototoxicity was observed under photoirradiation.[46]

4.1.5. *In vivo* PDT with fullerenes (C_{60})

In 1997, Tabata *et al.* were the first to report PDT *in vivo* with fullerenes (C_{60})[47] They modified C_{60} with polyethylene glycol (PEG), not only to make it soluble in water, but also to enlarge its molecular size. When injected intravenously in mice carrying tumor masses, the C_{60}-PEG conjugate exhibited higher accumulation and more prolonged retention in the tumor than in normal tissue. The conjugate was excreted without being accumulated in any specific organ. Moreover, the antitumor effect increased with increasing irradiation power and dose, and cures were obtained at a dose of 424 µg/kg at a fluence of 107 J/cm^2.

In another study, Otake *et al.* prepared a set of C_{60}–glucose conjugates to render C_{60} tumor specific, since it is known that glucose receptors are overexpressed in tumor cells. The cytotoxicity was studied in several cancer lines cultured with C_{60}-glucose conjugates and subsequently irradiated with UVA_1 light (340 to 400 nm). In addition, tests *in vivo* were carried out on melanoma bearing mice. PDT with the glycoconjugated fullerene exhibited no significant cytotoxicity against normal fibroblasts, indicating that PDT with these compounds targeted cancer cells.[48] In a more recent study, Li *et al.* tested 5-aminolevulinic acid-(5-ALA) loaded fullerene (C_{60}) nanoparticles (C_{60}-5-ALA) on tumor-bearing mice models. After intravenous injection or C_{60}-5-ALA, a significant accumulation in tumor and excellent PDT efficacy were observed. C_{60}-5-ALA at a dose of 30 mg/kg resulted in a significant delay of tumor growth after irradiation with 630 nm laser.[49] Shi *et al.* developed a multi-functional system in which they combined C_{60} as PS for PDT with magnetic iron oxide nanoparticles (IONPs) for radiofrequency thermal therapy (RTT).[50] An enhancement of the PDT effect was observed due to the synergestic effect of the radiofrequency thermal therapy. *In vivo*, PDT and RTT treatments induced 62% and 37% apoptosis, respectively. Combined RTT and PDT increased this rate up to 96%.

4.1.6. Fullerenes (C_{60}) uptake and biodistribution

It is considered that for any PS to produce cell killing, it is crucial that it is taken up inside the cell, as the production of ROS outside of it would not be in enough concentration for this purpose, unless it would be produced in extremely large amounts.[15] Despite fullerenes have been widely used for PDT, little information can be found about their biodistribution and interaction with different intracellular organelles. The main reason for this fact relays in their lack of fluorescence, in contrast to the vast majority of other PS. This fact hampers the examination of the intracellular uptake and subcellular localization of fullerenes. However, some other strategies have been proposed for the tracking of C_{60} into cells. Scrivens *et al.* were the first to demonstrate its uptake by human keratinocytes in tissue culture by preparing a radiolabeled fullerene.[51] In serum-free medium they found a time and concentration dependent uptake. Another group used indirect immunofluorescence staining with antibodies that recognize fullerenes and other organelle probes to show that a dicarboxylic acid derivative was localized in mitochondria and other intracellular membranes.[52] Lucafò *et al.* studied the cytotoxicity and mechanism of cellular uptake of a fluorescein bearing C_{60} derivative on human mammary carcinoma cells.[53] They found that this compound was unspecifically internalized within 12 h

after treatment and distributed throughout the cytoplasm, avoiding nucleus and secretory granules. A recent paper described the use of energy-filtered transmission electron microscopy and electron tomography to visualize the cellular uptake of pristine C_{60} nanoclusters. When human monocyte-derived macrophages were examined, C_{60} was found in the plasma membrane, lysosomes and nucleus.[54] Nevertheless, it is still considerably challenging to collect good biodistribution data of fullerenes.

4.1.7. Other photodynamic applications of fullerenes (C_{60})

Apart from cancer treatment, ROS can also be applied in antimicrobial therapy, an emerging alternative strategy for destroying microorganisms. Singlet oxygen is also involved in wastewater treatment or the production of fine chemicals.[55]

In particular, fullerenes have been used to inactivate enveloped viruses,[56] bacteria and fungi.[57] Tegos *et al.* demonstrated that the soluble functionalized fullerenes, were efficient broad spectrum antimicrobial PS, and could mediate photodynamic inactivation of various classes of microbial cells.[58] Spesia *et al.* reported a fulleropyrrolidinium iodide that induced photodynamic inactivation of Escherichia coli (E. coli) *in vitro*.[59] Lee *et al.* also showed that C_{60} derivatives efficiently inactivated E. coli and MS-2 bacteriophage (i.e. icosahedral, positive-sense single-stranded RNA virus).[60] In another work, Yin *et al.* used three highly water-soluble decacationic [60]fullerenyl malonate monoadducts (LC14, LC15 and LC16) to generate singlet oxygen after excitation by UVA or by white light and induce killing of pathogenic microbial cells (Gram-positive bacterium, methicillin-resistant Staphylococcus aureus (MRSA), Gram-negative bacterium Escherichia coli, and fungal yeast *Candida albicans*). LC15 was the most powerful broad spectrum antimicrobial photosensitizer followed by LC16, and LC14 was least powerful. Killing efficiency depended on both fullerene monoadduct concentration and light fluence.[61]

4.2. Aim of the work

As already mentioned in the previous section, the outstanding performance of C_{60} as singlet oxygen PS is completely blocked in aqueous media due to its intrinsic hydrophobicity, hindering its application in PDT. Other works have successfully stabilized other hydrophobic PS molecules by covalently linking to NCC.[62,63] Here we draw inspiration from them and set out to stabilize C_{60} with a similar strategy.

Therefore, we could anticipate that the hydrophilic nature of oxidized nanocrystalline cellulose (see Chapter 2), together with its biocompatibility make it a convenient alternative to avoid aggregation of C_{60} in water. In this Chapter, the covalent linking of two fullerene derivatives onto ox-NCC cellulose will be described. The functionalization will be complemented with the simultaneous introduction of C_{60} and fluorophore moieties onto ox-NCC, in a one-step reaction. In this way, the presence of the fluorescent label will serve to further study the uptake of the PS into cells.

4.3. Results and discussion

4.3.1. Synthesis and characterization of NCC-C_{60} derivatives

Nanocrystalline cellulose (NCC) was produced by hydrolysis of microcrystalline cellulose and subsequently oxidized as already described in Chapter 2.The oxidized nanocellulose used here corresponds to ox-NCC_3, and will henceforth be referred to as ox-NCC. The extent of carboxylic groups on ox-NCC was quantified by conductimetry resulting in a degree of oxidation (DO) of 0.15 corresponding to 0.95 mmoles -COOH/g of ox-NCC (see section 2.3.3).

Two fullerene derivatives, carrying an ending amino group, were prepared, one with a long chain (LC_C_{60}) and one with a short chain (SC_C_{60}), as shown in Figure 4. These derivatives were synthesized according to a procedure already reported in our group[64] whereas a fluorescein isothiocyanate (FITC) derivative with the same long chain (LC_FITC) was obtained using the procedure reported by Kaminati *et al* (Figure 4).[65]

The coupling was performed using the standard two-step carbodiimide coupling protocol depicted in Figure 4. The active ester of ox-NCC was produced with *N*-ethyl-*N'*-(3-dimethylaminopropyl) carbodiimide hydrochloride and *N*-hydroxysuccinimide in a 2-(*N*-morpholino)ethanesulfonic acid buffer solution at pH 5.7. Then, the amino-fullerene derivatives (LC_C_{60} or SC_C_{60}, as ammonium salt with triluoroacetate counter-anion, or the mixture (1:1, LC_C_{60}: LC_FITC) was dissolved in a water:DMF (1:1) solution, and added to the reaction dispersion. After stirring for three days at room temperature, the NCC-fullerene adduct was recovered by filtration, extensively washed with toluene:MeOH (9:1 v/v) to remove the amino-fullerene derivatives, the fluorescent starting material and coupling reagents and then with water (to remove salts). NCC-LC_C_{60}, NCC-SC_C_{60} and NCC-LC_C_{60}_FITC adducts were isolated in 86%, 72% and 78% yield, respectively.

4.3.2. Characterizations

FT-IR spectroscopy

The presence of C_{60} moieties on NCC materials was confirmed by FT-IR spectroscopy. In first place, a sharp signal around 525 cm^{-1} in the NCC-LC_C_{60}, NCC-SC_C_{60} and NCC-LC_C_{60}_FITC spectra could be ascribed to the C_{60} subunit (Figure 5).

In addition, to further confirm the covalent nature of the bonding between NCC and C_{60}, the region between 1400-1800 cm^{-1} of the spectra was analyzed in more detail (Figure 6). As expected, the carbonyl stretching of the carboxylic groups in ox-NCC was missing in NCC-LC_C_{60}, NCC-SC_C_{60} and NCC-LC_C_{60}_FITC spectra due to the formation of the amide bond with the amino-fullerene derivative. For the same reason, the ν(C=O) stretching of the trifluoroacetate counter anion (around 1681 cm^{-1} for LC_C_{60} and 1676 cm^{-1} for SC_C_{60}) was not observed in NCC-LC_C_{60}, **NCC-**SC_C_{60} and NCC-LC_C_{60}_FITC spectra, thus confirming the

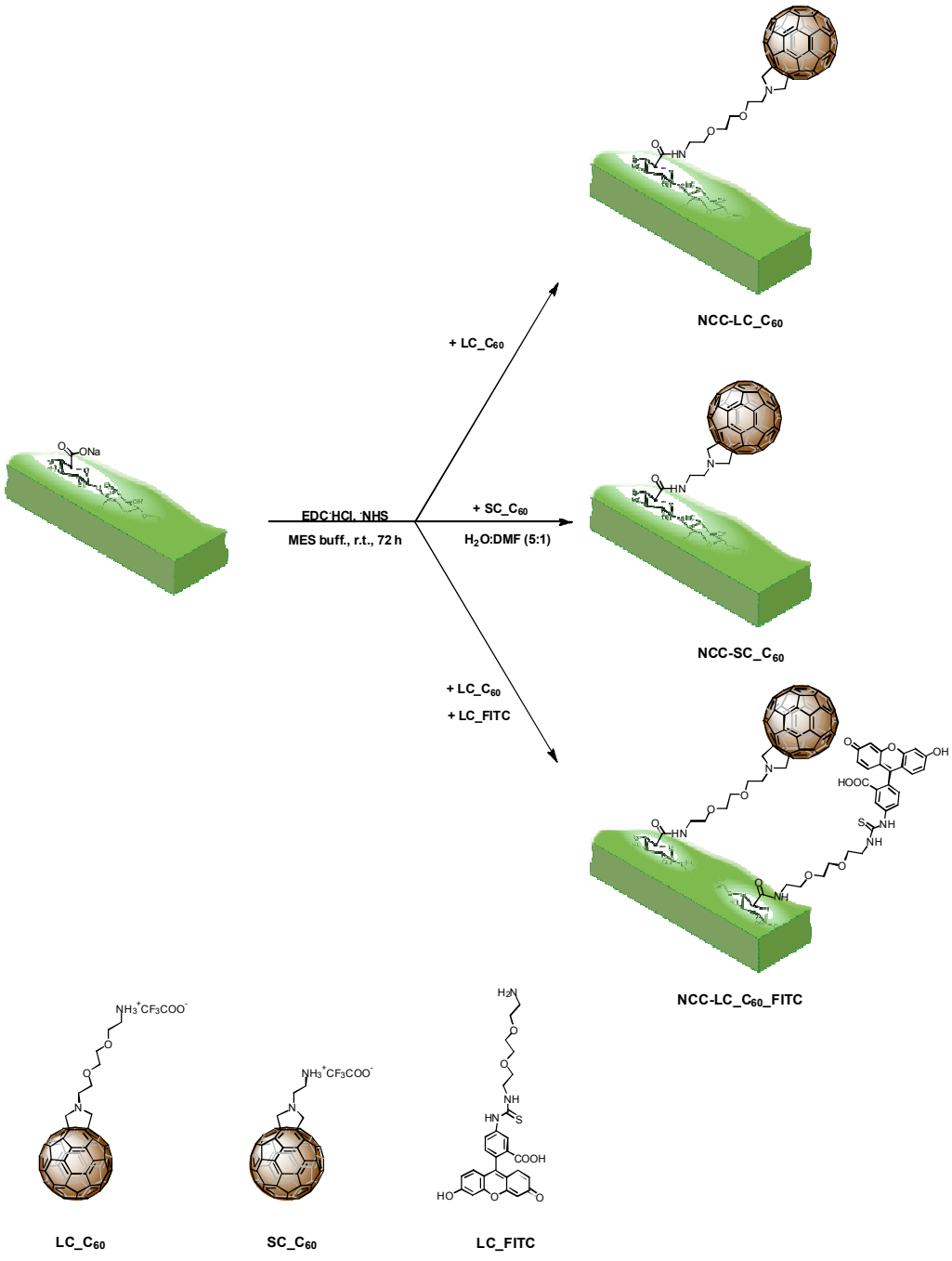

Figure 4. Schematic representation of NCC-LC_C_{60}, NCC-SC_C_{60} and NCC-LC_C_{60}-FITC syntheses.

effectiveness of the washing steps to remove the starting materials. The ν(C=O) stretching for NCC-LC-C_{60}, NCC-SC_C_{60} and NCC-LC_C_{60}_FITC, expected in the range 1740-1630 cm^{-1} (the so-called amide I stretching), could not be assigned unambiguously due to the overlapping with the bending signal of water tightly absorbed to cellulose which appears around 1640 cm^{-1}. On the other hand, the amide II signal, expected in the 1630-1510 cm^{-1} range was observed around 1600 cm^{-1} but it appeared as a shoulder rather than a sharp signal since the contribution from the cellulose inside the nanocrystals was dominant.

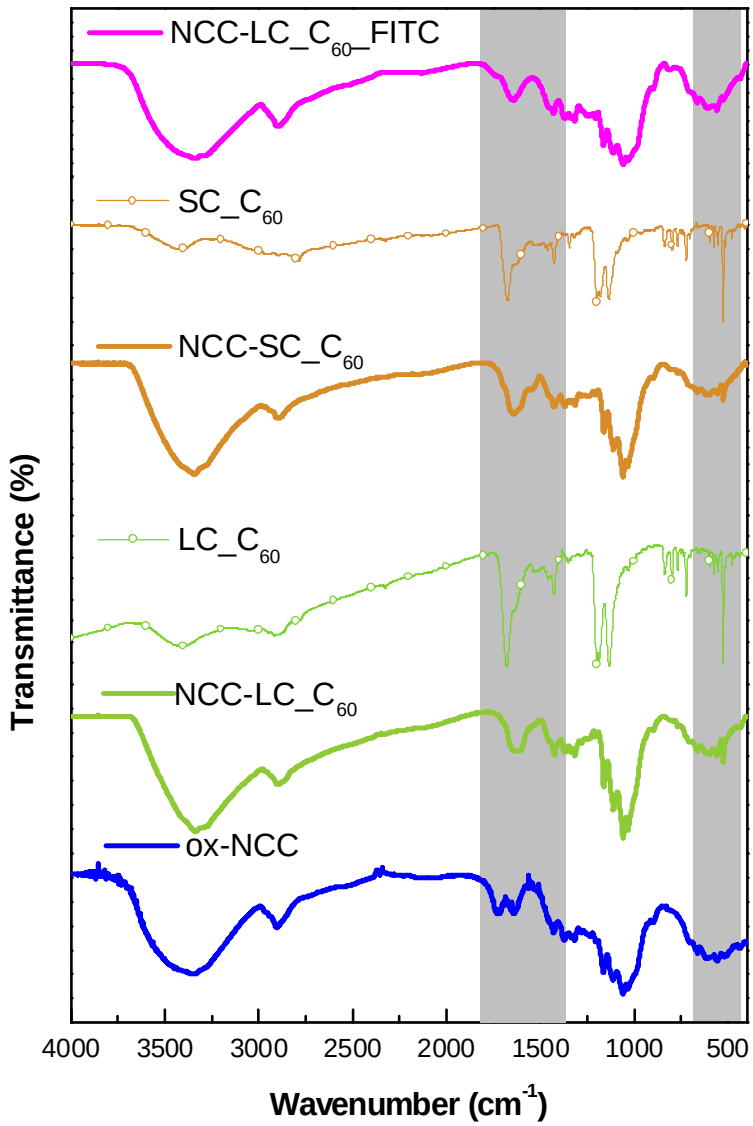

Figure 5. FT-IR spectra of ox-NCC, NCC-LC_C_{60}, LC_C_{60}, NCC-SC_C_{60}, SC_C_{60} and NCC-LC_C_{60}_FITC (KBr pellets).

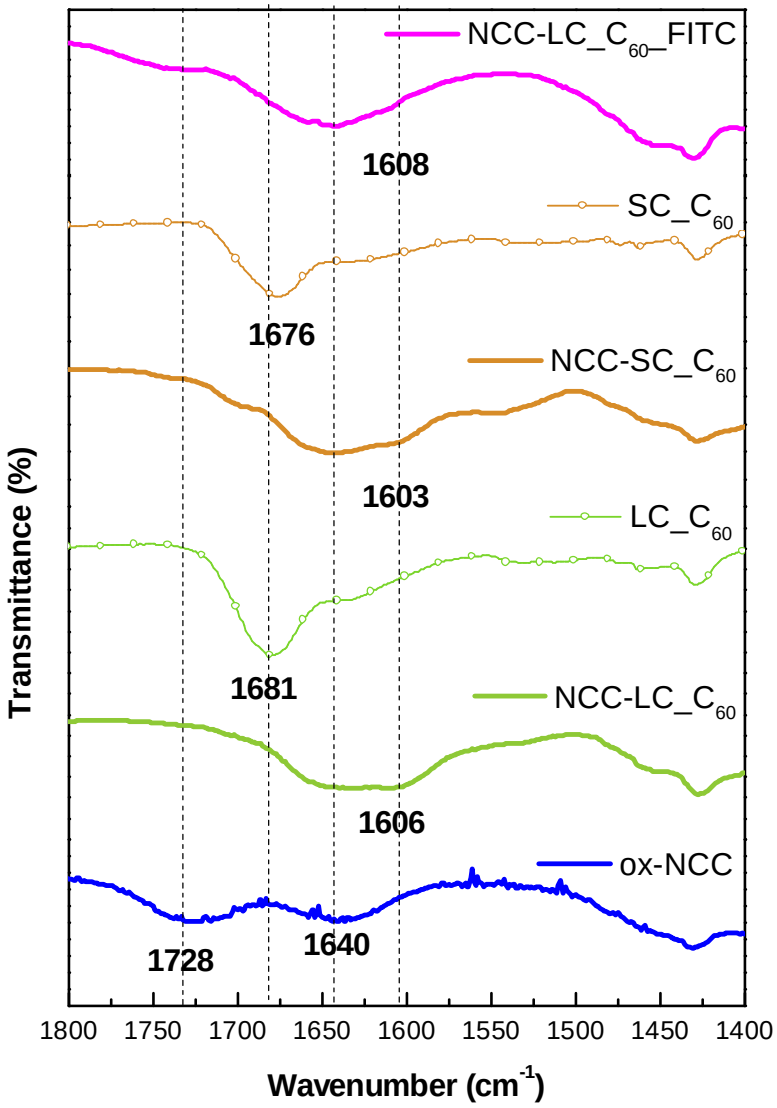

Figure 6. FT-IR ν (C=O) stretching spectral region for ox-NCC, NCC-LC_C_{60}, LC_C_{60}, NCC-SC_C_{60}, SC_C_{60} and NCC-LC_C_{60}_FITC.

Raman spectroscopy

In addition, we decided to further confirm the presence of C_{60} moieties on the samples by Raman spectroscopy since fullerenes are known to produce very intense and fingerprint signals.[66] Figure 7 reports the Raman spectra for ox-NCC, NCC-LC_C_{60} and NCC-SC_C_{60} acquired in air at room temperature with a micro Raman-spectrometer equipped with a laser source at 532 nm. Under the same conditions, Raman spectrum of NCC-LC-C_{60}_FITC was not obtained due to the presence of the FITC unit since fluorescence causes interference with Stokes bands.[67]

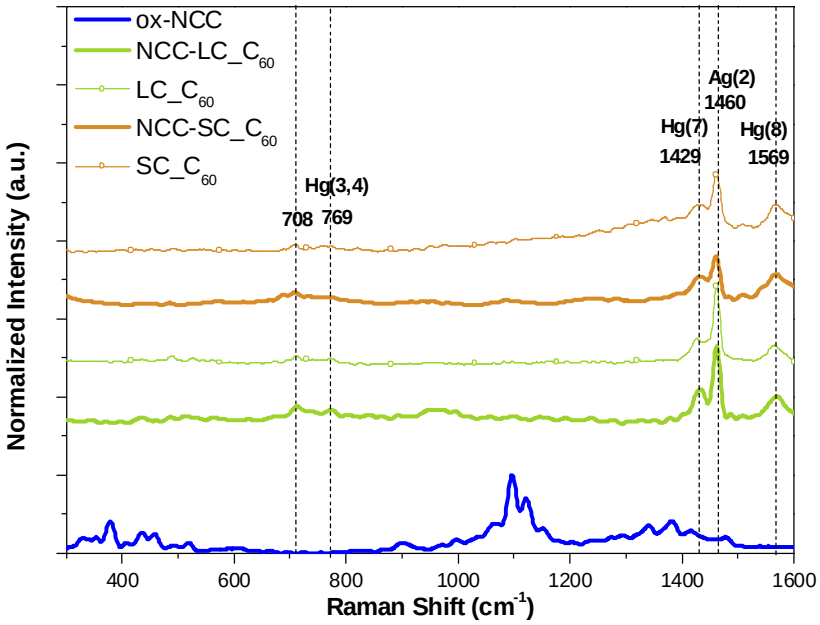

Figure 7. Raman spectra of ox-NCC, NCC-LC_C_{60}, LC-C_{60}, NCC-SC_C_{60} and SC_C_{60} at 532 nm irradiation.

The most intense signal of both NCC-fullerene derivatives (NCC-LC_C_{60} and NCC-SC_C_{60}) was at 1460 cm^{-1}, which corresponds to the so called pentagonal pinch mode (Ag(2)). Additional weaker lines, that together with the previous one constitute a finger print for C_{60}, were observed at 708 cm^{-1} (Hg(3)), 763 cm^{-1} (Hg(4)), 1429 cm^{-1} (Hg(7)), and 1569 cm^{-1} (Hg(8)). It should be pointed out that, despite it was possible to record a Raman spectrum for ox-NCC with a 532 nm laser irradiation source, the intensity of the signals were by far lower than those of fullerene derivatives. Therefore, in the Raman spectra of NCC-LC_C_{60} and NCC-SC_C_{60}, the features of the nanocellulose counterpart did not produce diagnostic indications.

X-ray photoelectron spectroscopy (XPS).

To further prove the grafting of fullerene moiety on nanocellulose surface and provide information about the superficial chemical composition we carried out an X-ray photoelectron spectroscopy (XPS) study. The survey spectra (Figure 8) revealed that the carbon (C1s signal around 285 eV) and the oxygen (O1s signal at 533 eV) were the predominant elements, as expected for carbohydrate compounds. As previously discussed in Chapter 2, ox-NCC samples contain Na from the carboxylate groups. After the coupling, Na was not found in any case for NCC-LC_C_{60}, NCC-SC_C_{60} and NCC-LC_C_{60}_FITC, evidencing that carboxylic groups on ox-NCC had underwent a reaction or at least a change of counterion during the synthesis. In addition, the presence of the nitrogen signal (N1s around 400 eV) for all NCC-fullerene derivatives corroborated the FTIR and Raman data thus confirming the presence of fullerene moieties on ox-NCC.

In order to ascertain the formation of the amide bond and so the covalent attachment of C_{60} and FITC moieties on ox-NCC, the deconvolution of N1s peaks for NCC-LC_C_{60}, NCC-SC_C_{60} and NCC-LC_C_{60}-FITC reported in Figure 9 indicated

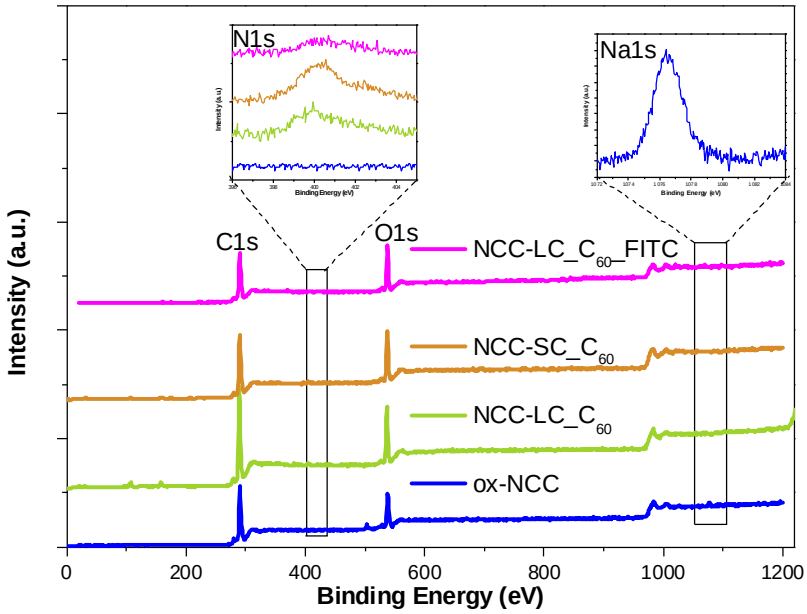

Figure 8. XPS survey spectra of ox-NCC, NCC-LC_C_{60}, NCC-SC_C_{60} and NCC-LC_C_{60}_FITC.

the presence of two components: the main component at 400 eV, arising by the amide nitrogen (C-N bond), and the component at higher binding energy (402.6 eV) due to pyrrolidine ring in the C_{60} moieties.

Thermal stability

The thermal stability of NCC derivatives after functionalization was analyzed by thermogravimetric analysis and compared to the starting material ox-NCC**.** Normalized thermogravimetric curves for weight loss (TG) and derivative of weight loss (DTG) are displayed in Figure 10. All experiments were carried out under N_2 atmosphere, starting with an isothermal treatment at 50 ºC for 10 min to remove residual moisture, followed by ramp heating up to 600 ºC. As previously discussed in Chapter 2, ox-NCC presents two weight losses in DTG, the first one, centered at 245 ºC, attributed to carboxylate groups on the surface and the second one, at 313 ºC corresponding to the inner core of the nanocrystals.

After the coupling, the weight loss coming from carboxylate groups was no more present for NCC-LC_C_{60}, NCC-SC_C_{60} and NCC-LC_C_{60}_FITC, confirming the functionalization of the nanocrystals. The main loss after functionalization was left shifted respect to that of ox-NCC for core fractions, and occurred at the same temperature in the three samples, namely 269 ºC. This could be for the similar surface composition after introduction of C_{60} moieties onto NCC lead to a similar stability. The effect of the functionalization in the charring behavior of the samples compared to ox-NCC was not clear, being charred residue 34.1, 51.6 and 42.9 for NCC-LC_C_{60}, NCC-SC_C_{60} nor NCC-LC_C_{60}_FITC, respectively, similar to the value of 44.9 in **ox-NCC**.

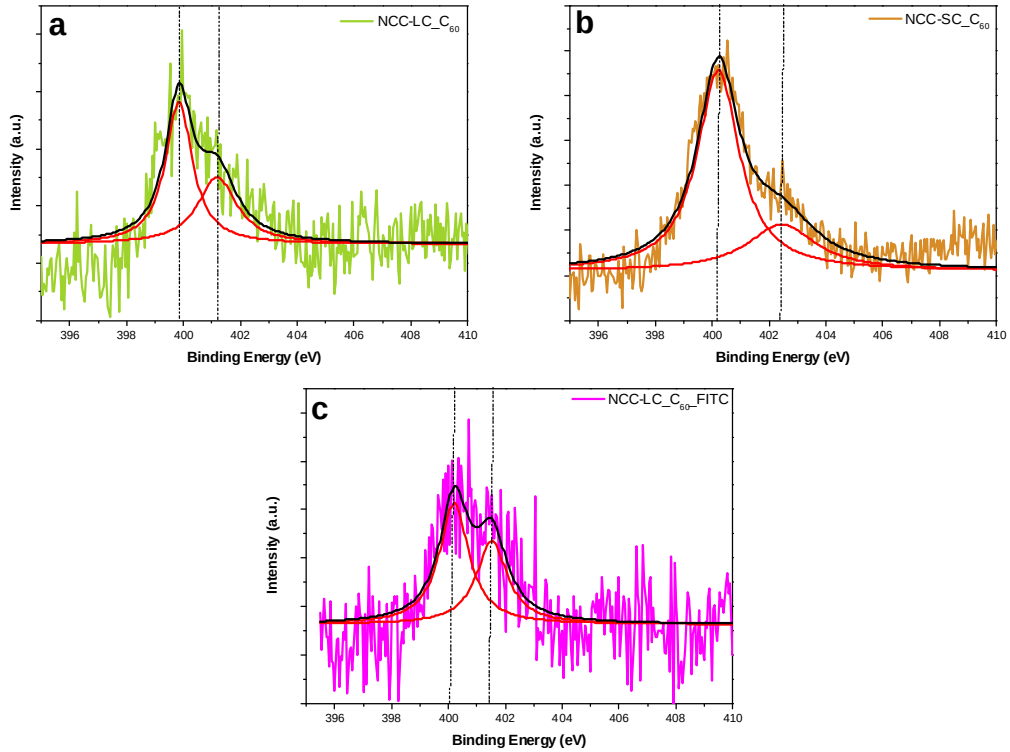

Figure 9. Deconvolution of N1s peaks for NCC-LC_C_{60} (a), NCC-SC_C_{60} (b) and NCC-LC_C_{60}_FITC (c).

Transmission electron microscopy (TEM)

The morphology of the starting nanocellulosic material as well as the NCC-C_{60} conjugates was analyzed by TEM. Aqueous suspensions of all samples were drop casted on carbon coated electron microscope grids and negatively stained with uranyl acetate solution for a better contrast. Although all the products showed the typical whisker-like morphology of nanocrystalline cellulose (Figure 11) in the case of NCC-LC_C_{60}, NCC-SC_C_{60} and NCC-LC_C_{60}_FITC, a marked tendency to form aggregates (probably due to a decreasing of hydrophilicity and to the intervention of fullerene-fullerene π-interactions) hindered the preparation of well-dispersed samples for TEM analysis.

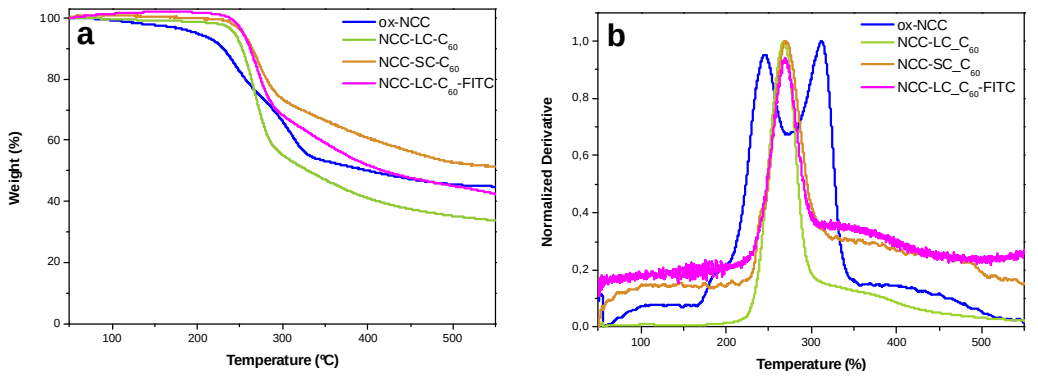

Figure 10. Normalized TG *(a)* and DTG *(b)* curves for ox-NCC, NCC-LC_C_{60}, NCC-SC_C_{60} and NCC-LC_C_{60}-FITC under N_2 atmosphere.

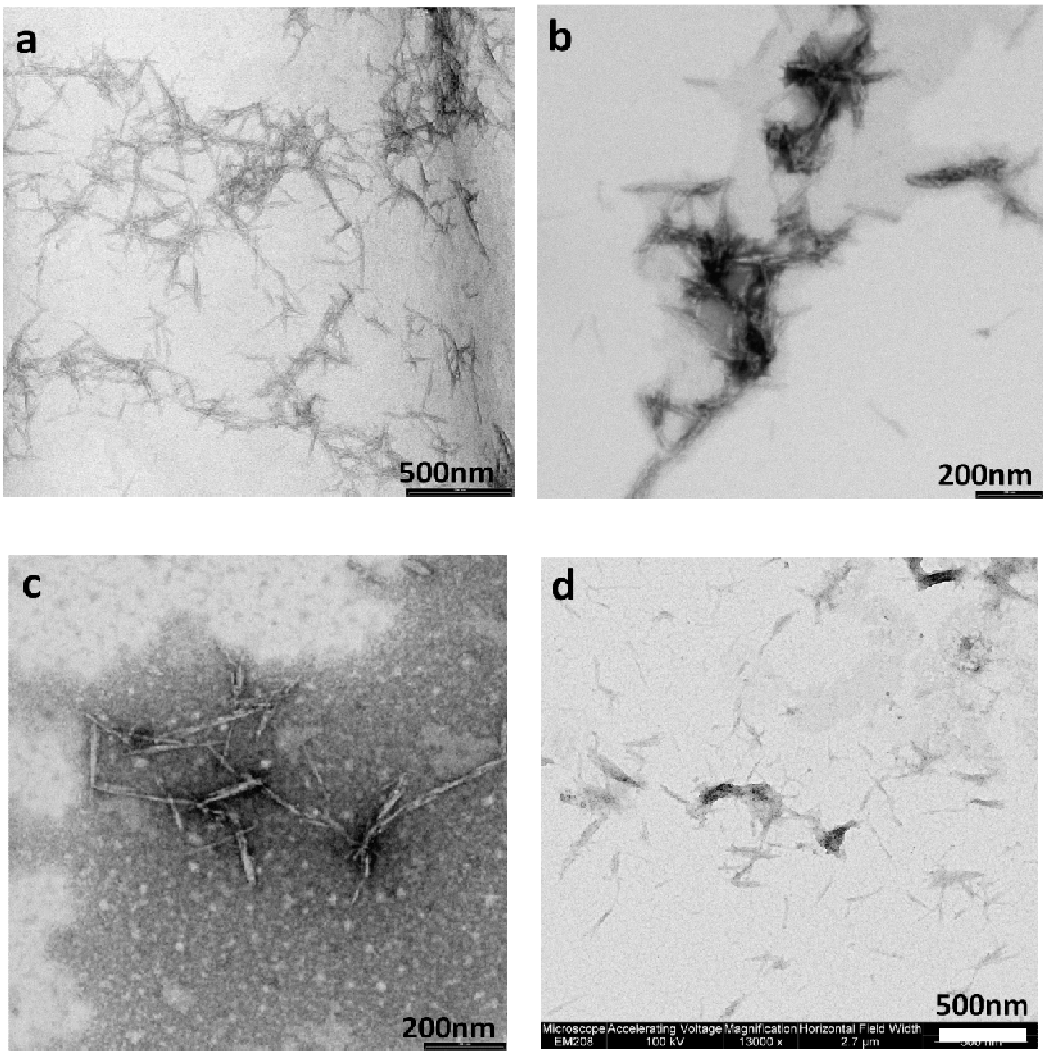

Figure 11. TEM images of ox-NCC, NCC-LC_C_{60}, NCC-SC_C_{60} and NCC-LC_C_{60}_FITC.

Stability of NCC-LC_C_{60} (a), NCC-SC_C_{60} (b), NCC-LC-C_{60}_FITC in water

All NCC-LC_C_{60}, NCC-SC_C_{60} and NCC-LC_C_{60}_FITC were brown solids, the characteristic color from fullerene monoadducts. When these solids were dispersed in water, brownish suspensions were obtained (Figure 12a, b and c). These suspensions were stable in water for weeks with negligible amounts of precipitate.

UV-Vis and fluorescence spectroscopies

Despite the stability of NCC-LC_C_{60}, NCC-SC_C_{60} and NCC-LC_-C_{60}-FITC suspensions in water, at a concentration of 0.5 mg/mL the UV-Vis spectra of the above aqueous suspensions do not show the typical fullerene bands. This has been observed also for other water-soluble fullerene derivatives and it has been ascribed to aggregation phenomena. However, when carried out in a o-DCB:DMF 1:1 mixture, the UV-Vis spectra of NCC-SC_C_{60}, NCC-LC_C_{60} and NCC-LC_C_{60}_FITC (Figure

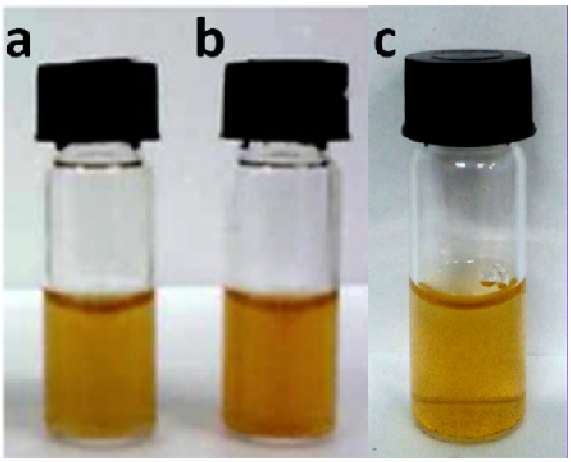

Figure 12. NCC-LC_C_{60} (a), NCC-SC_C_{60} (b), NCC-LC-C_{60}_FITC (c) suspension at 0.5 mg/mL in water.

13), at a concentration of 0.5 mg/mL, displayed an absorption band around 430 nm, attributed to the fullerene moiety. UV-Vis spectra of LC_C60 and LC_FITC in the same solvent mixture are also shown in Figure 13 for comparison purposes. LC_C_{60} showed a peak at 432 nm, typical spectroscopic signature of fulleropyrrolidine mono-adducts,[68] while LC_FITC presented two bands centered at 456 and 484 nm. The scattering in NCC samples did not permit to clearly asses the presence of bands from LC_FITC in NCC-LC_C_{60}_FITC UV-Vis spectrum

However, NCC-LC_C_{60}_FITC was observed under UV light, it emitted fluorescence, demonstrating also the presence of the FITC moiety in the sample (Figure 14a). Moreover, the optical properties of this derivative were also investigated by fluorescence spectroscopy in the same solvent mixture at room temperature. Excitation of this hybrid at 490 nm (FITC's absorbance peak) led to an emission band at 542 nm, confirming the presence of the fluorescent probe in the NCC hybrid as shown in Figure 14b. The intensity of emission was rather low, maybe due to a partial quenching caused by π-π stacking interactions of the FITC function with C_{60} moiety also present on NCC material.

UV-Vis spectra gave us a way to evaluate the amount of fullerene covalently grafted to **NCC**. To this purpose, we first evaluated the molar absorption (ε) of LC_C_{60} and SC_C_{60} in o-DCB:DMF (1:1). For this purpose, we made use of the well established Lambert-Beer law, which postulates that there is a linear relationship between absorbance and concentration of an absorbing species. The general Beer-Lambert law is usually written as:

$$A = \varepsilon \cdot b \cdot C \qquad (1)$$

where A is the measured absorbance at the corresponding wavelength, ε is the molar extinction coefficient ($L \cdot mol^{-1} \cdot cm^{-1}$) and b is the path length (cm).

Different solutions of LC_C_{60} and SC_C_{60} of known concentrations were prepared and their absorbance at 432 nm, divided by path length represented against

concentration in order to determine molar extinction coefficient (ε) for both molecules in the used mixture of solvents. Both curves displayed Lambert-Beer behavior in the given range of concentrations presenting high linear correlation and ε resulted to be 1747 $L \cdot mol^{-1} \cdot cm^{-1}$ and 2724 $L \cdot mol^{-1} \cdot cm^{-1}$ for LC_C_{60} and SC_C_{60}, respectively (Figure 15).

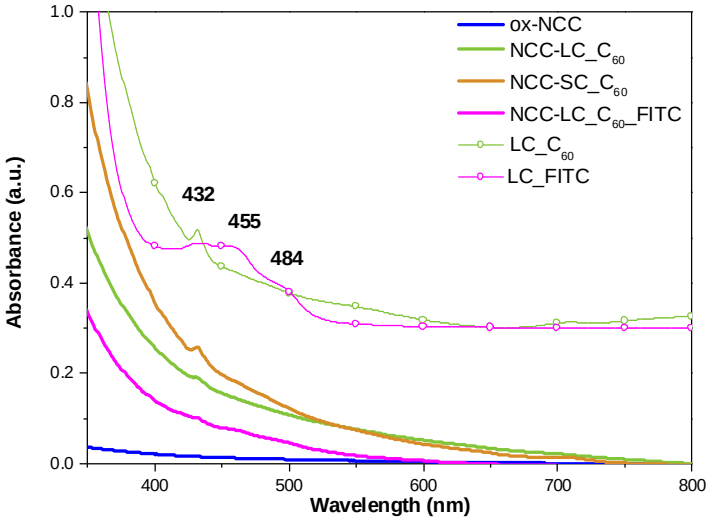

Figure 13. UV-Vis spectra of ox-NCC, NCC-LC_C_{60}, LC-C_{60}, NCC-SC_C_{60}, LC-C_{60} , NCC-LC_C_{60}-FITC in *o*-DCB:DMF (1:1).

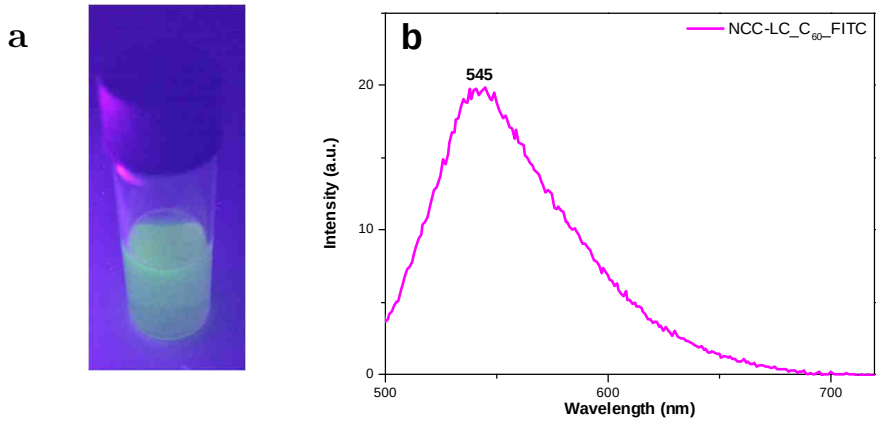

Figure 14. NCC-LC-C60-FITC in o-DCB:DMF (1:1) (a) and its emission spectrum at 490 nm excitation wavelength(b).

Assuming that the molar absorption of fullerene attached onto ox-NCC was not different from their amino counterparts LC_C_{60}, SC_C_{60}, we could estimate the concentration of C_{60} in NCC-LC_C_{60}, NCC-SC_C_{60} and NCC-LC_C_{60}_FITC from the absorbance of the dispersions at 432 nm. Knowing the concentration of NCC material, this value can be also expressed as C_{60} mols per gram of NCC (Table 7). It should be pointed out that these numbers refer to the bulk NCC crystals thus not considering that the entire core and half of the surface AGUs (due to the two-fold symmetry of the cellulose chains) are not involved in the functionalization. Therefore, it is more accurate to express these values referred to the degree of oxidation (DO), which was determined to be 0.15 or 0.87 mmol-COOH/g of ox-NCC (chapter 2,

section 3.3.1). Thus, surface functionalization for NCC-LC_C_{60}, NCC-SC_C_{60} and NCC-LC_C_{60}_FITC is of one fullerene moiety each 3.5, 5 and 7 carboxylic groups, respectively. Thus, for NCC-LC_C_{60}_FITC, degree of C_{60} functionalization was approximately half the one of NCC-LC_C_{60}, as it was expected, since for the synthesis of NCC-LC_C_{60}_FITC half the amount of LC_C_{60} was added into the reaction pot. This result indicates a similar reactivity of LC_C_{60} and LC_FITC. The different degree of functionalization between NCC-LC_C_{60} and NCC-SC_C_{60} could be ascribed to a more sterically hindered SC_C_{60} having a shorter linker.

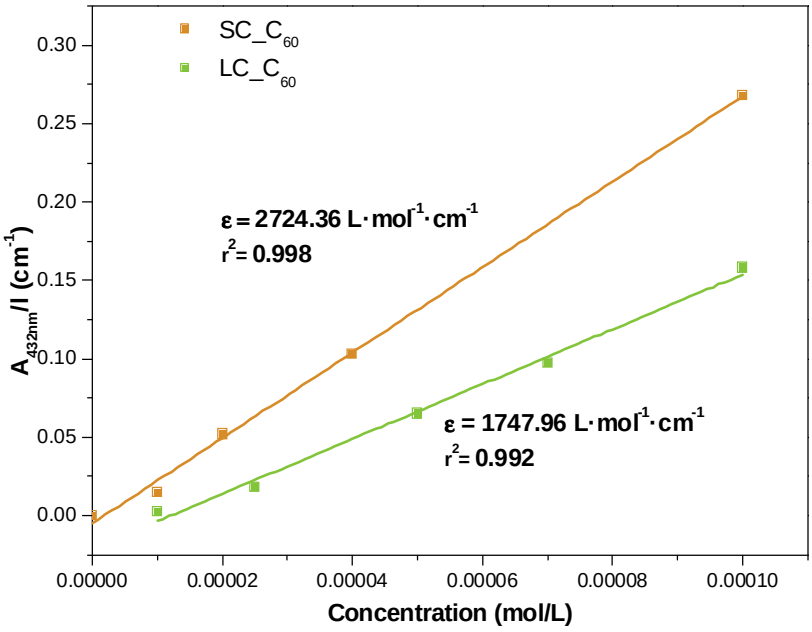

Figure 15. Lamber-Beer standard curves for LC_C_{60} and SC_C_{60}.

Table 7. C_{60} functionalization parameters for NCC-LC_C_{60}, NCC-SC_C_{60} and NCC-LC_C_{60}-FITC.

Compound	Concentration [mmol/L]	Concentration mmol/g	Absorbance	ε L · mol^{-1} · cm^{-1}
NCC-LC_C60	0.125	0.25	0.19079	1748
NCC-SC_C60	0.095	0.19	0.25838	2724
NCC-LC_C60_FITC	0.064	0.13	0.10147	1748

4.3.3. Singlet oxygen production studies

The aqueous solubility of all NCC-C_{60} derivatives prompted us to test their ability to act as sensitizers for singlet oxygen production under light irradiation. Singlet oxygen reacts primarily with five amino acids, which are tryptophan, histidine, tyrosine, methionine, and cystein.[69] In particular, methionine contains a sulfur atom with four

non-bonding electrons, which readily react with the electrophilic singlet oxygen. This sulfur-containing amino acid is known to react with singlet oxygen to produce methionine sulfoxide.[70] Therefore, methionine or its derivatives oxidation has been commonly used as a model reaction to test singlet oxygen sensitizers. According to literature, blocking the carboxyl group decreases the electron-attracting ability and hence increases the reducing power of the sulfur-containing group.[69] Thus, as a proof of concept we studied the photooxidation of L-methionine methyl ester to the corresponding sulfoxide in the presence of NCC-LC_C_{60}, NCC-SC_C_{60}, NCC-LC_C_{60}_FITC using conditions already described by our group (Figure 16).[62]

The reaction was carried out in D_2O since it is known that singlet oxygen has an elongated lifetime (68 μs) with respect to H_2O (2 μs).[71] Thus, NCC-LC_C_{60} was suspended in an oxygen-saturated solution of L-methionine methyl ester in D_2O and was irradiated with green light (490-590 nm bandwidth). The amount of the sulfoxide formed under various experimental conditions (Table 8) was quantified by ^{1}H-NMR acquired after centrifugation in the deuterated reaction solvent. The parameters considered for the optimization were: concentration of NCC-LC_C_{60}, power of the lamp, and irradiation time.

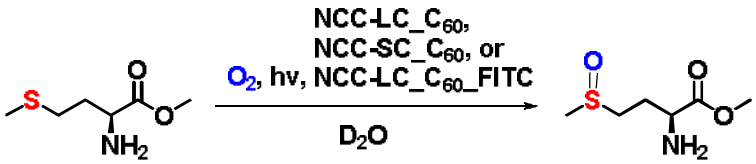

Figure 16. Photooxidation of L-methionine methyl ester catalyzed by NCC-LC_C_{60}, NCC-SC_C_{60}, NCC-LC_C_{60}_FITC.

Table 8. Results about the photooxidation of L-methionine-methylester in the presence of NCC-LC_C_{60}, NCC-SC_C_{60}, and NCC-LC_C_{60}_FITC as sensitizers for the production of singlet-oxygen.

Entry	Compound	Concentration [mg/mL]	Power (W/cm²)	Time (min)	Conversion (%)
1	NCC-LC_C_{60}	0.5	0.47	60	31
2		0.3	0.47	60	23
3		0.1	0.47	60	1
4		0.5	0.47	75	34
5		0.5	0.40	75	25
6	NCC-SC_C_{60}	0.5	0.47	75	66
7	NCC-LC-C_{60}_FITC	0.5	0.47	75	12

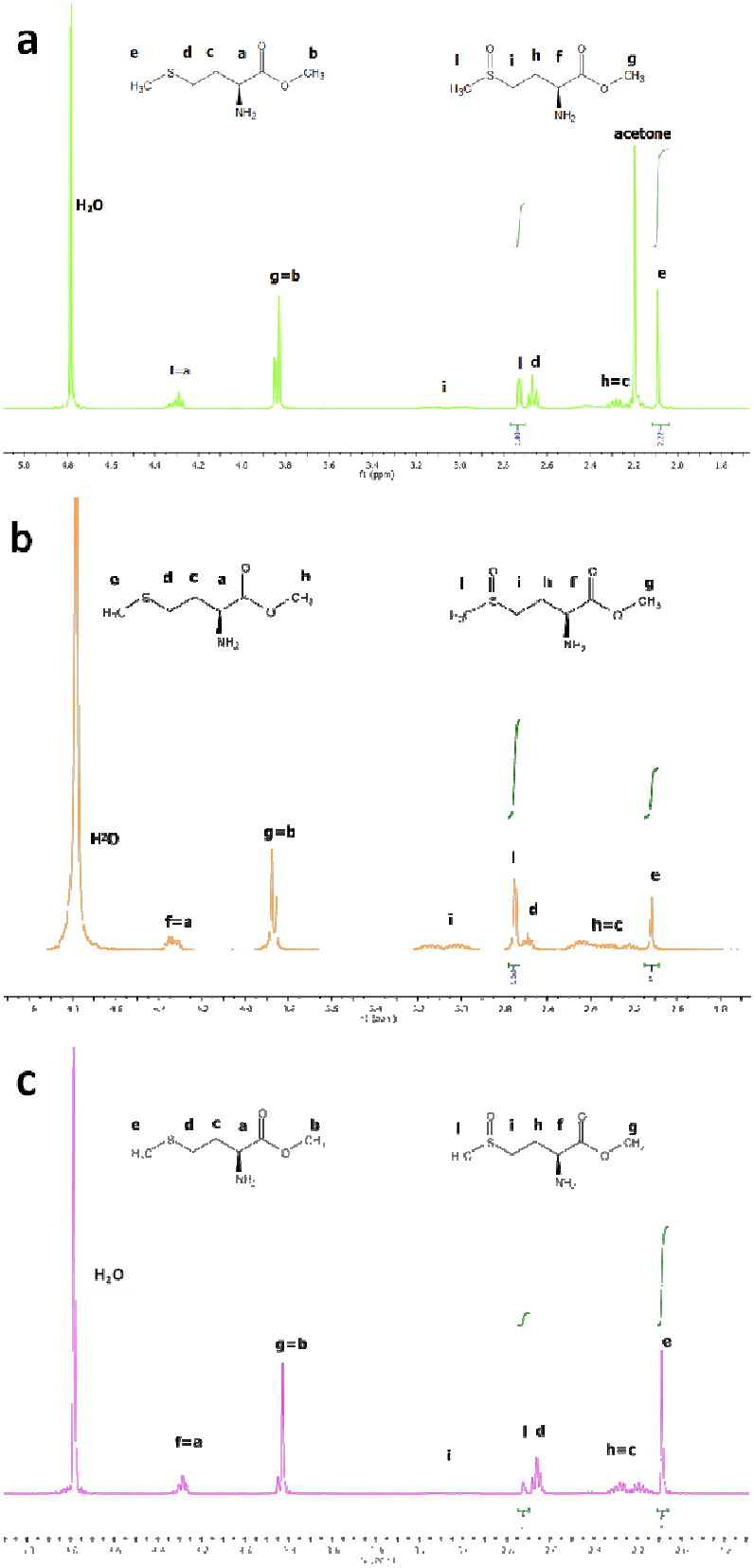

Figure 17. 1H-NMR spectrum in D_2O for photooxygenation experiment using NCC-LC_C_{60} (a), NCC-SC_C_{60} (b) and NCC-LC_C_{60}-FITC (c) at 0.5 mg/mL, irradiation power 0.47 W/cm² for 75 min.

The ^{1}H-NMR spectra before and after oxidation are essentially the same but for the signals corresponding to protons in the vicinities of sulfur. After oxidation, **e** and **d** protons (Figure 17) become the more deshielded **l** and **i**, respectively, because of the introduction of the electron withdrawing oxygen. Besides, multiciplity changes from singlet in the case of **e** to doublet in **l**, and passes from triplet in **d** to multiplet in **i**. This is due to the fact that protons belonging to residues spatially close to the site of oxidation undergo either slight chemical shift variation or splitting into two signals; what can be ascribed to new magnetic anisotropy and chirality connected with the sulfoxide group.[72] By integration of these signals (**e** and **l**) it is possible to estimate the relative ratio of the two species in the crude of reaction. Examples of ^{1}H-NMR obtained after photooxidation of L-methionine with NCC-LC_C_{60}, NCC-SC_C_{60} and NCC-LC_C_{60}_FITC (best conditions) are shown in Figure 17.

At a 0.5 mg/mL^{-1} concentration (Table 8, entry 1), NCC-LC_C_{60} produced the 31% of sulfoxide upon irradiation for 60 minutes at a power level of 0.47 W/cm^2. As expected, decreasing the amount of NCC-LC_C_{60} to 0.3 mg/mL (Table 8, entry 2) and to 0.1 mg/mL (Table 8, entry 3) led to lower conversions (23 and 1%, respectively). On the basis of these experiments, the amount of NCC-LC_C_{60} was set to 0.5 mg/mL. An increasing of the irradiation time to 75 minutes (Table 8, entry 4) determined a slight increasing of sulfoxide production (34%). On the other hand, irradiating for the same time but at a lower lamp power (Table 8, entry 5) gave a diminished amount of sulfoxide (25%).

Therefore, the best values of irradiation time and light power turned out to be 75 minutes and 0.47 W/cm^2, respectively. Using these optimized parameters, NCC-SC_C_{60} derivative (Table 8, entry 6) gave a remarkable production of sulfoxide of 66% whereas NCC-LC-C_{60}-FITC gave 12% corresponding to the difference of C_{60} loading compared to NCC-LC-C_{60} hybrid (Table 8, entry 7). The fact that NCC-LC_C_{60}, with a higher loading of C_{60} produced singlet oxygen in lower yield correlated with its solubility. The C_{60} loading is higher in NCC-LC_C_{60} and so a lower amount of negatively charged carboxylic groups are present on its surface. Both factors contribute to a higher degree of aggregation of NCC-LC_C_{60} and therefore C_{60} units are less available for reaction.

The good results of singlet oxygen photoproduction in water of our new derivatives, prompted us to test their effectiveness as PS in PDT *in vitro* studies.

Uptake studies

Thanks to the presence of the FITC motiety on NCC-LC_C_{60}_FITC, the uptake of this material could be investigated in cells by Fluorescence Activated Cell Sorting (FACS) and confocal microscopy techniques.

FACS is a laser-based, biophysical technology employed in cell counting, cell sorting, biomarker detection and protein engineering, by suspending cells in a stream of fluid and passing them by an electronic detection apparatus.[73] Each particle passes through one or more beams of light. Light scattering or fluorescence (FL) emission (if the particle is labeled with a fluorophore) provides information about the particle's properties. Fluorescence measurements taken at different wavelengths can provide

quantitative and qualitative data about fluorophore-labeled cell surface receptors or intracellular molecules. As the particle enters the laser beam spot, it will generate scattered light and fluorescence signals. The height and area, or maximum and integral, respectively, are used to measure signal intensity. Flow cytometers use separate channels and detectors to detect light emitted. There are three major filter types. In the case of FITC, the fluorophore used here, its maximum absorption falls within the blue spectrum. Therefore, the blue 488 nm laser, which is close to FITC's absorbance peak at 490 nm, is commonly used to excite this fluorophore.

Data are commonly represented as histograms that display measurement parameter (relative fluorescence or light scatter intensity) on the x-axis and the number of events (cell count) on the y-axis.

Figure 18 shows a typical FACS analysis of MCF-7 cells treated with NCC-LC_C_{60}_FITC at 5 and 10 µM of loaded C_{60} in H_2O for 24 h. These histograms display a single measurement parameter (relative fluorescence or light scatter intensity) on the x-axis and the number of events (cell count) on the y-axis. It is also important to precise that cells have autofluorescence coming from some cellular substructures like mithocondria or lysosomes. After incubation with the marked NCC-LC_C_{60}_FITC, an increasing in fluorescence (as a shift in x band position) is expected due to the contribution of internalized drug. The median fluorescence of cells observed increased after incubation with NCC-LC_C_{60}-FITC at 5 and 10 µM in a dose dependent manner, suggesting that the labeled photosensitizer was internalized into the cells.

In order to ascertain the precise location of the photosensitizer in the cells, the samples were inspected by confocal fluorescence microscopy. This microscopic technique generates information from a well-defined optical section rather than from the entire specimen, thereby increasing the contrast, clarity and sensitivity by eliminating the out of focus glare.[74] In addition, by using multiple labeling, two or more molecules can be observed simultaneously in the same cell or tissue. The light emitted from the different fluorophores upon excitation is split and diverted to separate photomultipliers. The resulting image can then be merged to map the

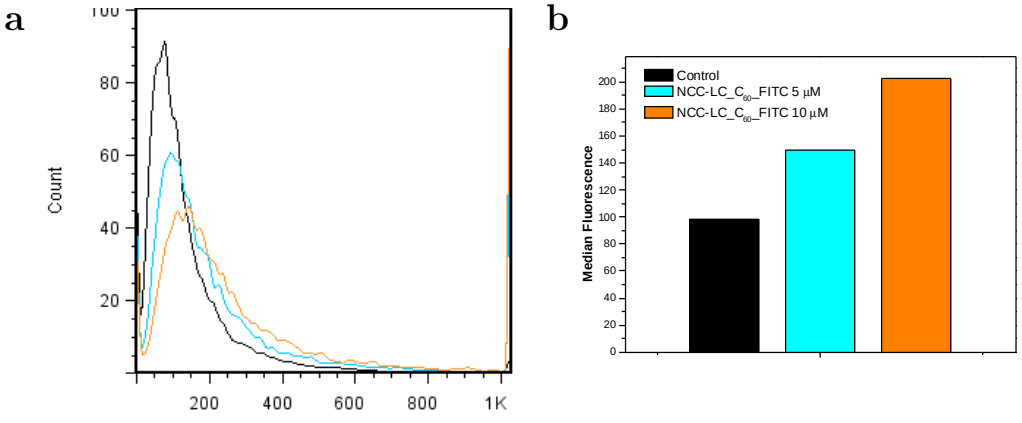

Figure 18. FACS spectra (a) and median fluorescence (b) of MCF-7 cells treated with NCC-LC_C_{60}-FITC at 5 and 10 µM in H_2O after 24 h of incubation.

distribution of the labels in the sample. Thus, if the first image is colored red and the second green, the overlapping regions appear yellow (Figure 19).

The cellular localization of NCC-LC_C_{60}_FITC after 24 hours of incubation was studied. MCF-7 cells treated with NCC-LC_C_{60}_FITC (5 μM in H_2O) and MitoTracker red, a specific dye for mitochondria (100 nM in H_2O). Typical images obtained for MCF-7 cells show that MitoTracker (red staining, Figure 19a) colocalizes with NCC-LC_C_{60}_FITC (green fluorescence, Figure 19b) as can be seen more clearly in the merge image (Figure 19c).

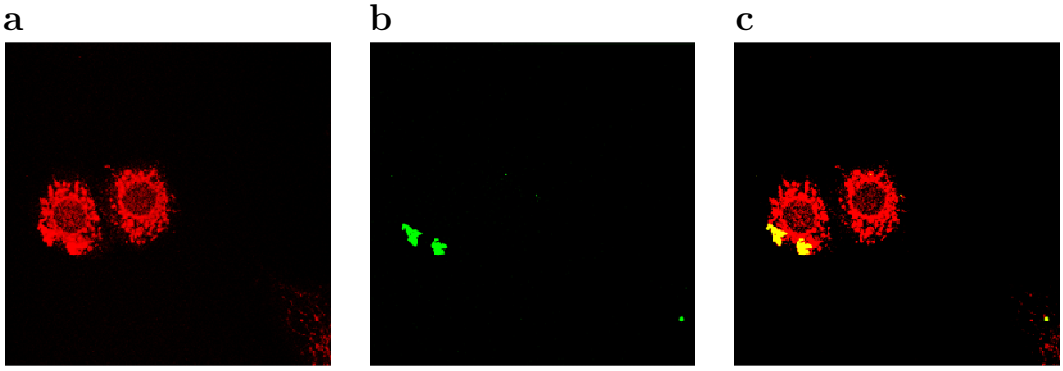

Figure 19. Fluorescence emitted by MitoTracker (a) NCC-LC_C_{60}-FITC (b) and merge of fluorescence from MitoTracker and NCC-LC_C_{60}_FITC (c).

Nevertheless, as observed in Figure 19, NCC-LC_C_{60}_FITC was found forming aggregates instead of dispersed in the cytosol, Thus it seems that the nanohybrid may be adhered to the cell membrane rather than internalized. This aggregation could be ascribed to the introduction of C_{60} moieties, along with the inherent tendency of NCC materials to form films.

In vitro photocytotoxicity studies

The photocytotoxicity of NCC-LC_C_{60} and NCC-SC_C_{60} was evaluated in human breast MCF-7 cancer cell lines: In view of the sample aggregation described above, it was apparent that the concentration needed to be lower in order for the photosensitizer to be internalized. For this purpose, cells were incubated with NCC-LC_C_{60} and NCC-SC_C_{60} at 250, 500, 750 and 1000 nM of loaded C_{60} in H_2O. Cells were then illuminated with a halogen lamp at the fluence of 7 J/cm^2, and analyzed by a standard resazurin assay after 24 and 48 h.

At the doses tested, there was no noticeable decrease in metabolic activity up to 48 h after treatment, as shown in Figure 20. Both photosensitizers showed the same behavior. This implies either a poor internalization, even at such low concentrations, or an insufficient amount of singlet oxygen generated at these low doses.

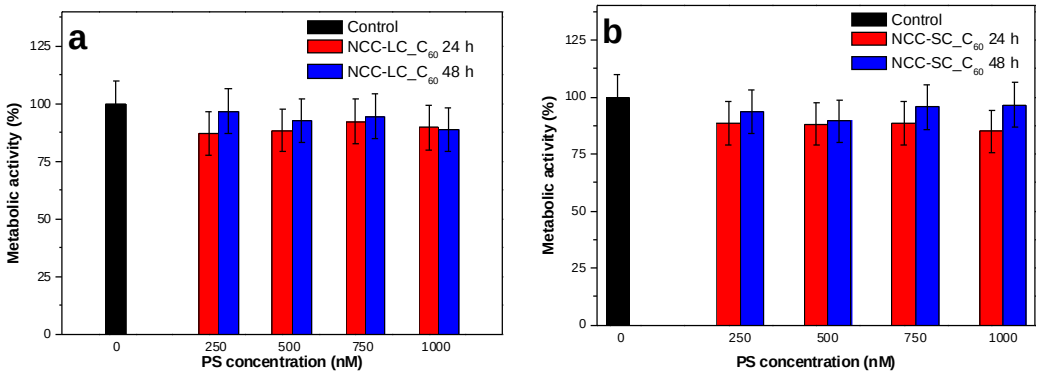

Figure 20. Metabolic activity of MCF-7 cells treated with NCC-LC_C_{60} (a) and NCC-SC_C_{60} (b) at 250, 500, 750 and 1000 nM in H_2O after 24 and 48 h.

4.4. Conclusions

New nanomaterials based on the covalent functionalization of ox-NCC with C_{60} derivatives *via* a two-step carbodiimide reaction were presented in this Chapter. The success of the functionalization was evaluated by means of different spectroscopic techniques. Characteristic features of fullerene C_{60} moieties attached to ox-NCC were present in UV-Vis, Raman and FT-IR spectra. Moreover, FT-IR and XPS confirmed the covalent nature of the bond formed between ox-NCC and C_{60}. UV-Vis spectroscopy allowed the determination of C_{60} loading on the different NCC materials.

In addition, using the same method, we were able to perform a double functionalization of ox-NCC and in one-pot introducing both a fluorescent target and the C_{60} unit. In this way a fluorescently marked photosensitizer, NCC-LC_C_{60}_FITC, analogue to NCC-LC_C_{60} and NCC-SC_C_{60} was obtained, in order to track the internalization of these PDT photosensitizers in the cells. This new compound had properties similar to NCC-LC_C_{60} and NCC-SC_C_{60} and the presence of C_{60} could be proved in the same way. Furthermore, the introduction of the fluorescent moiety was demonstrated by fluorescence spectroscopy.

These new hybrids could easily be dispersed in water and form highly stable suspensions at concentrations up to 0.5 mg/mL have been proved to be a good sensitizer for singlet oxygen production in water. The singlet oxygen production abilities of the materials were tested through the oxidation of L-methionine methyl ester to the corresponding sulfoxide. After irradiation, the ratio of sulfoxide in the crude of reaction was easily measured by ^{o}H-NMR. Encouraging results were obtained, as NCC-LC_C_{60}, NCC-SC_C_{60} and NCC-LC_C_{60}_FITC gave conversions of 31, 66 and 12% respectively.

Finally, the uptake of NCC-LC_C_{60}_FITC in human breast cancer cells (MCF-7) was investigated using FACS and confocal microscopy. NCC-LC_C_{60} and NCC-SC_C_{60} phototoxic activities were also measured. Cells were incubated with both photosensitizers and their metabolic activity was followed for 48 h. Despite the high yield of singlet oxygen generation of these novel photosensitizers, no phototoxic effect was observed, which could be explained for their poor internalization into cells.

However, due to their good singlet oxygen production properties, these materials still have potential to be employed in other applications that require generation of singlet oxygen in water, as antimicrobial agents or in water purification processes.

4.5. Experimental details

4.5.1. Generalities:

All reagents and solvents were used as received or purified using standard procedures. Milli-Q water was used in all experiments (System MilliQ plus). Microcrystalline Avicel® cellulose powder was purchased from Aldrich and used without further purification.

4.5.2. Techniques

Thermogravimetric analyses were performed on TgaQ500 (TA instruments) under N_2, by equilibrating at 50 °C, and following a ramp at 10°C/min up to 600 °C (approximately 1 mg of each compound).

Infrared spectra were recorded with a Fourier-transform infrared (FT-IR) spectrometer (Perkin-Elmer 2000). Spectral width ranged from 4000 to 400 cm^{-1}, a 4 cm^{-1} resolution and an accumulation of 8 scans. Samples were prepared as KBr pellets (approximately 1 % sample in anhydrous KBr).

Raman spectra were collected with an Invia Renishaw micro-spectrometer (100x) and a laser source at 532 or 785 nm.

Transmission electron microscopy (TEM) measurements were performed on a TEM Philips EM208, using an accelerating voltage of 100 kV. Samples were prepared by drop casting from dispersion (0.01% w/v) onto a TEM grid (200 mesh, nickel, carbon only), followed by staining with a 2 wt % uranyl acetate solution.

UV-Vis measurements were carried out on Cary 5000 spectrophotometer using quartz cuvettes with 10 mm path length.

Fluorescence emission spectra have been recorded on a Varian Cary Eclipse Spectrophotometer using 10 mm path length Hellma Analytics 117.100F-QS quartz cuvettes.

The X-ray photoelectron spectroscopy (XPS) analyses were performed with a VG-Microtech ESCA 3000Multilab, equipped with a dual Mg/Al anode. The spectra were excited by the un-monochromatized Al Kα source (1486.6 eV) run at 14 kV and 15 mA. The analyser was operated in the constant analyser energy (CAE) mode. For the individual peak energy regions, a pass energy of 20 eV set across the hemispheres was used. Survey spectra were measured at 50 eV pass energy. The pressure in the analysis chamber was in the range of 10-8 Torr during data collection. The constant charging of the samples was removed by referencing all the energies to that of C-C bond (C1s) set at 285.1 eV. The invariance of the peak shapes and widths at the beginning and at the end of the analyses ensured the absence of differential charging. Analyses of the peaks were performed with the software provided by VG, based on non-linear least squares fitting program using a weighted sum of Lorentzian and Gaussian component curves after background subtraction according to ShirleyR3 and SherwoodR4. Atomic concentrations were calculated from peak intensities using the

sensitivity factors provided with the software. The binding energy values are quoted with a precision of ± 0.15 eV and the atomic percentage with a precision of ± 10%.

Photo-production of singlet oxygen was carried out by using a TECLAS source PTL-Penta lamp equipped with green filter having a bandwith in the 490-590 range).

Singlet oxygen production

L-methionine methyl ester photooxidation: The corresponding NCC-C_{60} adduct (0.5 mg) was suspended in D_2O (1 mL) and sonicated to obtain a stable suspension, then L-methionine methyl ester · HCl (20 mg) was added. The suspension was transferred into a quartz cuvette capped with a septum and saturated with oxygen. The mixture was exposed for 75 minutes with a lamp at 0.47 W/cm^2 (through a filter with bandwidth of 490-590 nm) placed at 0.5 cm from the cuvette. The suspension was then centrifuged to remove the sensitizer and analyzed by ^{1}H-NMR. L-methionine methyl ester and the corresponding sulfoxide were identified according to a previous report.

Biological Experiments

The human breast cancer cell line MCF-7 was obtained from American Type Culture Collection (Rockville, MD, USA).

FACS: The MCF-7 cells were seeded in a 24 wells/plate at density of 5x10^4 cells. The treatment was performed with 5 and 10 μM of NCC-LC_C_{60}_FITC in H_2O for 24h. Then the cells were harvested , resuspended in 0.5 ml of PBS and washed twice and analysed by a FACScan (Becton Dickinson, San Josè, USA) equipped with a single 488 nm argon laser. A minimum of 10,000 cells for sample was acquired in list mode and analysed using Cell Quest software. The signal of FITC was detected by FL-1 in linear scale.

Cell culture and PDT treatment: In this study we used human breast cancer MCF-7 cells. The cells were maintained in exponential growth in Dulbecco's modified eagle's medium containing 100 U/ml penicillin, 100 mg/ml streptomycin, 20 mM L-glutamine and 10 % fetal bovine serum (Euroclone, Milano, Italy). The cells were seeded in a 96-well plate at a density of 5 x 10^3 cells/well. The following day they have been treated with 250, 500, 750 and 1000 nM NCC-LC_C_{60} and NCC-SC_C_{60} in H_2O in the dark and after 24 h, irradiated with metal halogen lamp with an irradiation of 8 mW/cm^2 for 15 min (fluence 7.2 J/cm^2). 24 h after irradiation the metabolic activity was determined by the resazurin assay following the manufacturer's instructions (Sigma–Aldrich, Milan, Italy). The fluorescence was measured with a spectrofluorometer Spectra Max GeminiXS (Molecular Devices, Sunnyvale, CA). The data are presented as the percentage of metabolic activity compared to untreated cells. The data are the average of at least three independent experiments.The protocol for PDT was the same for each type of experiment. MCF-7 cells were plated at day 0. One day after plating, the cells have been treated with porhyrins. After 24 h they have been irradiated with the halogen lamp (fluence 7.2 J/cm^2).

Cell metabolic assay: MCF-7 cells were seeded in a 96-well plate at a density of 5 x 10^3cells/well. Aftyer 24h the cells were treated with conjugates for 24h before light irradiation. The cell proliferation, in terms of metabolic activity, was determined by the resazurin assay following the manufacturer's instructions (Sigma-Aldrich, Milan, Italy). The values were obtained by using the spectrofluorimeter (EnSpire™ 2300 Multilabel reader, PerkinElmer, Finland).

Confocal microscopy: MCF-7 cells were plated on coverslips (diameter 24mm), and after 24h, were treated with 5 μM of NCC-LC_C_{60}_FITC. After 24h the cells were treated with 100 nM Mitotracker Red CMXRos (Invitrogen, Molecular Probes, Mialn, Italy) (to stain the mitochondria) for 35 min, washed twice with PBS and then fixed with 3% paraformaldehyde (PFA) in PBS for 20 min. After washing with 0.1 M glycine containing 0.02 %sodium azide in PBS to remove PFA and Triton X-100 (0.1% in PBS) the cells were incubated with 3,56 mM Hoechst 34580 (Sigma, Milan) to stain the nuclei. Finally the glasses were analysed with a Leica TCS SP1 confocal imaging system (Leica Microsystems, Heidelberg, Germany). Green fluorescence was excited with a 488 nm argon laser and red fluorescence was excited with a 543 nm He-Ne laser.

4.5.3. Synthesis

NCC-LC_C_{60} and NCC-SC_C_{60} synthesis: ox-NCC_3 (50 mg, 0.04 mmol of COONa groups) was suspended in a 50 mM MES buffer solution (25 mL) at pH = 5. The suspension was sonicated for 15 min then EDC·HCl (79 mg, 0.41 mmol) and NHS (48 mg, 0.41 mmol) were added. After stirring for 5 minutes, the fullerene derivative LC_C_{60} (50 mg, 0.049 mmol) or SC_C_{60} (38 mg, 0.041 mmol) dissolved in 5 mL of a mixture H_2O:DMF (5:1), was added. The suspension was stirred at room temperature for 3 days. The suspended solid was recovered with a Millipore filter (0.1 μm pores), then the solid was washed extensively with a toluene:MeOH (9:1) mixture until unreacted fullerene derivative was not detected UV spectroscopy on the washing. A further washing was carried out with water before drying the solid. Yields: 43 mg of NCC-LC_C60 (86 %) and 36 mg of NCC-SC_C60 (72 %).

NCC-LC_C_{60}_FITC synthesis: ox-NCC (41 mg, 0.036 mmol of COOH groups) was suspended in a 50 mM MES buffer solution (25 mL) at pH = 5. The suspension was sonicated for 15 min then EDC·HCl (67 mg, 0.035 mmol) and NHS (41 mg, 0.035 mmol) were added. After stirring for 5 minutes, the fullerene derivative LC_C_{60} (21 mg, 0.02 mmol) and LC_FITC (11 mg, 0.02 mmol) dissolved in 5 mL of a mixture H_2O:DMF (5:1), was added. The suspension was stirred at room temperature for 3 days. The suspended solid was recovered with a Millipore filter (0.1 μm pores), then the solid was washed extensively with a toluene:MeOH (9:1) mixture until unreacted fullerene derivative was not detected UV spectroscopy on the washing. A further washing was carried out with water before drying the solid. Yield: 32 mg of **NCC-LC_C_{60}_FITC** (78 %).

LC_C_{60}, SC_C_{60} and LC_FITC were available from the research group.[65,75]

4.6. References

(1) Daniell, M. D.; Hill, J. S. A History of Photodynamic Therapy. *Aust. N. Z. J. Surg.* **1991**, *61*, 340–348.

(2) Raab, O. Uber Die Wirkung Fluoreszierender Stoffe Auf Infusorien. *Zeitung Biol.* **1900**, *39*, 524–526.

(3) Kelly, J. F., Snell, M. E. Berenbaum, M. C. Photodynamic Destruction of Human Bladder Carcinoma. *Br. J. Cancer* **1975**, *31*, 237–244.

(4) Henderson, B. W.; Dougherty, T. J. How Does Photodynamic Therapy Work? *Photochem. Photobiol.* **1992**, *55* (1), 145–157.

(5) Dennis E.J.G.J. Dolmans, D. F. and R. K. J. Photodynamic Therapy for Cancer. *Nat. Rev.* **2004**, *14* (May), 380–387.

(6) Ochsner, M. Photophysical and Photobiological Processes in the Photodynamic Therapy of Tumours. *J. Photochem. Photobiol. B Biol.* **1997**, *39*, 1–18.

(7) Reports, B.; Santos, Z.; Jr, S.; Nove, U.; Bussadori, S.; Nove, U.; Porta, K.; Fernandes, S.; Nove, U.; Hamblin, M.; General, M. Animal Models for Photodynamic Therapy (PDT). *Biosci. Rep.* **2015**, *35*, 1–14.

(8) Mroz, P.; Yaroslavsky, A.; Kharkwal, G. B.; Hamblin, M. R. Cell Death Pathways in Photodynamic Therapy of Cancer. *Cancers (Basel).* **2011**, *3*, 2516–2539.

(9) Auten, R. L.; Davis, J. M. Oxygen Toxicity and Reactive Oxygen Species: The Devil Is in the Details. *Pediatr. Res.* **2009**, *66* (2), 121–127.

(10) Fruhwirth, G. O., Hemetter, A. Mediation of Apoptosis by Oxidized Phospholipids. *Subcell. Biochem.* **2008**, *49*, 351–367.

(11) Albertine, K. H.; Plopper, C. G. DNA Oxidation or Apoptosis. *Am. J. Respir. Cell Mol. Biol.* **2002**, *26* (27), 381–383.

(12) Dougherty, T. J.; Gomer, C. J.; Henderson, B. W.; Jori, G.; Kessel, D.; Korbelik, M.; Moan, J.; Peng, Q. Photodynamic Therapy. *J. Natl. Cancer Inst.* **1998**, *90* (12), 889–905.

(13) Gollnick, S. O.; Owczarczak, B.; Maier, P. Photodynamic Therapy and Anti-Tumor Immunity. *Lasers Surg. Med.* **2006**, *38* (July), 509–515.

(14) Agostinis, P.; Berg, K.; Cengel, K. .; Foster, T. .; Girotti, a. .; Gollnick, S. .; Hahn, S. .; Hamblin, M. .; Juzeniene, a.; Kessel, D.; Koberlik, M.; Moan, J.; Mroz, P.; Nowis, D.; Piette, J.; Wilson, B.; Golab, J. Photodynamic Terapy of Cancer: An Update. *CA Cancer J Clin.* **2011**, *61* (4), 250–281.

(15) Huang, Y.; Sharma, S. K.; Yin, R.; Agrawal, T.; Chiang, L. Y.; Hamblin, M. R. Functionalized Fullerenes in Photodynamic Therapy. *J. Biomed. Nanotechnol.* **2014**, *10* (September), 1918–1936.

(16) Huang, Z. A Review of Progress in Clinical Photodynamic Therapy. *Technol. Cancer Res. Treat.* **2005**, *4* (3), 283–293.

(17) http://www.kalandrakas.com/blue-light-skin-penetration/.

(18) Lucky, S. S.; Soo, K. C.; Zhang, Y. Nanoparticles in Photodynamic Therapy. *Chem. Rev.* **2015**, *115* (4), 1990–2042.

(19) Szeimies, R. M.; Karrer, S.; Abels, C.; Steinbach, P.; Fickweiler, S.; Messmann, H.; Bäumler, W.; Landthaler, M. 9-Acetoxy-2,7,12,17-Tetrakis-(β-Methoxyethyl)-porphycene(ATMPn), a Novel Photosensitizer for Photodynamic Therapy: Uptake

Kinetics and Intracellular Localization. *J. Photochem. Photobiol. B Biol.* **1996**, *34*, 67–72.

(20) Rosenthal, I.; Hur, B.; Lier, V. Phthalocyanines as Photodynamic Sensitizers. *Photochem. Photobiol.* **1991**, *53* (6), 859–870.

(21) Accorsi, G.; Armaroli, N. Taking Advantage of the Electronic Excited States of [60]fullerenes. *J. Phys. Chem. C* **2010**, *114*, 1385–1403.

(22) Arbogast, J. W.; Darmanyan, A. P.; Foote, C. S.; Rubin, Y.; Diederich, F. N.; Alvarez, M. M.; Anz, S. J.; Whetten, R. L. Photophysical Properties of C_{60}. *J. Phys. Chem.* **1991**, *95* (10), 11–12.

(23) Hotze, E. M.; Labille, J.; Alvarez, P.; Wiesner, M. R. Mechanisms of Photochemistry and Reactive Oxygen Production by Fullerene Suspensions in Water. *Environ. Sci. Technol.* **2008**, *42*, 4175–4180.

(24) Culotta, E.; De Koshland, J. Buckyballs: Wide Open Playing Field for Chemists. *Science* **1991**, *254*, 1706–1708.

(25) Bosi, S.; Da Ros, T.; Spalluto, G.; Balzarini, J.; Prato, M. Synthesis and Anti-HIV Properties of New Water-Soluble Bis- functionalized[60]fullerene Derivatives. *Bioorganic Med. Chem. Lett.* **2003**, *13* (MARCH), 4437–4440.

(26) López, A. M.; Scarel, F.; Carrero, N. R.; Vázquez, E.; Mateo-Alonso, A.; Ros, T. Da; Prato, M. Synthesis and Characterization of Highly Water-Soluble Dendrofulleropyrrolidine Bisadducts with DNA Binding Activity. *Org. Lett.* **2012**, *14* (c), 4450–4453.

(27) Hahn, U.; Vögtle, F.; Nierengarten, J. F. Synthetic Strategies towards Fullerene-Rich Dendrimer Assemblies. *Polymers* **2012**, *4*, 501–538.

(28) Nakamura, E.; Isobe, H. Functionalized Fullerenes in Water. The First 10 Years of Their Chemistry, Biology, and Nanoscience. *Acc. Chem. Res.* **2003**, *36* (11), 807–815.

(29) Yan, A.; Von Dem Bussche, A.; Kane, A. B.; Hurt, R. H. Tocopheryl Polyethylene Glycol Succinate as a Safe, Antioxidant Surfactant for Processing Carbon Nanotubes and Fullerenes. *Carbon N. Y.* **2007**, *45*, 2463–2470.

(30) Kojima, C.; Toi, Y.; Harada, A.; Kono, K. Aqueous Solubilization of Fullerenes Using Poly(amidoamine) Dendrimers Bearing Cyclodextrin and Poly(ethylene Glycol). *Bioconjug. Chem.* **2008**, *19*, 2280–2284.

(31) Ikeda, A.; Doi, Y.; Nishiguchi, K.; Kitamura, K.; Hashizume, M.; Kikuchi, J.-I.; Yogo, K.; Ogawa, T.; Takeya, T. Induction of Cell Death by Photodynamic Therapy with Water-Soluble Lipid-Membrane-Incorporated [60]fullerene. *Org. Biomol. Chem.* **2007**, *5* (8), 1158–1160.

(32) Deguchi, S.; Alargova, R. G.; Tsujii, K. Stable Dispersions of Fullerenes, C_{60} and C_{70}, in Water. Preparation and Characterization. *Langmuir* **2001**, *17*, 6013–6017.

(33) Brusatin, G.; Signorini, R. Linear and Nonlinear Optical Properties of Fullerenes in Solid State Materials. *J. Mater. Chem.* **2002**, *12*, 1964–1977.

(34) Yang, X. L.; Fan, C. H.; Zhu, H. S. Photo-Induced Cytotoxicity of Malonic Acid [C60]fullerene Derivatives and Its Mechanism. *Toxicol. Vitr.* **2002**, *16*, 41–46.

(35) Doi, Y.; Ikeda, A.; Akiyama, M.; Nagano, M.; Shigematsu, T.; Ogawa, T.; Takeya, T.; Nagasaki, T. Intracellular Uptake and Photodynamic Activity of Water-Soluble [60]- and [70]fullerenes Incorporated in Liposomes. *Chemistry* **2008**, *14*

(29), 8892–8897.

(36) Ikeda, A.; Matsumoto, M.; Akiyama, M.; Kikuchi, J.; Ogawa, T.; Takeya, T. Direct and Short-Time Uptake of [70]fullerene into the Cell Membrane Using an Exchange Reaction from a [70]fullerene-Gamma-Cyclodextrin Complex and the Resulting Photodynamic Activity. *Chem. Commun. (Camb).* **2009**, 1547–1549.

(37) Boyd, P. D. W.; Reed, C. A. Fullerene-Porphyrin Constructs. *Acc. Chem. Res.* **2005**, *38* (February), 235–242.

(38) Gebhart, S. C.; Lin, W. C.; Mahadevan-Jansen, A. In Vitro Determination of Normal and Neoplastic Human Brain Tissue Optical Properties Using Inverse Adding-Doubling. *Phys. Med. Biol.* **2006**, *51*, 2011–2027.

(39) Karotki, A.; Khurana, M.; Lepock, J. R.; Wilson, B. C. Simultaneous Two-Photon Excitation of Photofrin in Relation to Photodynamic Therapy. *Photochem. Photobiol.* **2006**, *82*, 443–452.

(40) Tokuyama, H.; Yamago, S.; Nakamura, E.; Shiraki, T.; Sugiura, Y. Photoinduced Biochemical Activity of Fullerene Carboxylic Acid. *J. Am. Chem. Soc.* **1993**, *115* (12), 7918–7919.

(41) Burlaka, A. P.; Sidorik, Y. P.; Prylutska, S. V; Matyshevska, O. P.; Golub, O. a; Prylutskyy, Y. I.; Scharff, P. Catalytic System of the Reactive Oxygen Species on the C_{60} Fullerene Basis. *Exp. Oncol.* **2004**, *26*, 326–327.

(42) Rancan, F.; Rosan, S.; Boehm, F.; Cantrell, A.; Brellreich, M.; Schoenberger, H.; Hirsch, A.; Moussa, F. Cytotoxicity and Photocytotoxicity of a Dendritic C_{60} Mono-Adduct and a Malonic Acid C_{60} Tris-Adduct on Jurkat Cells. *J. Photochem. Photobiol. B Biol.* **2002**, *67*, 157–162.

(43) Mroz, P.; Pawlak, A.; Satti, M.; Lee, H.; Wharton, T.; Gali, H.; Sarna, T.; Hamblin, M. R. Functionalized Fullerenes Mediate Photodynamic Killing of Cancer Cells: Type I versus Type II Photochemical Mechanism. *Free Radic. Biol. Med.* **2007**, *43*, 711–719.

(44) Li, Z.; Pan, L. L.; Zhang, F. L.; Wang, Z.; Shen, Y. Y.; Zhang, Z. Z. Preparation and Characterization of Fullerene (C60) Amino Acid Nanoparticles for Liver Cancer Cell Treatment. *J. Nanosci. Nanotechnol.* **2014**, *14* (6), 4513–4518.

(45) Jiang, G.; Yin, F.; Duan, J.; Li, G. Synthesis and Properties of Novel Water-Soluble Fullerene-Glycine Derivatives as New Materials for Cancer Therapy. *J. Mater. Sci. Mater. Med.* **2015**, *26* (1), 1–7.

(46) Akiyama, M.; Ikeda, A.; Shintani, T.; Doi, Y.; Kikuchi, J. I.; Ogawa, T.; Yogo, K.; Takeya, T.; Yamamoto, N. Solubilisation of [60]fullerenes Using Block Copolymers and Evaluation of Their Photodynamic Activities. *Org. Biomol. Chem.* **2008**, *6*, 1015–1019.

(47) Tabata, Y.; Murakami, Y.; Ikada, Y. Photodynamic Effect of Polyethylene Glycol-Modified Fullerene on Tumor. *Japanese J. Cancer Res.* **1997**, *88* (11), 1108–1116.

(48) Otake, E.; Sakuma, S.; Torii, K.; Maeda, A.; Ohi, H.; Yano, S.; Morita, A. Effect and Mechanism of a New Photodynamic Therapy with Glycoconjugated Fullerene. *Photochem. Photobiol.* **2010**, *86* (6), 1356–1363.

(49) Li, Z.; Pan, L. L.; Zhang, F. L.; Zhu, X. L.; Liu, Y.; Zhang, Z. Z. 5-Aminolevulinic Acid-Loaded Fullerene Nanoparticles for in Vitro and in Vivo Photodynamic Therapy. *Photochem. Photobiol.* **2014**, *90*, 1144–1149.

(50) Shi, J.; Wang, L.; Gao, J.; Liu, Y.; Zhang, J.; Ma, R.; Liu, R.; Zhang, Z. A Fullerene-Based Multi-Functional Nanoplatform for Cancer Theranostic Applications. *Biomaterials* **2014**, *35* (22), 5771–5784.

(51) Scrivens, W.; Tour, J. Synthesis of 14C-Labeled C60, Its Suspension in Water, and Its Uptake by Human Keratinocytes. *J. Am. Chem. Soc.* **1994**, *116* (10), 4517–4518.

(52) Foley, S.; Crowley, C.; Smaihi, M.; Bonfils, C.; Erlanger, B. F.; Seta, P.; Larroque, C. Cellular Localisation of a Water-Soluble Fullerene Derivative. *Biochem. Biophys. Res. Commun.* **2002**, *294*, 116–119.

(53) Lucafò, M.; Pacor, S.; Fabbro, C.; Da Ros, T.; Zorzet, S.; Prato, M.; Sava, G. Study of a Potential Drug Delivery System Based on Carbon Nanoparticles: Effects of Fullerene Derivatives in MCF7 Mammary Carcinoma Cells. *J. Nanoparticle Res.* **2012**, *14*, 830.

(54) Porter, A. E.; Gass, M.; Muller, K.; Skepper, J. N.; Midgley, P.; Welland, M. Visualizing the Uptake of C 60 to the Cytoplasm and Nucleus of Human Monocyte-Derived Macrophage Cells Using Energy-Filtered Transmission Electron Microscopy and Electron Tomography. *Environ. Sci. Technol.* **2007**, *41* (8), 3012–3017.

(55) DeRosa, M. C.; Crutchley, R. J. Photosensitized Singlet Oxygen and Its Applications. *Coord. Chem. Rev.* **2002**, *233-234*, 351–371.

(56) Käsermann, F.; Kempf, C. Photodynamic Inactivation of Enveloped Viruses by Buckminsterfullerene. *Antiviral Res.* **1997**, *34* (1), 65–70.

(57) Aoshima H, Kokubo K, Shirakawa S, Ito M, Y. S.; T., O. Antimicrobial Activity of Fullerenes and Their Hydroxylated Derivatives. *Biocontrol. Sci.* **2009**, *14*, 69–72.

(58) Tegos, G. P.; Demidova, T. N.; Arcila-Lopez, D.; Lee, H.; Wharton, T.; Gali, H.; Hamblin, M. R. Cationic Fullerenes Are Effective and Selective Antimicrobial Photosensitizers. *Chem. Biol.* **2005**, *12* (10), 1127–1135.

(59) Spesia, M. B.; Milanesio, M. E.; Durantini, E. N. Synthesis, Properties and Photodynamic Inactivation of Escherichia Coli by Novel Cationic Fullerene C60 Derivatives. *Eur. J. Med. Chem.* **2008**, *43*, 853–861.

(60) Lee, I.; Mackeyev, Y.; Cho, M.; Li, D.; Kim, J. H.; Wilson, L. J.; Alvarez, P. J. J.; Lee, J. Photochemical and Antimicrobial Properties of Novel C_{60} Derivatives in Aqueous Systems. *Environ. Sci. Technol.* **2009**, *43* (17), 6604–6610.

(61) Grinholc, M.; Nakonieczna, J.; Fila, G.; Taraszkiewicz, A.; Kawiak, A.; Szewczyk, G.; Sarna, T.; Lilge, L.; Bielawski, K. P. Antimicrobial Photodynamic Therapy with Fulleropyrrolidine: Photoinactivation Mechanism of Staphylococcus Aureus, in Vitro and in Vivo Studies. *Appl. Microbiol. Biotechnol.* **2015**, *99* (9), 4031–4043.

(62) Chauhan, P.; Hadad, C.; Sartorelli, A.; Zarattini, M.; Herreros-López, A.; Mba, M.; Maggini, M.; Prato, M.; Carofiglio, T. Nanocrystalline Cellulose-Porphyrin Hybrids: Synthesis, Supramolecular Properties, and Singlet-Oxygen Production. *Chem. Commun.* **2013**, *49* (76), 8525–8527.

(63) Feese, E.; Sadeghifar, H.; Gracz, H. S.; Argyropoulos, D. S.; Ghiladi, R. a. Photobactericidal Porphyrin-Cellulose Nanocrystals: Synthesis, Characterization, and Antimicrobial Properties. *Biomacromolecules* **2011**, *12*, 3528–3539.

(64) Kordatos, K.; Da Ros, T.; Bosi, S.; Vázquez, E.; Bergamin, M.; Cusan, C.; Pellarini, F.; Tomberli, V.; Baiti, B.; Pantarotto, D.; Georgakilas, V.; Spalluto, G.; Prato, M. Novel Versatile Fullerene Synthons. *J. Org. Chem.* **2001**, *66* (23), 4915–4920.

(65) Kamitani, R.; Niikura, K.; Okajima, T.; Matsuo, Y.; Ijiro, K. Design of Cell-Surface-Retained Polymers for Artificial Ligand Display. *ChemBioChem* **2009**, *10*, 230–233.

(66) Kuzmany, H.; Matus, M.; Burger, B.; Winter, J. Raman-Scattering in C_{60} Fullerenes and Fullerides. *Adv. Mater.* **1994**, *6* (10), 731–745.

(67) Douglas A. Skoog, Stanley R. Crouch, F. J. H. *Principles of Instrumental Analysis*; Learning, C., Ed.; 2006.

(68) Maggini, M.; Scorrano, G.; Prato, M. Addition of Azomethine Ylides to C_{60}: Synthesis, Characterization, and Functionalization of Fullerene Pyrrolidines. *J. Am. Chem. Soc.* **1993**, *115* (3), 9798–9799.

(69) Michaeli, a; Feitelson, J. Reactivity of Singlet Oxygen toward Amino Acids and Peptides. *Photochem. Photobiol.* **1994**, *59* (3), 284–289.

(70) Sysak, P. K.; Foote, C. S.; Ching, T. Y. Chemistry of Singlet Oxygen-XXV. Photooxygenation of Methionine. *Photochem. Photobiol.* **1977**, *26*, 19–27.

(71) Kajiwara, T.; Kearns, D. R. Direct Spectroscopic Evidence for a Deuterium Solvent Effect on the Lifetimes of Singlet Oxygen in Water. *J. Am. Chem. Soc.* **1973**, *95* (1964), 5886–5890.

(72) Concerti, A.; Gariboldi, P. Methionine Sulfoxide Formation in Proteins: NMR Study. *Biol. Met.* **1990**, *3*, 125–126.

(73) Jolene, B. *Flow Cytometry Basics*; 2015.

(74) A. Singh, K. . G. Confocal Microscopy: A Powerful Technique for Biological Research. *Curr. Sci.* **1998**, *74*, 10–25.

(75) Carini, M. New Approaches to the Multiple Funcionalization of Fullerene. PhD Thesis, University of Trieste, 2014.

Chapter 5: Exfoliation of 2D materials in aqueous suspension of ox-NCC: New nanohybrids for electronic devices.

5.1. Introduction

5.1.1. Production and properties of 2D materials

2-Dimensional materials are a class of nanomaterials defined by their property of being merely one or two atoms thick. As a consequence of the restriction in size with respect to the corresponding bulk materials, new fascinating properties arise. Optical and electronic properties change due to electron confinement, along with other changes in mechanical and chemical properties as a result of the high surface-bulk ratio.[1] The field of research in 2D materials was born with the discovery of graphene, a single layer of carbon atoms arranged in a hexagonal honeycomb lattice. During the last decades, an extensive effort was invested in obtaining graphene layers from bulk graphite, with the aim of having access to the predicted properties of a single layer of sp^2 carbon. Eventually, single layers of graphite were first isolated by Novoselov et al. in 2004, by mechanical exfoliation from small mesas of highly oriented pyrolytic graphite.[2] Graphene combined ultrahigh carrier mobility at room temperature (10 000 $cm^2 \cdot V^{-1} \cdot s^{-1}$), quantum hall effect, large theoretical specific surface area, excellent thermal conductivity, mechanical properties and optical transparency (97.7%). [3–6]

Concerning its production, a plethora of methods has been proposed for the preparation of graphene since it was first isolated. Depending on the strategy, they may be classified into bottom up or top down approaches. The former consist in the construction of graphene from a carbon source. The latter take advantage of the layered structure of graphite, in which graphene sheets are stacked together by weak van der Waals forces and thus can be easily cleavaged into single layers. A summary of the main graphene production techniques developed so far is illustrated inFigure 1.

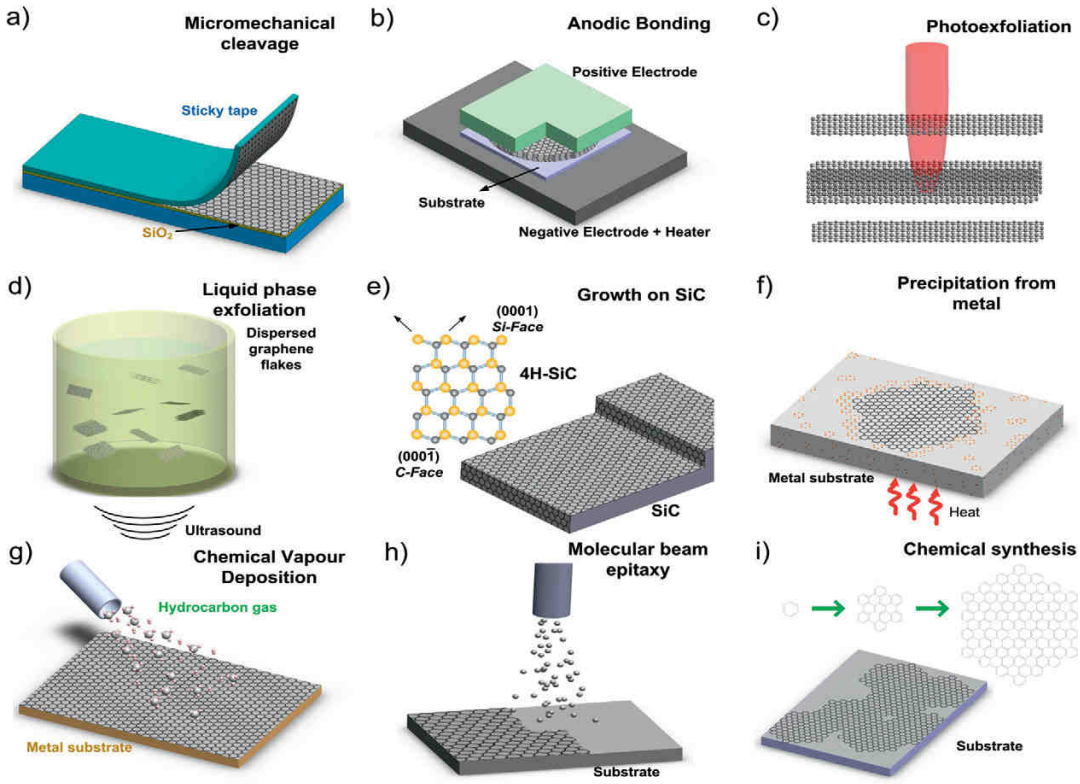

Figure 1. Schematic illustration of the main graphene production techniques. (a) Micromechanical cleavage. (b) Anodic bonding. (c) Photoexfoliation. (d) Liquid phase exfoliation.(e) Growth on SiC. (f) Segregation/precipitation from carbon containing metal substrate. (g) Chemical vapor deposition. (h) Molecular Beam epitaxy. (i) Chemical synthesis using benzene as building block.[19]

Bottom up methods include chemical vapor deposition (CVD),[7] metal precipitation,[8] synthesis on silicon carbide (SiC)[9] and molecular beam epitaxy,[10] whereas top down methods comprise micromechanical cleavage,[11] anodic bonding,[12] laser ablation,[13] liquid phase exfoliation, either in organic solvents or surfactant assisted in water,[14,15] lithium intercalation and exfoliation,[16] electrochemical exfoliation,[17] hydrothermal and solvothermal methods.[18]

Probably the method with most potential for scale up is liquid exfoliation, for its simplicity. In this process, successful exfoliation requires the overcoming of the van der Waals attraction between adjacent graphene layers. If the interfacial tension between solid and liquid is high, the flakes tend to adhere to each other instead of dispersing in the liquid. Solvents with surface tension (γ) (i.e. the property of the surface of a liquid that allows it to resist an external force, due to the cohesive nature of its molecules) of ~ 40 mJ/m^2 have been found to be the best solvents for the dispersion of graphene.[14] Unfortunately, the majority of solvents with γ 40 mJ/m^2 such as N-methyl-2-pyrrolidone (NMP – 40 mJ/m^2), N,N-dimethylformamide (DMF – 37.1 mJ/m^2), and ortho-dichlorobenzene (o-DCB – 37 mJ/m^2) have been found to have toxic effects on multiple organs.[20] Therefore, the search for additional solvents in this context is highly recommended in order to strengthen the universal character of this genuine approach. Water is a natural choice because of its non-toxicity and

availability. However, the exfoliation of graphene in water is particularly challenging due to the hydrophobic nature of the graphene sheets. Such a challenge can be overcome by using surfactants to promote the exfoliation of graphite in aqueous solutions. Proposed surfactants include small aromatic molecules, such as perylene or pyrene based molecules due to their strong π-π interactions with graphene layers, as well as ionic liquids or even polymers.[21] Moreover, the surfactants can prevent the reaggregation of the graphene sheets, and relatively high concentrations of suspended graphene have been reported. However, the main drawback of using surfactants is often the impossibility to remove them afterwards, which may affect the quality and properties of the resulting graphene.

Apart from graphene, the 2D materials family includes hexagonal boron nitride (h-BN), transition metal dichalcogenides (TMDs), with common formula of MX_2 (for example, WS_2, MoS_2, and WSe_2) or MXenes, derived from hexagonal carbides and nitrides that can accommodate various ions and molecules between their layers by intercalation, among others (Figure 2).[22]

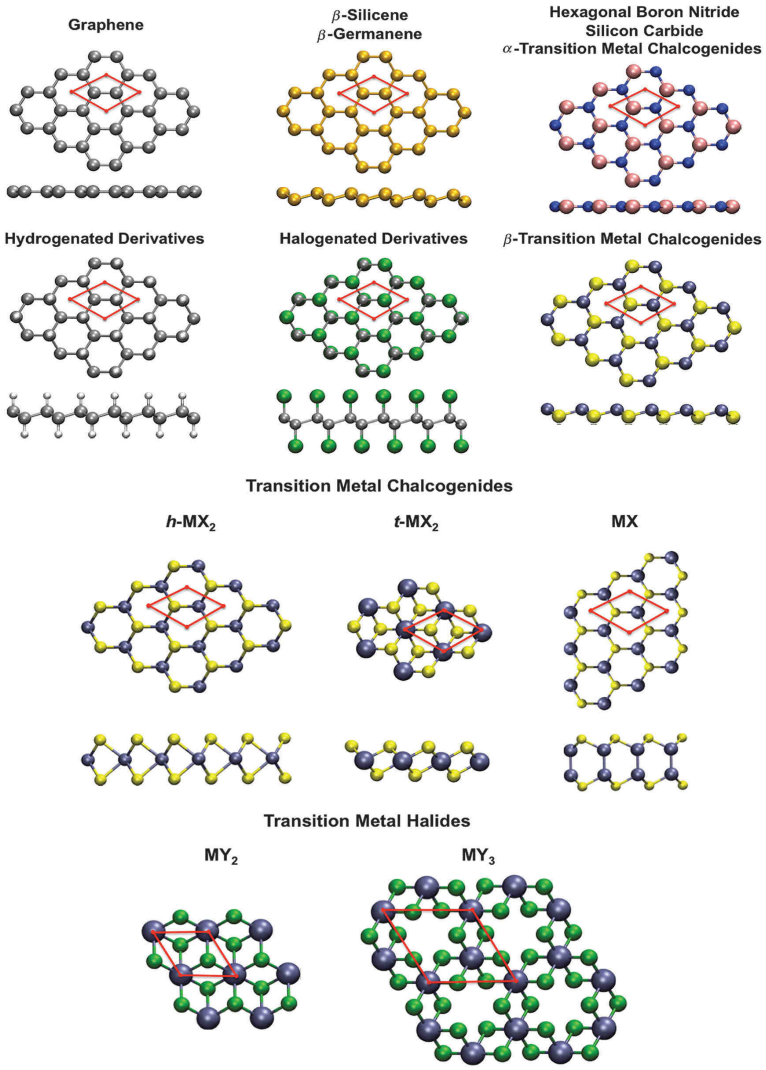

Figure 2. Structure of atomically thin 2D materials. Unit cells are depicted in red.[23]

2D materials have rapidly become an important field in current materials research because of the physicochemical characteristics, which differ from the bulk counterparts. It is important to highlight that electrical properties of 2D materials may be tailored by playing with the composition of the material. In this way, a new generation of conductors, metallic materials, semimetals, semiconductors or even insulators can be obtained from 2D materials.[22]

Most of the techniques used to obtain graphene may be extended to the production of other layered materials. As such, different single layer materials have been successfully exfoliated from their bulk crystals through mechanical exfoliation.[24] Monolayers of BN, MoS_2, $NbSe_2$, among others, have been prepared by rubbing a fresh surface of a layered crystal against another surface, leaving a variety of flakes attached to it.[24] Among the resulting flakes, single layers were always found. The resulting 2D materials so obtained exhibit high crystal quality and macroscopic continuity, as in the case of graphene. Liquid exfoliation by direct sonication in different solvents has also been studied. MoS_2 and WS_2 flakes with a thickness from single to few layers were obtained using NMP.[25] Zeng et al. developed an electrochemical Li intercalation and exfoliation method to prepare high-yield single-layer TMX_2, including MoS_2, WS_2, TiS_2, TaS_2, ZrS_2, $NbSe_2$, WSe_2, Sb_2Se_3 and Bi_2Te_3.[26,27] Smith *et al.* developed a method to exfoliate MoS_2 in aqueous surfactant solutions, which could be easily extended to other inorganic layered compounds.[28]

Regarding bottom-up approaches, several CVD methods for large-scale MoS_2 ultrathin films have been reported recently. A typical process follows these two steps: first, different Mo and sulfur precursors are heated to a high temperature to induce evaporation; second, MoS_2 deposit on the substrates at the cold zone. For example, molybdenum trioxide (MoO_3) and sulfur powder,[29] ammonium tetramolybdate precursor ($(NH_4)_2MoS_4$) containing both molybdenum and sulfur,[28,30–32] or molybdenum metal thin film on a substrate and sulfur powder[33] have been used.

2D nanostructures are anticipated to have an important influence on a wide variety of applications in the next years, ranging from high performance sensors, electronics to gas separation and storage, catalysis, inert coatings, support membranes, etc.[34] Energy applications in particular show high promise,[35]with breakthroughs expected in lithium-ion batteries, supercapacitors, and hydrogen storage.[36] Some 2D crystals are also promising for photovoltaics applications because of the good photocatalytic properties of their edges. The creation of hybrids with graphene and other nanomaterials, such as carbon nanotubes (CNTs), shows great promise in this field.[1,36]

However, a key requirement for real-life applications of these materials is the development of industrial scale, reliable and inexpensive production methods that balance materials quality with easy fabrication. In this context, compromise between cost and quality must be accomplished.

5.1.2. Dye sensitized solar cells

One of the most important challenges of this century is the use of clean and renewable energy technologies such as solar energy. Photovoltaic (PV) devices like

organic, inorganic and hybrid cells have been developed to harness this energy. A solar cell is a photonic device that converts photons with specific wavelengths to electricity.

The beginning of photovoltaics can be traced back to 1839, when Alexandre E. Becquerel discovered the photovoltaic effect. While experimenting with a solid electrode in an electrolyte solution, he saw a voltage developed when light fell upon the electrode. But it was not until the 1950s that research on photovoltaics started in a large extent, when Bell Labs made the first device that converted sunlight into electrical power.[37] These encouraging results have spurred continuous development in this area ever since. Many types and structures of solar cells have been devised. Traditional solar cells are mainly constructed from semiconductors, mostly silicon. These cells are based on p-n junctions, and are often referred to as first-generation solar cells. Second-generation PVs are based on thin-film technologies, and their efficiency is lower than silicon. The latest –third- generation of solar cells is based on organic molecules. After Gräetzel *et al.* created modern dye sensitized solar cells (DSSC) in 1991,[38] these photoelectrochemical devices emerged as a renewable energy source due to their relatively high efficiency, environmental friendliness and simple fabrication process. These cells work on the principles of photosynthesis, the naturally occurring process in plants which sustains life on Earth.

The structure of a DSSC is schematically represented in Figure 3. The cell is composed of four elements, namely, the transparent conducting photoanode and counter electrode, the dye molecules (sensitizer), and the electrolyte. The photoanode is composed of nanostructured TiO_2 film with adsorbed dye molecules. Such dye molecules are typically a metallorganic ruthenium complex.[39] The electrolyte generally consists of an acetonitrile solution containing a triiodide (I_3^-)/iodide (I^-) mixture, which has shown to be the most suitable redox couple,[40]and the counter electrode is usually made of platinum.[41] The transparent electrode and counter-electrode are coated with a thin film of transparent conductive oxide (TCO), such as indium tin oxide (ITO) or fluorine doped tin oxide (FTO).

The operation principle of a typical DSSC is depicted in Figure 4. Firstly, a photon reaches the cell through the transparent electrode and is absorbed by a dye molecule. The photon promotes an electron from the highest occupied molecular orbital

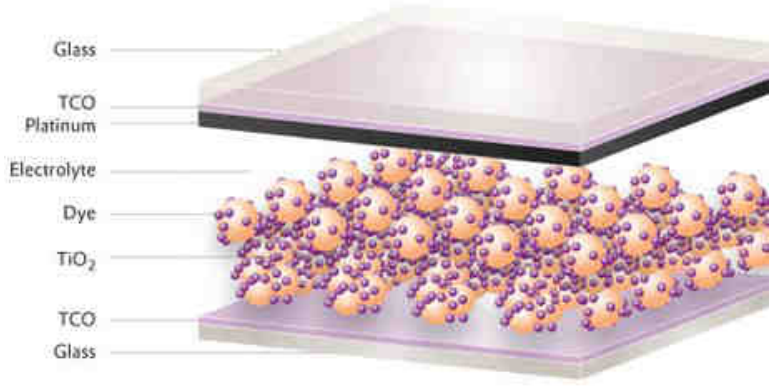

Figure 3. Schematic representation of DSSC structure.[42]

(HOMO) to the lowest unoccupied molecular orbital (LUMO) state of the dye. The energy of the LUMO is higher than the energy threshold of the conduction band in TiO_2 (wide band gap semiconductor). Thus, the electron is conducted towards the electric load of the circuit and the dye becomes oxidized. The dye recovers the lacking electron from a I^- ion present in the electrolyte solution that gets oxidized to I^{3-}. Finally, the I^{3-} ion is reduced back to I^- by receiving an electron from the external load, closing the cycle. In a global energy balance, part of the energy provided from the photon is employed in this process of regenerating oxidized dye molecules and hence complete the electric circuit.[43] Therefore, a catalyst that minimizes the energy consumption of the redox process contributes to increase the efficiency of the DSSC. This makes counter electrode (CE) one of the most important elements in the DSSC, since it has a double role, in fact, it back transfers electrons arriving from the external circuit to the redox system and it catalyzes the reduction of the electrolyte. A platinized catalyst is tipically used as a counter electrode for several reasons: it acts as a good catalyst that helps in regeneration of I^- from I_3^-,[44] possesses high exchange current density for the collection of electrons from the external load to the electrolyte and has high transparency.[45]

The key problem that has to be considered in the CE is the need to replace Pt, a noble metal in diminishing supply. In order to reduce the cost and improve the electrocatalytic activity of the counter electrode (CE), combinations of platinum with carbon nanoforms (nanofiber, carbon nanotubes, graphene) and polymers have been fabricated and intensively studied.[41] Although the catalytic performance has been improved, commercialization at a large scale is still a problem and recent research focuses on the development of totally platinum-free CEs.

Among the alternatives employed in the construction of this type of CE, conductive polymers, or transition metals (carbides, nitrides, oxides or sulfides), [41,47]graphene or its derivatives, the latter seems to be one of the best candidates.[48] Graphene

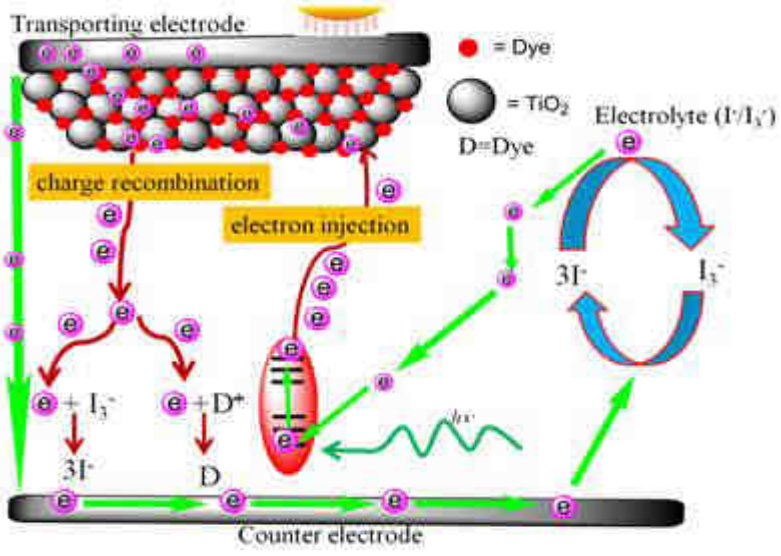

Figure 4. Schematic representation of the operation mechanism of a DSSC.[46]

matches all the counter-electrode requirements because of its high surface area, which is essential to help the I^{3-} reduction, high electric conductivity, low charge-transfer resistance, and lower cost than platinum.

To date, reported efficiencies (ŋ) of platinum-based cells range between 4.2 and 12%, depending on the conditions (where efficiency is defined as the cell's maximum power output divided by the input power from the light source).[49,50] Due to the high variability in Pt efficiency from one system to another, it is common practice to refer the efficiency of a given system to a Pt CE of control measured under the same experimental conditions of the particular work, rather than comparing between different systems.

So far, graphene oxide and hybrid structures of reduced graphene oxide (rGO) with carbon nanotubes (CNTs) have been used as counter electrodes in DSSCs, with results close to the state of the art with platinum. In particular, Roy-Mayhew *et al.* applied functionalized graphene sheets (FGSs) with oxygen-containing sites as a stand-alone catalyst in a dye-sensitized solar cell (DSSC), and demonstrated FGS-based cells with efficiencies only 10% lower than platinum-based cells.[50]Choi *et al.* proposed multi-walled carbon nanotubes grown vertically by chemical vapor deposition on graphene layers using iron catalyst. The demonstrated that catalytic properties were highly dependent on the structure of the electrode.[51] In another study, Kavan *et al.* prepared graphene nanoplatelets (sheets of functionalized graphene with an overall thickness ranging from~2 to~15nm, GNP) in the form of thin semitransparent films on F-doped tin oxide (FTO). GNPs exhibited high electrocatalytic activity for the $Co(bpy)_3$ $^{3+/2+}$ redox couple in acetonitrile electrolyte solution. The GNP film was superior to the traditional platinum electrocatalyst, both in charge-transfer resistance (exchange current) and in electrochemical stability under prolonged potential cycling.[52] Graphene nanoplatelets are now emerging as the best performing counter electrodes in DSSCs, reporting the highest ŋ to date (13%).[53]

It has been shown that pure graphene has an excellent conductivity, and is potentially a good alternative to platinum by itself. However, it has a limited number of active sites and intrinsic activity can be improved through chemical functionalization of the material. Another alternative that has seen a rising interest as counter electrodes in DSSCs is the combination of graphene with other 2D materials, such as chalcogenide semiconductors. A combination of highly electrocatalytic InS_2 and graphene on FTO have proven to be feasible substitutes for Pt. The resulting efficiency using graphene/$CuInS_2$/FTO counter electrode was 6.18%, only slightly lower than the 6.52% of Pt CE of reference.[54]

In particular, from the transition metal dichalcogenides, examples with molybdenum disulfide (MoS_2) in combination with graphene showed outstanding performance. MoS_2 is an earth-abundant inorganic compound comprising a Mo layer sandwiched between two S layers stacked and held together by weak van der Waals interactions. In the CE of a DSSC, MoS_2 would play the role of triiodide/iodide reduction catalyst, while graphene would provide a high surface area of electron pathways,[55] both fundamental processes for the good performance of the CE. A transparent MoS_2–graphene nanosheet (GNS) nanocomposite counter electrode (CE) was incorporated into a Pt-free dye-sensitized solar cell (DSSC). [56] The DSSC assembled with this

exhibited an impressive photovoltaic conversion efficiency of 5.81%, up to 93% of that obtained using the conventional Pt CE (6.24%).Liu *et al.* synthetized a nanocomposite of MoS_2 and graphene oxide (GO) by mixing GO nanosheets with a solution of ammonium tetrathiomolybdate ($(NH_4)_2MoS_4$) and then converting the solid intermediate into the corresponding reduced graphene oxide (RGO) MoS_2/RGO nanocomposite in a H_2 flow at 650 °C (Figure 5). The resulting CE reached a power efficiency of 6.04%, comparable to that of Pt (6.38%).[57] They showed that the functional groups in GO are critical to the immobilization of MoS_2 nanoparticles onto the graphene surface and the density of MoS_2 nanoparticles on graphene can be modulated by the concentration of ammonium tetrathiomolybdate.

The same group demonstrated that graphene flakes (GF) can be successfully embedded into a nanosheet-like molybdenum sulphide (MoS_2) matrix via an in situ hydrothermal route.[58] The conversion efficiency achieved was of 6.07% similar to the 6.41% of the conventional Pt CE.

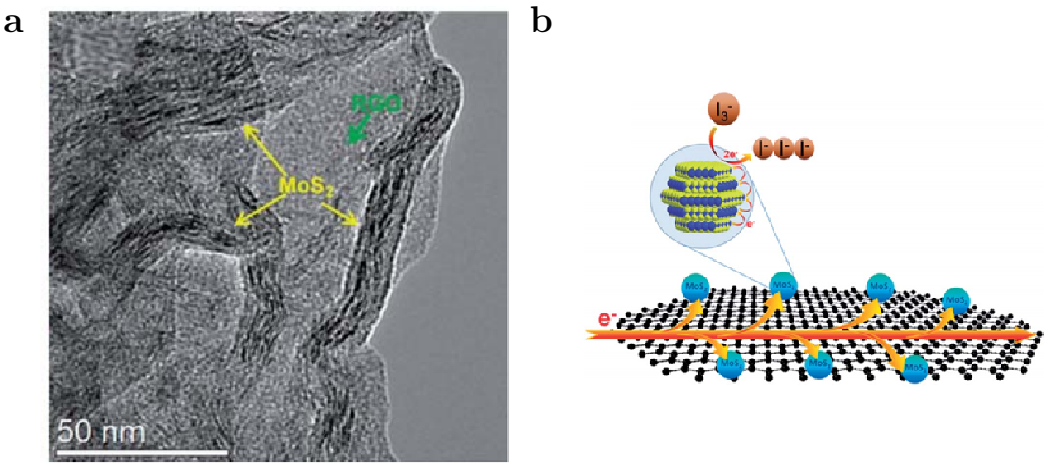

Figure 5. TEM image representing MoS_2 nanoparticles onto graphene flakes (a) and proposed catalytic mechanism for the reduction of I_3^-/I^- redox couple (b).[57]

These, among other examples, suggest that functionalization or hybridization of 2D materials, and in particular graphene and MoS_2, is an established and effective way to improve the catalytic properties of individual components and the hybrids as a whole.[59]

5.1.3. Hybrid NCC-based 2D materials

Growth of large area, high-quality, single-crystal 2D materials, required for the practical realization of 2D-based technologies and for high-volume manufacturing, is perhaps one of the most challenging tasks. The success of graphene and related materials for energy applications crucially depends on the development and optimization of production methods. High-volume liquid-phase exfoliation needs to be optimized to control the flake size and to increase the edge-to-surface ratio, which is crucial for optimizing electrode performance, and to move towards greener solvents

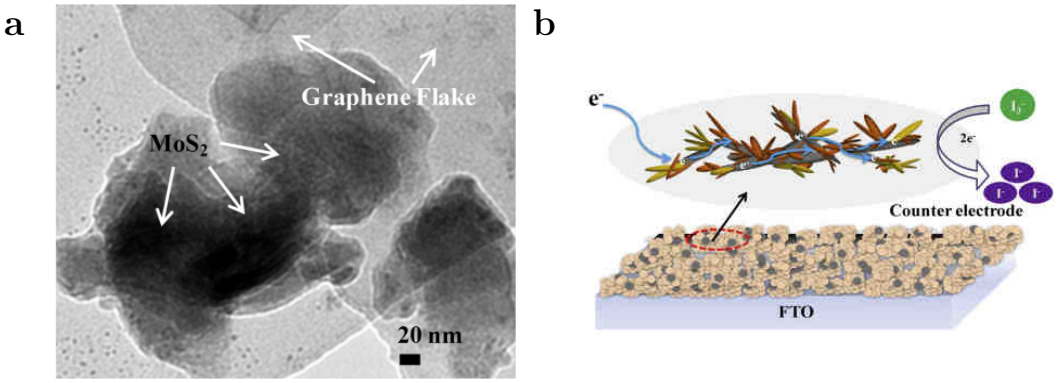

Figure 6. TEM image of the a MoS2/graphene flakes (GF) hybrid (a) and schematic for the possible synergistic effect on the enhanced electrocatalytic activity of the MoS_2/GF hybrid (b)

Nanocrystalline cellulose has turned out to be a very convenient choice for exfoliating graphene in an eco-friendly way, giving rise to very stable suspensions of this material in water. The first example of hybrid based on a combination of graphene and NCC was reported by Valentini *et al* (Figure 7).[60] A suspension of NCC was added to a dispersion of graphene oxide (GO) and mixed together using ultrasonication after which films were prepared from this mixture by drop casting. One of the disadvantages of using GO compared to graphene is the absence of charge carrier transfer due to the high resistance resulting from the presence of many defects (oxygen containing groups) on the surface. To address this problem, the author performed the thermal reduction of GO by applying a large current passing through the film, thereby heating it and inducing a de-oxygenation and consequently an increase in conductivity. These thin-film devices also present a reversible memory effect due to the presence of GO when applying a positive or negative bias voltage, inducing high/low conductivity states.[61] These results are of the highest importance since they showed the possibility of using nanocellulose in the field of data storage electronic devices fabrication. The same group reported also on the use of transparent and conductive graphene nanoplatelets (GNPs)/NCC film for the fabrication of polymer solar cells.[62]

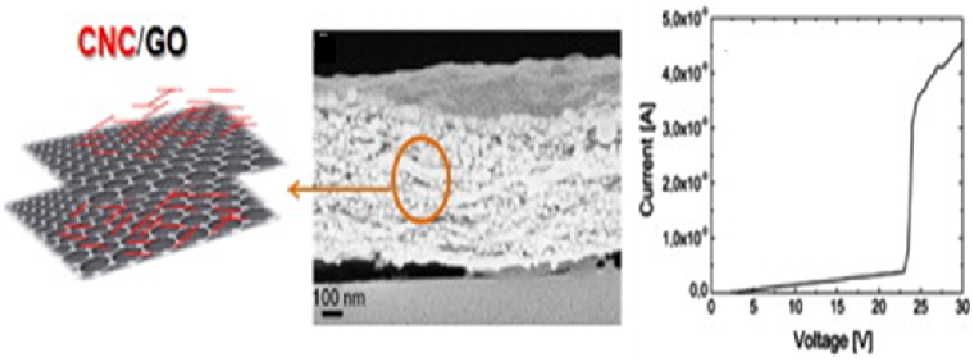

Figure 7. Schematic representation of NCC/GO, cross section (left), Field emission scanning electron microscopy (FESEM) image of NCC/GO composite film (center) and current–voltage curve of NCC/GO composite film (right).[60]

The best composition for the fabrication of the film, obtained by drop casting on an indium tin oxide (ITO) support, was found to be 10 mL of NCC suspension (0.5 wt%) with 10 mL of GNP (1 wt%) resulting in a good compromise between the problem phase separation due to an increase of the GNP concentration and the low conductivity of the film for higher NCC concentration. This optically transparent film, enabling light to go through was integrated in polymer solar cell. Even if the performance of such solar cells were modest, many parameters, such as the composition of the NCC based film, or the orientation of the NCC can be optimized to improve their power conversion efficiency (ŋ) as well as the optimization of the mechanical properties should lead to completely recyclable solar cell technology.

5.2. Aim of the work

As mentioned in the previous section, several works suggest that NCC materials may be a convenient choice to promote the exfoliation of 2D materials in aqueous medium and for the preparation of flexible nanodevices for energy storage applications.[61,62]

The work in this Chapter is oriented toward the development of a sustainable, scalable method for the exfoliation of graphite and bulk MoS_2 materials in aqueous environment. Ox-NCC is used as exfoliating and stabilizing agent. Several parameters will be studied in order to obtain the best conditions in terms suspensions stability in water, quality of exfoliation and electronic properties.

Moreover, thanks to the intrinsic film-forming properties of ox-NCC, graphene and/or MoS_2 containing films with high flexibility, transparency and different conductivities can be prepared by simple evaporation of the resulting suspensions.

These novel nanodevices are proposed as cost-effective alternative to platinum as counter electrodes in DSSCs and could also be used for other electronic applications.

5.3. Results and discussion

Ox-NCC_3 was chosen as dispersing agent for the exfoliation of 2D materials due to its better colloidal stability in water with respect to NCC. Synthesis and characterization of ox-NCC_3 was fully discussed in Chapter 2. In this chapter, ox-NCC will be referred to as ox-NCC for clarity.

As graphitic starting material, expanded graphite (EG) was preferred, since its pretreatment facilitates the exfoliation process. Normally this pretreatment involves sonication in small amount of stabilizating solvents, such as NMP, followed by filtration.[63] This implies a significant reduction of the time required to produce dispersions of solvent-exfoliated graphene from the obtained powder.

Molybdenum disulfide is an inorganic semiconductor with formula MoS_2, classified as a metal dichalcogenide. It was chosen as additional 2D material to mix with graphene, as it has been suggested that the combination of these two components is particularly suitable as CE of a DSSC.

5.3.1. Effect of sample preparation conditions

The liquid phase exfoliation of 2D materials yield is highly influenced by experiment parameters. For this reason, the effect of preparation conditions was studied in order to maximize the yield of exfoliation. All samples in this study were prepared following the same basic procedure (section 5.5.3). Briefly, ox-NCC was dispersed in water in a sonication bath, after which EG and MoS_2 powders were added. Exfoliation was promoted by ultrasonication in an ice bath to avoid overheating of the sample and minimize creation of defects in the exfoliated materials, and centrifugation was performed afterwards to remove eventual non-exfoliated sediment. Conditions were varied in order to find the best parameters, and are summarized in the next section. Corresponding blanks were prepared in absence of ox-NCC to study the effect of ox-NCC in stability and yield of exfoliation. The success of exfoliation was firstly judged by the color of the dispersions obtained and their stability.

EG or bulk MoS_2 load

In first place, dispersions with initial concentration of EG or MoS_2 powder from 10-60 mg were prepared (in 45 mL of ox-NCC 2 mg/mL). The dispersions were sonicated for 60 min. Then samples were centrifuged at 1000 rpm for 1 h, and the supernatant at 3000 rpm for 30 min (centrifugation protocol 1) to remove any non-exfoliated material. Conditions are summarized in Table 9.

The content of graphene in the suspensions was higher with increased initial loading of graphene or MoS_2, as expected. In order to further increase the 2D materials content in the suspensions, the highest concentrations were kept in all cases for the following tests and other conditions were varied.

Table 9. Sample preparation conditions to study the effect of .EG or bulk MoS_2 load.

Entry	ox-NCC [mg/mL]	EG (mg)	MoS_2 (mg)	Sonication Time (h)	Centrifugation protocol*
1†	2	10	-	1	1
2†	2	20	-	1	1
3†	2	30	-	1	1
4†	2	60	-	1	1
5†	2	-	10	1	1
6†	2	-	20	1	1
7†	2	-	30	1	1
8†	2	-	60	1	1
9†	2	30	30	1	1
10†	2	60	60	1	1

†: characterization not shown in the manuscript

*: centrifugation protocol 1: 1000 rpm, 1 h + 3000 rpm, 30 min.

Sonication time

It has been reported for various nanomaterials that prolonged sonication results in increased dispersion concentrations. In order to test the effect of sonication time on the exfoliation yield, high-load samples of EG and MoS_2 in 45 mL of 2 mg/mL **ox-NCC** suspension were sonicated for 1 and 2 hours (Table 10). The samples were then centrifuged at 1000 rpm, for 1h and supernatant again at 3000 rpm for 30 min (centrifugation protocol 1). The concentration of graphene or MoS_2 in the suspensions did not considerably increase by applying longer sonication time. In addition, longer sonication times have been related to higher amount of defects,[64] with a subsequent loss of electronic properties. Therefore, longer sonication times were discarded.

Table 10. Sample preparation conditions to study the effect of sonication time.

Entry	ox-NCC [mg/mL]	EG (mg)	MoS_2 (mg)	Sonication Time (h)	Centrifugation protocol*
1†	2	60	-	1	1
2†	2	60	-	2	1
3†	2	-	60	1	1
4†	2	-	60	2	1

†: characterization not shown in the manuscript,

*: centrifugation protocol 1: 1000 rpm, 1 h + 3000 rpm, 30 min.

Centrifugation protocol

The concentration of graphene in suspension is strongly influenced not only by sonication time but also centrifugation conditions.[65] In order to evaluate the effect of the centrifugation in the exfoliation yield, different centrifugation protocols were applied (Table 11).

Table 11. Sample preparation conditions to study the effect of centrifugation protocol.

Entry	ox-NCC [mg/mL]	EG (mg)	MoS_2 (mg)	Sonication Time (h)	Centrifugation Protocol*
1§	2	60	-	1	2
2†	2	60	-	1	3
3§	2	60	-	1	4
4†	2		60	1	2
5†	2		60	1	3
6†	2		60	1	4
7†	2	60	60	1	2
8†	2	60	60	1	3
9†	2	60	60	1	4

§: characterization shown in the manuscript

†: characterization not shown in the manuscript,

*: centrifugation protocol 2: 1000 rpm, 1 h; centrifugation protocol 3: 1000 rpm, 1 h + 2000 rpm, 30 min; centrifugation protocol 4: 1000 rpm, 1 h + 2000 rpm, 30 min + 3000 rpm, 30 min.

The highest concentration of 2D materials was obtained in all cases with protocol 2 (i.e 1000 rpm, 1 h). As expected, lower centrifugation speed resulted in less removal of graphene or MoS_2 flakes from the suspension, yet probably at expense of the size distribution.

ox-NCC concentration

For further application of the exfoliated material, it was of crucial importance to maximize the ratio of 2D materials to ox-NCC, maintaining stability of the exfoliated sheets in water. In view of this, the last experiment consisted in studying how decreasing ox-NCC to 1 mg/mL affected the yield compared to the corresponding samples using ox-NCC at 2 mg/mL (Table 12).

Both graphene and MoS_2 concentration and exfoliation yield were higher with the amount of ox-NCC of 2 mg/mL. However, the yield of exfoliation using 1 mg/mL the yield of exfoliation was more than half the one achieved with ox-NCC at 2 mg/mL in the same conditions. In other words, decreasing ox-NCC increased the relative ratio 2D material/ox-NCC in the dispersion.

Table 12. Sample preparation conditions to study the effect of ox-NCC concentration.

Entry	ox-NCC [mg/mL]	EG (mg)	MoS_2 (mg)	Sonication Time (h)	Centrifugation protocol*
1§	1	60	-	1	2
2†	1	60	-	1	3
3§	1	60	-	1	4
4§	1	60	60	1	2
5†	1	-	60	1	3
6†	1		60	1	4
7§	1	60	60	1	2
8†	1	60	60	1	3
9†	1	60	60	1	4

§: characterization shown in the manuscript

†: characterization not shown in the manuscript,

*: centrifugation protocol 2: 1000 rpm, 1 h; centrifugation protocol 3: 1000 rpm, 1 h + 2000 rpm, 30 min; centrifugation protocol 4: 1000 rpm, 1 h + 2000 rpm, 30 min + 3000 rpm, 30 min.

5.3.2. Characterizations

As seen above, many different samples, covering a wide variety of preparation conditions were studied. In the interest of brevity, in the following sections only a subset will be presented and discussed in detail. Selected samples and conditions are summarized in Table 13. These samples are representative of the whole and serve to illustrate the trends observed. The exfoliation of MoS_2 followed the same trend as graphene for all parameters studied, so influence is discussed for graphene and only best conditions are presented for MoS_2 and mixture graphene/MoS_2 samples. Intermediate conditions yielded correspondingly intermediate results and are omitted.

Table 13. Sample preparation conditions for the samples discussed in this Chapter.

Sample	Entry	ox-NCC [mg/mL]	EG (mg)	MoS_2 (mg)	Sonication Time (h)	Centrifugation protocol*
Blank EG	-	-	60	-	1	2
Blank MoS_2	-	-	-	60	1	2
Ox-NCC@G_1	Table 3, 1	2	60	-	1	4
Ox-NCC@G_2	Table 3, 3	2	60		1	4
Ox-NCC@G_3	Table 4, 1	1	60	-	1	2
Ox-NCC@G_4	Table 4, 3	1	60	-	1	2
Ox-NCC@MoS2	Table 4, 4	1	60	-	1	2
Ox-NCC@G/MoS_2	Table 4, 7	1	60	60	1	2

*: centrifugation protocol 2: 1000 rpm, 1 h; centrifugation protocol 4: 1000 rpm, 1 h + 2000 rpm, 30 min + 3000 rpm, 30 min.

Dispersion stability

Assuming that expanded graphite (EG) and bulk MoS_2 are insoluble, we can roughly estimate a qualitative exfoliation to few-layer graphene or MoS_2 in ox-NCC suspension. The stability of the obtained samples was evaluated over time. Some precipitate appeared after 24 - 48 h (Figure 8) but the remaining material was stable for weeks at room temperature. On the contrary when EG or MoS_2 were exfoliated in the same conditions using only water flakes settled down completely in the case of EG, and almost completely for MoS_2, within a few hours and without centrifugation. These samples are shown in Figure 8a and b for visual comparison. Upon centrifugation of the blanks, supernatant was colorless in both cases, proving that stability of the suspensions was provided by ox-NCC. Because of this complete precipitation, the blanks were not comparable with the rest of samples in the same conditions, and therefore will not be presented in the rest of characterization steps.

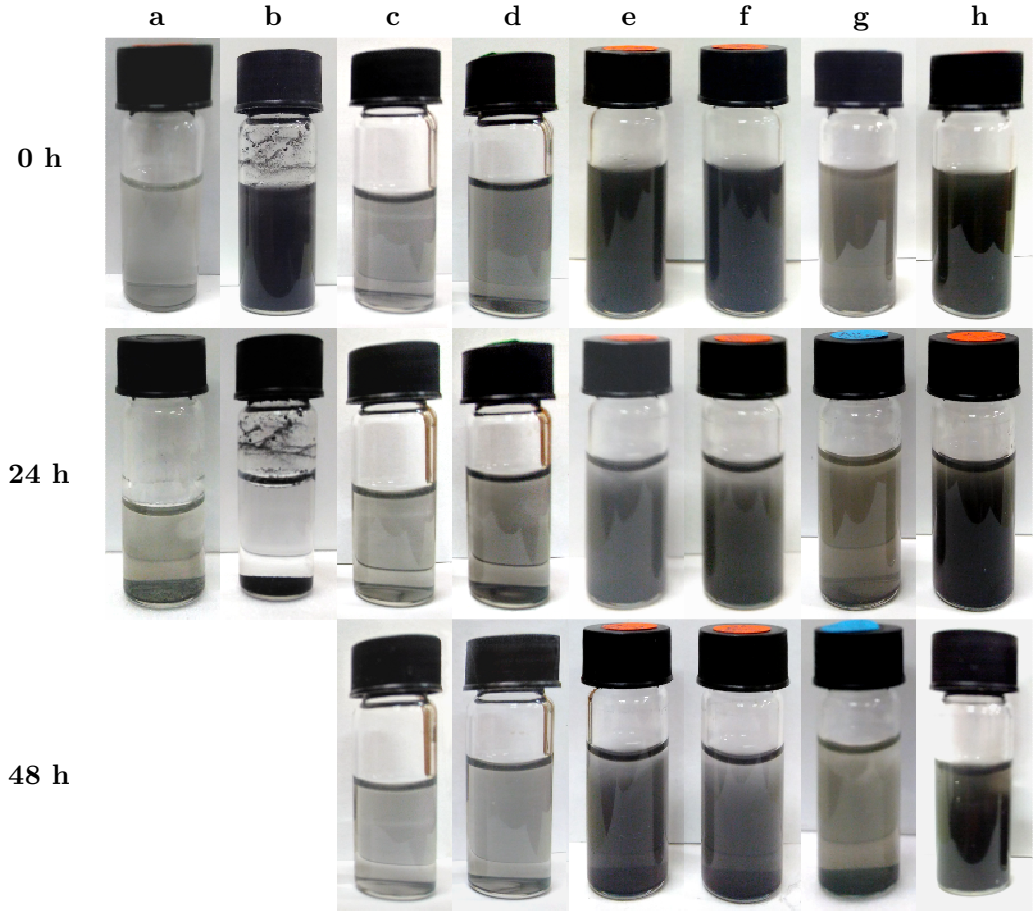

Figure 8. Stability of Blank MoS_2 (a), Blank graphene (b), ox-NCC@G_1 (c), ox-NCC@G_2 (d), ox-NCC@G_3 (e), ox-NCC@G_4 (f), ox-NCC@MoS_2 (g) and ox-NCC@G/MoS_2 (h) at 0 and 24 h. (Note that blank graphene and blank MoS_2 images are prior to centrifugation).

In order to remove ox-NCC after the exfoliation, some of the samples were filtered using Millipore 0.45 µM membranes. Suspensions were never allowed to dry in order to avoid undesired aggregation. The individual ox-NCC nanocrystal size is small

enough to go through the pores whereas graphene or MoS_2 sheets remain in the suspension above. Samples ox-NCC@G_3, ox-NCC@G_4, ox-NCC@MoS_2 and ox-NCC@G/MoS_2 were cleaned in this way, yielding ox-NCC@G_3-w, ox-NCC@G_4-w, ox-NCC@MoS_2-w and ox-NCC@G/MoS_2-w [w for washed samples], and their stability over time were also studied.

Washed samples presented a remarkable stability, showing that a minimal amount of ox-NCC was enough to stabilize graphene and MoS_2 flakes in water. Differences with respect to the unwashed samples started to be visible after 48 h, where slightly higher amounts of precipitate appeared in the washed samples (Figure 9).

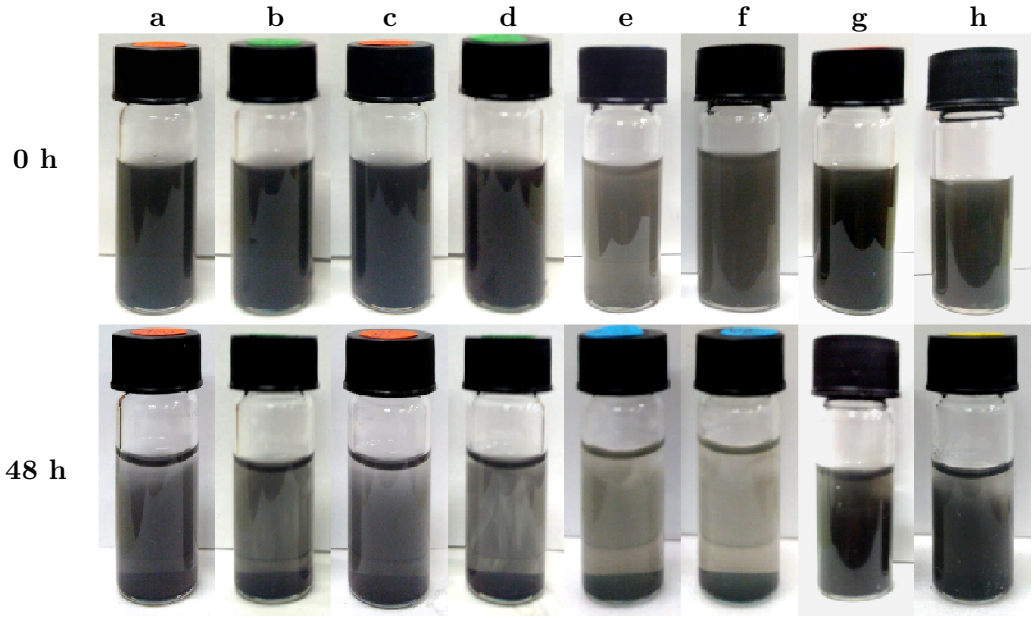

Figure 9. Stability of ox-NCC@G_3 (a), ox-NCC@G_3-w (b), ox-NCC@G_4 (c), ox-NCC@G_4-w (d), ox-NCC@MoS_2 (e), ox-NCC@MoS_2-w (f), NCC@G/MoS_2 (g) and ox-NCC@G/MoS_2-w (h) at 0 and 48 h.

The prolonged stability of the washed samples implies that the ratio of ox-NCC can be tuned after exfoliation by simple filtration, which may be useful for particular applications

UV-Vis spectroscopy

The good stability of the obtained graphene suspensions enables the weight content of graphene to be monitored using UV-Vis spectroscopy, providing a reliable way to determine the graphene exfoliation yield. Relationship between the absorbance and the relative concentrations of graphene at 660 nm has been observed to be linear, obeying the Lambert-Beer Law.[14,15] Thus, the optical absorbance of a graphene dispersion at 600 nm of wavelength obeys the following equiation:

$$A = \alpha C l \qquad (1)$$

where A is the absorbance of the graphene dispersions at 660 nm, α is the absorption coefficient, which is related to the absorbance, C is the concentration and l (value: 1 cm = 10^{-2} m) is the path length

Different values of molar extinction coefficient (α) appear in literature. This parameter depends on the solvent used or the presence of surfactants. Thus, a specific value of α at 660 nm for graphene in our particular solvent, i.e an aqueous suspension of ox-NCC, must be determined. In order to do this, graphene suspensions of known concentration in ox-NCC were prepared to obtain a calibration curve.

First, graphene dispersions were prepared through liquid-phase exfoliation in water, in the absence of ox-NCC. The graphene obtained in this way was then filtered and dried. Graphene suspensions of several known concentrations were then prepared by redispersing this dried graphene in a suspension of ox-NCC, and UV-Vis spectra were recorded. The inset in Figure 10 shows a typical UV-Vis spectrum of graphene suspension in aqueous ox-NCC. The spectrum is featureless in the Vis-IR region, as expected. Absorbance at 660 nm, divided by cell length was plotted against the concentration as seen in Figure 10. The resulting calibration had an r^2 value of 0.997, confirming the Lambert-Beer behavior in the concentration range under study. The extinction coefficient was determined to be 740.18 mL · mg^{-1} · m^{-1}.

This value is consistent with those found in literature for similar systems. For instance, Lotya *et al.* found a value of 1390 mL · mg^{-1} · m^{-1} when graphene was exfoliated in water using sodium dodecylbenzene sulfonate (SDBS) as surfactant, at a concentration of 0.5 mg/mL,[66] Wang et al. studied the effect of surfactant concentration on the extinction coefficient (α). They found that using a low concentration (0.1 mg/mL) of a given surfactant, a higher value of (1458

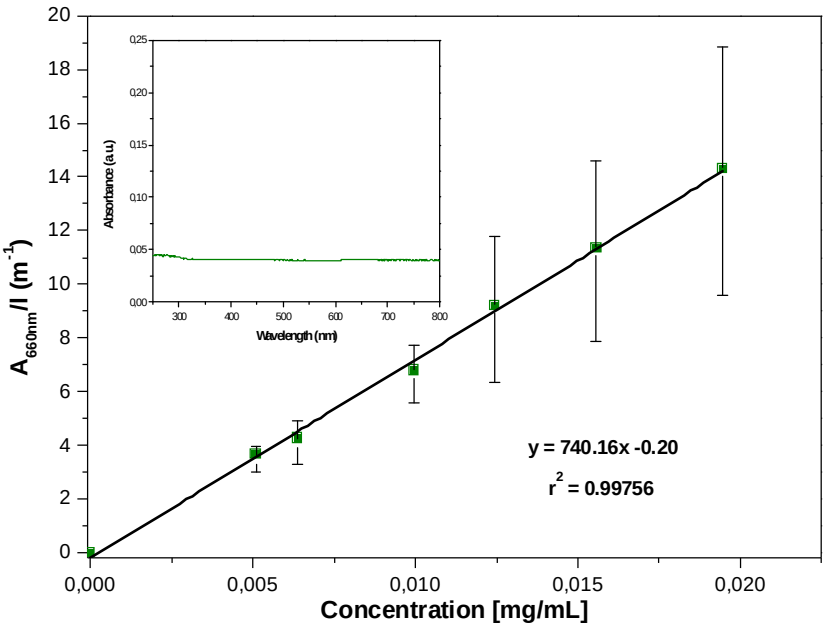

Figure 10. Absorbance per unit length (λ = 660 nm) as a function of graphene concentration. Inset: UV-Vis spectrum of graphene in ox-NCC aqueous suspension.

$mL \cdot mg^{-1} \cdot m^{-1}$) was found, whereas when the concentration reached 5 mg/mL, α value decreased to 578.5 $mL \cdot mg^{-1} \cdot m^{-1}$.[67]

By measuring the absorbance of our samples at 660 nm wavelength, the concentration of the supernatant exfoliated graphene could then be calculated. Graphene concentrations of 0.05, 0.09, 0.27 and 0.31 mg/mL were obtained for ox-NCC@G_1, ox-NCC@G_2, ox-NCC@G_3 and ox-NCC@G_4, respectively. As expected, higher graphene concentration was obtained when the centrifugation step was performed at lower rate (ox-NCC@G_3 and ox-NCC@G_4). Comparing samples centrifuged at the same centrifugation rate, i.e. NCC@G_1 with ox-NCC@G_2, and ox-NCC@G_3 with ox-NCC@G_4, slightly higher values of graphene concentration were observed when higher concentration of ox-NCC was present, i.e. in ox-NCC@G_2 and ox-NCC@G_4, respectively.

After washing, the concentration of ox-NCC in the suspension was no longer the same. Strictly speaking, solvent was different and molar extinction coefficient may have varied. (α) However, as the concentration of ox-NCC was unknown after washing, the same α was considered for the determination of graphene concentration in washed samples. The resulting concentrations were 0.27 mg/mL for ox-NCC@G_3-w and 0.31 mg/mL for ox-NCC@G_4-w, identical to the corresponding unwashed samples. This result proves that the molar extinction coefficient used was still valid despite the lower concentration of ox-NCC in the system, and shows that filtration is a good method to remove ox-NCC from the suspension without loss of graphene material.

The graphene concentration obtained with our method compares favorably with other examples in literature. For instance, Hernandez *et al.* reached maximum concentrations of graphene of 0.01 mg/mL using different organic solvents, such as N,N-Dimethylacetamide (DMA), g-butyrolactone (GBL) and 1,3-dimethyl-2-imidazolidinone (DMEU).[14] In the work of Lotya *et al.*, using SDBS as surfactant, graphene concentrations are observed in the range 0.002 - 0.05 mg/mL.

Besides, our results are in reasonable agreement with the concentrations of exfoliated graphene achieved using pristine NCC. The highest concentrations of graphene exfoliated in NCC suspensions were obtained by Carrasco *et al.*[68] Depending on sample preparation parameters, they found graphene concentrations varying between 0.3 and 1.08 mg/mL.[68]

In the case of MoS_2, it has been reported that the absorbance at 670 nm wavelength displays Lambert-Beer behavior and can be used to determine molar extinction coefficient in the same way described for graphene.[25] Thus, a calibration curve was obtained for MoS_2 suspensions following the same procedure. According to the results derived from UV-Vis spectra, the extinction coefficient of the as-prepared MoS_2 was 176.51 $mL \cdot mg^{-1} \cdot m^{-1}$, as can be seen in Figure 11. Other values reported in the literature for the molar extinction coefficient are 1020 $mL \cdot mg^{-1} \cdot m^{-1}$ in NMP,[69] or 1517 $mL \cdot mg^{-1} \cdot m^{-1}$ in water using sodium cholate as surfactant. Our value is slightly lower than these, but as it has been demonstrated with graphene, this value can vary widely depending on solvent and surfactant type and concentrations.[28]

The inset in Figure 11 shows a typical MoS_2 UV-Vis spectrum in an aqueous suspension of ox-NCC. Typical characteristic absorption bands of MoS_2 located at 672, 610, 454 and 397 nm are observed, which are in good agreement with few-layered MoS_2 obtained from a liquid-based exfoliation method.[25] The absorption peaks at 672 and 610 nm can be assigned to the direct excitonic transitions at the K point of the Brillouin zone with the energy difference arising due to spin−orbital splitting of the valence band. Peaks at 454 and 397 nm correspond to the direct excitonic transitions of M point between higher densities of state regions of the band structure.[70]

Using the calibration curve, MoS_2 concentration in ox-NCC@MoS_2 was measured. The value obtained of 0.27 mg/mL is similar to the concentration obtained for graphene in the same conditions.

Regarding the concentration of MoS_2 achieved with other methods, Coleman et al. found similar concentration (around 0.3 mg/mL) using NMP as solvent.[25] O'neill *et al.* reported concentrations of exfoliated MoS_2 as high as 40 mg/mL in NMP increasing sonication time up to 200 h,[69]whereas in aqueous suspension, using sodium cholate as surfactant, concentrations of 0.26 mg/mL where reached, and 0.5 mg/mL when increasing sonication time to 16 h.[28]

In the case of the hybrid sample ox-NCC@G/MoS_2, both components (graphene and MoS_2) contributed to the absorbance at the desired wavelengths. This made it impossible to determine the concentration of individual components in the sample using this method.

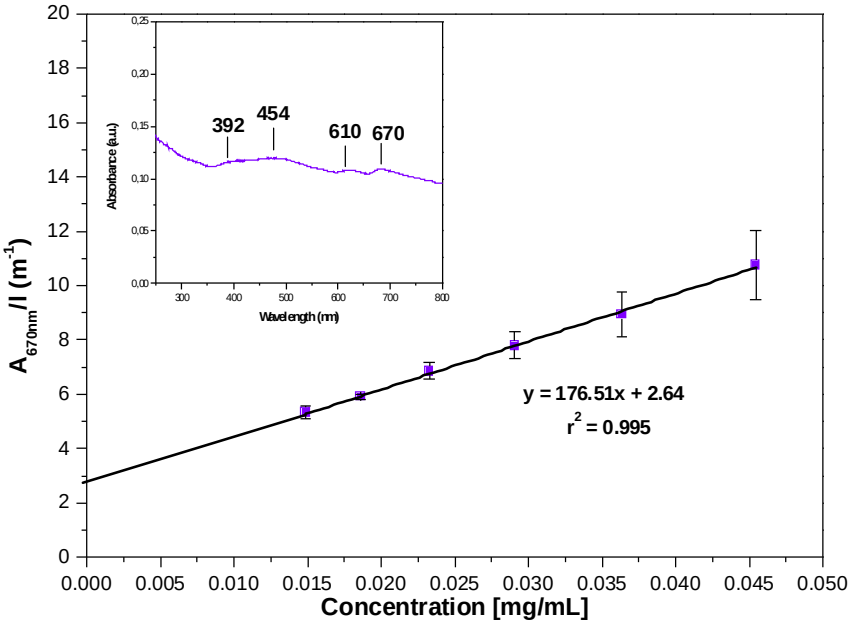

Figure 11. Absorbance per unit length (λ = 670 nm) as a function of graphene concentration. Inset: UV-Vis spectrum of exfoliated MoS_2 in ox-NCC aqueous suspension

Atomic force microscopy (AFM)

Morphological features of the prepared graphene, MoS_2 and G/MoS2 hybrid dispersions were analyzed using AFM. Figure 12 displays AFM images of the most representative graphene suspensions evaporated on cleaned silicon wafer supports. In all samples, mats of ox-NCC were found with graphene sheets embedded in them. In general, a lower number of graphene sheets and of smaller size were found in ox-NCC@G_1 and ox-NCC@G_2, which were produced using a higher centrifugation rate.

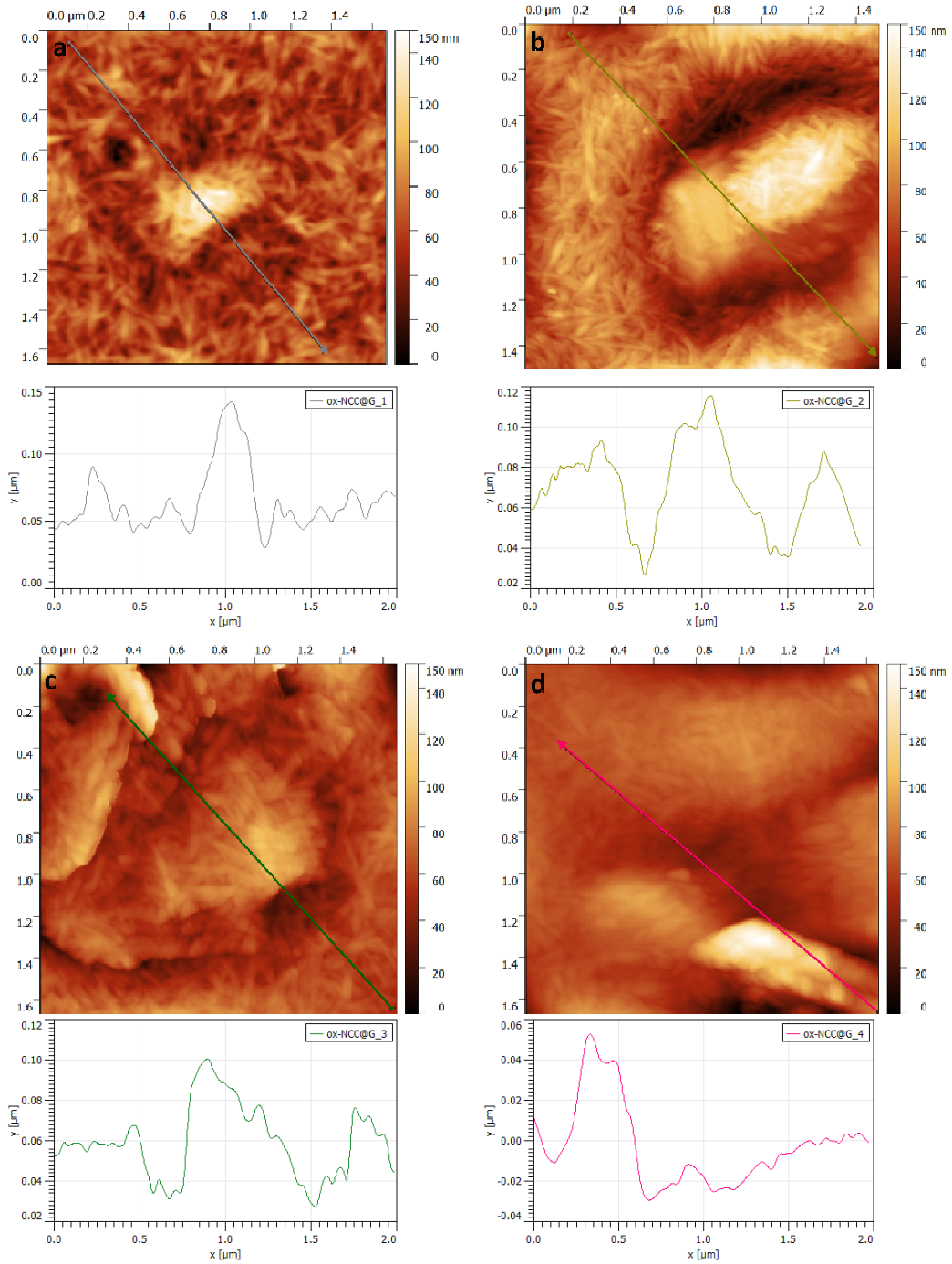

Figure 12. AFM images of ox-NCC@G_1 (a), ox-NCC@G_2 (b), ox-NCC@G_3 (c) and ox-NCC@G_4 (d). Height profiles are shown below the corresponding images.

This is consistent with a higher stability of the smaller graphene flakes in suspension, probably due to the lower weight of the individual particle. On the other hand, a higher amount of graphene, forming larger sheets, was found in ox-NCC@G_3 and ox-NCC@G_4 samples, but always surrounded by ox-NCC.

Cross-sectional height profiles were extracted from each sample and are shown below the corresponding images. Heights were found to be in the range of 50 – 150 nm. Typically, single layer graphene has a height of 0.35 – 1 nm,[71] and thus the number of layers can be easily estimated from AFM height profile measurements. However, this estimation was not possible for our samples, as they were always covered by ox-NCC films of variable thickness which also affected the orientation of the graphene sheet.

The successful removal of ox-NCC in the washed samples is evident from the AFM images. Figure 13 shows ox-NCC@G_3 and ox-NCC@G_4 after washing. Ox-NCC could still be found, but in much smaller amounts in both cases after the washing process. However, neither after washing was it possible to determine the height of the graphene layers (Figure 14) probably due to the presence of residual ox-NCC among the flakes, more difficult to remove.

As shown in Figure 14a. flakes of MoS_2 were also found covered by ox-NCC. MoS_2 flakes were in principle similar in size and shape to the corresponding graphene sample under the same conditions. This made it impossible to distinguish graphene from MoS_2 in the case of the hybrid sample, ox-NCC@G/MoS_2 (Figure 14c). Moreover, in these samples, where MoS_2 was present, the removal of ox-NCC was less effective after washing in the same conditions (Figure 14b and d). This seems to

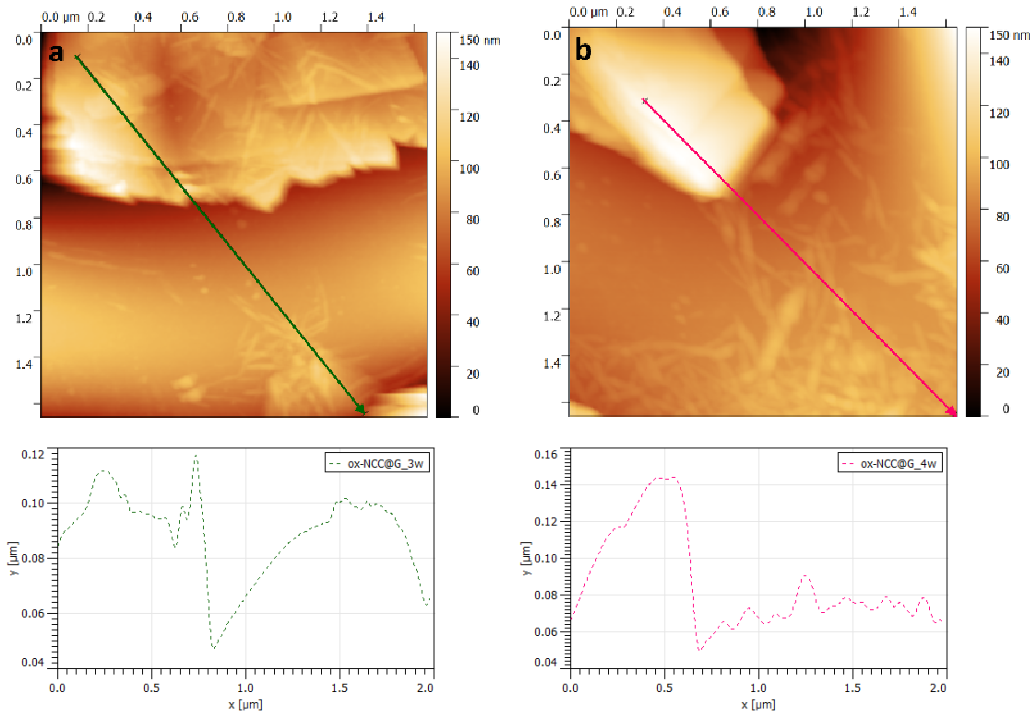

Figure 13. AFM images of ox-NCC@G_3 (a), ox-NCC@G_3-w (b), ox-NCC@G_4 (c) and ox-NCC@G_4-w (d). Height profiles are shown below the corresponding images.

indicate a stronger interaction between MoS_2 sheets and ox-NCC. As mentioned above, both before and after washings, the presence of ox-NCC hampered the layers height determination using this technique.

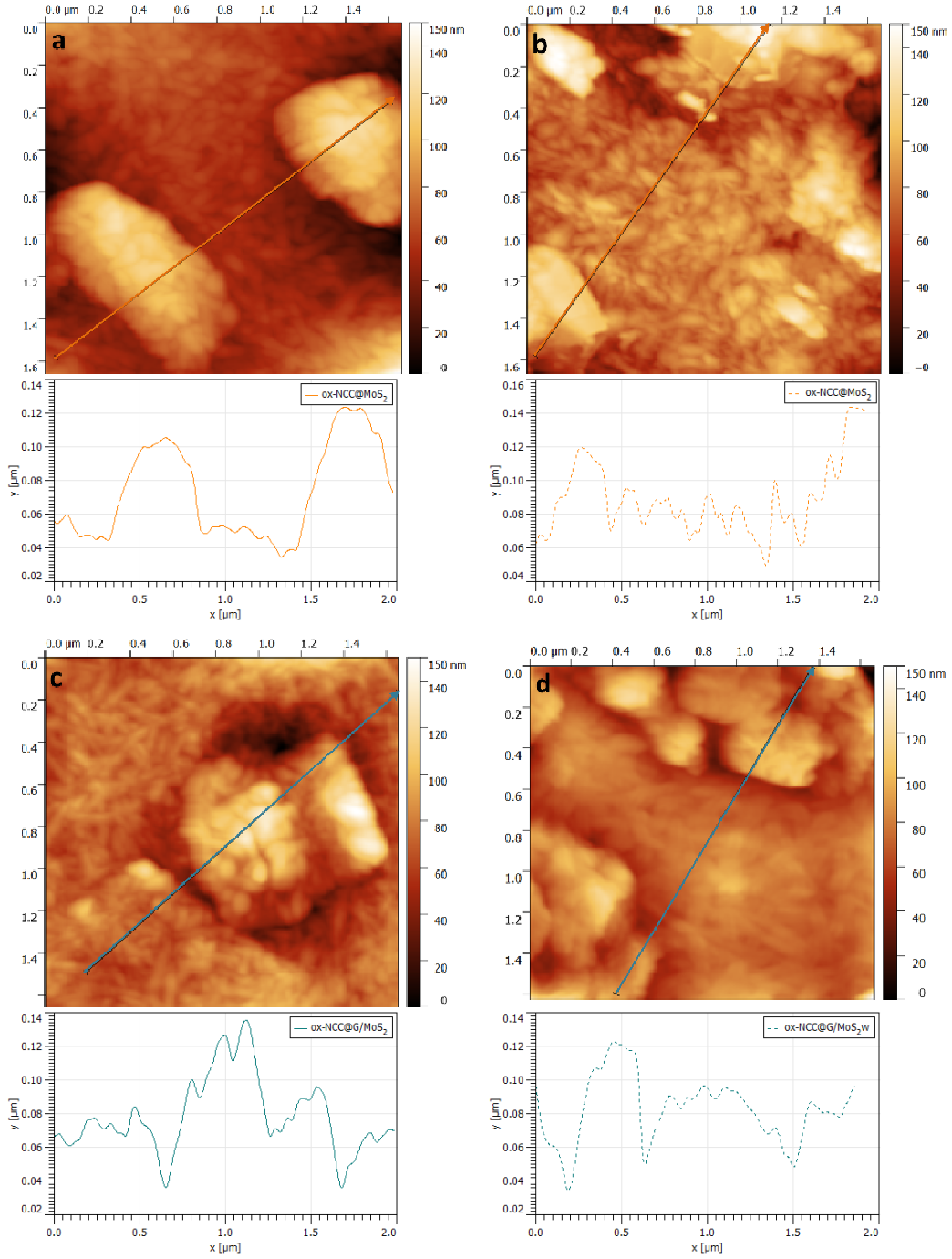

Figure 14. AFM images of ox-NCC@MoS_2 (a), ox-NCC@MoS_2-w (b), ox-NCC@G/MoS_2 (c) and ox-NCC@G/MoS_2-w (d). Height profiles are shown below the corresponding images.

Transmission electron microscopy (TEM)

Typical TEM images of the samples are displayed in Figure 15, where graphene and MoS_2 exfoliated flakes appear as dark sheets with scrolled edges and folded regions. Contrary to AFM, ox-NCC is barely visible in TEM images due to its low electronic density. The different contrast between ox-NCC and our 2D materials enabled the observation of graphene and MoS_2 without interference from ox-NCC. In all cases few layered graphene and MoS_2 fragments were found and thus it was possible to determine the size and number of layers using TEM.

Lateral sizes of the flakes ranged from 700 to 3500 nm for graphene, with ox-NCC@G_3 (Figure 15c) and ox-NCC@G_4 (Figure 15d) presenting higher abundance of larger sheets than ox-NCC@G_1 (Figure 15a) and ox-NCCG_2 (Figure 15b). In the case of ox-NCC@MoS_2 (Figure 15e), sheets presented lateral sizes between 200 and 1500 nm.

The similarity between graphene and MoS_2 in the TEM images makes it difficult to distinguish one from the other in the hybrid sample ox-NCC@G/MoS_2. In general, the MoS_2 flakes observed were of smaller size than those of graphene obtained under the same conditions. Thus, it is plausible that in the image corresponding to the hybrid sample (Figure 15f) the biggest sheet corresponds to few layer graphene with two smaller MoS_2 fragments below or on top of it. This dilemma could be resolved by an energy dispersive spectroscopy analysis (EDS), a technique that can determine the elemental composition of the sample. Unfortunately, this accessory was not available in the instrument used.

Raman spectroscopy

Raman spectroscopy is a useful tool to determine the exfoliation quality of 2D materials.[72] For EG, our starting material, the two most intense peaks are the G peak, at around 1580 cm^{-1}, and the 2D band, at around 2700 cm^{-1}. The G peak results from the doubly degenerate zone center E_{2g} mode, while the 2D band is the second order of zone-boundary phonons.[73] Besides the G and 2D peaks, the D band at around 1350 cm^{-1} is also present in EG. This band is caused by the breathing modes of sp^2 rings and requires a defect for its activation. Its intensity may not only result from the amount of disorder, but can also be assigned to the edges of sub-micrometer flakes.[74] Thus, its presence in EG indicates the introduction of some defects during the pre-treatment of graphite. On the other hand, the most intense peaks for ox-NCC appear at 2907 and 2887 cm^{-1} and are attributed to C-H stretching and CH_2 symmetric stretching, respectively.[75] Other Raman features of nanocellulosic materials were discussed in more detail in Chapter 2.

Raman spectra of ox-NCC@G_1, ox-NCC@G_2, ox-NCC@G_3 and ox-NCC@G_4, acquired at 532 nm, are presented in Figure 16, together with those of ox-NCC and EG for comparison. In order to avoid artifacts associated to sample thickness and inhomogeneity, at least 10 spectra at different points were acquired. The spectra shown are the mean of these measurements. All curves have been normalized to the strongest band of the spectrum.

For exfoliated samples, in all cases it was possible to observe the D, G and 2D bands characteristic of graphene-like material, but also bands from ox-NCC to a different extent. This technique could not be used to quantify the different components in the samples, since the intensity of the bands is not directly dependent on the concentration and the spectra might not be representative of the entire sample.

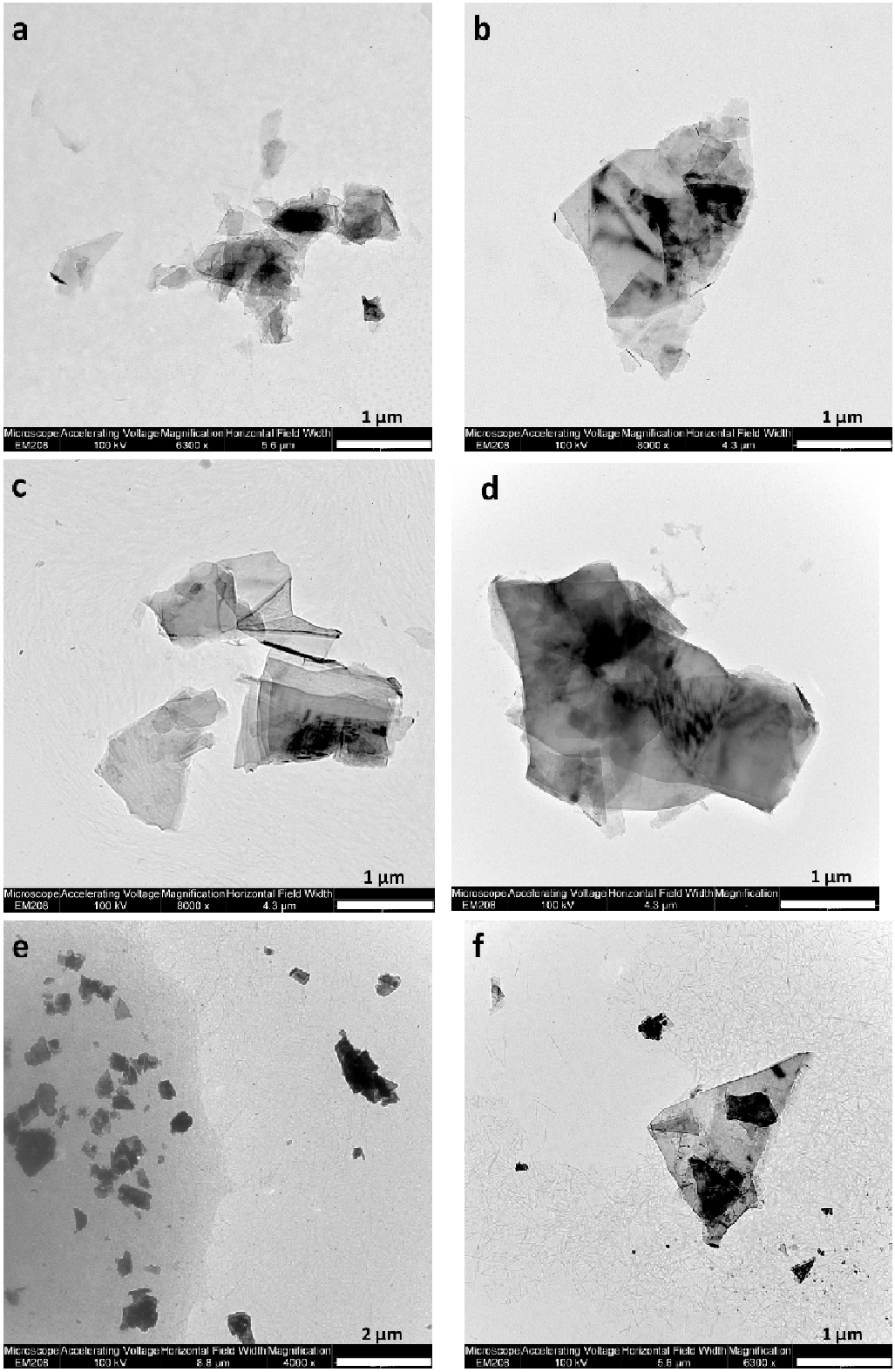

Figure 15. TEM images of ox-NCC@G_1 ***(a)*****, ox-NCC@G_2** ***(b)*****, ox-NCC@G_3** ***(c)*** **and ox-NCC@G_4** ***(d)*****, NCC@MoS_2 (e) and NCC@G/MoS_2** ***(f).***

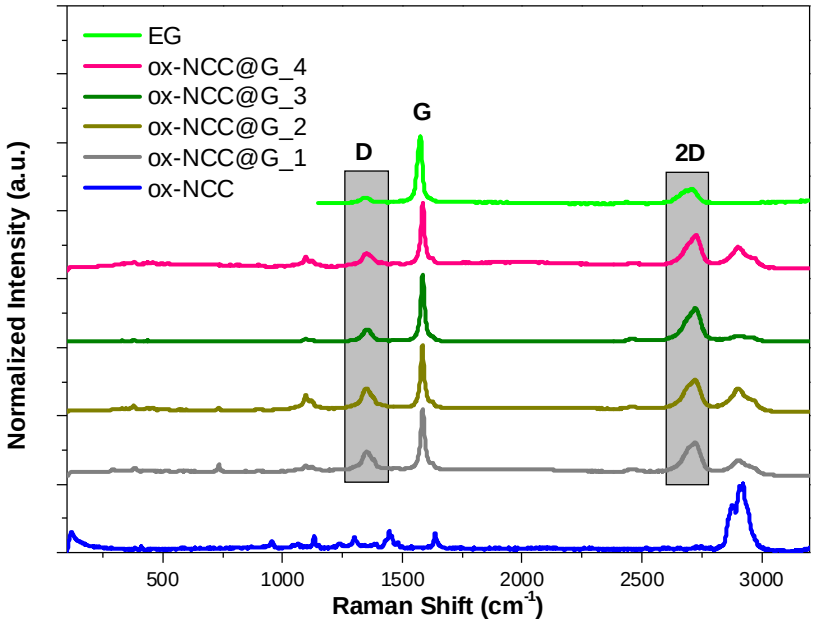

Figure 16. Raman spectra of ox-NCC@G_1, ox-NCC@G_2, **ox-NCC@G_3 and ox-NCC@G_4, at 532 nm excitation.**

However, we may attempt a qualitative assessment by comparing the relative intensity of the bands associated to ox-NCC (2907 cm^{-1}) and graphene (2700 cm^{-1}). The highest relative intensity of the band attributed to ox-NCC was found in ox-NCC@G_2, which is the sample were the highest ratio ox-NCC/graphene is expected, whereas in the case of ox-NCC@G_3, this band is barely visible. Also, different parameters in the graphene bands can be evaluated and compared among the samples, indicating eventual differences in the quality of exfoliation. For instance, the I(G)/I(2D) ratio of graphene is lower than that of EG because the relative intensity of 2D with respect to G band increases almost linearly up to 6–8 layers, whereas G peak position blue shifts from ~1580 toward ~1590 cm^{-1} with decreasing number of layers.[76] For a single layer, I(G)/I(2D) intensity ratio is ~0.24. On the other hand, I(D)/I(G) gives an indication about number of defects, an increase in this ratio evidences a higher amount of defects and edges in the sample. Values of G band position and the intensity ratios I(G)/I(2D) and I(D)/I(G) are summarized in Table 14.

Table 14. G band position, I(G)/(I2D) and I(D)/(G) of the graphene samples.

Sample	G band position (cm^{-1})	I(G)/I(2D)	I(D)/I(G)
EG	1576	4.54	0.08
ox-NCC@G_1	1584	2.02	0.36
ox-NCC@G_2	1584	2.16	0.35
ox-NCC@G_3	1584	2.01	0.18
ox-NCC@G_4	1584	1.92	0.24

The ratio of I(G)/I(2D) of the ox-NCC@G_n samples varied from 2.16 to 1.92 whereas the one of the parent EG material is 4.54. I(D)/I(G) values increased from 0.08 in EG to values from 0.18 to 0.36 in the exfoliated samples, showing a higher intensity of D band in samples ox-NCC@G_1 to ox-NCC@G_4, ascribed to higher number of edges and defects.

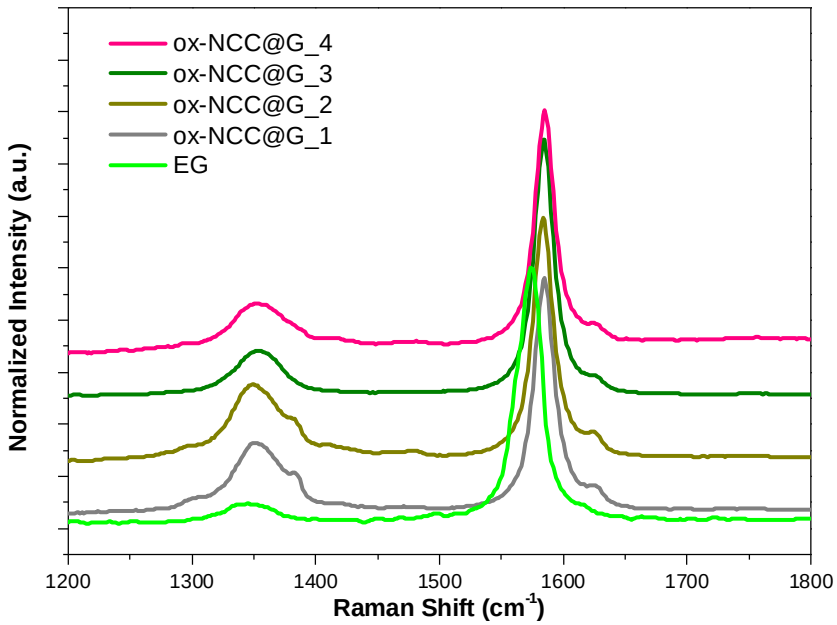

Figure 17. Zoomed 1200-1800 cm^{-1} region in EG, ox-NCC@G_1, ox-NCC@G_2, ox-NCC@G_3 and ox-NCC@G_4.

These differences in D band intensity and G band position are more clearly observed in Figure 17 which shows the region between 1200 and 1800 cm^{-1} in more detail. In ox-NCC@G_1 and ox-NCC@G_2, a broadening in D band is also observed. This broadening is normally ascribed to disorder defects in basal plane, as commonly found in GO or chemical reduced graphene. However in this case, it could be due to the vicinity of bands from ox-NCC which may overlap with D band rather than basal plane defects.

The 2D mode band gives valuable information about the extent of exfoliation. Its shape evolves significantly with the number of layers. The 2D mode in graphitic materials can be decomposed in two components, $2D_1$ and $2D_2$, whereas in bilayer graphene is best fitted to four components and in single layer graphene it has a single component.[77]

The shape of the 2D band of the samples was fundamentally different from that of EG, indicating exfoliation state of the graphene produced. The graphene bi-layers were identified by Lorentzian multi peak fit using Origin 8.0 software. The peak analysis for the 2D band of EG, ox-NCC@G_1, ox-NCC@G_2, ox-NCC@G_3 and ox-NCC@G_4 are shown in Figure 18. The four components of the 2D band in bilayer graphene are usually centered at 2617, 2652, 2676 and 2693 cm^{-1}.The deconvolution of 2D band in Raman spectra of our samples showed four components,

whereas that of EG was better fitted to 2 peaks. This revealed that bilayer and few layer graphene were formed after sonication, and confirmed that our method can successfully exfoliate bulk EG.

Raman spectra of ox-NCC@G_3-w and ox-NCC@G_4-w were acquired in the same conditions as the corresponding unwashed samples. The data in Figure 19 shows a lower ox-NCC band after washing, indicating that the ox-NCC content decreased with respect to the parent samples. The change is more noticeable in ox-NCC@G_4, where the initial concentration of ox-NCC was higher. Regarding the position, intensity and shape of the D, G and 2D bands from graphene, no significant changes were observed, indicating that the graphene sheets did not undergo re-aggregation after partial removal of ox-NCC.

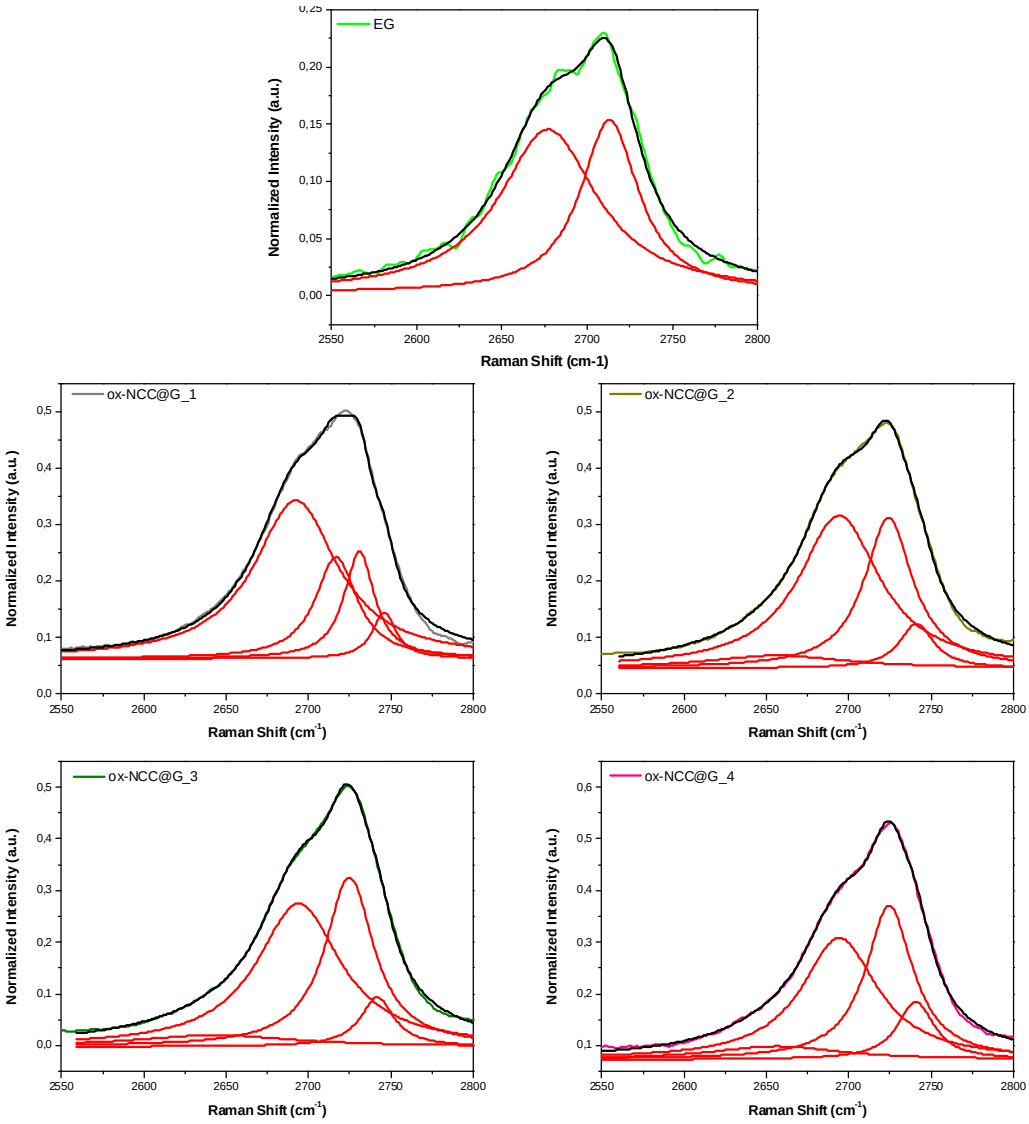

Figure 18. Multi-peak fitting of 2D graphene band in ox-NCC@G_1, in ox-NCC@G_2, in ox-NCC@G_3 and in ox-NCC@G_4.

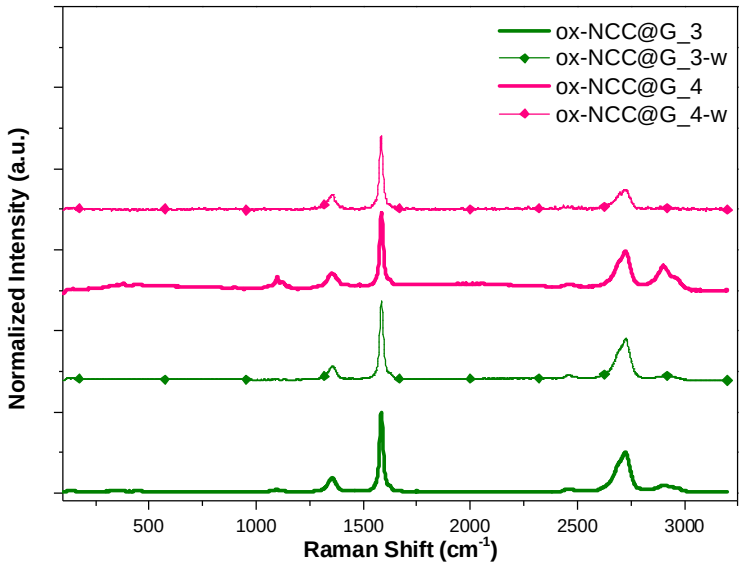

Figure 19. Raman spectra of ox-NCC@G_3, ox-NCC@G_3-w, ox-NCC@G_4 and ox-NCC@G_4-w, at 532 nm excitation.

The raman spectrum of bulk MoS_2 features four first-order active modes at 32 cm^{-1} (E^2_{2g}), 286 cm^{-1} (E_{1g}), 383 cm^{-1} (E^1_{2g}) and 408 cm^{-1} (A_{1g}). The E^2_{2g} mode arises from the vibration of an S–Mo–S layer against adjacent layers. The E_{1g} mode is forbidden in back-scattering geometry on a basal plane. The in-plane E^1_{2g} mode results from opposite vibration of two S atoms with respect to the Mo atom while the A_{1g} mode is associated with the out-of-plane vibration of only S atoms in opposite directions.[78,79]

For mono-layer-and few-layer MoS_2, the number of layers can be found by determining the distance between the two fingerprint peaks (observed at ~383 cm^{-1} and ~408 cm^{-1}). For 1-4 layer MoS_2 the mode at ~383 cm^{-1} shifts to lower frequencies and that ~408 cm^{-1} shifts to higher frequencies.[79] When the number of layers is higher than 4 the frequency of both peaks converge to the bulk values, which results in decreasing ability to differentiate between the layers of different thickness.

The two peaks observed in bulk MoS_2 spectrum (Figure 20) correspond to E^1_{2g} and A^1_g modes, at 383 and 408 cm^{-1}, respectively. (The E^2_{2g} mode is not detectable due to constraint of our Rayleigh line rejection filter (> 100 cm^{-1}). In the spectra of ox-NCC@MoS_2 and ox-NCC@MoS_2-w (Figure 20), no shift of the bands was observed. This can only mean that the MoS_2 flakes obtained after exfoliation still had at least 4 layers. On the other hand, the intensity of the MoS_2 bands was much higher than those of ox-NCC. This made it more difficult to determine if the washing steps to remove ox-NCC from the system were successful.

For the hybrid ox-NCC@G/MoS_2 sample, bands coming from all components were observed (Figure 21). The graphene G band was located at 1584 cm^{-1}, and the ratios I(G)/I(2D) and I(D)/I(G) were 2.15 and 0.5, respectively, whereas for MoS_2, no shift of the bands respect to the bulk material was observed, thus indicating number of layers higher than 4. This reveals that the quality of exfoliation in ox-NCC@G/MoS_2 did not differ from that of the individual components. Concerning the removal of ox-NCC, no significant decrease of the ox-NCC band was observed, what matches

results observed in AFM measurements. This could be due to a stronger interaction of MoS_2 with ox-NCC, since the latter was easily removed from the system when only graphene was present.

Sample ox-NCC@G/MoS_2 also featured the 2D band from graphene. Its deconvolution, shown in Figure 22, reveals the presence of bilayers and few-layers in the sample. In turn, this indicates that the presence of MoS_2 does not affect the quality of graphene exfoliation.

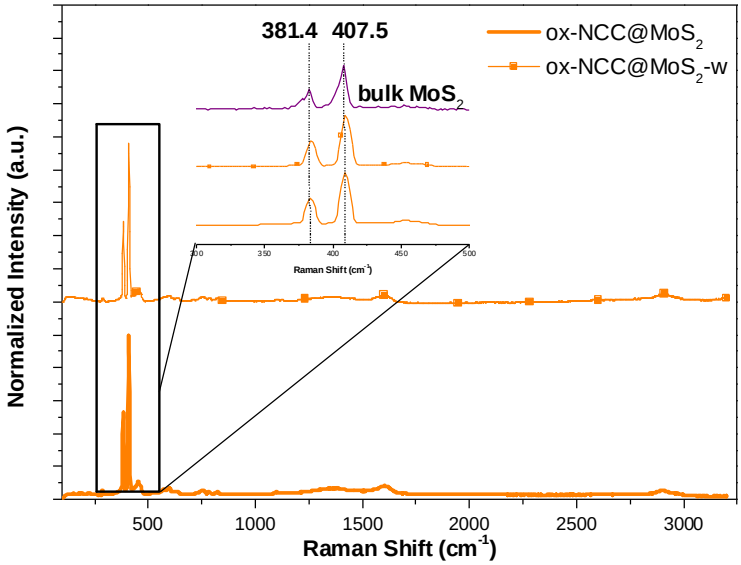

Figure 20. Raman spectra of ox-NCC@MoS_2 and ox-NCC@MoS_2-w, at 532 nm excitation.

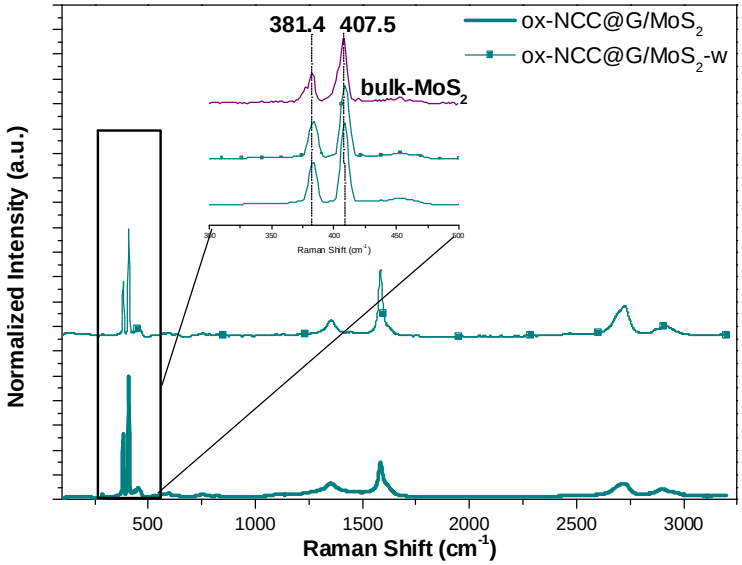

Figure 21. Raman spectra of ox-NCC@G/MoS_2 and ox-NCC@G/MoS_2-w, at 532 nm excitation.

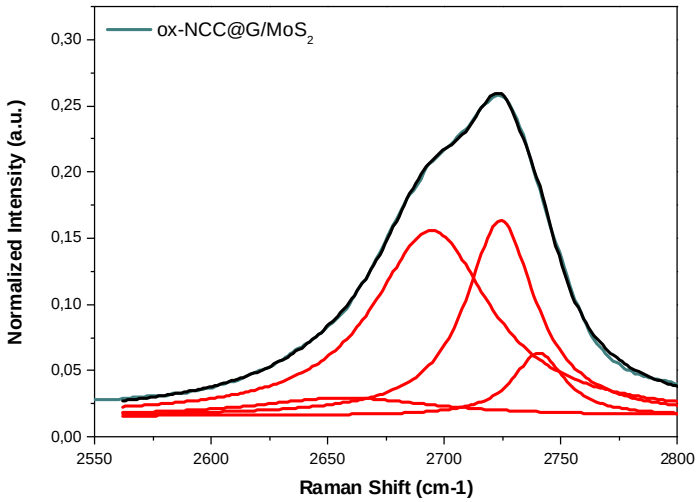

Figure 22. Multi-peak fitting of 2D graphene band in ox-NCC@G/MoS_2.

5.3.3. Production of films

Thanks to the presence of ox-NCC in the samples, self-standing films could be obtained by simple evaporation (Figure 23). Taking into account that film formation properties are exclusively due to ox-NCC, the volume of suspension used in the preparation of the film was adjusted so that the amount of ox-NCC was essentially the same.

Surprisingly, ox-NCC@G_1 and ox-NCC@G_4 did not produce self-standing films. For the former, the reason might be the low concentration of ox-NCC, probably combined with partial removal during during the high-speed centrifugation step. During this process, some ox-NCC may have been dragged by graphene flakes, leaving and insufficient amount to permit film formation. In the case of ox-NCC@G_4, the ratio of graphene exfoliated could be too high respect to ox-NCC, preventing film growth.

All films were easy to handle although slight differences in flexibility were observed depending on the content of graphene and MoS_2 content. In general, as the concentration of 2D materials increased, the films became more brittle. Thanks to the stability of the suspensions, which prevented reaggregation of the flakes during the long evaporation process, all the films obtained presented remarkable homogeneity. The transparency of the films was highly dependent on the concentration of 2D materials in suspension. Thus, ox-NCC film was completely transparent (Figure 23a), ox-NCC@G_2 still presented high transparency (Figure 23b), while the other films were more opaque as the ratio of graphene and/or MoS_2 grew (ox-NCC@G_3, ox-NCC@MoS_2 and ox-NCC@G/MoS_2, Figure 23c, d and e, respectively).

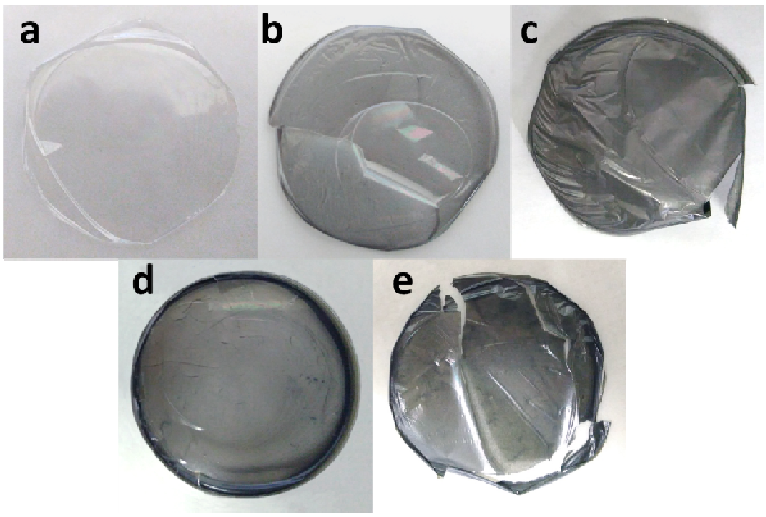

Figure 23. Self-standing films of ox-NCC (*a*), ox-NCC@G_2 (*b*), ox-NCC@G_3 (*c*), ox-NCC@MoS_2 (*d*) and ox-NCC@G/MoS_2 (*e*).

In the case of washed samples, no self-standing films could be obtained under the same conditions. Instead, only coatings not insufficiently robust to be handled by hand without breaking could be obtained. This was due to the too low amount of ox-NCC present in the samples after washing, which was not enough for the formation of the film in the conditions used.

The simplicity of the film formation process confirms the possibility to produce relatively large flexible electrodes. These results clearly demonstrate that ox-NCC is needed to obtain free-standing and flexible composite electrodes in a straightforward manner.

SEM

The morphology of the prepared films was observed by scanning electron microscopy (SEM). Ox-NCC produced a film with a very homogeneous and flat surface, as shown in Figure 24a. Individual crystals could not be observed due to their small size, which was beyond the resolution limit of the instrument. In the other samples, platelets of graphene and/or MoS_2 embedded in the ox-NCC matrix are observed. In general, a higher concentration of 2D materials was found in samples ox-NCC@G_3, ox-NCC@MoS_2 and ox-NCC@G/MoS_2 (Figure 24c, d and e) with than in ox-NCC@G_2 (Figure 24b).This was in agreement with the AFM and TEM results reported above.

The presence of graphene and/or MoS_2 flakes slightly increased the mesoscopic roughness of the sample, and thus the exposed surface. In addition, the images suggest that 2D materials were not only inside the ox-NCC matrix, but also exposed on the surface and thus more available for electron transfer in the eventually constructed electrodes.

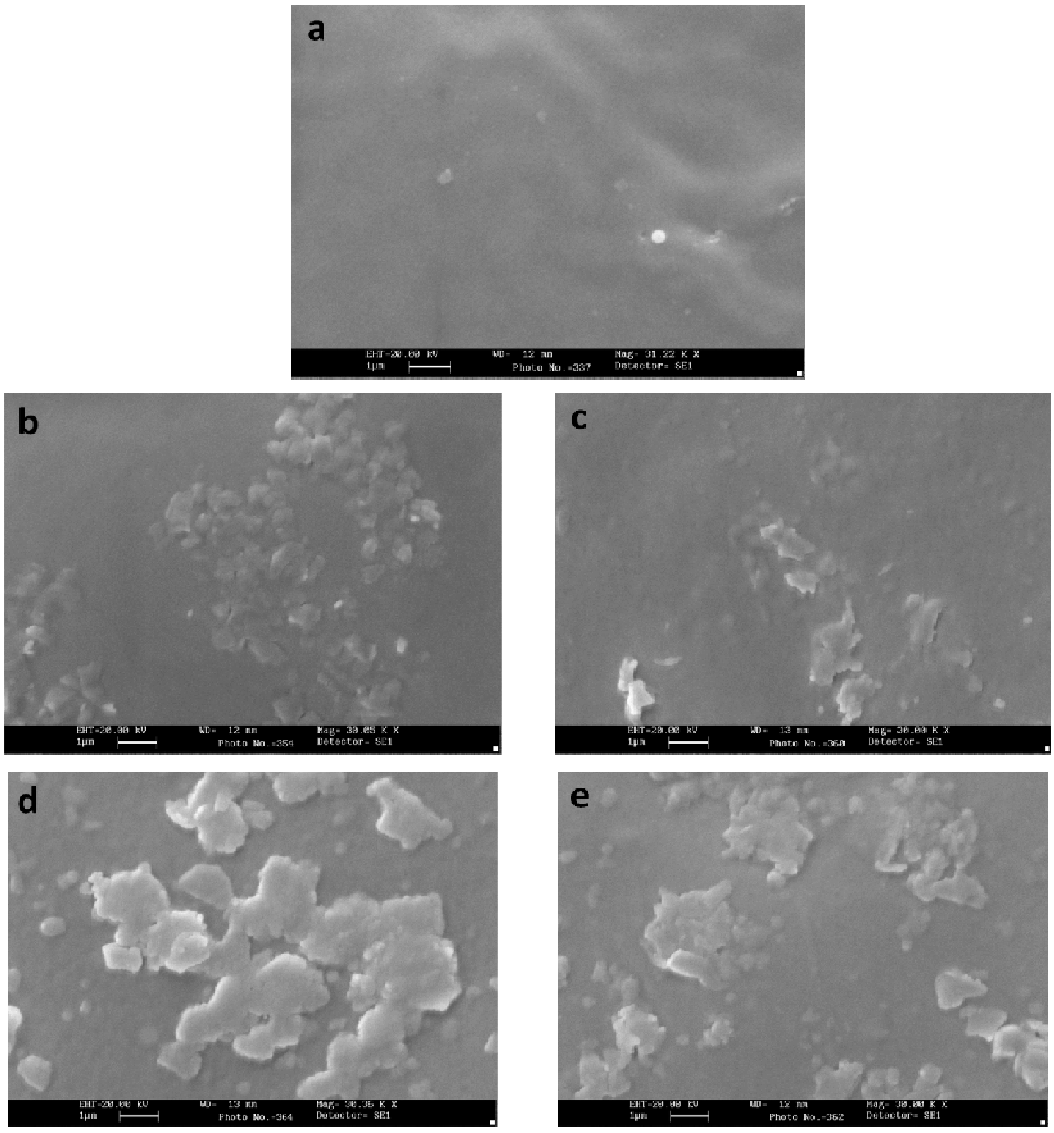

Figure 24. SEM images of ox-NCC (a), ox-NCC@G_2 (b), ox-NCC@G_3 (c), ox-NCC@MoS_2 (d), ox-NCC@G/MoS_2 (e) films (scale bars 1 µm).

Electrical properties

To understand whether the performance of the obtained graphene or hybrid films permits the replacement of platinum in solar cells and other optoelectronic applications, we first studied their electrical properties with a four-probe approach. The four probes are linearly arranged on the surface, and at equal distance (S) from each other. The method assumes that the sheet thickness of the sample much smaller than the probe distance (Figure 25). The current (I) flows between the two outer probes and the measure of voltages (V) is obtained between the two inner probes. The use of separate current and voltage contacts avoids problems with contact resistance.

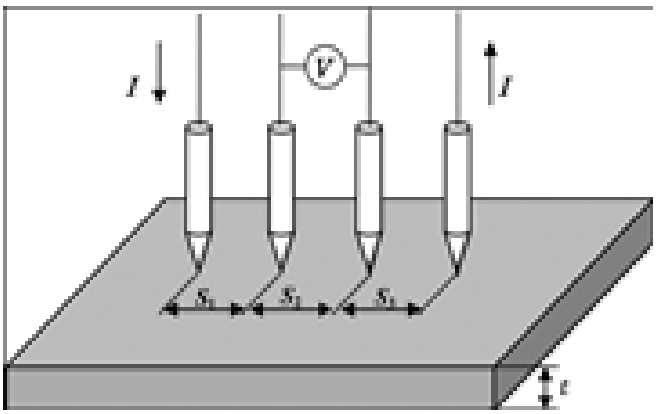

Figure 25 Schematic representation of a four point probe measurement.[80]

The four point methods allows to measure an important parameter in two dimensional systems, such as thin films, is the so called sheet resistance (Rs), measured in ohms per square (Ω/□). Strictly speaking, the unit for sheet resistance is the ohm. The reason for the name "ohms per square" is that a square sheet with a sheet resistance of 10 Ω/□ has an actual resistance of 10 Ω, regardless of the size of the square. Therefore, Rs gives a reliable way to compare absolute values of resistance (i.e. how strongly a given material opposes the flow of electric current) between different thin films, regardless of their size.

Electrical conductivity is reciprocal to resistance, and measures a material's ability to transport an electric charge. From sheet resistance it is also possible to obtain the electrical conductivity (S/cm), provided that thickness of the film is known, using the following equation:

$$\sigma = \frac{1}{R_s \times t} \qquad (2)$$

where R_S (Ω/□) is the sheet resistance and t (cm) is the thickness of the sample.

For each film, the thickness was measured with a micrometer, and the sheet resistance using the four-probe method described above. These values, along with the calculated conductivities are reported Table 15. Ox-NCC is a very poor electrical conductor, having the highest sheet resistance of 36 MΩ/□. The introduction of graphene in the sample had a beneficial effect, as can be seen from the lower sheet resistance in ox-NCC@G_2, roughly 12 MΩ/□. Increasing the graphene content from 0.09 mg/mL in ox-NCC@G_2 to 0.27 mg/mL in ox-NCC@G_3 (concentration referred to the parent suspension determined by UV-Vis) dramatically reduced sheet resistance in the latter to 3 kΩ/□. However, film containing MoS_2, which was formed under analogous conditions to ox-NCC@G_3 exhibits a very high sheet resistance, similar to that of ox-NCC alone. The hybrid graphene/MoS_2 sample, ox-NCC@G/MoS_2, is a better conductor than ox-NCC@MoS_2, but not as good as the sample containing only graphene. These results suggest that addition of MoS_2 to graphene did not cause any beneficial effect to the conductivity of the system,

Table 15.Electrical properties of self-standing films.

Film	Thickness (µm)	Sheet Resistance (MΩ/□)	Electrical Conductivity (µS/m)
ox-NCC	47 ± 21	35.9 ± 4.1	0.068 ± 0.03
ox-NCC@G_2	29 ± 8	11.8 ± 5.7	0.3 ± 0.024
ox-NCC@G_3	29 ± 9	0.0033 ± 0.0012	1283.6 ± 503
ox-NCC@MoS_2	38 ± 2	35.5 ± 6.1	0.184 ± 0.041
ox-NCC@G/MoS_2	38 ± 1	11.7 ± 2.5	0.279 ± 0.081

although this is difficult to judge not knowing the exact concentration of each component in the sample.

In terms of electrical performance, our results compare favorably with some reported values for graphene oxide (GO) or reduced graphene oxide (rGO) films. Gilje *et al.* reported a sheet resistance of $4 \cdot 10^{10}$ Ω/□ for a GO film. They also attempted to enhance the electrical conductivity by removal of the oxidized moieities through chemical reduction. The sheet resistance in reduced graphene oxide (rGO) decreased to $4 \cdot 10^{6}$ Ω/□.[81] Wu *et al.* reported reduced graphene oxide films of $5 \cdot 10^{3}$ kΩ /□. In this work, the graphene electrodes were deposited on quartz substrates by spin coating of an aqueous dispersion of GO, followed by a reduction process to reduce the sheet resistance

On the other hand, our films are not competitive with better results found in literature for graphene films.[82,83] For instance, Gomez de Arco *et al.* reported a graphene film with a sheet resistance value of 230 Ω /□ The graphene films were grown by chemical vapor deposition (CVD) on Ni surface.[84] A remarkably high value of conductivity, of $14.3 \cdot 10^{5}$ S/m was described by Capasso *et al.*[85] In that work, graphene films were produced by CVD of pyridine on copper substrates. They expected pyridine to lead to doped graphene by the insertion of nitrogen atoms in the growing sp^2 carbon lattice, improving the properties of graphene as a transparent conductor.

However, these examples employ harmful and costly methods, including toxic organic solvents or expensive techniques. Therefore, when it comes to scalability we believe to have reached a good compromise between properties, sustainability and production cost.

5.3.4. Counter electrode (CE) fabrication and characterization

To investigate the electrocatalytic activities of our samples toward I_3 reduction in the I^-/I_3^- redox shuttle of DSSCs, counter electrodes (CE) were prepared by drop casting (20 µL droplets) of the different samples on FTO surfaces (0.25 cm^2) and cyclic voltammetry (CV) tests were then conducted.

Cyclic voltammetry (CV) is an electrochemical technique in which the electrode potential in an electrochemical cell is ramped linearly over time in cyclical phases. The rate of voltage change during each of these phases is known as the experiment scan rate (V/s). The potential is applied between the working electrode and the reference electrode while the current is measured between the working electrode and

the counter electrode (Figure 26). The data are plotted as current (i) vs. applied potential (E).[86,87]

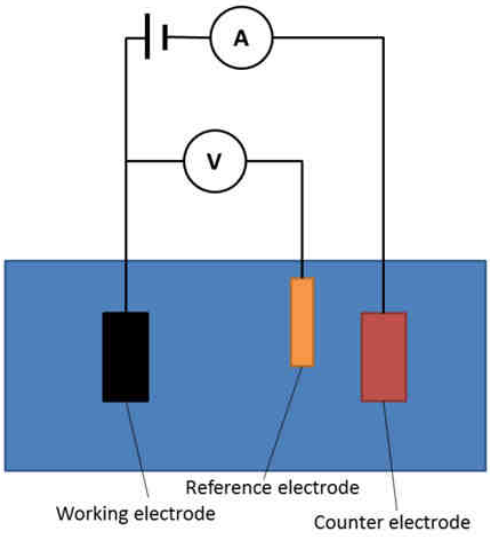

Figure 26. Scheme of a cyclic voltammetry (CV) experiment.[88]

Typically, the potential is first scanned negatively to cause a reduction. The corresponding peak potential is called the cathodic peak potential (E_{pc}), and is reached when all of the substrate on the surface of the electrode has been reduced. After the switching potential has been reached, the potential scans positively, resulting in an oxidation process. The peak potential in this case is called the anodic peak potential (E_{pa}), and is reached when all of the substrate on the surface of the electrode has been oxidized.

Other very commonly used parameters in cyclic voltammetry are the onset potential (E_{on}) and peak current density (i_p) which are very useful to assess the electrocatalytic activity of a CE. E_{on} can be defined like the potential at which the current is one-tenth of the peak current. It is important to note that E_{on} is an arbitrary magnitude which nevertheless can be used for qualitative purposes when results within the same work are compared. Regarding peak current densities, the comparison can be only considered acceptable if the current densities are normalized by the specific electrochemical active area.[89] In this work, all electrodes are compared in terms of macroscopic area, and the effects of roughness at the nanoscale are considered as part of the intrinsic efficiency of the electrode. It must be noted, however, that the specific area may change from sample to sample due to its roughness. This has not been considered here.

Since Pt is the benchmark catalyst for solar cells, all the cyclic voltammetry responses were always presented against this material. In Pt, two oxidation and reduction peaks appear in the studied potential range (Figure 27). The peak at low potential is attributed to the redox reaction triiodide/iodide ($I_3^- + 2e^- \rightarrow 3I^-$), while the second peak at higher potential corresponds to the iodine/triiodide redox reaction

($3I_2 + 2e^- \rightarrow 2I_3^-$).[90] As the counter electrode of a DSSC is responsible for catalyzing the reduction of I_3^- to I^- we will focus our interest on the peaks at lower potential.[50]

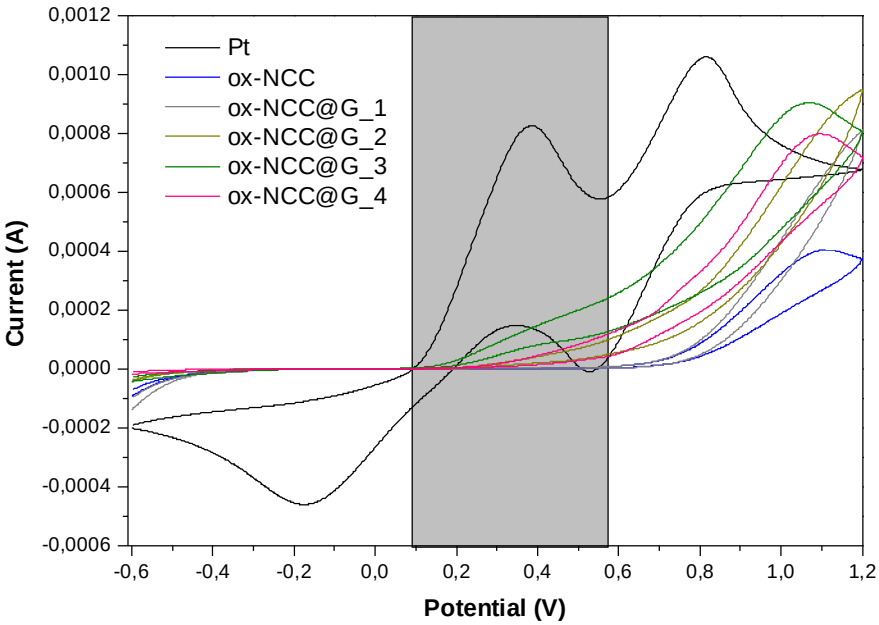

Figure 27. Cyclic voltammograms for Pt, ox-NCC@G_1, ox-NCC@G_2, ox-NCC@G_3 and ox-NCC@G_4.

Table 16. Voltammetry results for different sample compositions.

Sample	Graphene content [mg/mL]	Ox-NCC content [mg/mL]	Peak current density i_p (μA/mm²)	Onset potential E_{on} (V)
Ox-NCC@G_3	0.29	1	6.8	0.21
Ox-NCC@G_4	0.31	2	2.8	0.25
Ox-NCC@G_3-w	0.29	Unknown	0.25	0.23
Ox-NCC@G_4-w	0.31	Unknown	10	0.23
Ox-NCC@G/MoS_2	Unknown	1	3.6	0.19
Ox-NCC@G/MoS_2-w	Unknown	Unknown	5.2	0.15

Cyclic voltammograms of ox-NCC and graphene containing electrodes are presented in Figure 27. On ox-NCC modified FTO electrode, the electrochemical response of I_3^-/I^- and I^-/I_3^- redox couples is completely blocked due to the insulator character of this polymer. When graphene is incorporated into the CE at low concentration, the current increases but no peak appears defined in the CV, meaning that conductivity and activity of the material was not enough to promote the electron transfer from the iodine species. This was the case of ox-NCC@G_1 (0.05 mg/mL graphene, ox-NCC 1 mg/mL) and ox-NCC@G_2 (0.27 mg/mL graphene, ox-NCC 2 mg/mL).

When graphene ratio to ox-NCC is increased, a cathodic peak at a potential close to that of Pt starts to be noticeable. This is the case of ox-NCC@G_4 (0.31 mg/mL graphene, ox-NCC 2 mg/mL), This effect is more visible in the case of ox-NCC@G_3 (0.27 mg/mL graphene, ox-NCC 1 mg/mL), where lower E*on* value is observed,

together with higher cathodic peak current density, indicating its better performance for I_3^- redox process (Table 16). On the basis of these results, we conclude that with increasing graphene to ox-NCC ratio, the E*on* value becomes lower and the cathodic current density larger (Table 16).

We reasoned that the presence of ox-NCC was responsible for the low activity of the constructed electrodes, since it was probably preventing a good contact and subsequent electron transfer among graphene layers. To determine whether partial removal of ox-NCC could improve the performance of CE, CV measurements were conducted after washing of the best systems (i.e. ox-NCC@G_3-w and ox-NCC@G_4-w). It is important to highlight that even after partial removal of ox-NCC, graphene did not undergo reaggregation, as shown by Raman spectroscopy. Figure 28 shows the voltammograms obtained together with those of the corresponding unwashed samples for comparison. As expected, higher peak current densities were observed (Table 16), indicating an improvement in the activity.

In view of these results, CE from ox-NCC@MoS_2 and ox-NCC@G/MoS_2 as well as the corresponding washed counterparts were prepared in the same way in order to investigate the effect of adding MoS_2 to the system. The results are showed in Figure 29. In all cases, a better response after partial removal of ox-NCC was observed. As expected, ox-NCC@MoS_2 displayed much worse performance, comparable to that of ox-NCC. This result evidences that the catalytic activity of MoS_2 is negated probably because the presence of ox-NCC isolates individual flakes.

In spite of not knowing the exact graphene concentration in the hybrid ox-NCC@G/MoS_2, it is clear that the presence of graphene improved the performance with respect to ox-NCC@MoS_2 (Table 16). Likewise, the uncertainty in graphene concentration in this sample avoids a valid comparison with the corresponding sample containing only graphene, to evaluate if the addition of MoS_2 had an effect on the performance. These results, which are consistent with the film conductivity measurements, indicate that the principal effect is due to the presence of the carbonaceous material and highlight a poor contact between graphene and MoS_2 in the system, which leads to a lack of electron transfer between the two components.

Based on these results, we conclude that the electrocatalytic performance of our systems is not competitive with the state of the art, presented in the introduction of this Chapter. However, the approach used here is superior in other aspects, such as the employment of a greener technique. This method represents the basis for future improvements. Possible alternatives would be further optimization of the parameters to increase the amount of graphene in the system, removal of ox-NCC to a higher extent, or introducing an interconnecting element into the system to bridge graphene and MoS_2 and improve electron transfer. In a recent study, it has been shown that the incorporation of conductive networks of carbon nanotubes (CNTs) to a reduced graphene oxide (rGO)/MoS_2 counter electrode (CE) provides additional pathways for electron transport in the MoS_2/rGO-CNTs hybrid, which increases the charge-transfer rate at the CE/electrolyte interface. As a result, the MoS_2/rGO-CNTs CE exhibits greatly improved electrocatalytic activity compared with that of MoS_2/rGO alone.[91] In this way, this strategy could provide an interesting alternative to improve

the performance of our system, maintaining the concentration of ox-NCC, and thus the desired stability in suspension and film forming properties.

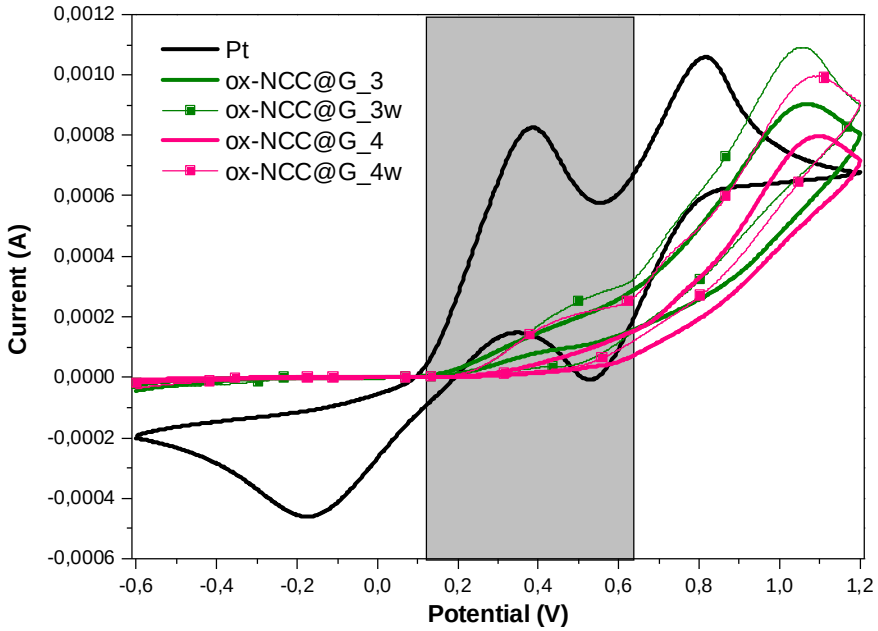

Figure 28. Cyclic voltammograms for Pt, ox-NCC@G_3, ox-NCC@G_3-w, ox-NCC@G_4 and ox-NCC@G_4-w.

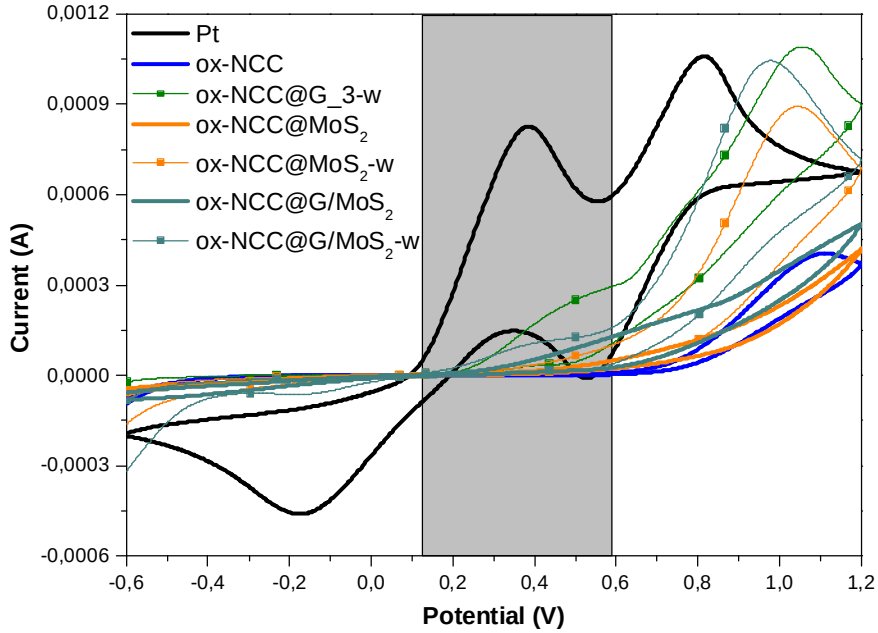

Figure 29. Cyclic voltammograms for Pt, ox-NCC, ox-NCC@MoS_2, ox-NCC@MoS_2-w, ox-NCC@G/MoS_2 and ox-NCC@G/MoS_2-w.

5.4. Conclusions

We have developed a simple and scalable exfoliation approach to produce high-quality few layer graphene and MoS_2 sheets in a one-step procedure. We used oxidized nanocellulose (ox-NCC) in aqueous suspension to exfoliate expanded graphite (EG) through ultrasonic force and we varied the concentration of the ox-NCC suspension, the ratio ox-NCC to 2D precursor, the time of sonication and the centrifugation conditions. After optimization of these parameters, stable dispersions of exfoliated graphene were obtained. The quality of the exfoliation was analyzed with Raman spectroscopy and AFM. Few layer graphene suspensions were obtained as evidenced from the shape of the 2D band in the Raman spectra even if some defects have been created on the graphene surface. For MoS_2, the Raman spectra evidenced that MoS_2 with more than 4 layers was obtained.

Flexible, transparent and conductive films were obtained by simple evaporation, demonstrating that the intrinsic film-forming ability of nanocellulose can be transferred in this way to graphene and MoS_2 materials and opening the way towards new applications. The structural and electrochemical properties of the formed films were examined by scanning electron microscopy and four point probe approach techniques. The films were found to be homogeneous and had graphene and/or MoS_2 flakes embedded in ox-NCC, while their conductivity depended on graphene content.

Graphene and MoS_2 nanosheets were compared to Platinum as catalysts in the redox process that takes place at the CE of a DSSC. To do so, the as-synthesized suspensions were deposited on fluorine-doped tin oxide (FTO) slides. It was found that the ox-NCC/graphene ratio played an important role in the quality of the counter-electrode and the catalytic performance towards triiodide species reduction, whereas the addition of MoS_2 to the system did not cause any synergistic effect in such catalytic performance.

5.5. Experimental details

5.5.1. Generalities

All reagents and solvents were used as received or purified using standard procedures. Milli-Q water was used in all experiments (System MilliQ plus). Powder graphite (grade SP1, batch Nº 04100, lot Nº 011705 was purchased from Carbon Bay. Microcrystalline cellulose Avicel® and MoS_2 powders were purchased from Aldrich and used without further purification. TEC 8 (8 Ω/□) Fluorine Tin Oxide (FTO) 20×20 cm conductive glass slides were obtained from Pilkington.

5.5.2. Techniques

The sonication was carried out using high-energy ultrasonic equipment Ultrasonic processor GEX 750 at 25% amplitude with a pulse length of 1 s and pulse-off duration of 1 s for 1 h.

Atomic force microscopy (AFM) images were obtained with a Nanoscope IIIa, VEECO Instrument. As a general procedure to perform AFM analyses, tapping mode using a n-type silicon µmash® SPM probe (HQ:NSC15/ALBS) with tip height 12-18 µm, cone angle < 40º (Resonant frequency 325 kHz; force constant 40 N/m) (MikroMasch) from drop cast of samples in an aqueous solution (concentration of ~0.1 mg/mL) on a Si wafer substrate was performed. The obtained AFM-images were analyzed with S3 Gwyddion 2.35.

Transmission electron microscopy (TEM) measurements were performed on a TEM Philips EM208, using an accelerating voltage of 100 kV. Samples were prepared by drop casting from dispersions onto a TEM grid (200 mesh, nickel, carbon only).

Scanning electron microscopy measurements SEM measurements were carried out with a Zeiss Supra microscope. Images were acquired collecting secondary electrons on a commercial SEM (Gemini SUPRA 40, Carl Zeiss NTS GmbH, Oberkochen). In order to prevent electron-induced surface charging, low accelerating voltages (0.61.0 keV) were used for film visualization. Samples were metallized prior to SEM imaging with a thin Au film.

Raman spectra were registered on a RENISHAW 1000 micro-Raman system equipped with a CCD camera and a Leica microscope. A 532 nm laser as excitation source was used. Measurements were taken with 10 s of exposure time and 1 % power with 4 accumulations for MoS_2 and 30 accumulations for graphene containing samples. The laser spot was focused on the sample surface using a 100x objective with short-focus working distance. Raman spectra were collected on numerous spots on the sample. The data was analyzed with Renishaw Wire and Origin software.

UV-Vis measurements were carried out on Cary 5000 spectrophotometer. All spectra were recorded with an interval of 1 nm, slit width 2 nm and scan speed of 200 nm/min. Samples were sonicated for 5 min and diluted with MilliQ water and measurements were carried out in a 1 cm quartz cell.

Film thicknesses were measured with a Mutitoyo micrometer as an average of 10 points throughout the sample.

Conductivity analyses were obtained with a Jadel RM3000 Model with an s = 0.064 cm distance between two probes at a current of 1 nA.

Cyclic voltammetry (CV) experiments were carried out at room temperature by using an Autolab potentiostat/galvanostat (Model 302N) and a RDE (Autolab), both equipped with a three-electrode cell under a stream of purified N_2 for 15 minutes prior to measurements. All potentials were measured with respect to Hg/Hg_2Cl_2, NaCl-saturated electrode (SCE) contained in a glass tube filled with the supporting electrolyte solution, separated from the solution by a Vycor frit and located close to the tip of the working electrode to minimize the ohmic drop. The counter electrode was a Pt ring directly dipped in the solution. The electrolyte was acetonitrile solution containing 10 mmol LiI, 1 mmol I_2, and 0.1 mol $LiClO_4$. Sample coated FTO electrodes were cleaned and modified following the protocol:

a) Sonicate 15' in soap, wash with MQ water
b) Sonicate 15' in acetone, wash with MQ water
c) Sonicate 15' in isopropanol, dry with air flux
d) Mask with nail varnish leaving bare area of 0.25 cm^2
e) Cast the surface with a 20 uL drop of each sample and let them dry at room temperature until the complete evaporation of the solvent (overnight).

CV experiments were performed in a range of applied potential from -0.6 V to 1.2 V at a scan rate of 50 mV/s.

5.5.3. Sample preparation

Production of ox-NCC: Procedure described in chapter 2 for ox-NCC_3 was followed.

Expanded Graphite (EG) preparation: Graphite (1 g) was sonicated in 10 mL NMP for 4 h with GEX 750 sonic tip apparatus in an ice bath, then filtered (Millipore 0.45 µm) and extensively washed with isopropanol.

ox-NCC@G_n preparation: In a typical experiment, ox-NCC suspensions with a concentration 1 or 2 mg/mL were prepared in deionized water by sonication for 10 min. EG powder was added into the resulting suspension. Exfoliation was performed by sonication of the obtained mixture suspension with GEX 750 (750W, at 25 % amplitude, pulse 1s for in an ice bath). Then centrifugation was carried out to remove eventual non-exfoliated graphitic residue. Conditions are summarized in section 5.3.1 of this Chapter.

ox-NCC@MoS_2 preparation: In a typical experiment, ox-NCC suspensions with a concentration 1 or 2 mg/mL were prepared in deionized water by sonication for 10 min. MoS_2 powder was added into the resulting suspension. Exfoliation was performed by sonication of the obtained mixture suspension with GEX 750 (750W, at 25 % amplitude, pulse 1s for in an ice bath). Then centrifugation was carried out to

remove eventual non-exfoliated graphitic residue. Conditions are summarized in section Chapter 5: of this Chapter.

ox-NCC@G/MoS_2 preparation: In a typical experiment, ox-NCC suspensions with a concentration 1 or 2 mg/mL were prepared in deionized water by sonication for 10 min. EG and MoS_2 powders were added into the resulting suspension. Exfoliation was performed by sonication of the obtained mixture suspension with GEX 750 (750W, at 25 % amplitude, pulse 1s for in an ice bath). Then centrifugation was carried out to remove eventual non-exfoliated graphitic residue. Conditions are summarized in section Chapter 5: of this Chapter.

Graphene and MoS_2 suspensions in water used for comparisons were prepared without any ox-NCC by employing the typical experimental procedure described above.

ox-NCC@G_n-w, **ox-NCC@MoS_2-w** and **ox-NCC@G/MoS_2-w preparation:** ox-NCC@G_n, ox-NCC@MoS_2 or ox-NCC@G/MoS_2 samples (10 mL) were filtered (Millipore 0.45 μM) while stirring and constantly refilling with MilliQ water (total volume 70 mL) to keep volume constant and avoid the sample to dry and aggregate.

Self-standing films preparation: 7 mL for ox-NCC@G_1 and ox-NCC@G_2, and 14 mL for ox-NCC@G_3, ox-NCC@G_4, ox-NCC@MoS_2 and ox-NCC@G/MoS_2 suspensions were deposited into a plastic Petri dish (Ø = 7 cm) and allowed to evaporate at room temperature for 48 h.

5.6. References

(1) Mas-Ballesté, R.; Gómez-Navarro, C.; Gómez-Herrero, J.; Zamora, F. 2D Materials: To Graphene and beyond. *Nanoscale* **2011**, *3*, 20–30.

(2) Novoselov, K. S.; Geim, A. K.; Morozov, S. V.; Jiang, D.; Zhang, Y.; Dubonos, S. V.; Grigorieva, I. V.; Firsov, A. A. Electric Field Effect in Atomically Thin Carbon Films. *Science* **2004**, *306*, 666–669.

(3) Zhang, Y.; Tan, Y. W.; Stormer, H. L.; Kim, P. Experimental Observation of the Quantum Hall Effect and Berry's Phase in Graphene. *Nature* **2005**, *438* (November), 201–204.

(4) Stoller, M. D.; Park, S.; Zhu, Y.; An, J.; Ruoff, R. S. Graphene-Based Ultracapacitors. *Nano Lett.* **2008**, *8*, 3498–3502.

(5) Lee, C.; Wei, X.; Kysar, J. W.; Hone, J. Measurement of the Elastic Properties and Intrinsic Strength of Monolayer Graphene. *Science* **2008**, *321* (2008), 385–388.

(6) Nair, R. R.; Grigorenko, A. N.; Blake, P.; Novoselov, K. S.; Booth, T. J.; Peres, N. M. R.; Stauber, T.; Geim, A. K. Fine Structure Constant Defines Visual Transparency of Graphene. *Science* **2008**, *320* (June), 1308.

(7) Zhang, Y. I.; Zhang, L.; Zhou, C. Graphene and Related Applications. *Acc. Chem. Res.* **2013**, *46*, 2329–2339.

(8) Baraton, L.; He, Z. B.; Lee, C. S.; Cojocaru, C. S.; Châtelet, M.; Maurice, J.-L.; Lee, Y. H.; Pribat, D. On the Mechanisms of Precipitation of Graphene on Nickel Thin Films. *EPL Europhys. Lett.* **2011**, *96*, 46003.

(9) Tromp, R. M.; Hannon, J. B. Thermodynamics and Kinetics of Graphene Growth on SiC(0001). *Phys. Rev. Lett.* **2009**, *102* (March), 1–4.

(10) Song, Can-Li; Wang, Yi-Lin; Jiang, Ye-Ping; Zhang, Yi; Chang, Cui-Zu; Wang, Lili; He, Ke; Chen, Xi; Jia, Jin-Feng; Wang, Yayu; Fang, Zhong; Dai, Xi; Xie, Xin-Cheng; Qi, Xiao-Liang; Zhang, Shou-Cheng; Xue, Qi-Kun; Ma, X. Topological Insulator Bi_2Se_3 Thin Films Grown on Double-Layer Graphene by Molecular Beam Epitaxy. *Appl. Phys. Lett.* **2012**, *97*, 143118.

(11) Lu, X.; Yu, M.; Huang, H.; Ruoff, R. S. Tailoring Graphite with the Goal of Achieving Single Sheets. *Nanotechnology* **1999**, *10*, 269–272.

(12) Moldt, T.; Eckmann, A.; Klar, P.; Morozov, S. V.; Zhukov, A. A.; Novoselov, K. S.; Casiraghi, C. High-Yield Production and Transfer of Graphene Flakes Obtained by Anodic Bonding. *ACS Nano* **2011**, *5*, 7700–7706.

(13) Dhar, S.; Barman, a. R.; Ni, G. X.; Wang, X.; Xu, X. F.; Zheng, Y.; Tripathy, S.; Ariando; Rusydi, A.; Loh, K. P.; Rubhausen, M.; Neto, A. H. C.; Zyilmaz, B.; Venkatesan, T. A New Route to Graphene Layers by Selective Laser Ablation. *AIP Adv.* **2011**, *1* (2011), 022109.

(14) Hernandez, Y.; Nicolosi, V.; Lotya, M.; Blighe, F. M.; Sun, Z.; De, S.; McGovern, I. T.; Holland, B.; Byrne, M.; Gun'Ko, Y. K.; Boland, J. J.; Niraj, P.; Duesberg, G.; Krishnamurthy, S.; Goodhue, R.; Hutchison, J.; Scardaci, V.; Ferrari, A. C.; Coleman, J. N. High-Yield Production of Graphene by Liquid-Phase Exfoliation of Graphite. *Nat. Nanotechnol.* **2008**, *3*, 563–568.

(15) Lotya, M.; King, P. J.; Khan, U.; De, S.; Coleman, J. N. High-Concentration, Surfactant-Stabilized Graphene Dispersions. *ACS Nano* **2010**, *4* (6), 3155–3162.

(16) Kumar, A.; Reddy, A. L. M.; Mukherjee, A.; Dubey, M.; Zhan, X.; Singh, N.; Ci, L.; Billups, W. E.; Nagurny, J.; Mital, G.; Ajayan, P. M. Direct Synthesis of Lithium-Intercalated Graphene for Electrochemical Energy Storage Application. *ACS Nano* **2011**, *5* (6), 4345–4349.

(17) Su, C.; Lu, A.; Xu, Y.; Chen, F.; Andrei, N. High Quality Thin Graphene Films from Fast Electrochemical Exfoliation-Supporting Information. **2011**, No. 3, 2332–2339.

(18) Choucair, M.; Thordarson, P.; Stride, J. A. Gram-Scale Production of Graphene Based on Solvothermal Synthesis and Sonication. *Nat. Nanotechnol.* **2009**, *4* (December 2008), 30–33.

(19) Bonaccorso, F.; Lombardo, A.; Hasan, T.; Sun, Z.; Colombo, L.; Ferrari, A. C. Production and Processing of Graphene and 2d Crystals. *Mater. Today* **2012**, *15* (12), 564–589.

(20) Gerald L. Kennedy, J. and H. S. Acute and Subchronic Toxicity of Dimethylformamide and Dimethylacetamide Following Various Routes of Administration. *Drug Chem. Toxicol.* **1986**, *9*, 147–170.

(21) Narayan, R.; Kim, S. O. Surfactant Mediated Liquid Phase Exfoliation of Graphene. *Nano Converg.* **2015**, *2*, 20–39.

(22) Xia, F.; Wang, H.; Xiao, D.; Dubey, M.; Ramasubramaniam, A. Two-Dimensional Material Nanophotonics. *Nat. Photonics* **2014**, *8* (12), 899–907.

(23) Miró, P.; Audiffred, M.; Heine, T. An Atlas of Two-Dimensional Materials. *Chem. Soc. Rev.* **2014**, *43*, 6537–6553.

(24) Novoselov, K. S.; Jiang, D.; Schedin, F.; Booth, T. J.; Khotkevich, V. V; Morozov, S. V; Geim, A. K. Two-Dimensional Atomic Crystals. *Proc. Natl. Acad. Sci. U. S. A.* **2005**, *102* (30), 10451–10453.

(25) Coleman, J. N.; Lotya, M.; O'Neill, A.; Bergin, S. D.; King, P. J.; Khan, U.; Young, K.; Gaucher, A.; De, S.; Smith, R. J.; Shvets, I. V.; Arora, S. K.; Stanton, G.; Kim, H.-Y.; Lee, K.; Kim, G. T.; Duesberg, G. S.; Hallam, T.; Boland, J. J.; Wang, J. J.; Donegan, J. F.; Grunlan, J. C.; Moriarty, G.; Shmeliov, A.; Nicholls, R. J.; Perkins, J. M.; Grieveson, E. M.; Theuwissen, K.; McComb, D. W.; Nellist, P. D.; Nicolosi, V. Two-Dimensional Nanosheets Produced by Liquid Exfoliation of Layered Materials. *Science* **2011**, *331*, 568–571.

(26) Zeng, Z.; Yin, Z.; Huang, X.; Li, H.; He, Q.; Lu, G.; Boey, F.; Zhang, H. Single-Layer Semiconducting Nanosheets: High-Yield Preparation and Device Fabrication. *Angew. Chemie - Int. Ed.* **2011**, *50*, 11093–11097.

(27) Zeng, Z.; Sun, T.; Zhu, J.; Huang, X.; Yin, Z.; Lu, G.; Fan, Z.; Yan, Q.; Hng, H. H.; Zhang, H. An Effective Method for the Fabrication of Few-Layer-Thick Inorganic Nanosheets. *Angew. Chemie - Int. Ed.* **2012**, *51*, 9052–9056.

(28) Smith, R. J.; King, P. J.; Lotya, M.; Wirtz, C.; Khan, U.; De, S.; O'Neill, A.; Duesberg, G. S.; Grunlan, J. C.; Moriarty, G.; Chen, J.; Wang, J. Z.; Minett, A. I.; Nicolosi, V.; Coleman, J. N. Large-Scale Exfoliation of Inorganic Layered Compounds in Aqueous Surfactant Solutions. *Adv. Mater.* **2011**, *23*, 3944–3948.

(29) Lee, Y. H.; Zhang, X. Q.; Zhang, W.; Chang, M. T.; Lin, C. Te; Chang, K. Di; Yu, Y. C.; Wang, J. T. W.; Chang, C. S.; Li, L. J.; Lin, T. W. Synthesis of Large-Area MoS_2 Atomic Layers with Chemical Vapor Deposition. *Adv. Mater.* **2012**, *24*, 2320–2325.

(30) Liu, B. K.; Zhang, W.; Lee, Y.; Lin, Y. Growth of Large-Area and Highly Crystalline MoS_2 Thin Layers on Insulating Substrates. *Nano Lett.* **2012**, *12*, 1538–1544.

(31) Wang, N.; Xu, Q.; Xu, S.; Qi, Y.; Chen, M.; Li, H. High-Efficiency Exfoliation of Layered Materials into 2D Nanosheets in Switchable CO2/surfactant/H2O System. *Sci. Rep.* **2015**, *5* (October), 16764.

(32) Kim, J.; Kwon, S.; Cho, D.-H.; Kang, B.; Kwon, H.; Kim, Y.; Park, S. O.; Jung, G. Y.; Shin, E.; Kim, W.-G.; Lee, H.; Ryu, G. H.; Choi, M.; Kim, T. H.; Oh, J.; Park, S.; Kwak, S. K.; Yoon, S. W.; Byun, D.; Lee, Z.; Lee, C. Direct Exfoliation and Dispersion of Two-Dimensional Materials in Pure Water via Temperature Control. *Nat. Commun.* **2015**, *6*, 8294.

(33) Zhan, Y.; Liu, Z.; Najmaei, S.; Ajayan, P. M.; Lou, J. Large-Area Vapor-Phase Growth and Characterization of MoS_2 Atomic Layers on a SiO_2 Substrate. *Small* **2012**, *8* (7), 966–971.

(34) Zhang, H. Ultrathin Two-Dimensional Nanomaterials. *ACS Nano* **2015**, *9*, 9451–9469.

(35) Fiori, G.; Bonaccorso, F.; Iannaccone, G.; Palacios, T.; Neumaier, D.; Seabaugh, A.; Banerjee, S. K.; Colombo, L. Electronics Based on Two-Dimensional Materials. *Nat. Nanotechnol.* **2014**, *9*, 768–779.

(36) Bonaccorso, F.; Colombo, L.; Yu, G.; Stoller, M.; Tozzini, V.; Ferrari, A. C.; Ruoff, R. S.; Pellegrini, V. 2D Materials. Graphene, Related Two-Dimensional Crystals, and Hybrid Systems for Energy Conversion and Storage. *Science* **2015**, *347* (January), 1246501.

(37) Chapin, D. M.; Fuller, C. S.; Pearson, G. L. A New Silicon P-N Junction Photocell for Converting Solar Radiation into Electrical Power. *J. Appl. Phys.* **1954**, *25*, 676–677.

(38) O'Regan, B.; Grätzel, M. A Low-Cost, High-Efficiency Solar Cell Based on Dye-Sensitized Colloidal TiO_2 Films. *Nature* **1991**, *353*, 737–740.

(39) Polo, A. S.; Itokazu, M. K.; Murakami Iha, N. Y. Metal Complex Sensitizers in Dye-Sensitized Solar Cells. *Coord. Chem. Rev.* **2004**, *248*, 1343–1361.

(40) Wu, J.; Lan, Z.; Hao, S.; Li, P.; Lin, J.; Huang, M.; Fang, L.; Huang, Y. Progress on the Electrolytes for Dye-Sensitized Solar Cells. *Pure Appl. Chem.* **2008**, *80* (11), 2241–2258.

(41) Thomas, S.; Deepak, T. G.; Anjusree, G. S.; Arun, T. A.; Nair, S. V; Nair, A. S. A Review on Counter Electrode Materials in Dye-Sensitized Solar Cells. *J. Mater. Chem. A Mater. Energy Sustain.* **2014**, *2*, 4474–4490.

(42) http://www.aerosil.com/product/aerosil/en/industries/electronics/dye-sensitized-solar-cells.

(43) Jasim, K. E. Dye Sensitized Solar Cells - Working Principles , Challenges and Opportunities. In *Solar cells-Dye sensitized devices*; Kosyachenko, L. A., Ed.; InTech, 2011.

(44) Papageorgiou, N. An Iodine/triiodide Teduction Electrocatalyst for Aqueous and Organic Media. *J. Electrochem. Soc.* **1997**, *144* (3), 876–884.

(45) Lee, Y. L.; Chen, C. L.; Chong, L. W.; Chen, C. H.; Liu, Y. F.; Chi, C. F. A Platinum Counter Electrode with High Electrochemical Activity and High

Transparency for Dye-Sensitized Solar Cells. *Electrochem. commun.* **2010**, *12* (11), 1662–1665.

(46) http://wraltechwire.com/business/tech_wire/news/blogpost/10536159/.

(47) Wu, M.; Ma, T. Recent Progress of Counter Electrode Catalysts in Dye-Sensitized Solar Cells. *J. Phys. Chem. C* **2014**, *118*, 16727–16742.

(48) Badhulika, S.; Terse-Thakoor, T.; Villarreal, C.; Mulchandani, A. Graphene Hybrids: Synthesis Strategies and Applications in Sensors and Sensitized Solar Cells. *Front. Chem.* **2015**, *3* (June), 38.

(49) Yella, A.; Lee, H.-W.; Tsao, H. N.; Yi, C.; Chandiran, A. K.; Nazeeruddin, M. K.; Diau, E. W.-G.; Yeh, C. Y.; Zakeeruddin, S. M.; Gratzel, M. Porphyrin-Sensitized Solar Cells with Cobalt (II/III)-Based Redox Electrolyte Exceed 12 Percent Efficiency. *Science* **2011**, *334* (2011), 629–634.

(50) Roy-mayhew, J. D.; Bozym, D. J.; Punckt, C.; Aksay, I. A. Functionalized Graphene as a Catalytic Counter Electrode in Dye Sensitized Solar Cells. *ACS Nano* **2010**, *4* (10), 6203–6211.

(51) Choi, H.; Kim, H.; Hwang, S.; Han, Y.; Jeon, M. Graphene Counter Electrodes for Dye-Sensitized Solar Cells Prepared by Electrophoretic Deposition. *J. Mater. Chem.* **2011**, *21*, 7548–7551.

(52) Kavan, L.; Yum, J.-H.; Grätzel, M. ESI: Graphene Nanoplatelets Outperforming Platinum as Electrocatalyst in Co-Bipyridine Mediated Dye-Sensitized Solar Cells. **2011**, *11*, 2–8.

(53) Mathew, S.; Yella, A.; Gao, P.; Humphry-Baker, R.; Curchod, B. F. E.; Ashari-Astani, N.; Tavernelli, I.; Rothlisberger, U.; Nazeeruddin, M. K.; Grätzel, M. Dye-Sensitized Solar Cells with 13% Efficiency Achieved through the Molecular Engineering of Porphyrin Sensitizers. *Nat. Chem.* **2014**, *6* (February), 242–247.

(54) Zhou, L.; Yang, X.; Yang, B.; Zuo, X.; Li, G.; Feng, A.; Tang, H.; Zhang, H.; Wu, M.; Ma, Y.; Jin, S.; Sun, Z.; Chen, X. Controlled Synthesis of $CuInS_2$/reduced Graphene Oxide Nanocomposites for Efficient Dye-Sensitized Solar Cells. *J. Power Sources* **2014**, *272*, 639–646.

(55) Kumar, N. A.; Dar, M. A.; Gul, R.; Baek, J. B. Graphene and Molybdenum Disulfide Hybrids: Synthesis and Applications. *Mater. Today* **2015**, *18*, 286–298.

(56) Lin, J. Y.; Chana, A. C. Y.; Choua, S. W. Electrophoretic Deposition of Transparent MoS2–graphene Nanosheet Composite Films as Counter Electrodes in Dye-Sensitized Solar Cells. *Chem. Commun.* **2013**, *49*, 1440–1442.

(57) Liu, C. J.; Tai, S. Y.; Chou, S. W.; Yu, Y.-C.; Chang, K. Di; Wang, S.; Chien, F. S.-S.; Lin, J. Y.; Lin, T. W. Facile Synthesis of MoS_2/graphene Nanocomposite with High Catalytic Activity toward Triiodide Reduction in Dye-Sensitized Solar Cells. *J. Mater. Chem.* **2012**, *22*, 21057.

(58) Lin, J. Y.; Yue, G.; Tai, S. Y.; Xiao, Y.; Cheng, H. M.; Wang, F. M.; Wu, J. Hydrothermal Synthesis of Graphene Flake Embedded Nanosheet-like Molybdenum Sulfide Hybrids as Counter Electrode Catalysts for Dye-Sensitized Solar Cells. *Mater. Chem. Phys.* **2013**, *143* (1), 53–59.

(59) David, L.; Bhandavat, R.; Singh, G. MoS_2/graphene Composite Paper for Sodium-Ion Battery Electrodes. *ACS Nano* **2014**, *8*, 1759–1770.

(60) Valentini, L.; Cardinali, M.; Fortunati, E.; Torre, L.; Kenny, J. M. A Novel

Method to Prepare Conductive Nanocrystalline Cellulose/graphene Oxide Composite Films. *Mater. Lett.* **2013**, *105*, 4–7.

(61) Valentini, L.; Cardinali, M.; Fortunati, E.; Kenny, J. M. Nonvolatile Memory Behavior of Nanocrystalline Cellulose/graphene Oxide Composite Films. *Appl. Phys. Lett.* **2014**, *105*, 153111.

(62) Valentini, L.; Bittolo Bon, S.; Fortunati, E.; Kenny, J. M. Preparation of Transparent and Conductive Cellulose Nanocrystals/graphene Nanoplatelets Films. *J. Mater. Sci.* **2014**, *49*, 1009–1013.

(63) Barwich, S.; Khan, U.; Coleman, J. N. A Technique to Pretreat Graphite Which Allows the Rapid Dispersion of Defect-Free Graphene in Solvents at High Concentration. *J. Phys. Chem. C* **2013**, *117*, 19212–19218.

(64) Bracamonte, M. V.; Lacconi, G. I.; Urreta, S. E.; Foa Torres, L. E. F. On the Nature of Defects in Liquid-Phase Exfoliated Graphene. *J. Phys. Chem. C* **2014**, *118*, 15455–15459.

(65) Lavin-Lopez, M. P.; Valverde, J. L.; Sanchez-Silva, L.; Romero, A. Solvent-Based Exfoliation via Sonication of Graphitic Materials for Graphene Manufacture. *Ind. Eng. Chem. Res.* **2016**, *55*, 845–855.

(66) Lotya, M.; Hernandez, Y.; King, P. J.; Smith, R. J.; Nicolosi, V.; Karlsson, L. S.; Blighe, M.; De, S.; Wang, Z.; Mcgovern, I. T.; Duesberg, G. S.; Coleman, J. N.; Blighe, F. M. Liquid Phase Production of Graphene by Exfoliation of Graphite in Surfactant / Water Solutions Liquid Phase Production of Graphene by Exfoliation of Graphite in Surfactant / Water Solutions. **2009**, No. 11, 3611–3620.

(67) Wang, S.; Yi, M.; Liang, S.; Shen, Z.; Zhang, X. The Effect of Surfactants and Their Concentrations on the Liquid-Exfoliation of Graphene.

(68) Carrasco, P. M.; Montes, S.; García, I.; Borghei, M.; Jiang, H.; Odriozola, I.; Cabañero, G.; Ruiz, V. High-Concentration Aqueous Dispersions of Graphene Produced by Exfoliation of Graphite Using Cellulose Nanocrystals. *Carbon N. Y.* **2014**, *70*, 157–163.

(69) O'Neill, A.; Khan, U.; Coleman, J. N. Preparation of High Concentration Dispersions of Exfoliated MoS_2 with Increased Flake Size. *Chem. Mater.* **2012**, *24*, 2414–2421.

(70) Nguyen, E. P.; Carey, B.; Daeneke, T.; Zhen, J.; Latham, K.; Zhuiykov, S.; Kalantar-zadeh, K.; Nguyen, E. P.; Carey, B. J.; Daeneke, T.; Ou, J. Z.; Latham, K. Investigation of Two-Solvent Grinding Assisted Liquid Phase Exfoliation of Layered MoS_2 Investigation of Two-Solvent Grinding Assisted Liquid Phase Exfoliation of Layered MoS_2. *Chem. Mater.* **2014**, *27*, 53–59.

(71) Nemes-Incze, P.; Osváth, Z.; Kamarás, K.; Biró, L. P. Anomalies in Thickness Measurements of Graphene and FLG Crystals by Tapping Mode AFM. *Carbon N. Y.* **2008**, *46*, 1435–1442.

(72) Lee, J.; Kim, M.; Cheong, H. Raman Spectroscopic Studies on Two-Dimensional Materials. **2015**, *45* (2011), 126–130.

(73) Tuinstra, F. Raman Spectrum of Graphite. *J. Chem. Phys.* **1970**, *53*, 1126–1130.

(74) Casiraghi, C.; Hartschuh, A.; Qian, H.; Pliscanec, S.; Georgia, C.; Fasoli, A.; Novoselov, K. S.; Basko, D. M.; Ferrari, A. C. Raman Spectroscopy of Graphene Edges. *Nano Lett.* **2009**, *9*, 1433–1441.

(75) Blackwell, J.; Vasko, P. D.; Koenig, J. L. Infrared and Raman Spectra of the Cellulose from the Cell Wall of Valonia Ventricosa. *J. Appl. Phys.* **1970**, *41* (1970), 4375–4379.

(76) Gupta, A.; Chen, G.; Joshi, P.; Tadigadapa, S.; Eklund, P. C. Raman Scattering from High-Frequency Phonons in Supported N-Graphene Layer Films. *Nano Lett.* **2006**, *6*, 2667–2673.

(77) Ferrari, A. C.; Meyer, J. C.; Scardaci, V.; Casiraghi, C.; Lazzeri, M.; Mauri, F.; Piscanec, S.; Jiang, D.; Novoselov, K. S.; Roth, S.; Geim, A. K. Raman Spectrum of Graphene and Graphene Layers. *Phys. Rev. Lett.* **2006**, *97*.

(78) Bertrand, P. A. Surface-Phonon Dispersion of MoS2. *Phys. Rev. B* **1991**, *44* (11), 5745–5749.

(79) Li, H.; Zhang, Q.; Yap, C. C. R.; Tay, B. K.; Edwin, T. H. T.; Olivier, A.; Baillargeat, D. From Bulk to Monolayer MoS_2: Evolution of Raman Scattering. *Adv. Funct. Mater.* **2012**, *22*, 1385–1390.

(80) Shimamoto, A.; Yamashita, K.; Inoue, H.; Yang, S.-M.; Iwata, M.; Ike, N. A Nondestructive Evaluation Method: Measuring the Fixed Strength of Spot-Welded Joint Points by Surface Electrical Resistivity. *J. Press. Vessel Technol.* **2013**, *135*, 0215011–0215017.

(81) Gilje, S.; Han, S.; Wang, M.; Wang, K. L.; Kaner, R. B. A Chemical Route to Graphene for Device Applications. *Nano Lett.* **2007**, *7*, 3394–3398.

(82) Kholmanov, I. N.; Magnuson, C. W.; Aliev, A. E.; Li, H.; Zhang, B.; Suk, J. W.; Zhang, L. L.; Peng, E.; Mousavi, S. H.; Khanikaev, A. B.; Piner, R.; Shvets, G.; Ruoff, R. S.; Ruo, R. S. Improved Electrical Conductivity of Graphene Films Integrated with Metal Nanowires. *Nanoletters* **2012**, *12*, 5679–5683.

(83) Woltornist, S. J.; Oyer, A. J.; Carrillo, J. M. Y.; Dobrynin, A. V.; Adamson, D. H. Conductive Thin Films of Pristine Graphene by Solvent Interface Trapping. *ACS Nano* **2013**, *7*, 7062–7066.

(84) Gomez De Arco L, Zhang Y, Schlenker, C. W., Ryu K, T. M. E.; Zhou, C. Continuous, Highly Flexible, and Transparent Graphene Films by Chemical Vapor Deposition for Organic Photovoltaics. *ACS Nano* **2010**, *4* (5), 2865–2873.

(85) Capasso, A.; Dikonimos, T.; Sarto, F.; Tamburrano, A.; De Bellis, G.; Sarto, M. S.; Faggio, G.; Malara, A.; Messina, G.; Lisi, N. Nitrogen-Doped Graphene Films from Chemical Vapor Deposition of Pyridine: Influence of Process Parameters on the Electrical and Optical Properties. *Beilstein J. Nanotechnol.* **2015**, *6*, 2028–2038.

(86) P.T. Kissinger and W.R. Heineman. Cyclic Voltammetry. *J. Chem. Ed. 60* **1983**, *60*, 702–706.

(87) Compton, R. G, Banks, C. E. *Understanding Voltammetry*; World Scientific: Singapore, 2007.

(88) http://physics.mff.cuni.cz/kfpp/povrchy/method/cv-principles.

(89) Elizabeth Santos, W. S. *Catalysis in Electrochemistry: From Fundamental Aspects to Strategies for Fuel Cell Development*; John Wiley & Sons, Ed.; Hoboken, New Jersey, 2011.

(90) Popov, A. I.; Geske, H. Studies on the Chemistry of Halogen and of Polyhalides. Iodine Species in Acetonitrile. *J. Am. Chem. Soc.* **1958**, *80* (10), 5346–5349.

(91) Lin, J.; Su, A.; Chang, C.; Hung, K.; Lin, T. Molybdenum Disulfide/reduced Graphene Oxide – Carbon Nanotube Hybrids as Efficient Catalytic Materials in Dye- Sensitized Solar Cells. *ChemElectroChem* **2015**, *2*, 720–725.